

Doctoral Dissertation
Doctoral Program in Metrology (34.th cycle)

# A new setup and methods for the fast production of ultracold atoms for atom-ion experiments

**Federico Berto**

* * * * *

**Supervisor**
Dr. C. Sias, Supervisor

Politecnico di Torino

I hereby declare that, the contents and organisation of this dissertation constitute my own original work and does not compromise in any way the rights of third parties, including those relating to the security of personal data.

. . . . . .

Federico Berto

Turin,

# Summary

Isolated quantum systems offer an ideal platform to study fundamental aspects of quantum physics and test emergent technological applications. Recent improvements in experimental techniques have made it possible to join different quantum systems in a single experimental setup, allowing for the study of their interaction and their enriched dynamics. Hybrid quantum systems of atoms and ions aim at bringing together ultracold atoms, which constitute the ideal playground for studying many-body physics, and trapped ions, which represent the ideal individual isolated quantum system. In these setups a key emerging feature is the atom-ion interaction, which originates from the dipole induced by the ion's charge on the approaching atom. Atom-ion systems have been proposed for a number of different experiments in the fields of quantum computation, quantum simulation, astrophysics, quantum chemistry, and metrology.

Atom-ion quantum systems require the integration of two complex setups, each dedicated to producing either cold atoms or cold ions. These two particles have considerable different production time scales: on the one hand, ions are generally produced by photo-ionization of hot atoms, and are trapped in deep Radio Frequency (RF) traps where fast cooling techniques (such as sideband cooling) are employed to bring the ion to its ground state of motion. The whole process can be completed in less than a second; furthermore, the same ion can be cooled and reused multiple times in an experiment. On the other hand, atoms must be first slowed and trapped using magneto-optical techniques, and are brought to degeneracy using evaporative cooling. In general, this process can take up to tens of seconds. Therefore, the preparation of a cold cloud of neutral atoms represent the major bottleneck to achieve a high repetition rate to perform repeated measures. For this reason, the development of new fast cooling techniques is a necessary step to streamline the experimental procedure in atomic physics setups.

This thesis examines a novel scheme for the fast cooling of neutral $^6$Li atoms. This new cooling scheme makes use of deep optical potentials generated using a cavity-enhanced optical lattice and resolved single-photon sideband cooling to cool particles toward their ground state of motion. First, a mathematical model of sideband cooling in optical potentials is developed. The model describes the vibrational state of particles trapped in non-harmonic state-dependent optical potentials.

Numeric simulations performed using wavefunction Monte Carlo show that, in experimentally feasible conditions, it is possible to reduce the particles' vibrational energy by more than 95 % of its initial value using a laser frequency sweep a few ms long.

A two-mirror high-finesse optical resonator was designed to be used for sideband cooling and evaporative cooling of the $^6$Li atoms. The resonator is made of vacuum-compatible materials and it is installed inside the chamber where $^6$Li atoms are prepared. The assembled resonator was characterized using optical techniques: the cavity finesse and linewidth were determined to be 28 800(80) and 78.6(2) kHz, respectively. Thanks to such a high finesse, a low-power laser diode coupled to the cavity can achieve an optical lattice sufficiently deep to perform single-photon sideband cooling. Due to the small cavity linewidth, considerable work has been done to characterize the coupled laser and its noise power spectrum.

# Acknowledgements

I would like to thank Prof. Inguscio Massimo and my supervisor Dr. Sias Carlo for giving me the opportunity of working on the interesting and ambitious project of developing the first hybrid quantum system in Italy. I thank Carlo in particular, for his constant support throughout this work, and his help in revising this thesis report. I sincerely wish him all the best for the continuation of his laboratory.

I would like to thank my colleagues Dr. Duca Lucia, Dr. Perego Elia, Dr. Detti Amelia for the time we spent together. Specifically, I thank Lucia for her patient with my novice questions and her help in several parts of this project. I give thanks to Elia for the time we spent talking about programming, which was inspirational and instructive. I thank Amelia for helping orient myself in the lab during the initial phase of my doctorate.

I'm extremely grateful for all the technical help and advice I received during these years, and I must acknowledge the devoted technicians working at LENS. I'm grateful to Giuntini Mauro for his infinite patience, for always finding time to answer my questions, even when overwhelmed by other jobs. His teachings on electronics were fundamental for several parts of this project. I want to pay special regards to Concas Roberto for all the time we wasted chit-chatting (which always brightened my day), for his tolerant attitude whenever we came up with some crazy project, and for all the wise advises in both electronic and life. I also thank Montori Alessio and Saverio Bartalini for their efforts in helping us fix the problem with our lithium laser system. Finally, I express my gratitude to Ballerini Riccardo for his support with our mechanics-related projects and issues, and for his constant reprimands of my naive mistakes, which were most instructive.

I would also like to thank the colleagues from the LiLab for their help any time we needed an instrumentation, suggestion on the lithium setup. In particular, I thank Dr. Roati Giacomo, for allowing us to borrow several material from his laboratory when we most needed it ... although I'm sure some components never came back. I'm grateful to Giulia and Alessandro for answering any of my questions related to their setup, and for their help in comparing the laser frequencies between our laboratories. I must also say thanks to Francesco for his valuable advices and suggestions on cavity systems, and for the beers we shared.

I cannot ignore all the help I've received from several laboratories around LENS

and UniFi throughout this project. Specifically, I would like to thank all the people from the K/Rb lab, from the Yb lab, and from the Cr/Li. Special thanks go to Dr. Trenkwalder Andreas for his invaluable help in several technical and experiment-related issues.

I'm grateful to Dr. Bertaina Gianluca for his help in performing Monte Carlo numerical simulations on the institute workstation.

The majority of data analysis and simulation presented in this project was performed using the open-source scientific Python framework. I'm extremely grateful to all the women and men that invest their time to develop and maintain the SciPy code and community.

All of this work would not have been possible if not for my life partner Aleksandra, she helped me and guided me through my darkest moments. Without her wisdom and experience I'm not sure this PhD would have found its completion. Thank you from the bottom of my heart.

Finally, I'm very grateful to my loving parents for their constant moral support in these years, which has been invaluable in helping me see this project to its end and giving me hope for my future.

# Contents

**List of Tables** XI

**List of Figures** XII

**List of Acronyms** XIV

**Introduction** 1

**1 Theory of atom-ion interactions** 5
- 1.1 Atom-ion collision theory . . . 5
  - 1.1.1 Elastic collisions . . . 6
  - 1.1.2 Inelastic collisions . . . 9
- 1.2 Applications . . . 11
  - 1.2.1 Quantum computation . . . 12
  - 1.2.2 Quantum simulation . . . 12
  - 1.2.3 Quantum chemistry . . . 13
  - 1.2.4 Metrology . . . 14

**2 Semiclassical theory of laser cooling** 15
- 2.1 Physics of neutral atom cooling . . . 15
  - 2.1.1 Laser cooling . . . 15
  - 2.1.2 Deceleration of an atomic beam . . . 19
  - 2.1.3 Optical molasses . . . 21
  - 2.1.4 Magneto-optical traps . . . 22
  - 2.1.5 Sub-Doppler cooling . . . 25
  - 2.1.6 Dipolar traps and evaporative cooling . . . 30
- 2.2 Physics of ion cooling and trapping . . . 32
  - 2.2.1 The linear Paul trap . . . 32
  - 2.2.2 Optical traps . . . 35
- 2.3 $Ba^+Li$ Physics . . . 36
  - 2.3.1 The $Ba^+Li$ experiment . . . 39

**3 Lithium setup** 41
3.1 Vacuum setup . . . 41
3.1.1 Lithium oven . . . 43
3.1.2 Zeeman slower . . . 44
3.1.3 MOT chamber . . . 46
3.1.4 MOT coils . . . 47
3.1.5 Sapphire window section . . . 50
3.1.6 System bake-out & oven loading . . . 52
3.2 Laser setup . . . 56
3.2.1 Optical breadboards . . . 56
3.2.2 Laser locking scheme . . . 65
3.2.3 Electro-optic modulator . . . 67
3.2.4 Experiment-side optics . . . 72
3.3 Magneto-Optical Trap of lithium . . . 75

**4 High-Finesse optical resonator** 79
4.1 General description of an optical cavity . . . 79
4.1.1 Stability condition of a linear cavity . . . 80
4.1.2 Eigenmodes . . . 81
4.1.3 Cavity losses . . . 82
4.1.4 Mode matching and misalignment of the input beam . . . 83
4.2 The lithium optical resonator . . . 84
4.2.1 Mechanical design . . . 85
4.2.2 Cavity alignment and characterization . . . 87
4.3 903nm laser linewidth . . . 93
4.3.1 Characterization of the 903 nm laser . . . 97

**5 Single photon sideband cooling in state-dependent potentials** 103
5.1 Sideband cooling in optical potentials . . . 103
5.2 1D mathematical model . . . 105
5.2.1 System Hamiltonian . . . 105
5.2.2 Spontaneous emission and master rate equation . . . 108
5.3 Sideband cooling of TLS in optical tweezers . . . 112
5.3.1 Numerical simulation of sideband cooling . . . 114
5.3.2 Wavefunction Monte Carlo simulation . . . 118
5.3.3 Results . . . 120
5.4 Sideband cooling of Lithium in optical lattice . . . 123

**6 Conclusions** 129

**A Drawings of MOT coils supports** 131

**B Drawings of Li optical resonator supports** 133

**C RWA and rotating-frame transformation** 137
C.1 Rotating wave approximation (RWA) . . . . . 137
C.2 Rotating frame transformation . . . . . 138

**D Equivalence of existing sideband cooling models** 141

**E Ion detection algorithm** 143
E.1 Implementation . . . . . 143

# List of Tables


1.1 List of possible inelastic processes in atom-ion hybrid systems. . . . 9
3.1 List of the target detunings with respect to the D1 or D2 transitions of the light beams that are needed to cool and trap fermionic lithium atoms. . . . 56
3.2 List of the laser light powers used in the preparation of the lithium Magneto-Optical Trap (MOT). . . . 76
4.1 Physical characteristics of the lithium high-finesse cavity and the mirrors used there in. . . . 85
5.1 Parameters used for simulating sideband cooling of a TLS trapped in an optical tweezer. . . . 113
5.2 Physical parameters of the trap used in the sideband cooling simulation. . . . 114

# List of Figures


1.1 Atom-ion effective interaction potential . . . 7
2.1 Velocity-dependent damping force in OM. . . . 22
2.2 Schematic diagram of MOT beams and atomic energy levels in 1D. 23
2.3 Processes leading to either heating or cooling for a trapped particle in the Lamb-Dicke regime. . . . 29
2.4 Grotrian diagram showing the ground and lowest excited states of $^{138}Ba^{+}$ [154]. . . . 38
2.5 Grotrian diagram showing the ground and lowest excited states of $^{6}Li$ [154]. . . . 38
2.6 3D CAD view of the complete vacuum setup at the $Ba^{+}Li$ experiment. 39
3.1 3D CAD view of the lithium vacuum setup at the $Ba^{+}Li$ experiment. 42
3.2 3D CAD view of the lithium oven and collimator. . . . 42
3.3 3D CAD view of the lithium oven section. . . . 44
3.4 3D CAD view of the lithium Zeeman slower coils and differential pumping section. . . . 45
3.5 Top-down view of the MOT chamber. . . . 46
3.6 3D CAD view of the MOT coils holder. . . . 49
3.7 FEM CHT simulation results of the MOT coils holder steady-state temperature. . . . 50
3.8 3D CAD view of the lithium sapphire window section. . . . 51
3.9 Lithium oven transversal fluorescence versus laser detuning. . . . 55
3.10 Optical circuit of the lithium board 1. . . . 58
3.11 Fibre polarization misalignment error versus waveplate angle. . . . 59
3.12 Optical circuit of the lithium board 2. . . . 61
3.13 Exploded view of the 3D CAD for the custom made TA opto-mechanics. 62
3.14 Power amplification (in dB) as a function of TA current. . . . 63
3.15 Optical circuit of the lithium board 3. . . . 64
3.16 Circuit schematic used for D1-D2 lasers offset lock. . . . 65
3.17 Schematic of the EOM electric circuit. . . . 69
3.18 CAD representation of the EOM assembly. . . . 71
3.19 EOM resonance frequency measured on the VNA $S_{12}$ parameter trace. 71
3.20 Optical circuit of the ZS breadboard placed on experimental table. . 72

3.21 Optical circuit of the MOT breadboard on the experimental table. . 73
3.22 Optical circuit for the MOT-z and imaging optics. . . . . 75
3.23 Photo of a cloud of lithium atoms trapped in the MOT at the $Ba^+Li$ experiment. . . . . 77
4.1 Spectrum of a non-degenerate Fabry-Perot resonator. . . . . 82
4.2 3D CAD view of the cavity supports. . . . . 86
4.3 Optical circuit schematic for coupling light from a fibre launcher to the lithium optical resonator. . . . . 87
4.4 Excited transversal modes observed during cavity alignment. . . . . 89
4.5 3D CAD view of the optomechanics used for coupling light to the lithium optical resonator. . . . . 91
4.6 Cavity transmission spectrum. . . . . 92
4.7 Cavity energy decay measured with ring-down method. . . . . 92
4.8 Schematic drawing of the setup for PDH stabilization. . . . . 94
4.9 903 nm laser frequency noise PSD. . . . . 98
4.10 903 nm laser frequency noise PSD with locking feedback loop. . . . 99
4.11 PID topology for laser frequency stabilization. . . . . 100
5.1 Sketch of optical trap potential and excitation spectrum. . . . . 111
5.2 Average occupation number as a function of time during sideband cooling. . . . . 120
5.3 Wigner quasiprobability distribution before and after cooling of Yb. 121
5.4 Average occupation number after the frequency sweep of the cooling laser versus the ground state Lamb-Dicke parameter. . . . . 122
5.5 Average occupation number after cooling versus the difference in polarizability $\Delta\alpha$. . . . . 123
5.6 Average occupation number after cooling versus the sweep duration $T_{\mathrm{sw}}$. . . . . 124
5.7 Average occupation number of Li atoms as a function of time. . . . 126
5.8 Final average occupation number as a function of the atoms' position along the trap radial axis $x$. . . . . 128
E.1 Visual representation of various steps of the ion-detection algorithm. 144

# List of Acronyms

| | |
|---|---|
| AOM | Acusto-Optic Modulator |
| BS | Beamsplitter |
| CAD | Computed-Aided Design |
| CCD | Charge-Coupled Device |
| CHT | Conjugate Heat Transfer |
| CM | Centre of Mass |
| cMOT | compressed Magneto-Optical Trap |
| ECDL | Extended-Cavity Diode Laser |
| EOM | Electro-Optical Modulator |
| FEM | Finite Element Model |
| FSR | Free Spectral Range |
| FWHM | Full Width Half Maximum |
| HFS | Hyperfine Structure |
| MOT | Magneto-Optical Trap |
| NEG | Non-Evaporative Getter |
| OBE | Optical Bloch Equations |
| ODT | Optical Dipole Trap |
| OM | Optical Molasses |
| PBS | Polarizing Beamsplitter |
| PCB | Printed Circuit Board |

PDH . . . . . Pound-Drever-Hall

PID . . . . . Proportional-Integral-Derivative

PSD . . . . . Power Spectral Density

PZT . . . . . Piezoelectric Transducer

RF . . . . . Radio Frequency

RMS . . . . . Root Mean Squared

RoC . . . . . Radius of Curvature

RPi . . . . . Raspberry Pi

RWA . . . . . Rotating Wave Approximation

TA . . . . . Tapered Amplifier

TLS . . . . . Two-Level System

TSP . . . . . Titanium Sublimation Pump

UHV . . . . . Ultra-High Vacuum

VNA . . . . . Vector Network Analyser

WFMC . . . . . Wavefunction Monte Carlo

ZS . . . . . Zeeman Slower

# Introduction

In the last decades, considerable progress has been made in the experimental preparation and manipulation of isolated quantum systems. Highly controllable and reproducible quantum systems can be used to study and test fundamental aspects of quantum physics as well as benchmark platforms for emergent technological applications (for example the newly emerged field of quantum technologies). A single atom represents one of the most fundamental quantum systems, with a well-known internal structure that can be manipulated using laser light. Thanks to improvement of experimental techniques as well as development in the Ultra-High Vacuum (UHV) industry and laser technology, it has become possible in recent years to trap ultracold clouds of atoms and single atoms or ions with a high degree of reproducibility. These systems can be prepared in a defined quantum state and used for fundamental or application-oriented studies and have led to several breakthroughs in atomic physics, condensed matter physics and in the field of quantum technologies.

Degenerate ultracold atoms constitute an ideal platform for studying many-body physics, where purely quantum mechanical effects become relevant at macroscopic scales. Nowadays, it is possible to exert a high degree of control over ultracold atomic clouds and tailor their Hamiltonian to study a specific coherent evolution [1]: inter-atom interactions can be tuned either magnetically (through Feshbach resonances [2]) or through field-induced long-range interactions (*e.g.* Rydberg excitations [3]) and can be made either attractive or repulsive. Optical traps, such as optical lattices obtained from interference of multiple laser beams, can be used to define potentials of arbitrary geometry and dimensionality [4, 5, 6]. Thanks to these capabilities, ultracold atoms have been extensively used to study weak and strong correlation effects in Bose-Einstein condensates and fermions paring in fermionic mixtures [7], cavity-QED [8], many-body physics [9, 10], and to perform quantum simulation [11, 12, 13], quantum information processing [14] and quantum metrology [15, 16].

Conversely, trapped ions represent the ideal isolated quantum system. Particles can be trapped using RF electric fields for very long times (up to months [17]) and can be prepared in a defined internal and motional state using optical pumping and resolved sideband cooling [18]. Once cooled, ions present extremely long

coherence times (more than one hour [19]), making it possible to perform precise measurements on the system useful for advancing metrology standards [20, 21]. At low temperatures, multiple ions trapped in the same RF trap can crystallize forming Coulomb crystals [22]. These ordered structures are of particular interest for studying few-body dynamics [23], stellar dynamics [24], performing quantum simulation [25] and implementing quantum gates [26]. Recently, a compact ion-based quantum computer that fits in a 19-inch rack and that can prepare up to 24 maximally-entangled qubits was demonstrated [27].

Cold hybrid atom-ion experiments aim at bringing together ultracold atoms and ions into a single experimental setup. These hybrid experiments exploit the best of both subsystems: on the one hand, ion traps allow for high spatial localization and precise positioning of the ions while still being able to address each ion separately; on the other hand, atomic systems offer scalability and long coherence times. The two subsystems have complementary features and enrich the dynamics of the hybrid setup: for example, long-range interactions mediated by phonons between trapped ions are not present in ultracold atomic systems [28], which may lead to complex dynamics in the atomic cloud. The key emerging feature of the atom-ion mixture is the atom-ion interaction, which originates from the dipole induced by the ion's charge on the approaching atom. This force has a characteristic range that is approximately two orders of magnitude larger than atom-atom (van der Waals) interactions. At low enough temperatures these interactions are magnetically tunable and present Feshbach resonances [29], and open the possibility of study different dynamics so far unseen. Most recently, Feshbach resonances have been observed between optically-trapped $^{138}Ba^{+}$ ions and $^{6}Li$ ultracold atoms [30].

Thanks to the afore mentioned properties, cold hybrid atom-ion systems have been proposed for a number of different experiments aimed at both studying fundamental physics and advancing technological applications: further understanding of the complex atom-ion dynamics is a necessary step to engineer future experiments [28], ions can act as reaction centres and promote chemical reactions such as charge exchange and molecule formation [31, 32] enabling control of chemical processes at a single particle level [33, 34]. Cold atom-ion collisions are also of interest for astrochemistry since similar collisional processes occur in interstellar clouds [35]. Hybrid atom-ion experiments have been proposed as possible quantum simulators for mimicking solid-state systems [36] and studying out-of-equilibrium phenomena, such as the Anderson orthogonality catastrophe [37]. Sympathetic cooling [38] of trapped ions via elastic collisions with ultracold atoms offers an additional method to cool ions with a complex internal structure [39] as well as the motional state of a trapped ions-based quantum computer. Finally, the immersion of charged particles in a fluid allows performing precise measurement of the density and the density-density correlations in the quantum gas [40].

Hybrid atom-ion experimental setups are extremely demanding from a technical point of view as they require the design and assembly of a hybrid trap capable

of trapping both ions and atoms in the same location. For this reason, only a few hybrid systems have been realized thus far [41, 42, 43, 44, 45, 46, 47, 48] (a more exhaustive list of existing experiments and their aim can be found in ref.s [28, 49, 50]). Different experiments make use of different trap configurations or atomic species combinations in order to enhance or suppress different dynamics in the combined atom-ion system. A major technical challenge consist in reducing the ion residual motional energy. In the majority of experiments the atom-ion collisional energy is determined by the residual ion micromotion in the RF trap [48], which prohibits the possibility of reaching the low temperatures required for the coherent evolution of the atom-ion mixture. In order to overcome this limitation, alternative ion trapping methods have been proposed: optical traps — both tweezers or lattices — for ions have been demonstrated [51, 52], electro-optical traps promise to be a compelling alternative [53]. Highly-excited Rydberg atoms [54] or photo-ionized atomic ions [55] can be created directly inside the cold atomic cloud using femtosecond laser pulses, removing the issue of micromotion but limiting the duration of the interaction.

The work presented in this P.h.D. thesis is part of a research effort that aims at realizing an ultracold mixture of lithium atoms and barium ions at LENS, Florence, Italy. In particular, this thesis examines, both theoretically and experimentally, the problem of quickly producing a cloud of ultracold lithium atoms, which will eventually interact with trapped $Ba^+$ ions. Repeated measures are required to accumulate statistically significant data. Therefore, a high repetition rate of the experimental procedure is ideal. On the one hand, ion trapping experiments can achieve a high repetition rate (on the order of 100 Hz) since the particles remain confined in the deep electric trap at the end of the experimental cycle, and reloading the ions is not necessary unless an inelastic collision (e.g. a chemical reaction) occurred. On the other hand, the preparation of ultracold atoms remain a major bottleneck: the experimental cycle in atom-ion experiments can take up to a minute [56]. The major portion of the work presented in this thesis is the conception of a novel cooling scheme that allows for the fast production of cold atomic gasses, and the design of parts of the experimental setup used in the production of ultracold $^6$Li atoms.

The choice of barium and lithium as the elements forming the atom-ion mixture is based on a number of considerations: first, unwanted charge-exchange collisions of the kind $Li + Ba^+ \rightarrow Li^+ + Ba$ are energetically forbidden in the ground state. Second, barium and lithium have a large mass ratio, which favours ion trapping and cooling in a Paul trap in the presence of neutral atoms [57, 58]. Finally, $^6$Li is a fermionic isotope that gives the possibility of controlling the atom-atom interactions, which can be set to zero (*e.g.* by using a spin-polarized Fermi gas) or to a specific value by using magnetic Feshbach resonances. The strategy for the production of the atom-ion mixture at the $Ba^+$Li experiment is to realize the two quantum systems separately in two connected UHV chambers, and then move the ultracold lithium cloud via optical transport. To overcome the high collisional

energy set by the residual ion micromotion observed in RF traps, this experiment aims at using of a novel electro-optical trap [53].

# Chapter 1

# Theory of atom-ion interactions

In this chapter a brief overview of atom-ion interaction theory is given. Section 1.1 presents the theory of atom-ion collisions and describes the different types of collision events (elastic or inelastic). Section 1.2 provides an overview of existing experiments and applications of atom-ion hybrid setups.

## 1.1 Atom-ion collision theory

The interaction between a charged atomic ion and a neutral atom is dominated by the ion's own electric field $\mathcal{E}(r) = Ze_0/(4\pi\epsilon_0 r^2)$, where $r$ is the distance between atom and ion, $\epsilon_0$ is the vacuum permittivity and $Ze_0$ is the ion charge. The dipole moment induced by the ion electric field is $p(r) = \alpha_0\mathcal{E}(r)$, where $\alpha_0$ is the static polarizability of the atom. As a result, the atom experiences an attractive force toward the ion caused by the potential

$$V(r) = -p(r)\mathcal{E}(r) = -\frac{C_4}{r^4}\,, \tag{1.1}$$

where $C_4 = \alpha_0 Z^2 e_0^2/(4\pi\epsilon_0)^2$. It is important to note that in writing eq. (1.1) a few implicit assumptions have been made: the additional quadrupole terms (decreasing as $r^{-6}$) have been neglected [28] and both the atom and the ion are assumed to be in a state with zero orbital angular momentum. Equation (1.1) only describes the long-range asymptotic behaviour of the interaction potential, at close range the interaction is dominated by the so-called *hard-core* short-ranged repulsion.

### 1.1.1 Elastic collisions

#### Classical approximation

In classical dynamics, collisions between two point particles can be described in terms of the impact parameter $b$, which represent the minimum distance between the two particles along unperturbed trajectories. In the Centre of Mass (CM) reference frame the energy associated with the relative motion of the particles is $E_{\text{coll}} = \mu v^2/2$ and the total angular momentum is $L = b\mu v$, where $\mu = m_{\text{ion}} m_{\text{atom}}/(m_{\text{ion}} + m_{\text{atom}})$ is the reduced mass and $v$ is the particles relative velocity. Due to the specific $r^{-4}$ asymptotic behaviour of the interaction potential, a critical value of the impact parameter can be defined: $b_c = (2C_4/E_{\text{coll}})^{1/4}$. If $b > b_c$ the collision is called *forward collision*[1] since the particles trajectories are only slightly curved toward the CM. On the other hand, if $b < b_c$ the particles approach at a short distance, and the collision is dominated by the hard-core repulsive potential. These collisions are referred to as *Langevin collisions* [59].

In first approximation, the scattering cross-section can be computed by taking into account only Langevin collisions contributions since these are the only collisions in which particles exchange a considerable amount of momentum. The Langevin cross-section is then given by

$$\sigma_{\text{Lang}} = \pi b_c^2 = \pi \sqrt{\frac{2C_4}{E_{\text{coll}}}}\,.$$

It follows from this result that the collisional rate $\Gamma = nv\sigma_{\text{Lang}}$ is independent on the collisional energy, but only depends on the particles density $n$ and their physical properties.

#### Semi-classical approximation

In order to discuss the collision between atom and ion at ultracold temperatures, a quantum treatment of the process is necessary. The Schrödinger equation describing the relative motion of two interacting particles can be written, most generally, as

$$\left(-\frac{\hbar^2}{2\mu}\boldsymbol{\nabla}^2 + V(r) + H_0\right)\Psi(\mathbf{r}) = E\Psi(\mathbf{r})\,,$$

where the first term on the left-hand side is the kinetic energy associated with the relative motion, the second term is the interaction potential, $H_0 = H_{\text{atom}} + H_{\text{ion}}$ is the particles rest Hamiltonian. Since the problem is separable, the wavefunction $\Psi$ can be written as sum of spherical harmonics $Y_{l,m}(\theta, \phi)$

[1] In literature, forward collisions are also called soft collisions.

$$\Psi(r,\theta,\phi) = \sum_{l,m} \frac{R_{l,m}(r)}{r} Y_{l,m}(\theta,\phi)\,,$$

where $R_{l,m}(r)$ are the radial wavefunctions. The summation terms that differ in the quantum number $l$ are usually referred to as *partial waves* or $l$-waves. The radial wavefunctions respect the one-dimensional radial Schrödinger equation

$$\left(-\frac{\hbar^2}{2\mu}\nabla^2 + V(r) + \frac{\hbar^2}{2\mu}\frac{l(l+1)}{r^2}\right) R_{l,m}(r) = E R_{l,m}(r)\,,$$

where the third term on the left-hand side is the so-called *centrifugal potential*, and its strength depends on the angular momentum $l\hbar$. The sum of the potential $V(r)$ and the centrifugal potential is usually called *effective potential*, and its shape is shown in fig. 1.1.

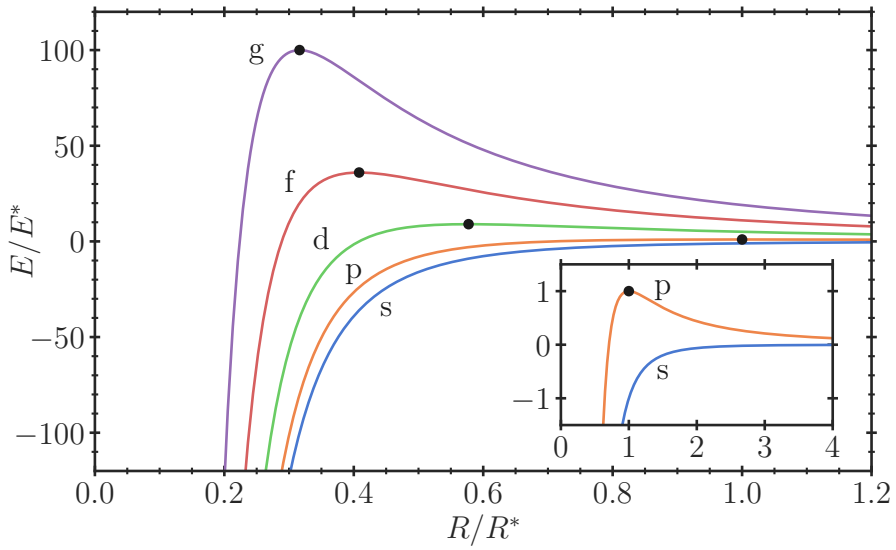


Figure 1.1: Effective potential for different values of $l$ quantum number as a function of the distance between atom and ion in units of characteristic energy $E^*$ and characteristic length $R^*$. The Black dots indicate the positions of the centrifugal barrier maxima. Inset shows a zoom on the two lowest potential curves.

The location and height of the maximum of the centrifugal barrier are given by:

$$R_l^{\max} = \sqrt{\frac{2}{l(l+1)}}R^*, \qquad E_l^{\max} = \frac{l^2(l+1)^2}{4}E^*,$$

where $R^* = \sqrt{(2\mu C_4)/\hbar^2}$ is the characteristic length of the potential, and $E^* = \hbar^2/(2\mu(R^*)^2)$ is the characteristic energy, which determines the onset of the s-wave regime.

The total cross section of a scattering from a central potential can always be written as the sum of scattering cross-sections of different partial waves (ref. [60], page 120):

$$\sigma = \frac{4\pi}{k_{\text{coll}}^2} \sum_{l=0}^{\infty} (2l+1) \sin(\delta_l) \,,$$

where $\hbar k_{\text{coll}} = \sqrt{2\mu E_{\text{coll}}}$ is the momentum of the colliding particles. It is noticeable that the total scattering cross-section is completely determined once the phase shifts $\delta_l$ are given. In order to calculate the contributions from the partial waves with $l < L$, the exact shape of the hard-core potential must be known. Determination of the hard-core shape thought *ab initio* calculations is not possible and requires the theoretical calculations to be corrected using experimental data [61]. Without *a priori* knowledge of the hard-core potential, it is reasonable to assume that the phase shifts are uniformly distributed, and that their sine can approximated with the average value: $\sin(\delta_l) \approx 1/2$ for $l < L$. For partial waves with $l > L$ the semi-classical approximation,

$$\delta_l \approx \frac{\pi \mu^2 C_4}{4\hbar^4} \frac{E_{\text{coll}}}{l^3} \,,$$

can be used. The total scattering cross-section then results [62]:

$$\sigma = \pi \left( \frac{\mu C_4^2}{\hbar^2} \right)^{1/3} \left( 1 + \frac{\pi^2}{16} \right) E_{\text{coll}}^{-1/3} \,.$$

It follows that the collisional rate is not energy independent but goes as $E_{\text{coll}}^{-1/6}$.

For a given $E_{\text{coll}}$ it can be seen that there exists an angular momentum $L = (1/\hbar)\sqrt{(2\mu\sqrt{2C_4 E_{\text{coll}}})}$ such that only partial waves with $l < L$ provide a non-negligible contribution to the scattered wave phase shift. The reason for this is that, for partial waves with $l > L$, the classical inversion point (where the height of the barrier is equal to the collisional energy) is found at large values of $r$ where $V(r) \approx 0$. Therefore, these partial waves will be barely influenced by the potential $V$ and will have small phase shifts (ref. [60], page 121). It follows that the main contributions to the dynamics are given by partial waves from $l = 0$ to a maximum $l \approx L$. The same result can be explained by noting that as $l$ increases also the barrier height $E_l^{\max}$ increases, therefore, partial waves with a high $l$ value will provide little contribution to the collisional physics, unless effects of resonant tunnelling through the centrifugal barrier are present. The cases of scattering with partial waves having $l < L$ or $l > L$, correspond to the afore mentioned Langevin collisions and forward collisions, respectively.

This marks the importance of studying collisions in the ultracold regime: if many partial waves are involved in the collision, then each contributes to the dynamics with widely different phase shifts incoherent from each other. Hence, the dynamics

are classical. Conversely, if only the s-wave ($l = 0$) provides a non-negligible phase shift, then the dynamical evolution of the colliding particles is purely quantum, and effects such as Feshbach resonances can be observed.

### 1.1.2 Inelastic collisions

Atom and ions can undergo *inelastic collisions*, these are events in which the particles' internal state is changed. Inelastic collision that lead to changes in the chemical nature of the colliding particles are sometimes referred to as *reactive collisions*.

The scattering cross-section for inelastic collisions can be determined, in first approximation, by considering that inelastic processes are dominated by the scattering potential at small internuclear distances [63]. Thus, in the semiclassical view, only partial waves with $l < L$ will contribute to the inelastic processes. Classically, this means that inelastic collisions occur with a maximum impact parameter $b_c$, therefore, the scattering cross-section for inelastic events corresponds to the classical Langevin cross-section:

$$\sigma_{\text{in}} = \pi b_c^2 = \sigma_{\text{Lang}} \,.$$

The semiclassical calculation (summing all partial waves up to $L$ with $\sin(\delta_l) \approx 1/2$) would give the same result times a factor of two.

| | | | | | | | |
|---|---|---|---|---|---|---|---|
| $A^+\|\uparrow\rangle$ | + | $B\|\downarrow\rangle$ | $\rightarrow$ | $A^+\|\downarrow\rangle$ | + | $B\|\uparrow\rangle$ | Spin-exchange |
| $A^+\|\uparrow\rangle$ | + | $B\|\uparrow\rangle$ | $\rightarrow$ | $A^+\|\downarrow\rangle$ | + | $B\|\uparrow\rangle$ | Spin-relaxation |
| $A^+$ | + | B | $\rightarrow$ | A | + | $B^+ + \gamma$ | Radiative charge exchange |
| $A^+$ | + | B | $\rightarrow$ | A | + | $B^+$ | Non-radiative charge exchange |
| $A^+$ | + | 2 B | $\rightarrow$ | $A^+$ | + | $B_2$ | Three-body recombinations |
| $(A^+)^*$ | + | B | $\rightarrow$ | $A^+$ | + | B | Quenching reaction |
| $A^+$ | + | B | $\rightarrow$ | $(A\,B)^+$ | | | Formation of charged molecules |

Table 1.1: List of possible inelastic processes in atom-ion hybrid systems.

Inelastic events also differentiate based on whether the energy change in the internal state is released through a photon (radiative processes) or by increasing the kinetic energy of the particles (non-radiative processes), both processes can occur with considerably different rates. Table 1.1 shows a list of inelastic processes that have been observed and characterized experimentally in hybrid atom-ion systems.

#### Spin-exchange and spin-relaxation

In *spin-exchange* collisions the total angular momentum of the colliding particles is conserved, but their hyperfine state changes. As an example, if the colliding particles are fermions, the complete wavefunction has to be anti-symmetrical, and

therefore, same-spin states and opposite-spin states will interact through two different potentials. Introducing the total spin operator $\hat{S} = \hat{S}_{\text{ion}} + \hat{S}_{\text{atom}}$, the state of the two particles can be described as a superposition of singlet and triplet states. During the collision the phases of singlet and triplet state evolve according to two different potentials, as a result after the collision the spin configuration of both particles has changed.

Experimentally, spin-exchange processes have been studied in spinor quantum gases [64], ultracold polar molecules [65], two-orbital quantum gases [66, 67], and have been used to create entanglement in neutral atoms trapped in optical lattices [68]. So far, the quantum regime of atom-ion spin-exchange interactions has yet to be reached.

When the orientation of the electronic spin is the same (with respect to a given quantization axis), the colliding particles can undergo a *spin-relaxation* collision that will result in the modification of one of the two spin orientations. The reasons for these type of reactions is connected to the spin-orbit coupling [47].

### Radiative and non-radiative charge transfer

For a given atom-ion pair there are two possible charge configurations: $A^+ - B$ and $A - B^+$. The former is the ground state of the system only if the ionization energy of A is lower than the one of B. If the two particles are separated by large internuclear distances, both electronic configurations are stable, but when brought in close proximity the induced interaction can cause a transfer on an electron between atom and ion.

If energetically favourable, the reaction

$$A^+ + B \rightarrow A + B^+ + \text{energy}$$

can occur during a collision. The released energy is dissipated in one of two ways: in *non-radiative charge exchange* events, it is transformed into the kinetic energy of the colliding particles, resulting in the heating or even the loss of the newly formed ion [31]. In *radiative charge exchange* events, the energy is released as a photon, which causes a considerable smaller change in the ion kinetic energy with respect to non-radiative events. The newly formed ion $B^+$ can be trapped in the same RF trap used for the $A^+$ ions, if its mass and kinetic energy make it possible. In general, $B^+$ ions will be transparent to the laser light used to cool and image the crystal of $A^+$ ions. As a result, in experiments where charge exchange collisions are observed, the initial crystals of $A^+$ ions start showing "dark ions", as some of the $A^+$ ions are replaced $B^+$ ions [69].

Charge exchange collisions have been studied in several experiments [70, 71, 34, 72]. However, these processes are often undesired. With the proper choice of the A and B atomic species, it is possible to introduce a considerable activation energy for charge exchange reactions, making their contribution negligible.

### Three-body recombinations

In *three-body recombination* processes, two neutral atoms B interact with the same ion $A^+$ to form a neutral molecule $B_2$. In this process, the ion absorbs part of the kinetic momentum in order to ensure momentum conservation. Due to the attractive long-ranged atom-ion potential, three-body recombination events can cause heating and loss of atoms [32]. The three-body recombination rate has been shown to be an important parameter to estimate, in order to correctly model loss and heating dynamics [73]. The rate of these reactions has also been shown to increase as the collisional energy is reduced and may play an important role in the ultracold regime of atom-ion interactions [74].

### Quenching reactions

Collisions between atoms and ions can lead to a relaxation of the internal excitations of the particles. These collisions have been observed causing de-excitations in metastable states [34] and have been proposed as a sympathetic cooling mechanism for molecular ions [75]. Collisional quenching can cause a reduction in the excited state lifetime, and thus plays an important role in experiments in quantum information and frequency metrology [76], where an excited metastable state of the ion is used to encode the $|1\rangle$ qubit state.

### Formation of charged molecules

During a collision event atom and ion can enter a chemical bond and form a charged, cold ionic molecule. These type of processes have been studied in several experiments [77, 78, 79, 80] in different energy regimes, due to their relation with research of chemistry in interstellar clouds [35, 81]. The molecule formation can occur by either radiative reactions (with the emission of a photon) or by three-body recombination ($A^+ + 2\,B \rightarrow (A\,B)^+ + B$), in the latter case the increase in kinetic energy can cause the molecular ion to follow very large trajectories [32] or even escape the RF trap.

## 1.2 Applications

Although control over the coherent evolution of atom-ion interactions has yet to be demonstrated, many theoretical works have explored the possibility of using these systems for quantum information processing, chemistry and metrology. In this section, a brief review of the different proposed applications is given.

### 1.2.1 Quantum computation

The complementary features of atom-ion quantum systems make them a promising platform for quantum computation: the long coherence times of the internal spin degree of freedom of atom loaded in optical traps makes them ideal as a quantum register for storing information, while the strong long-ranged interaction introduced by the ion allows for quantum gate with fast operation time.

In ref. [82] a possible scheme for making a universal CNOT gate based on spin-dependent atom-ion interactions is presented. In this theoretical work atoms are loaded in a 2D optical lattice where each site is occupied by a single atom (Mott insulator), the ion is trapped in a RF trap and is moved to interact with specific lattice sites effectively acting as a read-and-write head. This arrangement creates a two-qubit gate where the information is stored in the hyperfine states of both particles. The effects of micromotion on such gate were found to cause unwanted excitations unless the gate operation time is increased [83]. To circumvent this problem, a possible solution is to increase the distance between atom and ion while increasing the strength of their interaction. For this reason, ref. [84] explored the possibility of coupling atoms to Rydberg states to increase their polarizability, before interacting with the ions. The authors show that the Rydberg atoms can be brought to interact with the ions without influence from the micromotion and, by using biromantic optical fields, they can be used as a Mølmer-Sørensen type gate [85] with ms operation times.

### 1.2.2 Quantum simulation

An analogue quantum simulator is a physical system with accessible and controllable parameters specifically build to simulate, *i.e.* reproduce, a model dynamics which approximates a more complex system over which no control can be exerted. The idea of simulating physical problems using quantum systems was initially proposed by Richard Feynman [86]. Complex dynamics governed by strong many-body interactions are difficult or impossible to describe using theoretical or numerical methods available today. The goal of quantum simulation is to study these dynamics in a controlled system in which all the parameters can be precisely tuned. To this end both neutral atoms [11] and ions [87] based simulators have been succesfully implemented and used to study condensed-matter physics models.

Nonetheless, both platforms present some drawbacks. Long-range interactions in neutral atom setups are difficult to achieve. In solid-state systems long-range interactions are mediated by the phononic modes of the ion lattice. When periodic systems are simulated with optical lattices, the distance between lattices sites is not influenced by the atomic density, but uniquely determined by the laser light. Therefore, simulating the effects of phononic modes remains challenging.

A long ion chain immersed in an atomic cloud can be used to mediate long-range

atom-atom interactions [88]. When the chain is assumed to be infinitely long, the atoms experience a periodic potential due to the atom-ion interaction described by a Hamiltonian similar to the cavity-atom interaction Hamiltonian [89]. The effect is caused by the interaction of all atoms with the vibrational modes of the chain, *i.e.* the long-range interaction is mediated by phonons.

In ref. [36] a possible atom-ion quantum simulator implementation is presented. The authors consider a chain of ions immersed in an ultracold bath of fermionic atoms, in this system atom-ion interaction plays the role of the Coulomb potential between electron and ion in solid-state systems and fermion-phonon coupling raises naturally as the atoms are affected by the chain vibrational state. As the temperature of bath is decreased, a phase transition from the linear conductive ion chain to a structured (zig-zag) isolating ion chain is predicted.

In ref. [90], the authors propose to control the dynamics of a degenerate quantum gas in a Josephson junction using a single ion. A single tightly-bound ion is placed at the centre of the junction and, due to the state-dependent atom-ion interaction, the quantum tunnelling probability is affected by the ion presence allowing the creation of large ion-matterwave entangled states. Multiple ion-controlled Josephson junctions might be used to engineer complex Hamiltonian for quantum simulation.

Additionally, an ion immersed in an atomic cloud can be interpreted as a localized impurity in a many-body system. Sudden changes in the impurity state would lead to an out-of-equilibrium evolution of the many-body system. This allows studying dynamical phenomena such as the Anderson orthogonality catastrophe [37].

### 1.2.3 Quantum chemistry

Quantum-controlled chemistry aims at achieving control over the quantum mechanical degrees of freedom in a chemical reaction [91] in order to identify fundamental interaction processes and steer a chemical reaction at the single-particle level. Quantum control of chemical reactions has been achieved in the past using fast laser pulses on both organic [92, 93] and inorganic [94] molecules.

Hybrid atom-ion quantum systems provide a new tool to study chemical reactions and several studies have been performed with different reactant and energy regimes [31, 71, 70, 95]. Atom-ion interactions can be controlled by manipulating the particles states [34] or spin [33] in order to change the cross-section (and thus the rate) of different reactive collisions. An additional feature of studying reactive processes in atom-ion systems is that molecular ions can be re-captured in the RF trap and thus allow for measuring branching ratios and reaction products [96, 97].

### 1.2.4 Metrology

Optical clocks constitute the most precise and stable clocks available today [98, 99] and have been implemented both using neutral atomic [100] and trapped ions [101]. Recently, optical clocks have entered the $1 \times 10^{-18}$ uncertainty range [102, 20] and have been used, *e.g.*, to study gravitational shifts due to earth gravitational field [103].

Nevertheless, concerning the implementation of ion-based optical clocks major improvements can be foreseen along two main directions. First, collisions with the background gas may cause collisional frequency shift in the ion clock transition. In UHV collision rates are low and uncertainty budgets currently use conservative estimates based on semiclassical models, usually for hydrogen as a dominant background gas [104, 105]. Second, reactive collisions leading to the formation of molecular ions, although rare events, lead to the interruption of the clock operation since new ions must be loaded in the trap. By studying the dominant reaction products it would be possible to determine methods to control and ideally reduce the rate of ion loss, for instance by dissociating the molecule created by the collision, allowing to "recycle" the clock ion.

Atom-ion hybrid quantum systems can be used to diagnose the behaviour of atom-ion collisions occurring in ion-based clocks. By immersing the ion in a bath of cold atoms it would be possible to artificially increase the rate of atom-ion collisions. This would allow for a systematic study of atom-ion collisions: the contributions from forward and Langevin collisions can be determined thanks to different energy dependence of the associated cross-section; the rate of reactive collisions, reaction products and collisional frequency shifts can be studied for varying atomic densities, number of ions and collisional energies. Additionally, atom-ion systems could allow for sympathetic cooling of clock-relevant ions which are normally difficult to laser cool [106] and performing precision spectroscopy on cold ionic molecules [107].

# Chapter 2

# Semiclassical theory of laser cooling

In this chapter an overview of the semiclassical theory of laser cooling methods is presented. These methods have become the *de facto* standard for preparing cold atoms or ions in laboratories around the world, and are part of the experimental sequence that will be used at the $Ba^{+}Li$ experiment. An understanding of laser cooling fundamentals is necessary to comprehend the results presented in the following chapters.

The semiclassical theory of atom-light interaction is presented in section 2.1, in this section details about specific cooling methods are also given: Doppler cooling (section 2.1.3), sub-Doppler cooling (section 2.1.5) and evaporative cooling (section 2.1.6). The discussion is based on the material presented in Laser Cooling and Trapping [108]. Methods for cooling charged particles and an analysis of the RF trap are presented in section 2.2. Properties of lithium and barium and considerations related to their specific interactions are presented in section 2.3.

## 2.1 Physics of neutral atom cooling

### 2.1.1 Laser cooling

In the semiclassical treatment of atom-light interactions, for a Two-Level System (TLS) with states $|g\rangle$ and $|e\rangle$ interacting with photons having an electric field $\boldsymbol{\mathcal{E}} = \boldsymbol{\mathcal{E}}_0 \cos(\mathbf{k}\cdot\mathbf{r} - \omega t)$ the interaction Hamiltonian is written in the $|g\rangle$, $|e\rangle$ basis as

$$H' = \frac{\hbar\Omega}{2}\begin{pmatrix} 0 & e^{-i\omega t} \\ e^{i\omega t} & 0 \end{pmatrix}, \tag{2.1}$$

where $\Omega$ is the Rabi frequency

$$\Omega = \frac{e_0}{\hbar}\langle e|\mathbf{r}|g\rangle\,\boldsymbol{\mathcal{E}}_0\,,$$

which, in general, is a function of space if $\boldsymbol{\mathcal{E}}_0$ is not homogeneous. A more detailed derivation of eq. (2.1) is presented in appendix C. The force acting on an atom can be expressed as the expectation value of the corresponding quantum operator

$$\mathbf{F} = \langle \boldsymbol{\mathcal{F}} \rangle = \frac{\mathrm{d}}{\mathrm{d}t} \langle \mathbf{p} \rangle = \frac{i}{\hbar} \langle [H', \mathbf{p}] \rangle = - \langle \boldsymbol{\nabla} H' \rangle \ ,$$

where the Ehrenfest theorem was used, and $\partial p / \partial t = 0$. Using the relation $\langle O \rangle = \mathrm{tr}\{\rho O\}$, relating the expectation value of an operator to the trace of the density matrix $\rho$; the force acting on the atom results in

$$\mathbf{F} = -\frac{\hbar}{2} (\boldsymbol{\nabla}\Omega(\mathbf{r})\rho_{ge} + \boldsymbol{\nabla}\Omega^*(\mathbf{r})\rho_{eg}) \, .$$

Since in most cases the laser field can be written as an exponential (plane wave) or a sum of exponential terms, it is convenient to write the gradient of $\Omega$ in terms of its logarithmic derivative

$$\boldsymbol{\nabla}\Omega(\mathbf{r}) = \Omega(\mathbf{r}) \, \boldsymbol{\nabla} \log(\Omega(\mathbf{r})) = (\mathbf{q}_r + i\mathbf{q}_i)\Omega(\mathbf{r}) \, ,$$

where $\mathbf{q}_r$ and $\mathbf{q}_i$ are real quantities related to the gradient of the amplitude and the gradient of the phase of $\Omega$, respectively. Thus, the force $\mathbf{F}$ results

$$\begin{aligned} \mathbf{F} &= i\frac{\hbar}{2}\mathbf{q}_i(\Omega\rho_{ge} - \Omega^*\rho_{eg}) + \frac{\hbar}{2}\mathbf{q}_r(\Omega\rho_{ge} + \Omega^*\rho_{eg}) \\ &= \mathbf{F}_{\mathrm{sp}} + \mathbf{F}_{\mathrm{dip}} \, . \end{aligned} \tag{2.2}$$

Equation (2.2) is a general expression of the force acting on an atom interacting with light. The expression of $\rho_{eg} = \rho_{ge}^*$ is determined by the Optical Bloch Equations (OBE), which need to be solved independently. The two terms of eq. (2.2), are referred to as the *radiation pressure*, proportional to $\mathbf{q}_i$, and the *dipolar force*, proportional to $\mathbf{q}_r$.

### Radiation pressure

As mentioned before, the first term of eq. (2.2) is referred to as the *radiation pressure* (or scattering force) and it is proportional to the value of $\mathbf{q}_i$. As an illustrative example, one may consider a travelling plane-wave with field

$$\boldsymbol{\mathcal{E}}(\mathbf{r}) = \boldsymbol{\mathcal{E}}_0 \left( e^{i(\mathbf{k}\cdot\mathbf{r} - \omega t)} + \mathrm{c.c.} \right) ,$$

in this case the amplitude is homogeneous ($\mathbf{q}_r = 0$) while the phase is not ($\mathbf{q}_i = \mathbf{k}$). For an atom at rest, the expression of $\rho_{eg}$ is given by the steady-state solution of the OBE

$$\rho_{eg} = \frac{i\Omega}{2(\gamma/2 - i\delta)(1+s)} \, ,$$

where $\gamma$ is the atomic linewidth (or radiative decay rate), $\delta = \omega - \omega_0$ is the detuning between the laser frequency and the atomic transition frequency $\omega_0$. The saturation parameter $s$ is given by $(|\Omega|^2/2)/(\delta^2 + \gamma^2/4)$. It follows that

$$\Omega\rho_{ge} = -\frac{\Omega^2\delta + i\Omega^2\gamma/2}{2\left(\frac{\gamma^2}{4} + \delta^2\right)(1+s)} = -\delta\frac{s}{1+s} - i\frac{\gamma}{2}\frac{s}{1+s}\,, \tag{2.3}$$

and the force due to photon scattering is

$$\mathbf{F}_{\rm sp} = i\frac{\hbar}{2}\mathbf{q}_i(\Omega\rho_{ge} - \Omega^*\rho_{eg}) = \hbar\mathbf{k}\frac{\gamma}{2}\frac{s}{1+s} = \hbar\mathbf{k}\gamma\rho_{ee}\,,$$

where the OBE solution for $\rho_{ee}$ was used in the last step. The expression of the scattering force has a simple interpretation: it corresponds to the momentum per photon $\hbar\mathbf{k}$ multiplied by the scattering rate $\gamma\rho_{ee}$. By introducing the dimensionless intensity parameter $s_0 = 2|\Omega|^2/\gamma^2$, the scattering force can be rewritten in a more useful way

$$\mathbf{F}_{\rm sp} = \frac{\hbar\mathbf{k}s_0\gamma/2}{1 + s_0 + (2\delta/\gamma)^2}\,. \tag{2.4}$$

For an atom moving at a velocity $\mathbf{v}$, the expression of the scattering force is modified by including the Doppler effect $\delta' = \delta - \mathbf{k}\cdot\mathbf{v}$

$$\mathbf{F}_{\rm sp} = \frac{\hbar\mathbf{k}s_0\gamma/2}{1 + s_0 + (2(\delta - \mathbf{k}\cdot\mathbf{v})/\gamma)^2} \approx \mathbf{F}_{\rm sp}^{(0)} - \beta\mathbf{v}\,, \tag{2.5}$$

where in the last equation it was assumed that $\mathbf{k}\cdot\mathbf{v}$ can be considered small with respect to the other terms, $\mathbf{F}_{\rm sp}^{(0)}$ is the scattering force for an atom at zero velocity and the damping coefficient $\beta$ is given by

$$\beta = -\hbar k^2\frac{4s_0(\delta/\gamma)}{\left(1 + s_0 + (2\delta/\gamma)^2\right)^2}\,. \tag{2.6}$$

### Dipole force

The second term of eq. (2.2) is proportional to $\mathbf{q}_r$, *i.e.* proportional to the gradient of the light intensity and is the so-called *dipole force*. As an example, one may consider a standing wave composed by two identical counter-propagating beams

$$\boldsymbol{\mathcal{E}}(\mathbf{r}) = \boldsymbol{\mathcal{E}}_0\cos(\mathbf{k}\cdot\mathbf{r})\left(e^{-i\omega t} + \text{c.c.}\right).$$

In this case, $\mathbf{q}_r \neq 0$ and $(\mathbf{q}_i = 0)$. Using eq. (2.2) and eq. (2.3), the dipole force for an atom at rest in a standing wave is

$$\mathbf{F}_{\rm dip} = -\frac{\hbar}{2}\mathbf{q}_r\delta\frac{s}{1+s}\,.$$

Since the gradient of the saturation parameter is

$$\boldsymbol{\nabla} s = \frac{|\Omega|\,\boldsymbol{\nabla}|\Omega|}{\delta^2 + \gamma^2/4} = 2s\frac{\boldsymbol{\nabla}|\Omega|}{|\Omega|} = 2s\,\mathbf{q}_r\,,$$

the dipole force is conveniently written as

$$\mathbf{F}_{\rm dip} = -\delta\frac{\hbar}{2}\frac{\boldsymbol{\nabla} s}{1+s} = -\delta\frac{\hbar}{2}\boldsymbol{\nabla}\log(1+s) = -\boldsymbol{\nabla} V_{\rm dip}\,, \tag{2.7}$$

where the dipole potential $V_{\rm dip}$ is given by

$$V_{\rm dip} = \delta\frac{\hbar}{2}\log(1+s) = \delta\frac{\hbar}{2}\log\left(1+\frac{s_0}{1+(2\delta/\gamma)^2}\right). \tag{2.8}$$

The dipole force depends directly on the detuning $\delta$ and, thus, changes sign depending on whether the laser is red detuned ($\delta < 0$) or blue detuned ($\delta > 0$) with respect to the atomic transition. For the case of a red detuned laser, the force is attractive ($V_{\rm dip} < 0$), whereas in the case of a blue detuned laser, the force is repulsive ($V_{\rm dip} > 0$). The dipole force is fundamentally different from the scattering force: the scattering force is dissipative, and it arises from the momentum transferred during the absorption or the emission of a photon. Thus, it can be used for cooling atoms. The dipole force, instead, is a conservative force (since it is written as the gradient of a scalar field) and cannot be used for cooling atoms; it can also be made arbitrarily large by increasing the laser intensity.

Equation (2.8) is seldom used in practice. The reason is that atoms are multi-level systems and the dipole potential experienced by an atom in a given electronic configuration depends on the different contributions from different energy levels. In the two-level approximation, and in the case of a far off resonance laser ($\delta \gg \gamma$) the dipole potential can be simplified

$$V_{\rm dip} = \frac{\hbar\gamma^2}{8\delta}s_0 = \frac{\hbar\gamma^2}{8\delta}\frac{I}{I_{\rm sat}}\,,$$

where $I_{\rm sat} = \pi hc\gamma/(3\lambda^3)$ is the transition saturation intensity, and $\lambda$ is the transition wavelength. To include the contributions from the multi-level structure of the atom, the dipole potential can be written as the product of the laser intensity profile $I(\mathbf{r})$ and the atomic polarizability $\alpha(\omega)$

$$V_{\rm dip}(\mathbf{r}) = \frac{1}{2\epsilon_0 c}\,\mathrm{Re}[\alpha(\omega)]I(\mathbf{r})\,. \tag{2.9}$$

The atom polarizability is defined as the coefficient that relates the atomic dipole moment to the driving electric field amplitude. In the most general case, $\alpha(\omega)$ is a c-valued function, that depends on the electronic configuration of the atom

and on the driving field frequency $\omega$. Therefore, the atomic polarizability carries information on the complexity of the atomic structure. The dipole potential is typically written in terms of the irreducible components of the polarizability ([109], page 350)

$$\begin{aligned} V_{\text{dip}} = &-\frac{1}{2}\alpha_J^{(0)}(\omega)|\boldsymbol{\mathcal{E}}(\mathbf{r})|^2 \\ &+\frac{m_J}{2J}\alpha_J^{(1)}(\omega)|\boldsymbol{\mathcal{E}}^*(\mathbf{r})\times\boldsymbol{\mathcal{E}}(\mathbf{r})| \\ &-\frac{1}{2}\alpha_J^{(2)}(\omega)\left(\frac{3m_J^2-J(J+1)}{J(2J-1)}\right)\frac{3\mathcal{E}_z(\mathbf{r})-|\boldsymbol{\mathcal{E}}(\mathbf{r})|^2}{2} \end{aligned}$$

where $J$ and $m_J$ are the quantum numbers of the angular momentum and of the angular momentum component along the quantization axis, respectively. The three irreducible terms $\alpha_J^{(0)}, \alpha_J^{(1)}$ and $\alpha_J^{(2)}$ are referred to as the scalar, vector and tensor polarizabilities, respectively. Their expression is given by (ref. [110], chapter 2)

$$\begin{aligned} \alpha_J^{(0)}(\omega) &= \frac{2}{3(2J+1)}\sum_{J'}\frac{\omega_{J',J}}{\omega_{J',J}^2-\omega^2}|\langle J'\|\mathbf{r}\|J\rangle|^2(\delta_{J-1,J'}+\delta_{J,J'}+\delta_{J+1,J'}), \\ \alpha_J^{(1)}(\omega) &= -\frac{1}{(2J+1)}\sum_{J'}\frac{\omega}{\omega_{J',J}^2-\omega^2}|\langle J'\|\mathbf{r}\|J\rangle|^2\left(-\frac{\delta_{J-1,J'}}{J}-\frac{\delta_{J,J'}}{J(J+1)}-\frac{\delta_{J+1,J'}}{J+1}\right), \\ \alpha_J^{(2)}(\omega) &= \frac{2}{3(2J+1)}\sum_{J'}\frac{\omega_{J',J}}{\omega_{J',J}^2-\omega^2}|\langle J'\|\mathbf{r}\|J\rangle|^2\times \\ &\quad\times\left(-\delta_{J-1,J'}+\frac{2J-1}{J+1}\delta_{J,J'}-\frac{J(2J-1)}{(J+1)(2J+3)}\delta_{J+1,J'}\right), \end{aligned}$$

where the summations run over all possible $J' \neq J$, $\langle J'\|\mathbf{r}\|J\rangle$ is the reduced dipole matrix element, and $\delta_{J',J}$ is the Kronecker delta function.

### 2.1.2 Deceleration of an atomic beam

To perform atomic physics experiments, atoms must be slowed down from either room temperature or from hot vapours evaporated from an oven (typically at a few hundreds of kelvin) to sub-K temperatures, so that they may be optically trapped and further cooled to degeneracy. The simplest method to slow down a beam of atoms is to shine a laser light opposite to the atoms' trajectory, exploiting the radiation pressure to reduce the atoms' velocity. Upon setting the light on resonance with a specific closed atomic transition, atoms reduce their velocity along the laser beam axis by absorbing the laser's photons. After each absorption, the atoms decay to their ground state by spontaneous emission. Although emission is also accompanied by a change in momentum, it is spatially symmetric, and the net momentum transfer due to spontaneous emission averages to zero over several absorption-emission cycles. The scattering force is highly frequency-dependent

and, due to the Doppler shift, the resulting force acting on the atoms is velocity dependent. A dissipative velocity-dependent force leads to a compression of the atom distribution in phase space, hence it not only decelerates but also cools the atomic beam.

The scattering force acting on a moving atom saturates for high laser powers, as can be noted by taking the limit $s_0 = I/I_{\text{sat}} \to \infty$ in eq. (2.5). This leads to a maximum force $\mathbf{F}_{\max}$ and a maximum deceleration $\mathbf{a}_{\max}$ acting on the atoms

$$\mathbf{F}_{\max} = m\mathbf{a}_{\max} = \hbar\mathbf{k}\frac{\gamma}{2}\,.$$

Since this maximum deceleration depends on the atomic parameters and the laser wavelength, it is possible to define a minimum stopping length $L_{\min} = \bar{v}^2/(2a_{\max})$ and minimum stopping time $t_{\min} = \bar{v}/a_{\max}$, where $\bar{v} = 2(k_b T/m)^{1/2}$ is the Root Mean Squared (RMS) atom velocity and $T$ is the temperature of the atoms before deceleration[1].

As the atoms slow down, the change in Doppler shift will change their resonance frequency, eventually they will stop decelerating as they become out of resonance with the laser beam. The changes in Doppler shift must be compensated if one wishes to continuously cool the atoms. To do so two common strategies are used: one may sweep the laser frequency, sometimes called *chirp cooling* [111] or the atomic resonance frequency may be changed spatially using external fields [112].

The Zeeman Slower (ZS) is an experimental apparatus which makes use of a spatially-varying magnetic field to change the atomic levels and ensure that the atoms remain at resonance with the laser while decelerating. In its simplest design, the ZS is formed by a long narrow tube, aligned to the atomic beam trajectory, surrounded by coils of wire of different dimensions that generate the appropriate magnetic field needed to compensate the Doppler shift. In order for atoms to experience a uniform deceleration $a = \eta a_{\max}$ throughout their trajectory, the ideal field profile is

$$B(z) = B_0\sqrt{1 - \frac{z}{z_0}}\,, \tag{2.10}$$

where $z_0 = mv_0^2/(\eta\hbar k\gamma)$ is the magnet length, $v_0$ is the maximum initial velocity that the ZS is capable of cooling: atoms at velocities higher than $v_0$ will never be resonant with the laser beam. $\eta < 1$ is the so called *safety parameter*, it is a design parameter that determines the length of the magnet and the atoms final velocity. The value of the magnetic field $B_0$ in eq. (2.10) is $B_0 = \hbar k v_0/\mu'$, where $\mu' = (g_e M_e - g_g M_g)\mu_B$, the subscripts $g, e$ refer to the atom in the ground or excited state of the employed atomic transition, $g_{g,e}$ is the Landé g-factor, $M_{g,e}$ is the magnetic quantum number and $\mu_B$ is the Bohr magneton.

[1] Atoms are assumed to be in a thermal distribution near equilibrium before deceleration.

Choosing the various parameters of the ZS requires taking into account several considerations: the maximum initial velocity $v_0$ that can be cooled should be determined based on the oven temperature to ensure the largest possible quantity of decelerated atoms. Since the MOT collection efficiency is sensitive to the solid angle subtended by the MOT volume with respect to the oven exit, the ZS tube should be made as short as possible while still ensuring sufficient deceleration for succesfully confining the atoms in a MOT.

### 2.1.3 Optical molasses

Equation (2.5) shows how the scattering force acting on a moving atom can be approximated as the sum of a zero-velocity term ($\mathbf{F}_{\text{sp}}^{(0)}$) and a viscous damping term ($-\beta\mathbf{v}$). This suggests that by combining two identical counter-propagating laser beams, one may obtain a purely viscous force

$$\mathbf{F}_{\text{sp}} + (-\mathbf{F}_{\text{sp}}) \approx \mathbf{F}_{\text{sp}}^{(0)} - \mathbf{F}_{\text{sp}}^{(0)} - \beta\mathbf{v} + \beta(-\mathbf{v}) = -2\beta\mathbf{v}\,.$$

Optical Molasses (OM) [113] are a laser cooling technique that makes use of the isotropic viscous force produced by 3 pairs of counter-propagating beam arranged along orthogonal axes to achieve cooling in all 3 physical dimensions. As long as the laser light is red detuned ($\delta < 0$), the damping coefficient $\beta$ is positive, hence the force opposes the atom velocity leading to cooling. In the atom frame of reference, the laser beam opposing the atom motion will be Doppler shifter closer to resonance, while the laser beam parallel to the atom motion will be shifted further out of resonance. Therefore, atoms will scatter photons with a higher rate from the laser beam that is counter-propagating with respect to their motion. Although OM allow for 3D cooling of atoms, they cannot be used as a trap: there is no restoring force that recalls atoms toward a "centre point", so atoms will eventually abandon the molasses region.

The velocity-dependent force experienced by atoms in optical molasses is shown in fig. 2.1, the linear behaviour $\mathbf{F} \propto \mathbf{v}$ is observed only for low velocities. The force shows a maximum at $\|\mathbf{v}\| = (\gamma'/2k)(X/\sqrt{3})$, where $\gamma' = \gamma\sqrt{s_0+1}$ is the power broadened linewidth, $X = (x - 1 + 2\sqrt{x^2+x+1})^{1/2}$ and $x = (2\delta/\gamma')^2$. By convention, the maximum velocity for which particles can be efficiently cooled using OM is called *capture velocity*, and is defined as $v_c = \gamma/k$, since for most OM configurations $x \approx 1$ and $X \approx \sqrt{3}$.

In OM the lowest theoretically achievable temperature is the so-called *Doppler temperature* $T_D = \hbar\gamma/(2k_B)$. This limit is due to the quantized nature of the momentum transfer between atom and light: each photon carries a momentum $\hbar\mathbf{k}$ which changes the kinetic energy of the atom (during either absorption or emission) by $E_{\text{rec}} = \hbar^2k^2/(2m)$. When the heating rate $E_{\text{rec}}2\gamma_p$, where $\gamma_p = s_0\gamma/2/(1 + s0 + (2\delta/\gamma)^2)$, equals the cooling rate $\mathbf{F}\cdot\mathbf{v}$, *i.e.* the power of the cooling force, the

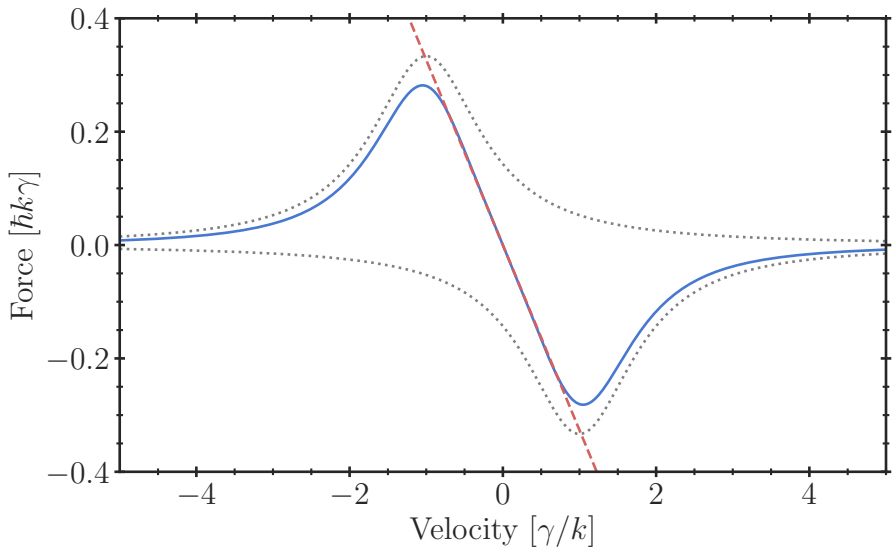


Figure 2.1: Velocity-dependent damping force in OM. Dashed line shows the linear approximation, dotted lines show the force from single laser beams. Calculated for $\delta = -\gamma$ and $s_0 = 2$.

atom cannot be cooled further. The residual kinetic energy shows a minimum for $\delta = -\gamma/2$ and its equivalent temperature corresponds to $T_D$.

### 2.1.4 Magneto-optical traps

To obtain an actual trapping force, OM has to be combined with an additional inhomogeneous magnetic field. The resulting configuration is the so-called Magneto-Optical Trap (MOT), which is a robust trapping method that has become a common technique in atomic physics experiments.

Figure 2.2 shows an illustrative 1D example: an atom with a single ground state and 3 Zeeman levels in the first excited state ($J_g = 0 \rightarrow J_e = 1$ transition) is immersed in a linearly-changing magnetic field $B(z) = bz$, where $b$ is the field gradient expressed in $\mathrm{G\,m^{-1}}$. As the atom moves away from the trap centre ($z = 0$), the Zeeman shift will bring one of the Zeeman sublevels closer to resonance. If the laser beam polarizations are chosen such that when the atom is in the $z < 0$ ($z > 0$) region it will scatter mostly from the $\sigma^+$ ($\sigma^-$) beam, then the atom will experience a restoring force toward the zero field point.

It is important to note that the polarizations $\sigma^\pm$ are defined with respect to the atom quantization axis, fig. 2.2 shows also the polarization defined with respect to the direction of motion of the photon. Although highlighting the polarization with respect to the photon direction of motion is not common in established literature

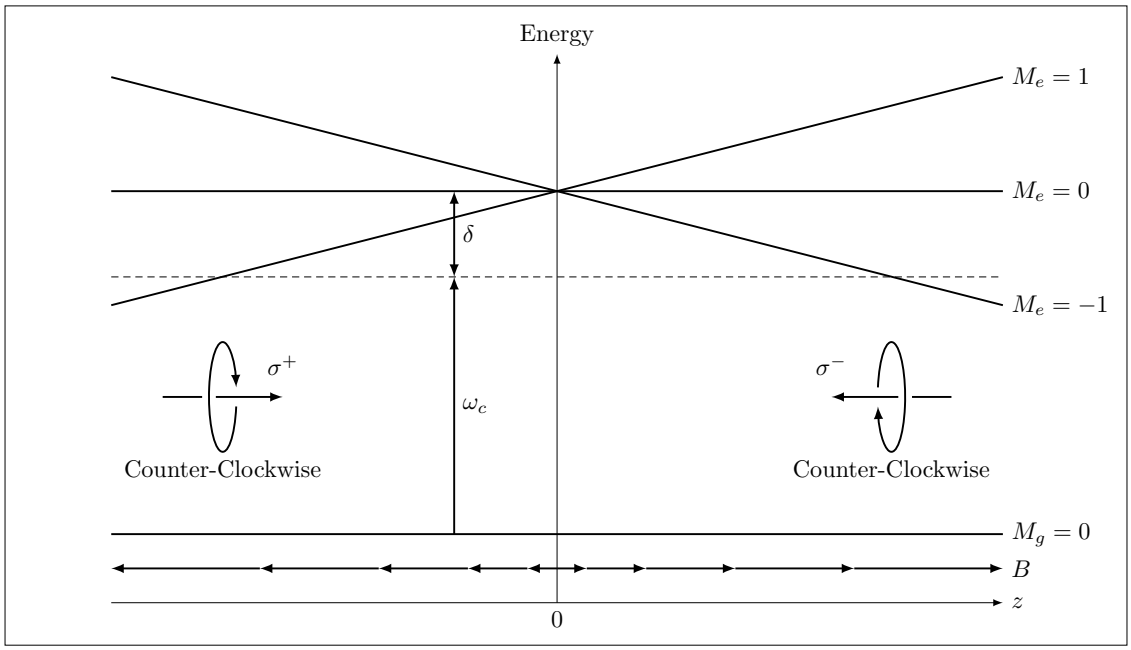


Figure 2.2: Schematic diagram of MOT beams and atomic energy levels in 1D. The dashed line represents the laser frequency in the laboratory frame of reference. The magnetic field's direction and magnitude are indicated by the horizontal arrows marked $B$.

(*e.g.* [114, 115, 108]), this difference in definition can lead to misunderstanding during the realization of an experiment. The polarization of light should be clockwise (counter-clockwise) for both laser beams, if the magnetic field is pointing inward (outward) with respect to the trap centre. Therefore, the correct light polarization can be realized by using a quarter-waveplate before the retro-reflecting mirror[2], as can be seen in fig. 3.21.

The expression of the force acting on an atom is given by the sum of the scattering forces exerted by the two opposing beams. The detuning of each laser beam depends on both the Doppler shift and the Zeeman shift

$$\delta' = \delta - \mathbf{k} \cdot \mathbf{v} + \frac{\mu' b \|\mathbf{r}\|}{\hbar} ,$$

where the magnetic field $\mathbf{B}(\mathbf{r}) = b\mathbf{r}$ is generalized to the 3D case. If the Doppler and Zeeman shifts are small with respect to $\delta$ the force can be linearized

$$\mathbf{F} = -2\beta\mathbf{v} - 2\mathcal{K}\mathbf{r} ,$$

[2]This optics configuration will change both the direction of the photon and the direction of rotation of the photon's electric field. Hence the polarization defined with respect to the photon's direction of motion remains unchanged.

where $\mathcal{K} = \mu' b\beta/(\hbar k)$. Thus, the force in a MOT is given by the same viscous damping force of the OM plus an elastic force with spring constant $\mathcal{K}$. For field gradients commonly used in laboratory, the atomic motion is over-damped, that is the oscillation frequency $(\mathcal{K}/m)^{1/2}$ is much smaller than the cooling rate. Generally, this is the most efficient trapping condition. MOTs suffer the same theoretical limit as OM concerning temperature: atoms cannot be cooled to temperatures below the Doppler limit $T_D$ by pure photon scattering.

Two important quantities define the MOT: the capture range and the capture velocity. The capture range is defined as the physical distance from the trap centre at which an atom at rest is resonant with the laser beam, that is $\delta' = 0$

$$r_c = -\frac{\delta\,\hbar}{\mu' b}\,,$$

and $\delta < 0$ for red detuned beams. The value of $r_c$ poses a lower boundary on the size of the laser beams used to create the MOT: if the beam waist is smaller than $r_c$, atoms may be able to exit the trapping volume. The capture velocity is the maximum velocity that the atoms can have so that they are stopped before the end of the trapping volume. If the MOT volume is $2r_c$ and the maximum damping force is $F = \hbar k\gamma/2$, an estimate of the capture velocity is given by

$$v_c = \sqrt{\frac{2r_c\hbar k\gamma}{m}}\,.$$

**CMOT**

After loading a sufficient amount of atoms in the MOT, it is common to perform a so-called compressed Magneto-Optical Trap (cMOT) stage [116, 117]. In this stage the field gradient is increased, leading to a compression of the MOT volume and an increase of the atomic density. For the specific case of atoms with dark states (such as lithium), the intensity of the repumper light is also reduced to a fraction of the value used during the MOT. By allowing the atoms to spend time in a dark state, photon scattering is reduced leading to lower temperatures. Since atoms in dark states do no interact with the MOT laser beams, they will exit the trapping volume and be lost. Therefore, this stage is performed for small amounts of time and it is used to facilitate the transfer of atoms from the MOT to other traps characterized by a small volume of confinement, such as optical dipole traps.

For the case of lithium, the D2 line is commonly used during the MOT and cMOT sequences, since it contains the only theoretically closed transition $^2\mathrm{S}_{1/2}\ F = 3/2 \rightarrow {}^2\mathrm{P}_{3/2}\ F = 5/2$. Nonetheless, repumper light is required, since the hyperfine splitting of the $^2\mathrm{P}_{3/2}$ level is smaller than the atomic linewidth, leading some atoms to decay into the $^2\mathrm{S}_{1/2}\ F = 1/2$ level. This consideration, in addition to the off-resonant scattering from the D1 line, makes cooling on the D2 line slightly

inefficient. In fact, a typical value for the temperature reached by a lithium MOT is approximately 1.5 mK, well above the Doppler limit for lithium ($T_D \approx 140\,\mu K$), and the cMOT sequence can reach 300 µK [118]. Although cooling on the D1 line would be more efficient, such transition presents a saturation intensity of $7.59\,mW\,cm^{-2}$ considerably higher than that of the D2 line ($2.54\,mW\,cm^{-2}$), making the D2 line more attractive for the initial cooling phase.

### 2.1.5 Sub-Doppler cooling

The theoretical limit for the temperature that can be achieved in OM and MOTs is the Doppler temperature $T_D$. However, the first observation of sub-Doppler temperatures was done in atoms cooled in 3D OM [119], even though this method was expected to be Doppler-limited. The discrepancy between experimental data and the model presented in section 2.1.3 is due to the over-simplistic nature of the model itself. Real atoms are rarely just TLS, and the complete sublevel structure of the atom and the optical pumping between these sublevels has to be taken into account. The theoretical explanation of this phenomenon [120] lead to what is now known as *polarization gradient cooling*.

As a simplified example, one may consider an atom moving in the periodic potential created by the interference of the two counter-propagating beams forming the OM. As the atom moves it periodically converts kinetic energy into potential energy and back again. The potential can be considered as a series of "valleys and hills". If different atomic states experience potentials with different amplitude or different phase, it is possible to dissipate energy by optically pumping the atom between two states at the appropriate time: an atom in a state that increases its potential energy as it moves up the potential hill could be pumped to a state associated with a lower potential energy at a valley of the optical potential, thus, resulting in a reduction of the atom's energy. The excess energy is radiated away during the optical pumping process, as it involves a spontaneous decay. The light shift of atomic levels in a standing wave detuned from resonance constitute an example of a system with multiple potentials that are periodic and that depend on the atom's state.

If the two potentials that are used for cooling are in opposite phase with one another, then it is possible to optically pump the atom from the hill of one potential to the valley of the other. Effectively, forcing the atom to constantly move up hill. Thus, this cooling method was given the name of *Sisyphus cooling* due to its resemblance with the myth of king Sisyphus from Greek mythology [121].

The temperature achievable by Sisyphus cooling is ultimately limited by the recoil energy $E_{\text{rec}} = \hbar^2 k^2/(2m)$ since it represents the minimum change in energy of the atom. This limit is enforced by spontaneous emission, which increase the atomic momentum in a random direction by $\hbar k$ on every optical cycle. To overcome this limit velocity-selective dark state can be used, so that once the atom has reached a

sufficiently low momentum it falls into a dark state and ceases its interaction with lights [122].

### Polarization gradient cooling

Polarization gradient cooling is a sub-Doppler cooling scheme in which the periodic potentials used for Sisyphus cooling are generated by the varying polarization of the light field. Two configurations are possible:

- Linear $\perp$ linear polarization: In this configuration two counter-propagating beams have both linear polarization but orthogonal to one another. The resulting standing wave has a polarization that varies from linear (at 45° with respect to input beams polarization), to $\sigma^+$, to linear aligned to one of the two input beams, to $\sigma^-$ with the same periodicity as the trapping potential. In the case of an atom with $J_g = 1/2$ the sublevels with $M_g = 1/2$ will experience a trapping potential in opposite phase with respect to the $M_g = -1/2$ sublevel. As the light field changes polarization, a moving atom's state is redistributed between the two states. By properly choosing between red detuned or blue detuned light, the atoms can be forced to constantly move up hill and thus loose energy.

- $\sigma^+ - \sigma^-$ polarization: Here two counter-propagating beams with opposite circular polarization are used. The resulting standing wave has linear polarization everywhere but the angle of the polarization is not spatially uniform. Effectively, the linear polarization rotates around the axis of the standing wave. In this case, cooling is not caused by the presence of hills and valleys of potential but to the population imbalance caused by the atom motion. As a simple model, consider an atom with $J_g = 1$: for an atom at rest the quantization axis is dictated by the local light polarization; since the polarization is linear, the sublevels with $M_g = \pm 1$ will be populated equally. If the atom starts moving, the quantization axis will change as the polarization of the light field changes, optical pumping will cause a redistribution of the population between the $M_g = 0, \pm 1$ states. If the atom is moving sufficiently fast, this population will "lag behind", in other words the population will not be exactly the ideal steady state distribution for the local polarization. This imbalance between the $M_g = 1$ and $M_g = -1$ levels will cause the atom to scatter more photons from one beam than the other: if the atom is moving toward the $\sigma^+(\sigma^-)$ beam the population of the $M_g = 1(M_g = -1)$ level will be slightly higher, thus favouring scattering from the beam that directly opposes the atom's motion.

### Gray-molasses

Gray-molasses [123, 124] is a cooling method that makes use of velocity-selective coherent-population trapping and the presence of dark states to cool atoms below the Doppler limit. In the simplest implementation of this method, an atom is immersed in a standing wave formed by two counter-propagating beams with linear polarization at an angle $\phi$ from one another, so that $0° < \phi < 90°$. For this example, a $\Lambda$-type atomic transition is considered (*e.g.* $J_g = 1 \rightarrow J_e = 1$). In the low saturation limit ($s_0 \ll 1$), the excited state can be adiabatically eliminated and one is left with an effective Hamiltonian for the two ground states with $M_g = \pm 1$. As a result, the systems holds at least one dark state, *i.e.* a state that does not interact with light. The state of the system can be written in terms of this dark state $|NC\rangle$ and the orthogonal state $|C\rangle$, called the coupled state [125].

Therefore, this system will have a lower constant energy level $E_{\mathrm{NC}}$ (associated with the non-coupled state) and a higher modulated energy level $E_{\mathrm{C}}$ that depends on the light intensity. Eventually, all atoms will be optically pumped from the coupled state to $|\mathrm{NC}\rangle$, via absorption followed by spontaneous emission. Atoms at rest ($v = 0$) remain trapped in the non-coupled state. Atoms not at rest ($v \neq 0$) will be transferred from $|\mathrm{NC}\rangle$ to $|\mathrm{C}\rangle$ via non-adiabatic passage. If the lasers are blue detuned $\delta > 0$, the population transfer from $|\mathrm{NC}\rangle$ to $|\mathrm{C}\rangle$ will occur near the minima of $E_{\mathrm{C}}$. The atom will then have to climb the potential hill of the $|\mathrm{C}\rangle$ state, losing kinetic energy, before it will be optically pumped back to $|\mathrm{NC}\rangle$.

Gray-molasses are commonly used for sub-Doppler cooling of lithium samples [126]. Although other methods have been used, such as polarization gradient cooling [127], the fraction of cooled atoms is only 30 % of the atoms trapped in the MOT. Conversely, gray-molasses performed on the D1 line of lithium have been proven to be capable of cooling more than 75 % of the atomic sample at approximately 40 µK [126], making them a preferable alternative.

### Resolved sideband cooling

Sideband cooling is an optical cooling method used to bring trapped particles close to their motional ground state. If a harmonic trap confining a two-level particle is characterized by a frequency $\omega_{\mathrm{tr}}$ that is larger than the particle's excited state linewidth $\gamma$, distinct sidebands appear in the excitation spectrum. These sidebands are associated with changes in the motional state of the particle and can be used for cooling beyond the Doppler limit.

The Hamiltonian of a TLS trapped in a harmonic potential, interacting with a near-resonance laser is written (in direct coupling formalism) as

$$H = H_0 + \frac{1}{2} m\, \omega_{\mathrm{tr}}\, x^2 - \mathbf{d} \cdot \boldsymbol{\mathcal{E}}_{\mathrm{c}}, \tag{2.11}$$

where the fist term is the Hamiltonian of the free TLS system, the second term is

the trap Hamiltonian and the last one is the atom-light interaction with the laser electric field $\mathcal{E}_c = \boldsymbol{\epsilon}\,\mathcal{E}_0^{(c)}\cos(k_c x - \omega_c t)$, where $\boldsymbol{\epsilon}$ is the light polarization, $\mathcal{E}_0^{(c)}$ the field amplitude, $k_c$ the laser wavevector, and $\omega_c$ the laser pulsation.

By considering the Fock space given by the tensor product of the space spanned by the atomic states $|g\rangle, |e\rangle$ and the trap states $|n\rangle, n = 0, 1, \ldots, \infty$, on may write the quantized form of eq. (2.11) as

$$H = \frac{\delta}{2}|e\rangle\langle e| + \hbar\omega_{tr}\left(a^\dagger a + \frac{1}{2}\right) + \frac{\hbar\Omega}{2}(U_{nm}|g,m\rangle\langle e,n| + U_{nm}^\dagger|e,n\rangle\langle g,m|)\,, \quad (2.12)$$

where $\delta = \omega_c - \omega_0$ is the laser detuning, $a$ and $a^\dagger$ are the ladder operators of the harmonic oscillator, and the Rotating Wave Approximation (RWA) approximation has already been performed. In the last term $\Omega = -e\mathcal{E}_0^{(c)}d_{eg}/\hbar$ is the Rabi frequency, and the matrix terms $U_{nm} = \langle m|e^{ik_c x\cos(\theta)}|n\rangle$ are responsible for coupling different vibrational states, the angle $\theta$ is the angle between the trap axis and the photons' momentum $k_c$.

The matrix elements $U_{nm}$ can be written in terms of the so-called *Lamb-Dicke parameter*

$$\eta = \frac{\hbar k_c}{2m\omega_{tr}}\cos\theta\,. \quad (2.13)$$

The square of the Lamb-Dicke parameter is proportional to the ratio between the recoil energy and the spacing between harmonic oscillator states. If $\eta \ll 1$ then spontaneous emission occurs predominantly without any change in the motional quantum number $n$; this is a necessary condition for sideband cooling to be efficient, otherwise particles will experience strong recoil heating. The condition $\eta \ll 1$ identifies the so-called *Lamb-Dicke regime*, in this working regime the elements $U_{nm}$ can be expanded in powers of $\eta$ and retain only first-order terms

$$\begin{aligned} U_{nm} &= \langle m|1 + ik_c x\cos\theta - (k_c x\cos\theta)^2 + \ldots|n\rangle \\ &= \delta_{nm}\left[1 + \frac{1}{2}\eta^2(2n+1)\right] + i\eta\left(\sqrt{n+1}\,\delta_{n+1,m} + \sqrt{n}\,\delta_{n-1,m}\right) + O(\eta^2)\,, \end{aligned}$$

where $\delta_{nm}$ is the Kronecker's delta and the relation $x = \hbar(a^\dagger + a)/(2m\omega_{tr})$ has been used. It is clear that in this working regime the laser beam couples states with either the same motional number $n = m$, this transition is referred to as the *carrier transition*, or states that differ by a single quantum of vibration $n = m \pm 1$. The transition associated with the loss of vibrational quantum is called *red sideband transition*, the one associated with the gain of a vibrational quantum is called *blue sideband transition*. If the carrier has a relative intensity of 1, the two sidebands are expected to have a relative intensity of $\eta^2$. However, since the ground state of the trap cannot be cooled further, it does not possess a red sideband transition. Therefore, the actual intensity of the red sideband depends on the particle's probability of occupying the trap ground state. This effect can be used as a spectroscopic method for measuring the temperature of an ensemble of particles [128].

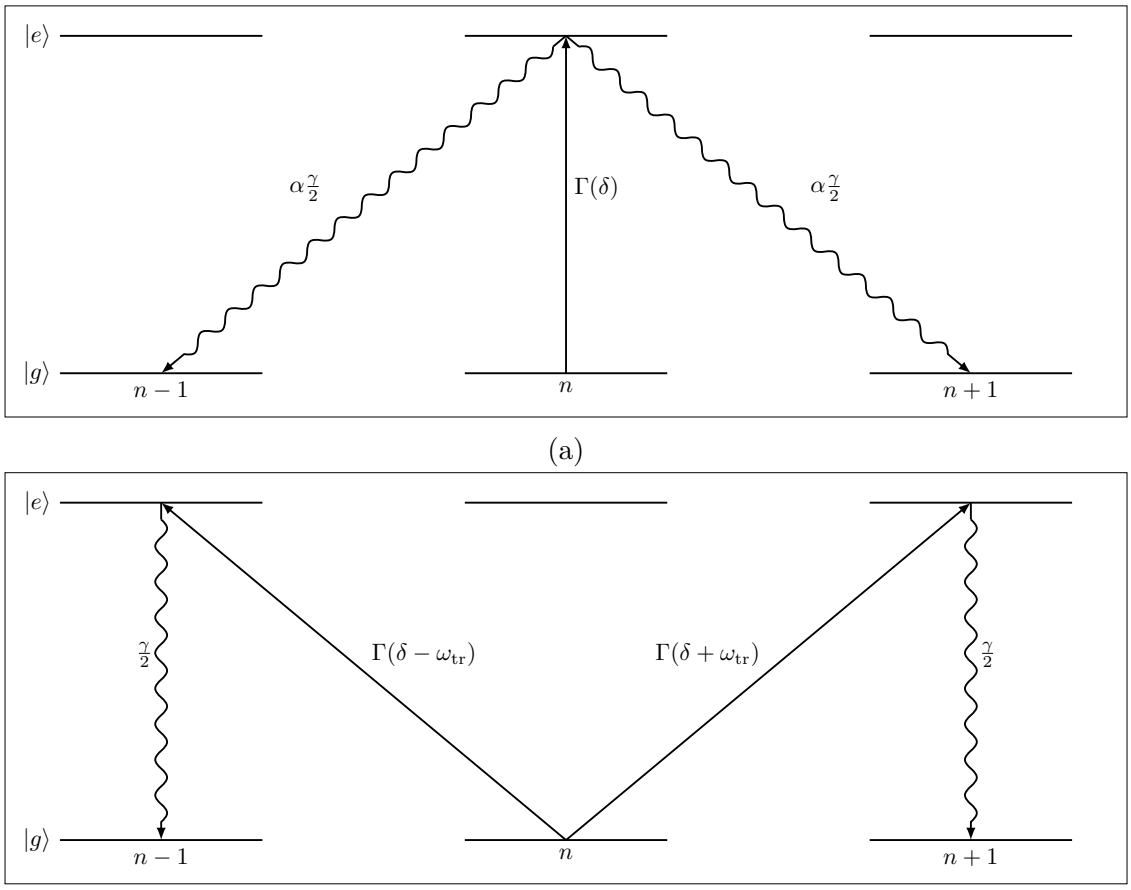


Figure 2.3: Processes leading to either heating or cooling for a trapped particle in the Lamb-Dicke regime. (a) The cooling laser excites the carrier transition at a rate $\Gamma(\delta)$, changes in the motional state occur during spontaneous emission. (b) The cooling laser excites either the red or blue sideband at a rate $\Gamma(\delta \pm \omega_{\mathrm{tr}})$ followed by spontaneous emission.

Figure 2.3 shows the individual processes occurring in the Lamb-Dicke regime that may lead to either heating or cooling. Oscillator states are coupled by spontaneous emission with a rate $\alpha\gamma/2$, where $\alpha = 2/5$ is related to the spread of spontaneous emission[3]. The induced upward transitions occur at a rate determined by the detuning through the Lorentzian shape of the spontaneous emission rate as a function of the detuning $\Gamma(\delta) = s_0\gamma/2/(1 + s0 + (2\delta/\gamma)^2)$. Thus, it is possible to

[3]This factor takes into account that only photons that have a non-zero component of momentum parallel to the trap axis can contribute to changes in the motional state, this is due to the presence of the factor $\cos\theta$ in the expression of $U_{nm}$ [129].

write the heating ($A_+$) and cooling ($A_-$) rates as

$$\begin{aligned} \eta^2 A_+ &= \eta^2\gamma[\alpha\Gamma(\delta) + \Gamma(\delta + \omega_{\mathrm{tr}})]\,, \\ \eta^2 A_- &= \eta^2\gamma[\alpha\Gamma(\delta) + \Gamma(\delta - \omega_{\mathrm{tr}})]\,. \end{aligned} \tag{2.14}$$

In both expressions, the first term on the right-hand side represents the contribution from the spontaneous decay at the carrier frequency, while the second term is the contribution from a sideband transition. With these rates, it is possible to write a master rate equation governing the population $\Pi_n$ of the n-th motional state [129]

$$\dot{\Pi}_n = -\eta^2\{[(n+1)\,A_+ + n\,A_-]\Pi_n + (n+1)\,A_-\,\Pi_{n+1} + n\,A_+\,\Pi_{n-1}\}\,, \tag{2.15}$$

The steady state solution of eq. (2.15) can be found by solving $\dot{\Pi}_n = 0$, this yields

$$A_-\,\Pi_{n+1} = A_+\,\Pi_n\,,$$

with a normalized solution in the form

$$\Pi_n = (\chi + 1)\chi^n\,,$$

and $\chi = A_+/A_-$. As long as $\chi < 1$, *i.e.* the laser beam is cooling rather than heating, this is a physically acceptable solution. With the steady-state distribution one may calculate the final average occupation number

$$\langle n\rangle = \frac{\chi}{1-\chi}\,,$$

which, for sufficiently low values of $\chi$, corresponds to a large probability of occupancy of the ground state of motion. In trapped ion systems, for instance, occupancy up to 99.9 % has been observed [18].

### 2.1.6 Dipolar traps and evaporative cooling

Optical dipole traps are a commonly used tools for confining and controlling particles like atoms [130, 131], molecules [132, 133], and, more recently, ions [51, 53]. These traps permit precise control of atomic positions even with highly complex geometries obtained with techniques such as holographic trapping [134].

In general, if an atom interacts with a laser having non-plane wavefronts (such as a Gaussian beam), it will experience both scattering and dipole force. Since the radiation pressure depends on the laser detuning as $1/\delta^2$ while the dipole force changes as $1/\delta$, by using a far-off-resonance laser, 3D confinement can be achieved with minimal scattering-induced heating. Therefore, a single high-power beam can be used to trap large atomic clouds [135] or, by focusing a laser to a sub-µm spot, single atom manipulation can be achieved [136]. Since the trapping potential

depends directly on the beam intensity (see eq. (2.9)), it is possible to fine tune the trap depth by changing the laser power.

One of the major aim of atomic physics is to study different quantum phases and phase transitions that occur at ultra-low temperatures, such as the Bose-Einstein condensation. Although laser cooling methods capable of achieving sub-recoil temperature do exist, such as Raman cooling using short laser pulses [137], reaching quantum degeneracy with laser cooling is extremely challenging. Only recently, quantum degeneracy was achieved by purely laser cooling methods using induced-transparency techniques [138], or by using release-and-retrap compression coupled with Raman sideband cooling [139].

To achieve condensation, a commonly used technique is *evaporative cooling* [140]. The key ideal of this cooling technique is that the hottest particles of an atomic sample are either let to evaporate from the trap (by reducing the trap depth) or forcefully pushed out (by pumping them to unbound states), so that the remaining particles thermalize at a lower temperature via mutual collisions. Generally, with this method the temperature can be decreased by several orders of magnitude at the cost of severe loss of atoms.

A simplified model of evaporative cooling [141] can be devised under the assumption that the atomic sample is far from any quantum phase transition, the ergodic hypothesis is valid, and that the interactions between atoms are limited to the s-wave scattering regime, such that the scattering cross-section is $\sigma = 8\pi a^2$ with $a$ the scattering length. In this model the phase-space density is found to scale as $\rho' = \rho\nu^{-\zeta(\xi+3/2)}$, here $\xi$ is a parameter dependent on the dimensionality and shape of the trapping potential (for a 3D harmonic potential $\xi = 3/2$), $\zeta = \log(T'/T)/\log(N'/N)$, $N$ and $N'$ are the number of atoms before and after evaporation, respectively, and $T$, $T'$ are the temperatures before and after the evaporation, respectively. This scaling suggests that as atoms evaporate both the temperature and the phase-space density $\rho$ change by orders of magnitude, while the number of atoms changes relatively slowly. Although these assumptions are rarely verified in practice, the model helps understand the relevant quantities intervening in the cooling process

Ultimately, the efficiency of this method is limited by the scattering rate and the speed of evaporation. If the evaporation rate is too fast atoms don't have the time to thermalize, leading to loss of atoms without real improvement of the sample's density. If the evaporation is too slow, the inelastic collisions occurring between the trapped particles will lead to losses. The final temperature achievable through evaporation depends on the ratio between the collision rate and $\sigma$, for most alkali atoms this result in a theoretical limit of approximately 1 nK ([108], chapter 12).

## 2.2 Physics of ion cooling and trapping

According to Earnshaw's theorem a collection of point charges cannot be maintained in a stable stationary equilibrium configuration solely by the electrostatic interaction of the charges. It follows that it is not possible to trap ions using only electrostatic fields since, at any given moment in time, the electric field will generate a trapping potential that has at least one non-confining axis. Different trapping scheme were invented to overcome this limitation, the most commons ones are:

- **Penning traps** [142]: it makes use of a combination of magnetic and electric fields to trap charged particles. Radial confinement is ensured by a strong homogeneous axial magnetic field and a quadrupole electric field confines the particles along the trap axis.
- **Paul (or RF) traps** [143]: this trap makes use of a dynamic electric field that is switched between two configurations having different non-confining axes. If this switching is performed fast enough (typically at RF), the ions will experience a pseudo-potential that ensures confinement in all directions.

### 2.2.1 The linear Paul trap

Although different configurations of a Paul trap exists, one of the most common one is the *linear* Paul trap. This configuration is realized by four equidistant electrodes, typically four cylindrical rods or four metal blades, that generate a dynamic radially-confining potential. An additional electrostatic field is added to ensure confinement along the trap axis. The time-averaged confining field is generated by applying a RF field at two opposing electrodes, while the other two electrodes are either connected to ground (the simplest configuration) or connected to a second RF signal with a 180° phase difference with respect to the first RF signal. This creates a deeper trapping field but it is technically more complex to set up.

In the most general case, in the trap centre the sum of the electrostatic and RF potentials can be expressed as

$$V(x,y,z,t) = \frac{V_0^{\mathrm{RF}} k_{\mathrm{RF}}}{2r_0^2}(\alpha x^2 + \beta y^2 + \gamma z^2)\cos(\omega_{\mathrm{RF}} t) + \frac{V_0^{\mathrm{DC}} k_{\mathrm{DC}}}{2z_0^2}(\alpha' x^2 + \beta' y^2 + \gamma' z^2)\,,$$

where $\omega_{\mathrm{RF}}$ is the RF frequency, $V_0^{\mathrm{RF}}$ and $V_0^{\mathrm{DC}}$ are the RF peak-to-peak voltage amplitude and the DC voltage applied to the electrodes, respectively. The $k_{\mathrm{RF}}$ and $k_{\mathrm{DC}}$ geometric coefficients take into account electrodes shapes and shielding effects, $r_0$ and $z_0$ are the distances between the RF and DC electrodes, respectively. The real-valued coefficients $(\alpha, \beta, \gamma)$ and $(\alpha', \beta', \gamma')$ are determined by the trap geometry. The resulting potential must satisfy the Laplace equation $\nabla^2 V = 0$,

placing constraints on the possible values of the coefficients. For a linear Paul trap, the coefficients can be taken as[4] $(\alpha, \beta, \gamma) = (1, -1, 0)$ and $(\alpha', \beta', \gamma') = (-1, -1, 2)$, where $\gamma = 0$ is an approximation valid only assuming that the trap electrodes are infinite along the $z$-axis. The resulting field thus is

$$V(x, y, z, t) = \frac{V_0^{\mathrm{RF}} k_{\mathrm{RF}}}{2r_0^2}(x^2 - y^2)\cos(\omega_{\mathrm{RF}} t) + \frac{V_0^{\mathrm{DC}} k_{\mathrm{DC}}}{2z_0^2}(x^2 + y^2 + 2z^2)\,.$$

The force acting on a particle of charge $Ze_0$ is given by: $\mathbf{F} = -Ze_0 \boldsymbol{\nabla} V(x, y, z, t)$. Thus, the Newtonian equation of motion is

$$m_{\mathrm{ion}} \frac{\mathrm{d}^2\mathbf{x}}{\mathrm{d}t^2} = \mathbf{x}\left[\begin{pmatrix} -\frac{Ze_0 V_0^{\mathrm{RF}} k_{\mathrm{RF}}}{r_0^2} \\ +\frac{Ze_0 V_0^{\mathrm{RF}} k_{\mathrm{RF}}}{r_0^2} \\ 0 \end{pmatrix} \cos(\omega_{\mathrm{RF}} t) + \begin{pmatrix} \frac{Ze_0 V_0^{\mathrm{DC}} k_{\mathrm{DC}}}{z_0^2} \\ \frac{Ze_0 V_0^{\mathrm{DC}} k_{\mathrm{DC}}}{z_0^2} \\ -\frac{2Ze_0 V_0^{\mathrm{DC}} k_{\mathrm{DC}}}{z_0^2} \end{pmatrix}\right].$$

After some manipulation, the equation of motion can be written as a system of Mathieu equations

$$\frac{\mathrm{d}^2\mathbf{x}}{\mathrm{d}\tau^2} + (\mathbf{a} + 2\mathbf{q}\cos(2\tau))\mathbf{x} = 0\,,$$

where $\tau = \omega_{\mathrm{RF}} t/2$ and

$$\mathbf{a} = (-1, -1, 2)\, a = (-1, -1, 2)\, \frac{4Ze_0 V_0^{\mathrm{DC}} k_{\mathrm{DC}}}{m_{\mathrm{ion}} z_0^2 \omega_{RF}^2}\,,$$
$$\mathbf{q} = (1, -1, 0)\, q = (-1, -1, 2)\, \frac{2Ze_0 V_0^{\mathrm{RF}} k_{\mathrm{RF}}}{m_{\mathrm{ion}} r_0^2 \omega_{RF}^2}\,,$$

are the dimensionless Mathieu parameters. General solutions to the Mathieu equation are determined by the Floquet's theorem

$$x_j(\tau) = e^{i\beta_j \tau} F(a_j, q_j, \tau), \qquad j = 1,2,3$$

where $\beta_j$ are the (complex) characteristic Mathieu exponents and $F(a, q, \tau)$ is a periodic function of $\tau$ with period $\pi$. The exponents $\beta_j$ are function of $a$ and $q$ and do not depend on the initial conditions. In order for these solutions to be stable the characteristic exponents have to be real, else the particle's trajectory will diverge exponentially in time, eventually leading to the loss of the ion. Therefore, the dimensionless parameters $a$ and $q$ univocally determine the stability region of the trap, independently of the initial condition of motion. The region containing the $(a, q) = (0, 0)$ point is the *lowest-stability region* and it is the most commonly used in practical experiments.

[4]The frame of reference is defined such that the $z$-axis is oriented along the electrodes axis and the $x$-axis crosses the centres of two opposing electrodes.

To the lowest approximation order, the form of a stable solution can be determined by assuming $\|\mathbf{a}\|, \|\mathbf{q}\| \ll 1$

$$x_j = x_{0,j} \cos(\omega_j t + \phi_j) \left(1 + \frac{q_j}{2} \cos(\omega_{\mathrm{RF}} t)\right), \qquad j = 1,2,3 \tag{2.16}$$

where $x_{0,j}$, $\phi_j$ and $\omega_j \approx \omega_{\mathrm{RF}}/2\sqrt{(a_j + q_j^2/2)} \ll \omega_{\mathrm{RF}}$ are the amplitude, phase and frequency of the so-called *secular motion*, this motion describes a slow oscillation around the trap centre. The second term appearing in eq. (2.16) is the *micromotion*, which represents a fast oscillation at the RF frequency superimposed to the secular motion. Due to the $q_j/2$ factor, the amplitude of the micromotion is much smaller than the secular one.

The relation between secular motion and micromotion amplitudes in eq. (2.16) suggests that it might be possible to reduce both amplitudes to zero through laser cooling. In fact, this is true only for the approximated classical result. A purely quantum mechanical treatment shows that micromotion has a minimum non-zero amplitude [144] $x_j^{\min} = q_j/2\sqrt{\hbar/(2m_{\mathrm{ion}}\omega_j)}$, independent of the secular motion. Therefore, micromotion is an intrinsic property of the trapping method used and, once the ion is properly cooled, it becomes the dominant term in the ion kinetic energy. For example, the collisional energy between the ion and the surrounding atoms is mostly determined by the residual micromotion.

In practical experiments *excess micromotion*, *i.e.* additional contributions to micromotion, are always present. These contributions arise from few different factors [145]:

- **In-phase micromotion**: It is caused by electrostatic fields that displace the average position of the ion from the centre of the trap. It will cause an oscillation along the axis of displacement with an amplitude proportional to the displacement distance.
- **Out-of-phase excess micromotion**: It occurs when the RF applied to opposing electrodes is out-of-phase. This creates an asymmetry in the potential causing the ion to oscillate with an amplitude proportional to the phase delay between electrodes.
- **Imperfections of trap electrodes**: any imperfection in the electrodes surface regularity, alignment, and their finite dimension will cause additional asymmetries in the trapping fields, yielding additional micromotion.

Micromotion detection can be performed using several methods: direct measurement of the ion trajectory using high numerical aperture imaging [146], through spectroscopy methods [145], by inducing parametric resonances through RF modulation [147]. In atom-ion hybrid quantum systems, ion micromotion can be estimated by measuring atom losses [148]. Excess micromotion can, in principle, be compensated by introducing additional DC or RF fields.

To cool an ion trapped in a Paul trap, a single red-detuned laser beam can be used. In first approximation, the potential realized by a Paul trap can be considered to be harmonic. The radiation pressure (see eq. (2.5)) introduced by a red-detuned laser beam will provide a friction term $-\beta\mathbf{v}$ that results in a reduction of the ion secular motion. The constant term $\mathbf{F}_{\mathrm{sp}}^{(0)}$ will only cause a change in the trap centre. If the laser beam used has non-negligible projection on all three axis of the trap, a single laser can be used to cool all the ion's degree of motion.

### 2.2.2 Optical traps

In atom-ion collisions the ion's instantaneous velocity has a contribution from the micromotion that is in general not negligible. After the collision event, this micromotion component is coupled into the secular motion of the ion. As a result, atom-ion collisions in the presence of micromotion increase the energy of the ion. Although, micromotion can theoretically be compensated down to its quantum limit, it is not sufficient to avoid heating. Placing the ion at the centre of the trap (the only point which is micromotion free) is also not sufficient, as it will be displaced from such position, since atom-ion collisions occur at the centre of mass of the atom-ion pair [57]. As a result, even if micromotion is perfectly compensated, the contribution of micromotion in atom-ion collisions is not negligible. Thus, to reach the ultracold regime of atom-ion collisions, a micromotion-free trapping scheme is required.

A possible alternative to Paul traps is to use optical potentials, created by far-off resonance light beams, which would remove micromotion all together. Optical confinement of ions has been investigated in single beam dipole traps [51, 149] and optical lattices [150, 151]. Although successful confinement and laser cooling was demonstrated, the ion lifetime in these traps remains limited due to shallow confinement and off-resonant scattering [152].

An increase of trap depth can be achieved by properly choosing the Optical Dipole Trap (ODT) light wavelength since, as it follows from eq. (2.9), it determines the atom polarizability. When trapping particles optically, it is convenient to work at the magic wavelength such that the light shifts of ground and excited states are equal. Thus, an ideal wavelength for optical trapping should have three characteristics: first, it should be associated with a large value of polarizability $\alpha(\lambda)$; second, it should be a magic-wavelength; and, finally, it should be experimentally feasible to work with. The depth of the optical trap can be further increased by making use of an optical cavity thus exploiting the intra-cavity resonance.

## 2.3 $Ba^+Li$ Physics

The choice of the atomic species involved in the atom-ion mixture plays an important role in determining the type of collisions and chemical reactions that may occur as a result of the interaction between the two particles. Reaching the s-wave scattering regime requires that the major contribution to the scattering cross-section is provided by partial waves with zero angular momentum. In other words, the collisional energy must be lower than the height of the centrifugal barrier of the p-wave molecular potential $E^*$, as defined in section 1.1. The higher is the barrier, the higher is the collisional energy (and thus the temperature) at which the collision regime can no longer be reduced to a single partial wave contribution. Since $E^*$ is proportional to the inverse of the reduced mass $\mu$ of the system, in choosing the atomic species, one aims at minimizing $\mu$. One may intuitively choose to use two light particles, but a better choice is to select an atom-ion pair such that $m_{\text{ion}} \gg m_{\text{atom}}$ and that the atom has a relatively low mass. Choosing a heavy ion has a major benefit: during the collision the ion accelerates toward the incoming atom, causing a displacement from the trap centre, which in turn leads to an increase in the collisional energy due to micromotion in RF traps [153]. The larger is the ion's mass, the smaller is the displacement. In the specific case of $^{138}Ba^+$ and $^6Li$, the reduced mass is $\mu = 5.75u$, where $u$ is the atomic mass unit. The corresponding height of the centrifugal barrier for p-wave scattering is $E^* \approx 8.76\,\mu\text{K} \times k_B$.

Additionally, the choice of the atom-ion pair results in different rates for inelastic scattering events. As shown in section 1.1.2, several types of inelastic collisions may occur during atom-ion interactions. Some of these inelastic collisions lead to changes that may be unwanted in certain experiments. For example, charge exchange processes lead to neutralization and loss of the ion, this is clearly a detriment to experiments working in quantum simulation, computation or optical clocks. A major advantage of the $Ba^+$-Li combination is the possibility of controlling certain inelastic processes:

- *Charge-exchange is energetically unfavourable.* The $Ba^+$-Li mixture in the electronic ground state constitutes the absolute ground state of the system and 0.2 eV are required to reach the charge exchanged mixture Ba-$Li^+$.

- *Three-body recombination is suppressed by Pauli's principle.* As long as collisions occur in the s-wave scattering regime and spin-polarized fermionic lithium is used, the wavefunction of two atoms interacting with the same ion will be described by a triplet state multiplying an anti-symmetric spatial wavefunction. This asymmetry will lead to a vanishing scattering cross-section for even-numbered waves (such as the s-wave).

- *Spin relaxation is forbidden by angular momentum conservation.* Spin relaxation is induced by the spin-orbit coupling occurring during the collision. If the collision occurs at zero angular momentum (s-wave), no change in the total angular momentum can occur.

- *Spin exchange is energetically unfavourable.* Due to the different Landé g-factor of barium and lithium, with a field of only 1 G, spin exchange would require $200\,\mu K \times k_B$ of energy to occur. Since this value is much larger than the p-wave barrier $E^*$, in the s-wave scattering regime this type of reaction is strongly suppressed.

Concerning the choice of the isotopes in the $Ba^+Li$ mixture, the best option is $^6Li$ for the atom species, as this is the fermionic isotope of lithium, allowing to tune the atom-atom interaction using Feshbach resonances. For the ion species $^{138}Ba^+$ is the most common isotope and does not have hyperfine splitting, thus ensuring an easier setup for laser cooling. The Grotrian diagrams in figs. 2.4 and 2.5 show the main transition lines that will be used in the experiment. With the exception of the clock transition, all other wavelengths used for cooling are in the visible region.

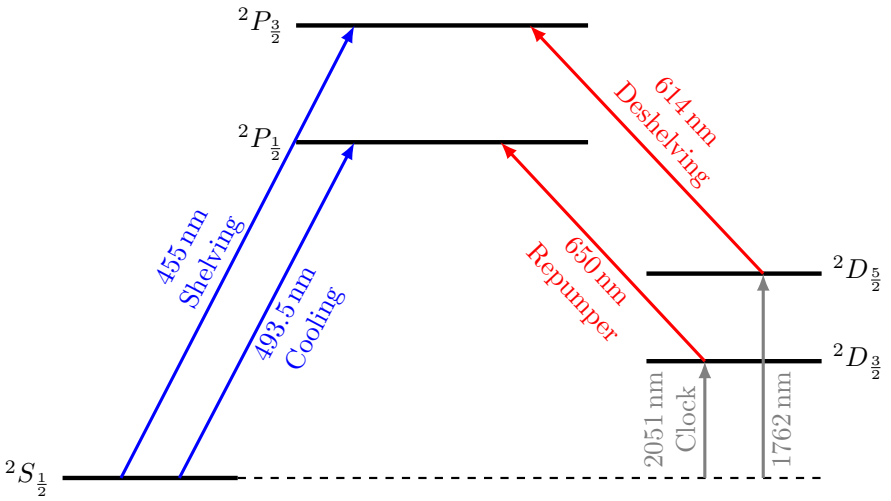


Figure 2.4: Grotrian diagram showing the ground and lowest excited states of $^{138}Ba^+$ [154].

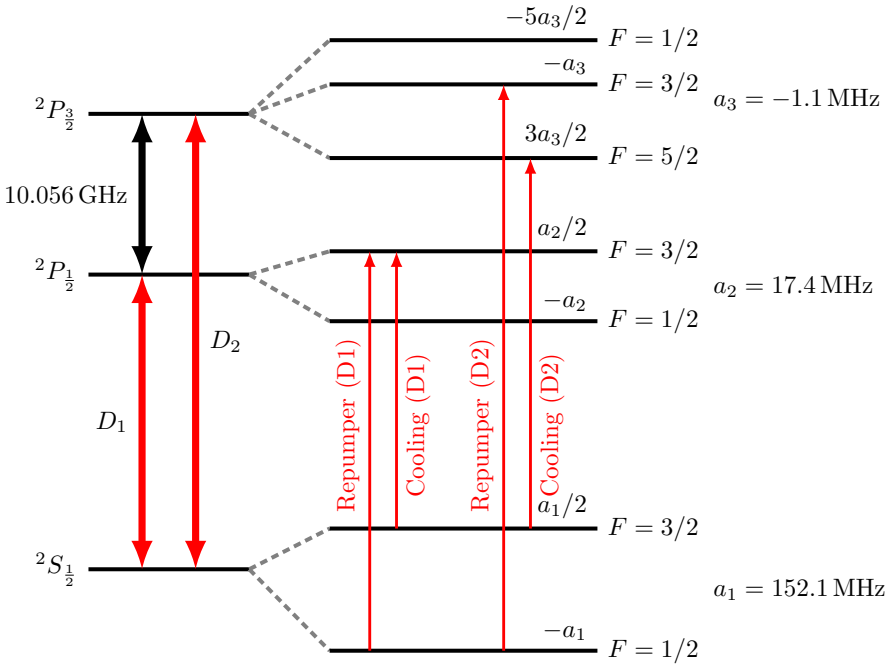


Figure 2.5: Grotrian diagram showing the ground and lowest excited states of $^6Li$ [154].

### 2.3.1 The $Ba^+Li$ experiment

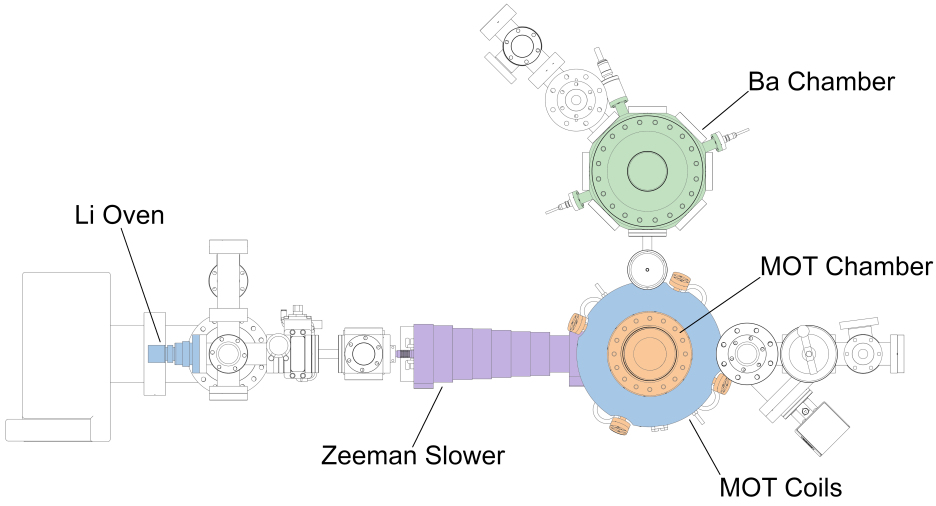


Figure 2.6: 3D CAD view of the complete vacuum setup at the $Ba^+Li$ experiment.

The $Ba^+Li$ experiment aims at realizing a mixture of $^6Li$ and $^{138}Ba^+$ capable of reaching the s-wave scattering regime. To do so an UHV setup consisting of two separate chambers was designed. A top view of the setup is shown in fig. 2.6. Each of the two chambers is dedicated to producing and cooling either $Ba^+$ ions or ultracold clouds of fermionic $^6Li$.

The barium chamber contains the ion trap used to cool the ions. Hot barium atoms are evaporated from a metallic source placed in an oven placed under the trap. The oven points toward the trap centre. The barium atoms are ionized via a two-photon photo-ionization process with 413 nm light. In order to trap the ions, a two stages hybrid ion trap was designed. In a first cooling stage, the ions generated by photo-ionization are trapped in a linear Paul trap and are cooled using standard laser techniques. Once the ions are sufficiently cold, they are transferred to the the second cooling stage. In this stage, ions are trapped using a optical dipole trap with a wavelength of $\lambda = 451.7\,\text{nm}$. This is a magic-wavelength for the $6\,S_{1/2} \rightarrow 6\,P_{1/2}$ transition of barium [155], which ensures that the optical trap depth is not dependent on the barium internal state, and corresponds to a relatively high atomic polarizability $\alpha_{Ba^+}(451.7\,\text{nm}) = -4460\,\text{au}$. This wavelength is blue-detuned with respect to the cooling transitions of $Ba^+$, thus it would create a repulsive potential. In order to trap with blue-detuned light beams, an optical-lattice-based scheme has to be used, where the ions are trapped in the minima of intensity.

For this reason, in the $Ba^+Li$ experiment a bow-tie cavity is used. The optical lattice is generated by the interference of the two beams crossing at an angle $2\theta$.

The cavity is designed such that $\theta = 5°$, leading to a spacing between consecutive sites of approximately 2.6 µm. The optical lattice has only 2 confining directions, thus an additional electric quadrupole is used to ensure trapping on the third axis. The resulting *electro-optical trap* is described in detail in [156, 53]. The intermediate trapping using the RF trap is necessary as optical dipole traps are typically not deep enough to be able to confine particles at the temperature of evaporation from the oven.

In the proposed experimental sequence, while barium ions are being produced, the lithium setup independently prepares an ultracold degenerate cloud of lithium. $^6$Li atoms are evaporated from an enriched metallic source placed in an oven; the hot vapours are slowed down and cooled using the ZS and MOT. The MOT is then compressed to increase the cloud density before transferring it to a cavity-enhanced optical dipole trap. In this optical trap, evaporative cooling is performed to bring the atoms to degeneracy. Finally, the ultracold atoms are optically transported to the barium chamber with a 1064 nm laser. In order to speed up the evaporative process, a novel cooling scheme can be used between the cMOT and the evaporative cooling stages: single-photon sideband cooling can be performed on neutral atoms trapped in a deep optical potentials, while the atoms are cooled via a D1 gray-molasses along the weakly-binding axes of the optical trap. With this scheme the atoms' energy can be further reduced and, therefore, evaporative cooling can be performed for a reduced amount of time before degeneracy occurs. The application of this cooling stage will be crucial for the fast production of ultracold atoms, and for exploring the atom-ion physics in an experiment with a high repetition rate. A relevant part of this thesis is devoted to provide a viable scheme for sideband cooling of Li atoms in a deep optical potential. The design of the high-finesse optical resonator which is intended to be used to generate the deep optical lattice is shown in chapter 4, the theoretical analysis of this method is presented in chapter 5.

# Chapter 3

# Lithium setup

This chapter describes the experimental setup for the preparation of a cold lithium cloud. The bulk of this setup is constituted by a UHV-compatible chamber made up of several components, which are described in section 3.1. The assembly, baking and preparation of the vacuum system are presented in section 3.1.6. To generate the proper light beams used in trapping and cooling the lithium atoms a two-laser optical circuit was designed and realized. Such optical circuit is described in section 3.2. Section 3.3 reports on the first experimental results of the lithium MOT at the $Ba^+Li$ experiment.

## 3.1 Vacuum setup

Producing ultracold atoms typically requires a setup that contains regions with considerable temperature differences. On the one hand, production of lithium requires a source of atomic vapours, typically obtained from heating up chunks of metallic lithium at a few hundred degree Celsius. On the other hand, the ultimate goal of this setup is the production of ultracold gasses at a few hundred nK. Additionally, the gases must be confined in an UHV environment in order to minimize collisions with the background gas. Therefore, the overall apparatus must be designed in such a way that both a very hot vapour and an ultracold cloud of atoms can co-exist in the same UHV environment. The 3D Computed-Aided Design (CAD) view of the setup used at the $Ba^+Li$ experiment is shown in fig. 3.1. The system can be divided in four major sections: the oven chambers, which comprise the oven itself (containing the metallic lithium chunks) as well as a dedicated ion pump, shutter and gate valve to pinch off the oven from the rest of the system; the ZS and the differential pumping stage; the MOT chamber and the ZS input window section. Each part is described in details in the following sections.

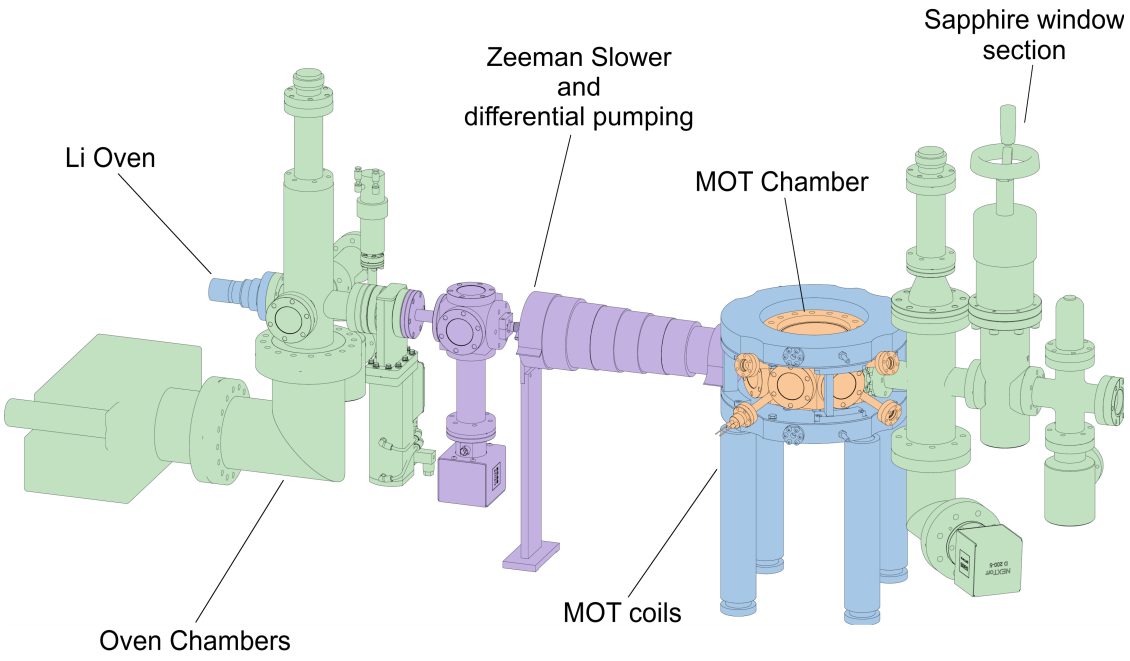


Figure 3.1: 3D CAD view of the lithium vacuum setup at the $Ba^{+}Li$ experiment. Different section of the setup are described in the main text.

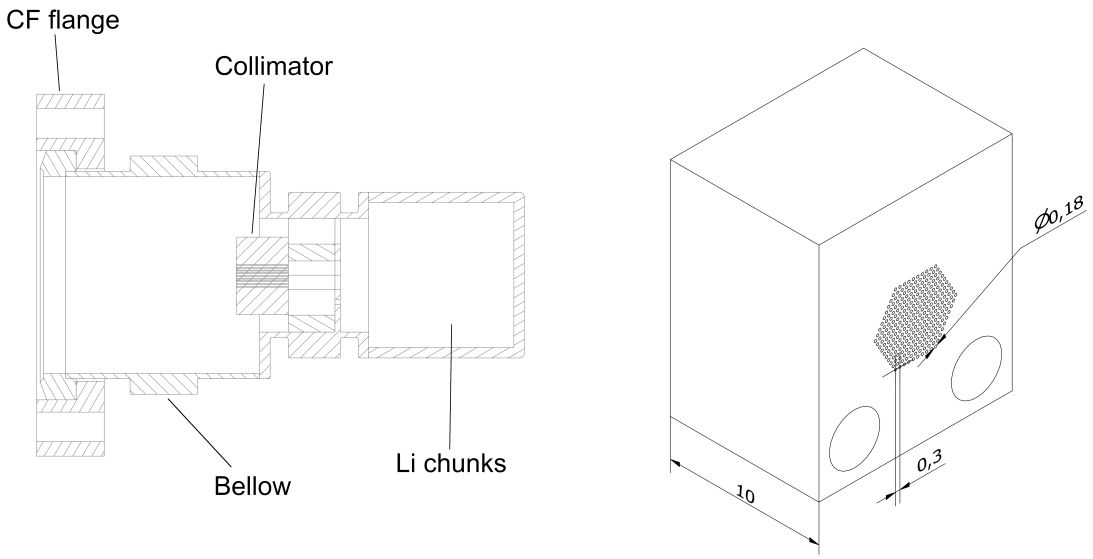


(a) (b)

Figure 3.2: (a) 3D CAD section view of the lithium oven. (b) 3D CAD view of the lithium oven collimator.

### 3.1.1 Lithium oven

Figure 3.2a shows a cross-section view of the lithium oven. The oven has a cylindrical shape with an external diameter of 32 mm, the exit slit for lithium vapours is 6 mm in diameter. Lithium chunks are located in the right-most chamber, which is wrapped externally by heating tapes, a type K thermocouple is placed between the oven walls and the heating tapes and it is used for temperature stabilization. The hot atomic vapour is forced through a collimation stage in order to limit the angular distribution on the transversal axis of the atomic beam which would result in coating the chamber internal walls.

This compact collimator is shown in fig. 3.2b, the total width of the collimator is 10 mm. To avoid the issue of having to drill micro-sized holes along the entire 10 mm width, the collimator is formed by 3 components: two plates having a width of 2 mm and a spacer 6 mm in width. Micro-sized holes with a diameter of 200 µm arranged in a hexagonal grid spaced by 300 µm (centre-to-centre) are drilled in the two plates. The spacer is placed in between the two plates, and keeps the two arrays of holes aligned thanks to two precision dowels. The maximal angular dispersion of atoms traversing this collimator is the same as if the collimator was made as a single component 10 mm long. This angular dispersion can be computed as $\arctan(0.2/10) \approx 1.15°$. The corresponding velocity is $v_T = v_0\, 0.2/10 \approx 34\,\mathrm{m\,s^{-1}}$, where $v_0 = (3k_BT/m)^{1/2} \approx 1700\,\mathrm{m\,s^{-1}}$ is the particles' forward velocity calculated using the equipartition theorem. The associated temperature is $T = v_T^2 m/k_B \approx 830\,\mathrm{mK}$. The collimator is held by two M3 screws directly in front of the oven exit aperture. In case the atomic beam direction needs to be adjusted, the oven can be angled thanks to a bellow soldered between the CF40 flange and the oven cylinder.

The components that constitute the oven section are shown in fig. 3.3. The oven is mounted on a 6-way asymmetric cross, facing the ZS axis. Due to the relatively high temperature of evaporation of lithium ($\approx 400\,°\mathrm{C}$), while the oven is heated the worst vacuum condition is expected in this part of the system. Therefore, a dedicated ion pump[1] is connected below the oven through a 90° CF100 elbow. To further improve the vacuum, this section houses a Titanium Sublimation Pump (TSP)[2]. TSPs are used to coat the internal surfaces of the vacuum system with a layer of titanium, this layer acts as a getter material and further reduces the amount of free particles present in the system. A shutter[3] allows for blocking the atomic beam when it is not needed and an all-metal gate valve[4] separates the oven chambers from the rest of the vacuum setup. Both the shutter and the gate valve

[1] Agilent, VacIon Plus 75 Pump

[2] Agilent, TSP Cartridge

[3] Kurt J. Lesker Company, DS600VPS-P

[4] MDC precision, SKU #307001

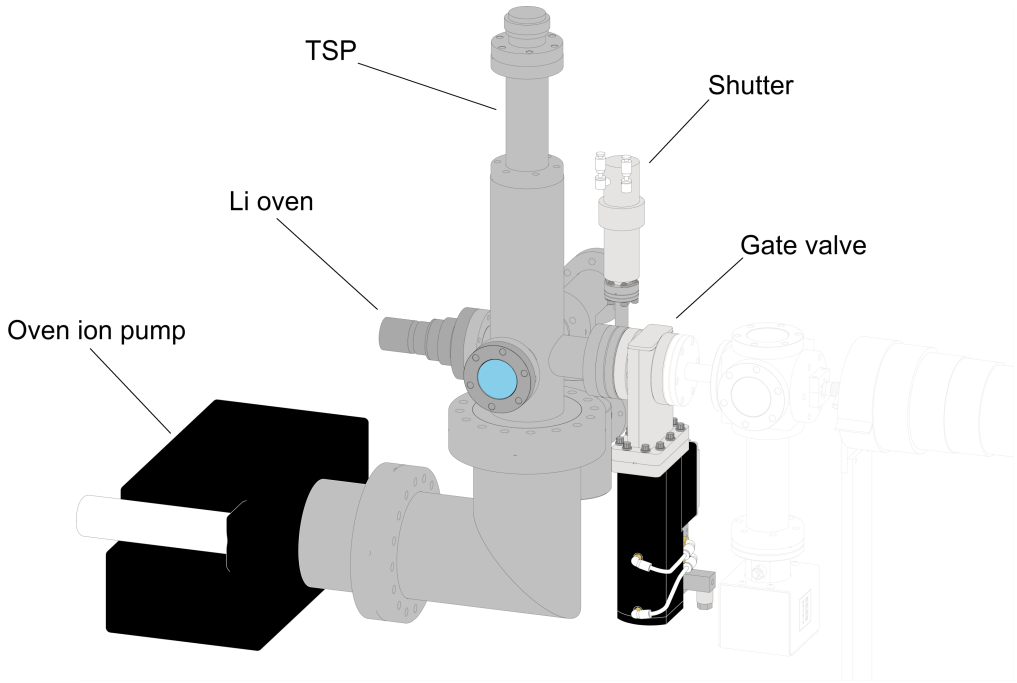


Figure 3.3: 3D CAD view of the lithium oven section. A dedicated ion pump is placed under the oven and the entire section can be isolated from the rest of the system through an all-metal gate valve.

are pneumatically actuated and are connected to a simple custom-made circuit that allows for either manual or automatic control (via a TTL signal). Thanks to a vacuum isolation valve[5] installed on the side of the oven chambers, it is possible to vent and vacuum the oven section while it is isolated from the rest of the system, in case maintenance on the oven is to be performed. The presence of a shutter ensures the possibility of turning off the source of hot atoms during the production of the ultracold gas, and avoid collisions between hot and cold atoms, without the need of lowering the oven temperature. Two viewports are mounted to the sides of the oven, for visual inspection and for performing spectroscopy.

### 3.1.2 Zeeman slower

The ZS coils and differential pumping section are shown in fig. 3.4. This section is connected to the lithium oven chambers by a narrow (8 mm diameter) straight tube with CF40 flanges. The narrow connection between the two regions increases the flow resistance in the vacuum system acting as a differential pumping stage, and

[5] Allectra, 512-AMV40-C40

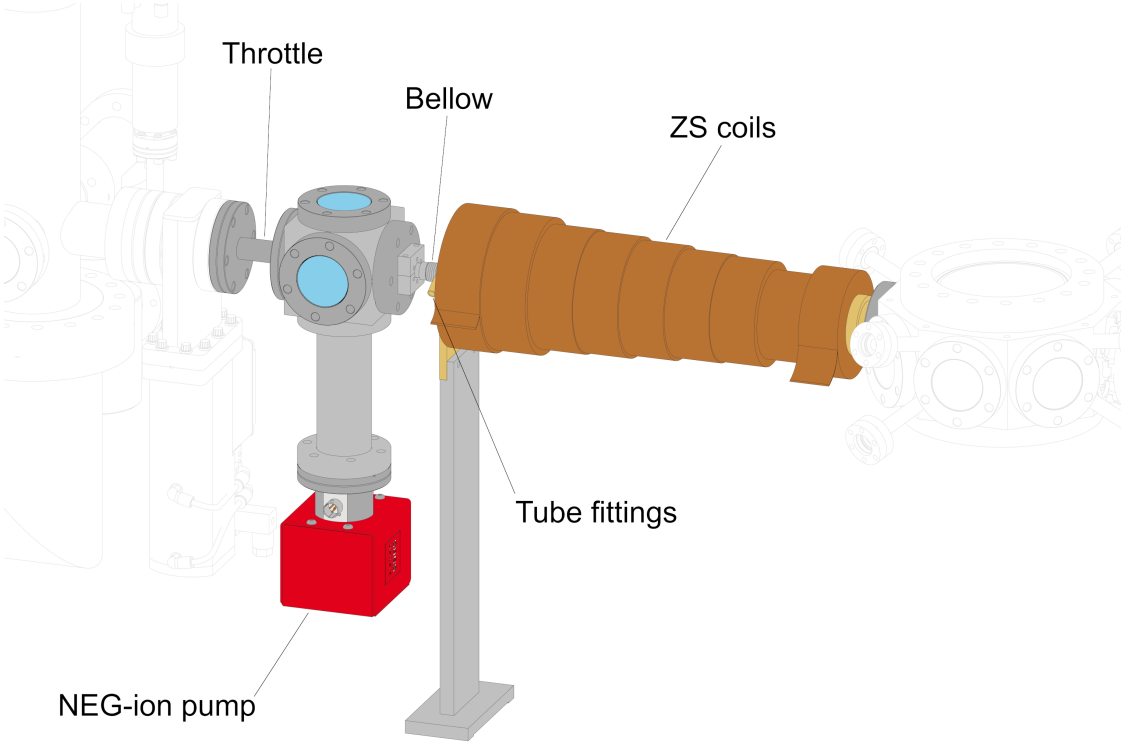


Figure 3.4: 3D CAD view of the lithium Zeeman slower coils and differential pumping section.

reducing the influence that the bad vacuum condition in the oven chamber has on the rest of the system. After the straight tube, a 6-way cube is used to install two lateral viewports, a Non-Evaporative Getter (NEG)-ion combination pump[6] and the ZS tube. The NEG-ion pump combines getter materials technology (which is highly efficient in pumping lighter elements such as $H_2$) and ion pumps technology (which pumps efficiently larger molecules such as $N_2$ or $O_2$ and inert gases like Ar) in order to provide the best pumping speed for all contaminants.

The ZS tube is connected to the cube with a CF40 to CF10 zero-length reducer and a custom-made CF10 flange composed by two metallic pieces that pinch a CF10 gasket and press it against the blade on the CF40-CF10 reducer. The ZS tube (9 mm in diameter) has a small 17 mm long bellow at the tip which allow for angling the entirety of the oven section with respect to the ZS axis. The ZS tube length is approximately 400 mm, this compact design increases the solid angle subtended by the MOT volume; therefore, it increases the collection efficiency of

[6]Saes Group, NEXTORR D200–5

the MOT.

The ZS magnetic field is generated by an array of nine coils made out of flat (2 mm × 1 mm) copper wire. The coils are configured in a ZS-MOT merging configuration: the coil diameter decreases along the ZS axis except for the last coil which is larger than the previous one. This ensures that the magnetic field of the ZS decreases along its axis and that the field smoothly merges with the field generated by the MOT coils. The first eight coils constitute the main body of the ZS and are run at 5.85 A while the ninth coil is the merging coil and is kept at 3.4 A.

Due to the high current, the ZS coils tend to heat up during operation; therefore, the manufacturer was asked to wrap them directly on a hollow brass tube where two water pipes are soldered. During normal operation water at 14 °C flows through these pipes and cools the internal side of the coils. The temperature measured on the surface of the first (largest) coil was found to be approximately 80 °C after a few hours of operation at 5.85 A. This heating can be further reduced by running the coils only during the ZS and MOT loading sequences, and turning them off afterwards when not needed.

### 3.1.3 MOT chamber

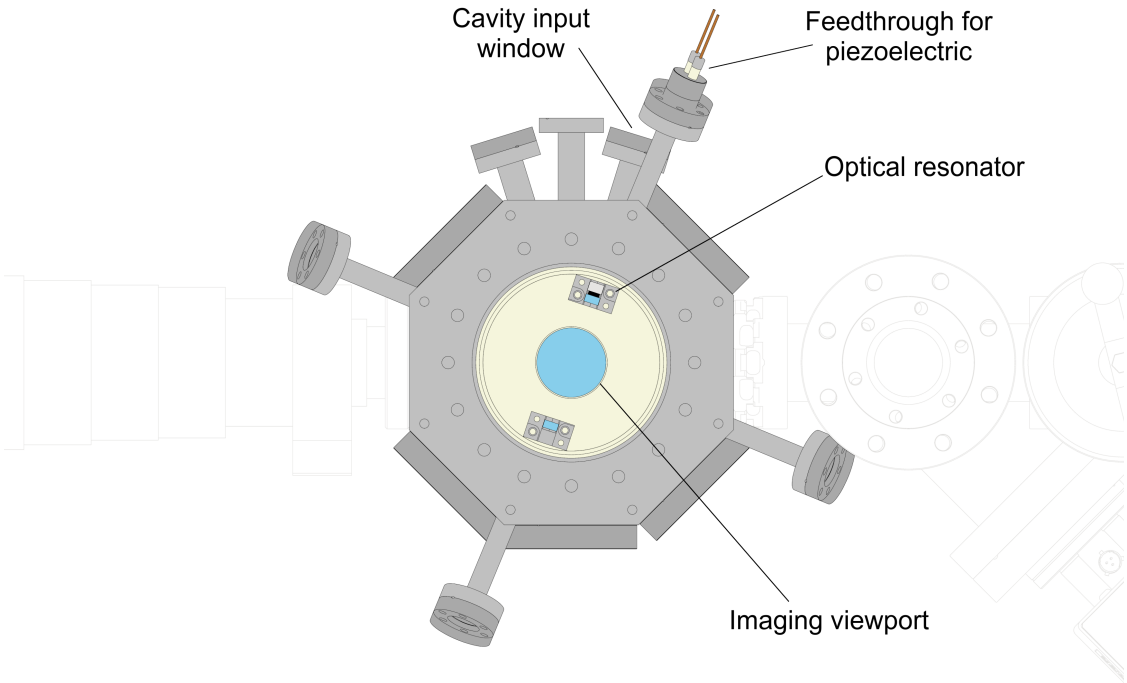


Figure 3.5: Top-down view of the MOT chamber.

The MOT chamber geometry is shown in top view in fig. 3.5. The MOT chamber is a custom-made octagon having seven CF40 flanges and (on the eighth face) three

CF16 straight connectors. Five of the seven CF40 flanges are used as viewports for inserting the MOT beams and the optical transport beam, the remaining two are connected to the ZS tube and to the ZS laser beam input section. Of the three CF16 straight connectors present on the eighth face, one is used for the optical transport of the atoms and it is directly connected to a gate valve separating the lithium and barium chambers. A second CF16 connector is used to inject the beam used for the in-vacuum optical resonator. Height narrow tubes protrude from the octagon at an angle of 15°, four of them angled upward, the other four angled downward, all facing toward the centre of the chamber. These tubes (with the exception of three of them) are equipped with viewports and can be used for inspection of the atomic cloud in the MOT or for inserting additional light beams for future experiments. Of the three tubes that are not used as viewports, two of them do not offer optical access to the centre of the chamber because they are blocked by the resonator support, while a third is used for the electronic feedthrough connected to the piezoelectric transducer of the resonator.

To ensure good optical access, the top viewport is a CF100 re-entrant flange equipped with a quartz window 60 mm in diameter. The flange also sustains a vertical cage support that is used for the optical elements for the vertical beams. The bottom viewport is also a re-entrant CF100. However, in this case the flange is formed by a single piece of steel with a CF-compatible blade and six threaded holes on the air-side that can be used to attach CF40 flanges. This design ensured the possibility of machining the metal parts of the CF100 flange, and equip it with the mechanical mounts of the optical resonator. The actual viewport is a custom re-entrant CF40 flange housing a 3.3 mm thick piece of quartz 36 mm in diameter. With this configuration the re-entrant CF100 flange could be sent for machining without risk of damaging the quartz viewport.

### 3.1.4 MOT coils

The arrangement and geometric parameters of coils are crucial aspects in the realization of magnetic fields with specific attributes. In particular, in quantum gases experiments, it is important to realize highly uniform magnetic fields. This is ensured by the so-called Helmholtz configuration, in which two coils of radius $R$ are spaced by $R$ and have their generated magnetic field parallel to each other. The resulting magnetic field in between the two coils is uniform and double the field of a single coil. In the anti-Helmholtz configuration the coils are driven to generate anti-parallel fields, this result in a field that is null at the mid point between the two coils and linearly increasing along the coils' axis. This is the configuration used to generate the field for the MOT.

Each coil[7] is formed by 4 stacked layers, each of which is made of 24 loops of 1.4 mm × 4 mm wire and is immersed in resin. The resulting coil has an inner diameter of 178(1) mm, an external diameter of 244(1) mm, and a height of 17.15(10) mm. Using the 4-terminal sensing method, the electric resistance and coil inductance were measured to be 225(1) mΩ and 309(1) µH, respectively.

As mentioned in chapter 2, in the preparation of a quantum gas a stage of evaporative cooling is practically necessary. The scattering lengths of $^6$Li atoms at 0 G is approximately $47a_0$ [157], where $a_0$ is the Bohr radius, for all the combinations of Zeeman sublevels in the ground state manifold. This value makes evaporative cooling at 0 G very inefficient. A common solution is to exploit Feshbach resonances to increase the scattering length. To this end, the narrow Feshbach resonance between the states $|1/2, 1/2\rangle$ and $|1/2, -1/2\rangle$ located at 543 G can be used [158].

Since no other coil pair is present on the MOT chamber, in order to perform evaporative cooling, the MOT coils are required to generate a strong uniform magnetic field of 543 G. To achieve this, one of the coils' polarity is flipped using an H-bridge circuit based on insulated-gate bipolar transistor, thus reaching a true Helmholtz coil configuration. Even if the evaporation sequence may lasts a few ms, the high current involved (≈ 110 A) and relatively high electrical resistance of the coils result in a large power dissipation. Therefore, water cooling is necessary to avoid damaging the coil wires and excessive heat dissipation in air that may cause flickering in the laser beam trajectories.

To address the cooling issues a holding structure that allows for the immersion of the coils in water flow was designed. Figure 3.6 shows the 3D CAD view of the coils holders in their assembled configuration, detailed mechanical drawings are presented in appendix A. Due to the narrow space available around the MOT chamber, the design of the coil holder had to be compact enough to fit within other components, while still allowing for full immersion of the coils. A major problem was the asymmetric 4-way cross attached to the MOT chamber, which was almost in contact with the bare coils. A 20 mm straight CF40 connector between the cross and the chamber was added in order to provide more space for the coil structure. The supports are composed of two main components: a U-shaped holder where the coil are inserted and a cap housing two Viton o-rings for sealing.

The U-shape holder is designed to have an internal region 1 mm larger than the coil in all directions, allowing for a narrow channel of water to run around the coil. On one side of the U-shape a 8 mm hole with an 10 mm undercut provides space and exit slit for the coils wires. To seal the hole where the coil wires exit the holder, a "cable cap" piece presses a 15 mm Viton o-ring against the holder side in a triangular o-ring groove. The remaining empty space between the wires and the

[7] manufactured by Oswald Elektromotoren GmbH

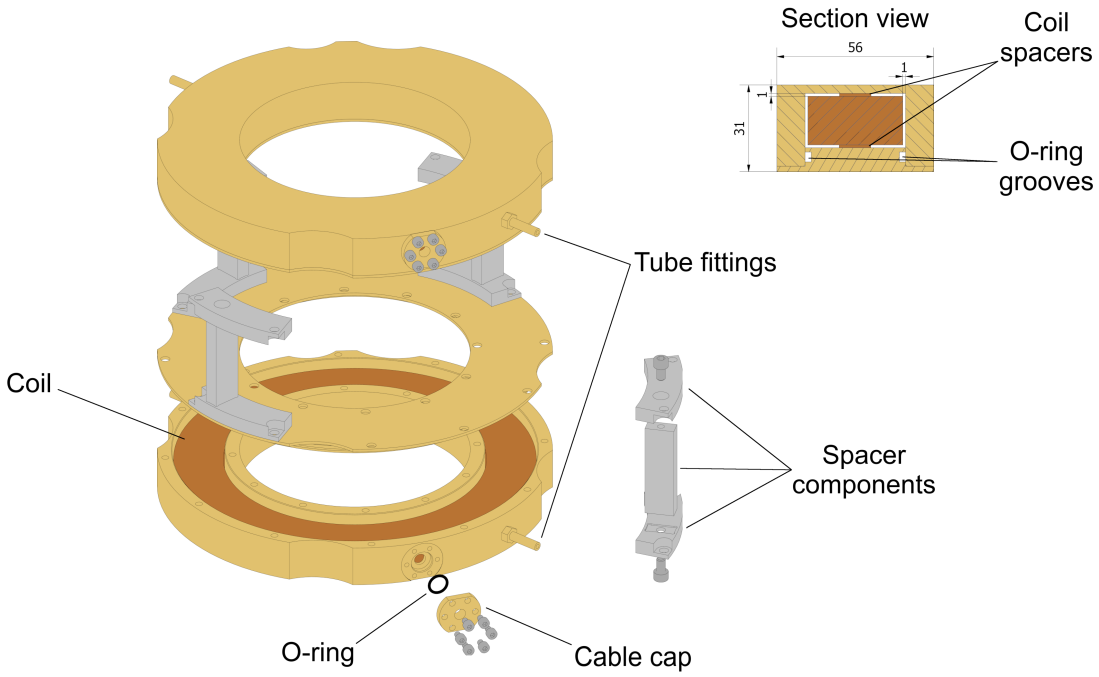


Figure 3.6: 3D CAD view of the MOT coils holder.

cable cap is filled with epoxy glue[8]. Before inserting the coils, several 1 mm-thick circularly-shaped copper pieces are placed with equal spacing at the bottom of the U-shape in order to ensure that the coil is slightly elevated, thus ensuring a flow of water below the coils.

The U-shape is closed by a cap which houses two Viton o-rings with internal diameter 236 mm and 176 mm with a cross-section of 2.62 mm. Before the cap is placed, additional 1 mm-thick copper pieces are placed on top of the coil to ensure that it is unable to move freely. The two coils are kept at a defined distance by four stainless steel separators. In order to avoid Galvanic corrosion between metals with highly different Galvanic indices, all components directly in contact with water are made out of either copper or brass and the cooling water runs on an isolated circuit.

In order to test the validity of the coil holder design, a Finite Element Model (FEM) Conjugate Heat Transfer (CHT) simulation was performed using the SimScale commercial software. The coil was simulated as a single piece of copper[9],

[8]Cotronics EE4538–10 Epox-Eez

[9]This is a considerable approximation since the thin layer of insulator around the coil wires can change the thermal flow within the coil itself. A complete FEM simulation of the coil internal geometry would require a very dense grid and thus a computing power beyond what was available during this study.

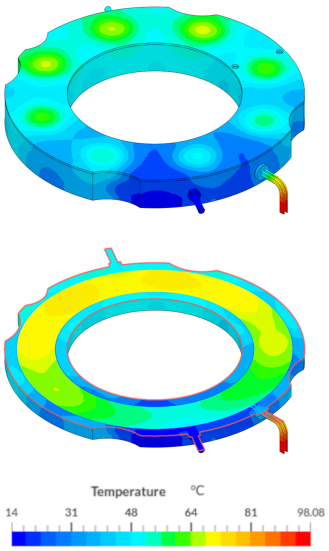


(a)

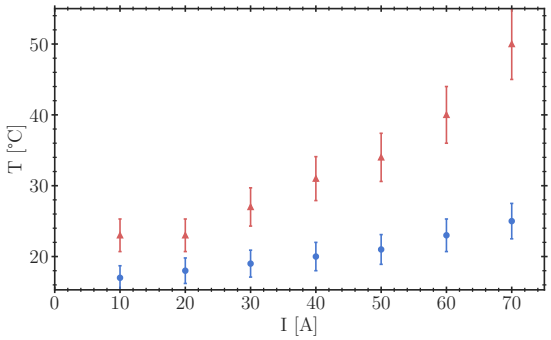


(b)

Figure 3.7: (a) FEM CHT simulation results for the MOT coils holder while coils are traversed by 100 A. Bottom model shows the temperature field measured on a plane cutting the coil in half. (b) Steady state temperatures measured at different current values with probes placed on the external side of the coils holder (dots) and on the coil cable just outside of the holder (triangles).

the water enters the system at a constant temperature of 14 °C and at a constant pressure of 1.5 bar. Figure 3.7a shows the simulation results for the steady state temperature. Both the coil body and the holder surface do not exceed 70 °C, only small regions of the holder (the ones where the thin copper pieces are placed) are heated above room temperature. The hottest components are the coil wires outside the holder which are cooled only by air. Figure 3.7b shows the steady state temperature measured on the holder body and the coil cables at different current values. The results are better than what is expected from the FEM simulation, this is probably due to the fact that the simulation does not take into account air cooling from the surface of the holder.

### 3.1.5 Sapphire window section

Figure 3.8 shows the CAD view of the ZS beam input window section. This section is connected directly to the MOT chamber with a 4-way asymmetric cross, below which a NEG-ion combination pump[10] is installed. This cross also houses

[10]Saes Getters, NEXTorr D100–5

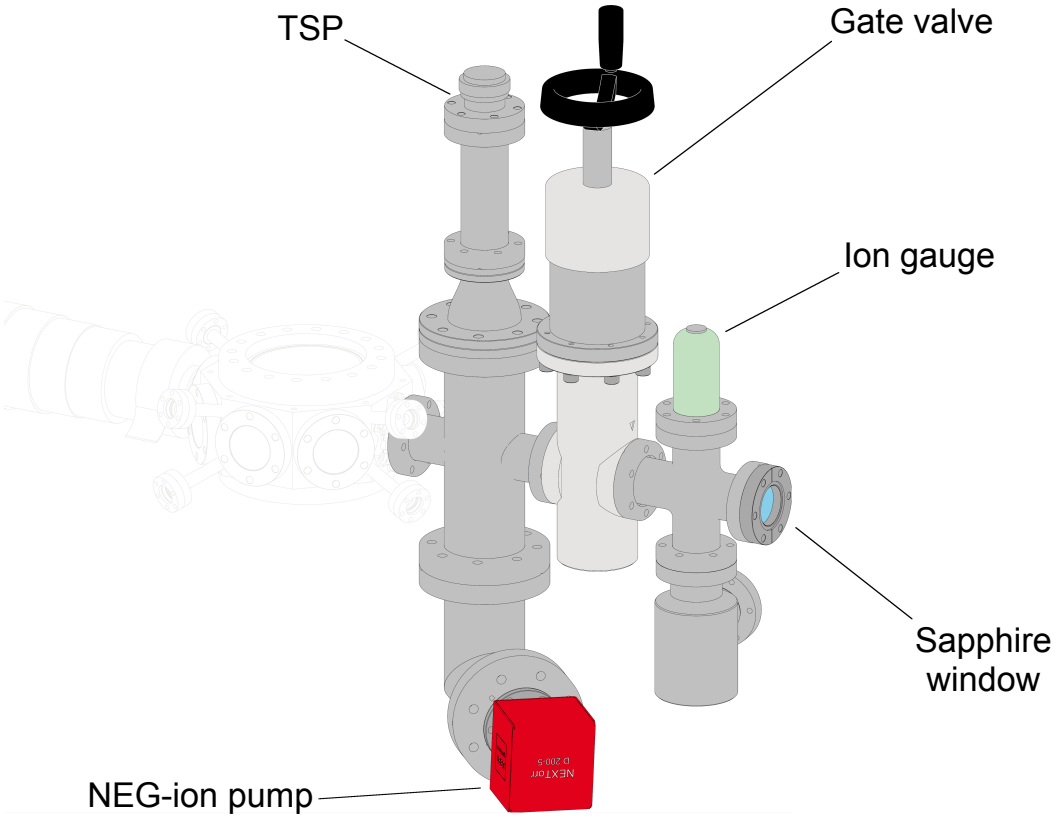


Figure 3.8: 3D CAD view of the lithium sapphire window section. This window is used as input for the ZS beam and it is directly in the path of the hot atomic beam.

an additional TSP[11]. A second 4-way cross is used to mount an ion gauge, an additional vacuum isolation valve and the ZS beam input window. An all-metal gate valve[12] separates the two crosses.

Since the ZS beam has to be anti-parallel to the atomic beam direction, an input window placed straight ahead of the beam path is needed. If the viewport is kept at room temperature, it will soon be coated with lithium, making it reflective to 671 nm light. To avoid this the viewport is made of sapphire rather than quartz, since sapphire can withstand higher temperatures, and it is kept at 210 °C. Viewports in general are quite sensitive to thermal stress, which can cause cracks

[11] Agilent, TSP Cartridge

[12] VAT Group AG

and leaks in the quartz or sapphire. Thus, the viewport is wrapped in aluminium foil (leaving a hole for optical access) to ensure that a minimal thermal gradient is present, the temperature is stabilized with a type K thermocouple. Any change in the temperature value is performed with a slow ramp of $2\,\mathrm{K\,min^{-1}}$.

### 3.1.6 System bake-out & oven loading

#### High-temperature bake-out

UHV is the vacuum regime defined by a pressure between $1 \times 10^{-9}\,\mathrm{mbar}$ and $1 \times 10^{-12}\,\mathrm{mbar}$. Reaching such low pressure using ion or getter pumps is typically limited by outgassing from the vacuum chamber surface. Outgassing is a process by which atoms and molecules (typically $O_2$, $H_2O$ and $H_2$) initially adsorbed on a surface or otherwise trapped in bulk materials are released in the surrounding volume. In order to speed up outgassing, thus freeing the vacuum chamber surfaces of adsorbed materials, a bake-out stage is performed [159]. Since most of the vacuum system components are made of stainless steel, they can easily withstand temperatures up to 400 °C[13], it is convenient to perform a two-step bake procedure where steel components are baked at high temperature for many hours and then, after the more delicate components (such as optics, Viton o-rings and viewports) are assembled, a second baking at a lower temperature around 100 °C is performed.

All stainless steel components of the lithium vacuum system were mounted in a temporary configuration on an optical table separate from the rest of the experimental system, all viewports were substituted with blank flanges in stainless steel. Gate valves, isolation valves, shutters, ion pumps as well as other delicate components such as the ZS coils and tube and the in-vacuum optical resonator were not mounted during this stage as they cannot resist high temperatures. A single turbomolecular pump was directly connected to the system without a vacuum isolation valve. After wrapping the system in heating tapes and covering it with a large quantity of aluminium foil, the temperature was raised with a slow ramp ($0.1\,\mathrm{K\,min^{-1}}$) up to 200 °C[14] and it was kept in these conditions for approximately six weeks with the pump running.

Since most joints are already in their final configuration, a leak test was performed using Ar gas to test each flange connection.

[13] Austenitic steel can cope with even higher values, but while cooling it might develop magnetic response since many steel alloys contain magnetic contaminant that diffuse at high temperatures.

[14] Due to the large size of the system reaching higher temperatures was found to be difficult.

### Lithium oven loading

Alkali metals are well-known to possess a high chemical reactivity in particular with water, even when it is dispersed in air as a vapour. Lithium is the least reactive of the alkali metals (due to having the highest ionization energy), nonetheless it must be handled carefully since it still poses a danger to humans and any exposure to air will quickly cause contamination of the sample. First, lithium is slightly toxic and corrosive, direct skin contact should be avoided as well as breathing any dust or particles [160]. Lithium fires cannot be extinguished with water and will continue burning even in nitrogen atmosphere. Second, if exposed to air, the surface of the metal will quickly turn grey and then black as oxidation takes place. Interestingly, lithium is one of the few elements that reacts with $N_2$ forming an ammonia-like compound (ref. [161], section 4 chapter "The elements").

In order to avoid oxidation, enriched lithium is typically sold in mineral oil. However, any oil impurity would irreversibly contaminate the vacuum system, making it impossible to reach the UHV condition. The process of cleaning lithium from mineral oil can be performed using both chemical and mechanical methods. The material used in this experiment was cleaned by AmesLab[15] and repackaged in an argon-filled glass pipe in the form of small chunks of approximately 20 mm in size.

Due to the small entrance slit of the oven used in the $Ba^+Li$ experiment, the metallic chunks had to be manually cut prior insertion in the oven. The whole operation was performed under argon atmosphere inside a glovebox. The lithium pieces were cut using wire cutters and pincers and unstuck by hand from the blade. The smaller pieces were inserted into the oven using plastic tweezers. Once the oven was filled, the collimator was screwed in place, the oven was then removed from the glovebox and quickly connected to the vacuum system. All metal tools that came into contact with lithium were cleaned by immersing them into water for a few minutes and scraping off any residual lithium trace.

### Low-temperature bake-out

The vacuum system was brought to high vacuum conditions with two turbomolecular pumps and slowly ($0.1\,°C\,min^{-1}$) heated to avoid thermal stress up to 105 °C, this temperature is maintained constant for three weeks. During this process the shutter and gate valves actuators were unmounted to protect them from thermal damage since they contain plastic and Viton components. After a week of bake the ion gauge was turned on with an emission current of 2 mA and let to outgass its hot filaments. TSPs were also cleaned during this period by turning on their filaments to 40 A for a few minutes. Once the system pressured entered the UHV regime ($\approx 1\times10^{-9}$ mbar), the temperature was slowly ramped down to 27 °C.

[15] U.S. department of energy, Iowa State University

Before the ion-NEG pumps can be used, they require an activation process. In this process the pump getter material is heated to 500 °C for at least one hour in order to remove any trace of $H_2$ contaminant adsorbed in the getter material while the pump was exposed to air. The two NEXTORR pumps were activated after the low temperature bake-out was completed in two steps: first, a 1-hour conditioning at 250 °C was performed to clean the pump surfaces from contaminants (such as $H_2O$) that might still be present; second, the actual activation at 500 °C was carried out. The titanium deposition was performed by first cleaning each of the three filaments in the TSP by turning them on for 180 s at 40 A, then by turning on each filament in sequence at 48 A for 60 s.

The large ion pump located under the lithium oven was unable to start at first due to an internal short-circuit. Ion pumps are known to form small spikes on the internal electrodes during manufacturing, these spikes can cause a "virtual short-circuit" when a high voltage field is applied to the electrodes. This "virtual short-circuit" is due to the tip-effect, *i.e.* the fact that electric field line are denser on the tip of conductors, the resulting high field-effect current can trigger the short-circuit protection on the pump controller. This was not the case, though, since the short-circuit was visible even with a simple multimeter that measured an ohmic resistance of 2 Ω. The problem was most likely due to a contaminant flake unfortunately placed in such a way to cause electric contact between electrodes, the issue was cleared after simply applying approximately 100 mA using a linear power supply.

### Transversal velocity distribution

In order to test the validity of the collimator design presented in section 3.1.1 and to characterize the velocity distribution of the atomic beam, a spectroscopy measurement along the transversal axis of the atomic beam was performed. During this measurement the oven was brought to 480 °C to ensure that any oxidation that might be present on lithium is removed.

A 671 nm laser tuned to the D2 transition of lithium was used to illuminate the atomic beam using the two viewports before the ZS tube. With a waist of approximately 1 mm and power 2 mW, the laser intensity is well above the saturation intensity for the D2 transition of lithium ($I_{sat} = \pi hc/3\lambda^3\tau \approx 2.54\,\mathrm{mW/cm^2}$). During the measurement the laser was stabilized on a reference cavity, by changing the cavity length using a piezoelectric it was possible to scan a large range of frequencies. The laser frequency was read on the lab's wavelength meter[16].

A Raspberry Pi (RPi) camera was used for imaging the atoms' fluorescence. Since these cameras are equipped with a pre-installed fixed-focus lens, a $f = 75$ mm

[16]High-Finesse GmbH, model WS8–10.

lens placed at 75 mm from the atomic beam was used to collimate the fluorescence and reduce stray light. The camera integration time was set to 1 s and the average pixel intensity (where atomic fluorescence is observed) is recorded.

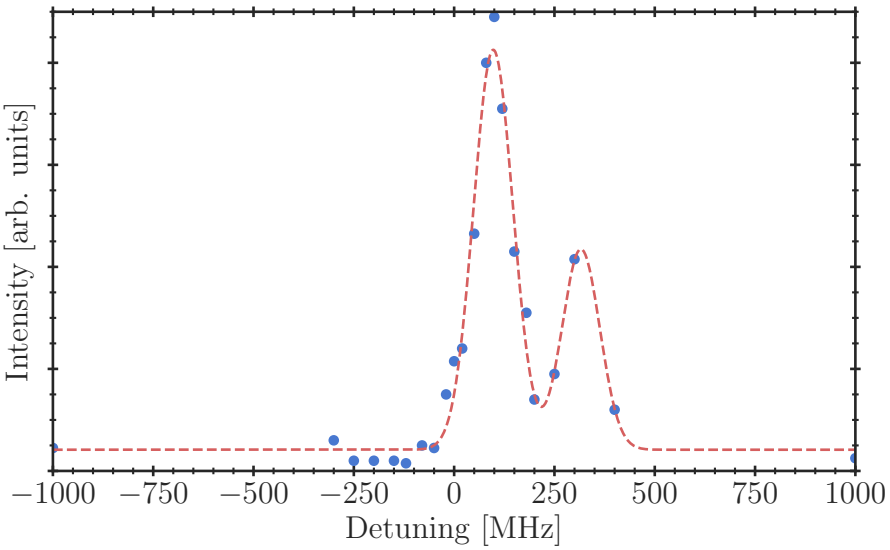


Figure 3.9: Lithium fluorescence intensity as a function of laser detuning measured on the transversal axis of the atomic beam (dots), fitted two-Gaussian model (dashed line). X-axis reports detunings with respect to the frequency 446.800 00 THz measured on the wavelength meter.

The values of the laser frequency were set in random order during the measurement. For each point the pixel intensity was recorded with both the shutter open and closed, the two values were then subtracted from one another. The obtained data are shown in fig. 3.9, the fit model is given by the sum of two Gaussian curves and a constant baseline.

From the fitted model, the peak distance is 218(8) MHz and the peaks height ratio is 1.9(3). Both values are compatible with the expected frequency difference (230 MHz) and transition branching ratio (2.0) of the $^2S_{1/2}, F = 3/2 \rightarrow {}^2P_{3/2}$ and $^2S_{1/2}, F = 1/2 \rightarrow {}^2P_{3/2}$ transitions. Here the $^2P_{3/2}$ hyperfine splitting is disregarded since it is on the order of a few MHz and it cannot be resolved with the precision used for this measurement. Therefore, in calculating the branching ratio the line strengths of all the possible transitions from the levels $^2P_{3/2}, F = 5/2, 3/2, 1/2$ were summed together.

The angular spread of the atomic beam can be obtained from the Full Width Half Maximum (FWHM) of the Gaussian curves. The average FWHM of the two curves is 48(4) MHz, using the Doppler shift relation $\Delta\omega = kv$ the transversal velocity is determined to be $v_T = 32(3)\,\mathrm{m\,s^{-1}}$, corresponding to a temperature of $T = 740\,\mathrm{mK}$. The forward velocity of the beam is calculated from the energy

equipartition principle $v_0 = (3k_BT/m)^{1/2} \approx 1700\,\mathrm{m\,s^{-1}}$, the angular spread results $\theta = \arctan(v_T/v_0) \approx 1.1(1)°$. By modelling the collimator as two slits 0.2 mm in diameter separated by a 10 mm distance, the expected maximum angle of particle traversing the collimator without bouncing is $\mathrm{atan}(0.2/10) \approx 1.15°$. The measured angle and the expected one are compatible within one error bar.

The actual distribution of an atomic beam traversing a two-slit collimator can be found in [162]. In general, the distribution is not Gaussian but has a complex Lorentzian-like shape. Considering the limited resolution of this measurement due to laser linewidth and the power-broadening contributions, the measured line shape can be approximated by a Gaussian curve. The FWHM of the actual angular distribution is 1.134°, which is also compatible with the measured value.

## 3.2 Laser setup

### 3.2.1 Optical breadboards

| Transition | Use | Detuning |
|---|---|---|
| D2 | MOT cooling | $-3.4\Gamma$ |
| | MOT repumper | $-36.4\Gamma$ |
| | ZS cooling | $-21.9\Gamma$ |
| | ZS repumper | $-17.9\Gamma$ |
| | Imaging at 0 G | 0 |
| | Imaging at 1000 G | $160\Gamma$ |
| D1 | grey molasses cooling | $5.4\Gamma$ [126] |
| | grey molasses repumper | $44\Gamma$ [126] |

Table 3.1: List of the target detunings with respect to the D1 or D2 transitions of the light beams that are needed to cool and trap fermionic lithium atoms.

Table 3.1 shows the target detunings of the laser beams to perform cooling on $^6$Li, based on data in the literature and from other $^6$Li setups at LENS [163, 118, 164]. The ZS and MOT laser lights work on the D2 transition. In both cases the transition addressed in the laser cooling is the $^2\mathrm{S}_{1/2}\ F = 3/2 \rightarrow {}^2\mathrm{P}_{3/2}\ F = 5/2$ transition. However, the system is not closed, and a repumper laser light resonant with the$^2\mathrm{S}_{1/2}\ F = 1/2 \rightarrow {}^2\mathrm{P}_{3/2}\ F = 3/2$ transition is needed to depopulate the $^2\mathrm{S}_{1/2}\ F = 1/2$ state in which atoms can spontaneously decay. Grey molasses cooling is performed on the D1 line and it too requires both a *cooler* light ($^2\mathrm{S}_{1/2}\ F = 3/2 \rightarrow {}^2\mathrm{P}_{1/2}\ F = 3/2$) and a *repumper* light ($^2\mathrm{S}_{1/2}\ F = 1/2 \rightarrow {}^2\mathrm{P}_{1/2}\ F = 3/2$).

For a given transition (either D1 or D2) the required laser detunings are close enough that a single laser diode and a combination of Acusto-Optic Modulators

(AOMs) can be used to obtain several beams at the proper frequencies. Conversely, due to the relatively high frequency shift between D1 and D2 transitions (10.056 GHz), two distinct lasers are required, the first addressing the D1 transition and the second addressing the D2 one.

The D1 and D2 frequencies are generated by two Extended-Cavity Diode Lasers (ECDLs), as they can be run in a single longitudinal mode operation and have a relatively low cost. However, their output power is not sufficient for trapping a large number of atoms [165]. Therefore, an amplification stage is needed for both the D1 and the D2 lines. Since in the experimental sequence (which was explained in section 2.3.1) D1 and D2 lasers are never used at the same time, it is convenient to design an optical circuit that uses the same amplifiers and actuators for both D1 and D2 lasers. Using a single amplification stage rather than two distinct ones reduces the complexity and the cost of the overall setup.

To this end the lithium laser setup was designed and constructed over three optical boards, each with a different task:

- Board 1: here the two ECDLs are installed and their optical paths are merged.
- Board 2: on this board laser light is amplified and frequency shifted to obtain beams for MOT and ZS.
- Board 3: here additional frequency shifts are performed to obtain the laser light for the imaging of the atomic cloud.

Each board is discussed in details in the following sections.

### Board 1

Figure 3.10 shows the schematic for the optical board 1 of the lithium setup. Two commercial Toptica DL pro 670 nm ECDLs with integrated opto-isolators provide linearly-polarized light for the D1 and D2 transitions. Both lasers are followed by an anamorphic prism pair[17] in order to circularize the beam shape, which is initially elliptical.

In order to be able to use a single amplification stage, the D1 and D2 laser beams have to follow the same optical path. But since only one of the frequencies is needed at a given time, the system must be designed to quickly switch between D1 and D2 laser beams, ideally in less than a ms in order not to damage the optical amplifiers. To achieve this, the two beam paths are merged using a Polarizing Beamsplitter (PBS), thus keeping the beams' polarization orthogonal. A combination of Pockels cell[18] and Glan-Taylor polarizer is used to selectively rotate the

[17] Thorlabs, PS873-A

[18] Leysop Ltd., Basildon, United Kingdom

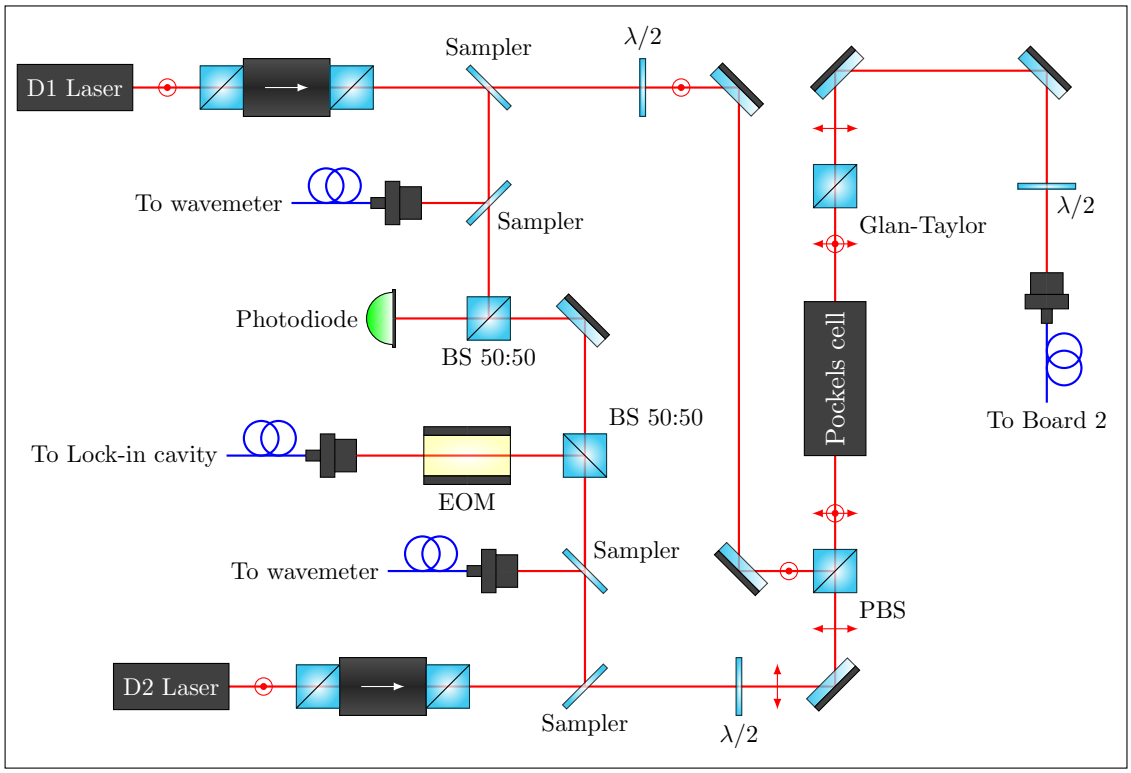


Figure 3.10: Optical circuit of the lithium board 1. Arrows and circles placed on the beam path indicate horizontal and vertical light polarization, respectively.

polarization of the beams, one of which will be completely transmitted and the other completely reflected. The transmitted beam is injected into a fibre connected to the amplification stage, while the reflected beam is sent to a beam dump.

A Pockels cell is capable of rotating the light polarization when an external electric field is applied and operates by exploiting the redistribution of charges observed in non-linear crystals when an electric field is present (Pockels effect). The cell used in this setup rotates the laser polarization by 90° when an external field is applied. The Pockels cell ideal work voltage corresponds to the so-called half-wave voltage, *i.e.* the voltage required to introduce a phase change of $\pi$ is the optical wave, this value also corresponds to the maximum of optical transmission of the cell. The ideal value was found to be 3.6 kV.

Glan-Taylor polarizers act similarly to PBSs, but present a major advantage: thanks to a different construction method (air-spaced birefringent material rather than two cemented glass pieces with a dielectric coating) Glan-Taylor polarizers are better capable of separating the s-polarized and p-polarized waves. Thus, the Glan-Taylor and Pockels cell combination is capable of extinguishing the transmission of

a beam with an extinction ratio[19] of approximately $1 \times 10^{-3}$.

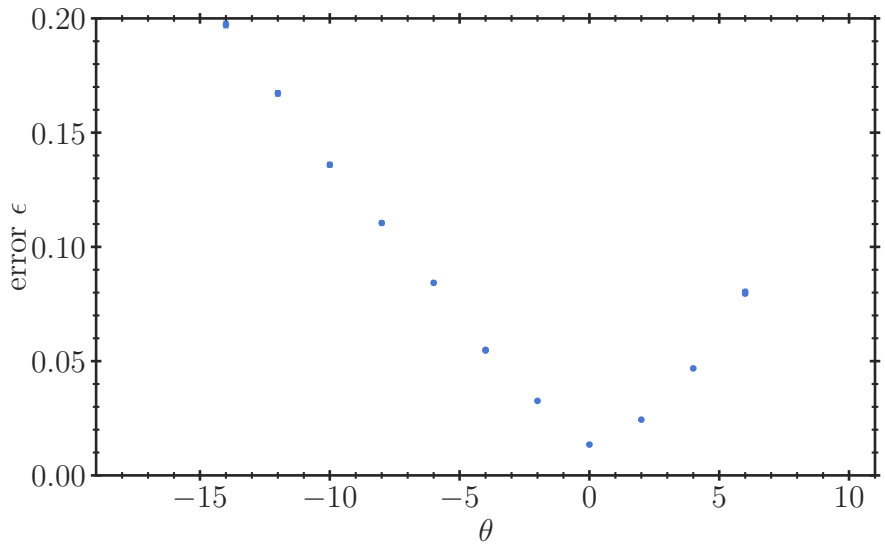


Figure 3.11: Misalignment error as a function of waveplate angle. The central minimum indicates that when the laser polarization is aligned with one of the fibre principal axes.

The Tapered Amplifiers (TAs) used in board 2 are sensitive to the input laser polarization, in particular they amplify only light that has a polarization parallel to the TA's junction axis. Therefore, a polarization-maintaining fibre is used to connect board 1 and board 2. These types of fibre have a non-cylindrical symmetry and two principal axes of the fibre can be identified. If the light polarization is aligned to one of these axes, its polarization state is preserved along the fibre length. To align the light polarization to the fibre axis a half-waveplate is placed right before the fibre launcher, a PBS is placed at the fibre output coupler and the reflected power is measured. The fibre is then stressed (through bending or thermal stress) and the power reflected by the PBS is recorded as a function of the waveplate angle. The misalignment error can be defined as $\epsilon = (P_{\max} - P_{\min})/(P_{\max} + P_{\min})$, where $P_{\max}$ and $P_{\min}$ are, respectively, the maximum and minimum power measured during the fibre stress. Figure 3.11 shows the results of the alignment procedure. The minimum visible in the centre of the plot indicates that at this angle the waveplate rotates the laser polarization so that it is aligned to one of the fibre principal axis, and even under stress the polarization state is maintained. The residual error (1.34 %) corresponds to a fluctuation of approximately 0.5 mW. Such small fluctuation (which occurs only if the fibre is under thermal stress) can be

[19]The extintion ratio is defined as the ratio of the power transmitted through the optical system over the input power.

easily corrected by either controlling the ECDL output power, or the currents of the TAs placed after the fibre coupling.

Since thermal, electrical and mechanical changes in the laser cause fluctuations in the laser frequency, the laser must be locked to a stable reference when performing atomic physics experiments. To this end, the laser light is sampled right after the anamorphic prisms. Part of this sample is injected into a fibre connected to a wavelength meter[20], the remaining light is used for the frequency lock scheme. For the D2 laser, part of the sampled light traverses an Electro-Optical Modulator (EOM) and is sent, via a fibre, to an optical cavity. The D1 laser is stabilized by offset locking on the D2 laser (further details on the locking scheme will be discussed in section 3.2.2).

After the anamorphic prism pair the laser power is approximately 25 mW for both lasers, almost all the power ($\approx 22.5$ mW) reaches the fibre connected to board 2. The light is coupled into the fibre with an efficiency of 60 %, and the power output 14 mW is sufficient to inject the first TA on board 2.

### Board 2

Figure 3.12 shows the schematic for board 2. On this board, laser light is amplified and the proper frequency shifts are applied in order to obtain the laser beams needed for ZS and MOT. Since only 14 mW of light power reach board 2 from board 1, an amplification stage is necessary before the laser light can be split into cooler and repumper branches. This pre-amp stage uses a custom assembled TA, which brings the laser power from the initial value to approximately 400 mW.

To generate the cooler and repumper beams, after the pre-amplifier the laser is split into two arms, each traversing a different AOM in a double-pass configuration. Due to the relatively low efficiency ($\approx 45$ %) of the double pass configuration worsened by the non-Gaussian shape of the TA's output mode, a second stage of amplification is necessary. Cooling and repumper light are independently amplified by two additional TAs which, while working with an input power of 25 mW, can provide an output power of nearly 500 mW in each arm. The cooling and repumper arms, after the second amplification stage, are joined together with the same polarization state by using a Beamsplitter (BS). The obtained beam is split with a 50:50 BS to form the ZS branch and the MOT branch. Each beam passes in a single-pass AOM in order to perform final adjustments of the laser frequency and it is then injected into optical fibres connected to the experimental chamber.

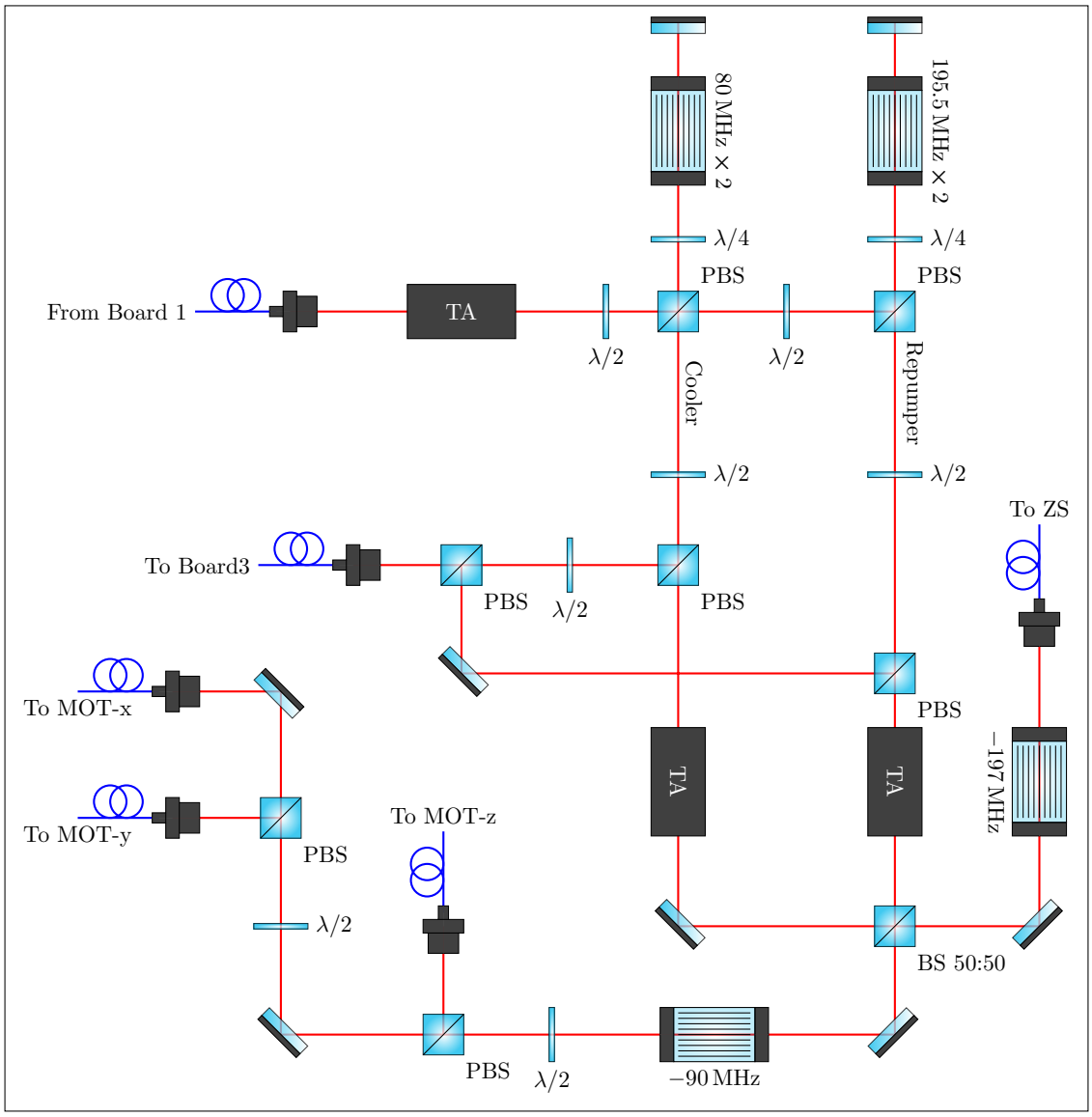


Figure 3.12: Optical circuit of the lithium board 2.

### Tapered amplifiers optomechanics

TAs are optical amplifier having a tapered section. Different implementations of TAs exists, for this experiment a semiconductor TA chip[21] was used. The input side of the TA is a narrow waveguide that, usually, supports only one mode

[20] High-Finesse GmbH, model WS8–10.

[21] Eagleyard EYP-TPA-0670.

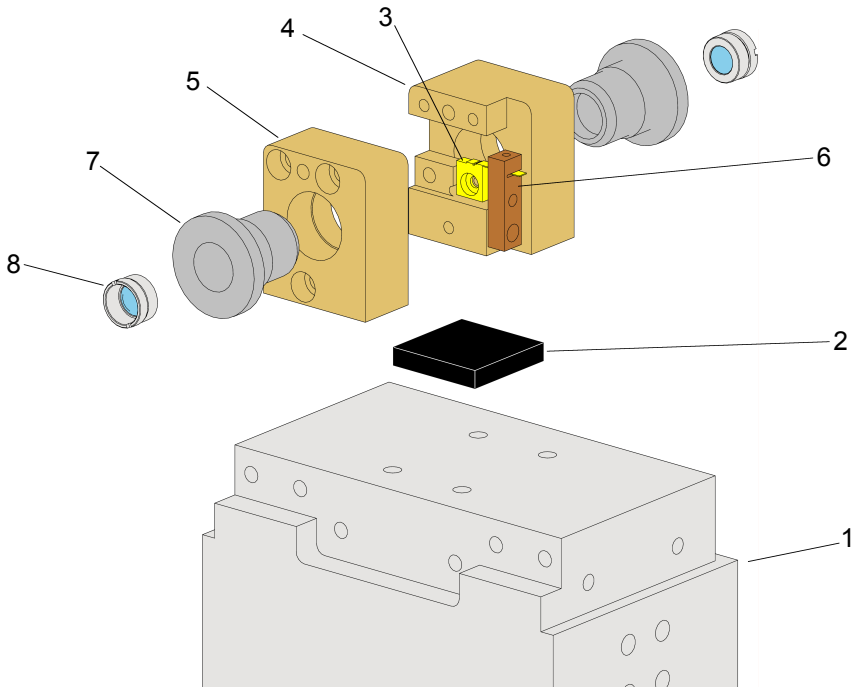


Figure 3.13: Exploded view of the 3D CAD for the custom made TA opto-mechanics. (1) Water cooled heat exchanger, (2) Peltier cell, (3) TA chip, input (4) and output (5) brass supports, (6) cathode clamper, (7) Lens holders, (8) aspheric lenses Thorlabs C330TMD.

of propagation, while the tapered region has a non-constant cross-section that expands horizontally (usually the height is kept constant). An externally supplied current keeps the entire waveguide valence band populated, this allows for stimulated emission of laser light when a light beam is coupled to the input of the waveguide. When the coupled light reaches the tapered region it continuously expands, irradiating the whole TA cross-section uniformly. This ensures a relatively high-quality beam output of elliptical shape (due to the chip different horizontal and vertical dimensions) which can be then circularized.

The TA chip needs proper thermal dissipation and input and output collimation lenses. Figure 3.13 shows the exploded view of the custom-made mechanical mount used in the $Ba^{+}Li$ experiment. The TA chip (3) is screwed on a brass support (4), since the metallic body of the chip coincides with its anode, this ensures a good electrical contact to ground as well as a good thermal contact. A copper clamper (6) is used to connect the chip cathode to the current generator, this element is attached to the side of the input brass support via a Teflon screw and an o-ring to avoid electrical contact with the grounded elements. A second brass piece (5) is screwed onto the first. Each brass element hold an aspheric lens (8) installed in a custom lens holder (7), this lens is used either for input light focusing or for the

output light collimation. The lens holders (7) have a male thread with micrometre pitch that matches a corresponding female thread on the brass elements (4, 5), this allows for the precise positioning of the input and output lenses. The brass assembly is cooled by a Peltier cell[22] (2) and is mounted on a heat exchanger (1) via 4 Teflon screws, to avoid thermal contact between cooled and heated parts, the heat exchanger is water cooled to maintain its temperature low and avoid thermal drift of the Peltier cell[23]. The temperature is measured using a Pt100 sensor positioned on one of the two brass pieces. The TA chips were found to be easily damaged by frequent turn on and turn off operation, therefore they are kept powered overnight at a lower current ($\sim 400\,\mathrm{mA}$), other groups working with lithium had similar issues with commercially bought Toptica BoostTA at 670 nm [163].

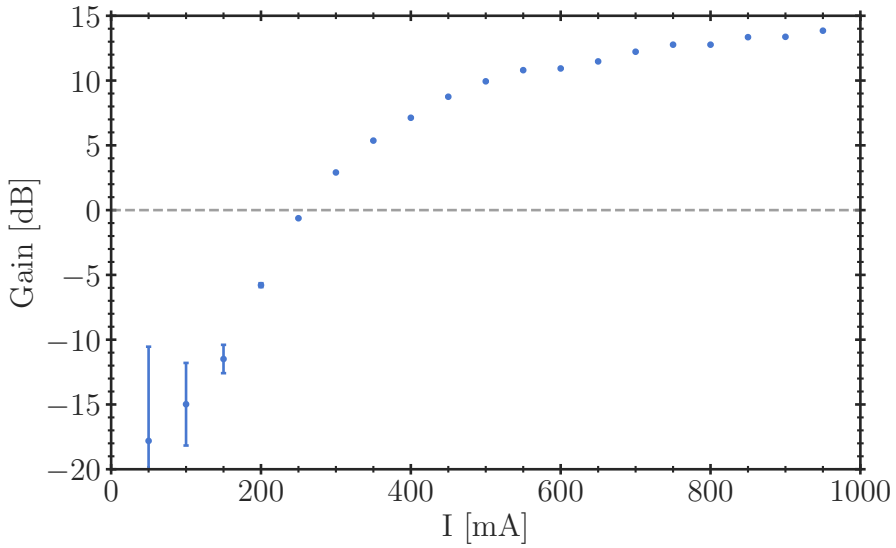


Figure 3.14: Power amplification (in dB) as a function of TA current. The coupled input laser power is 14 mW.

Figure 3.14 shows the power amplification $P_{\mathrm{out}}/P_{\mathrm{in}}(\mathrm{dB})$ as a function of the current applied to the TA, for an input power of 14 mW. The input light is effectively amplified only when at least 200 mA are supplied to the device. For the used TA chip, the maximum sustainable current is 1 A and the maximum achievable gain

[22] Adaptive ET–071–10–13–RS

[23] Peltier cells are known to enter a positive-feedback loop when operating at too high current: assuming that the cell is used to stabilize the temperature of a device with a temperature controller, the heat generated by the Peltier cell itself (due to the current traversing it) heats the cold side of the device. The controller increases the current going to the cell, in the attempt to stabilize the increasing temperature and this causes additional heat to reach the cold side. At this point the temperature becomes uncontrollable.

is 15 dB. The light output of the TA is an astigmatic, highly elliptical beam. In order to collimate the output beam, an aspheric lens[24] is placed on the threaded lens holder and is used to collimate only the fast axis divergent axis (the major axis of the ellipse), while a cylindrical lens ($f = 40\,\text{mm}$) placed outside of the TA mount is used to collimate the slow axis to obtain a circular beam. The use of a cylindrical lens also allows for partially correcting the astigmatism present in the output beam.

A major limitation of this setup is the alignment between the input and output lenses and the emission point of the TA chip. Although the mechanical components where build by a precision workshop, the semiconductor emission point position (with respect to the metallic body) is well-defined only with a 0.1 mm precision, thus misalignments are common. A misaligned collimation lens results in a comet-shaped output beam, rather than an ellipse, due to diffraction effects within the lens itself. This comet-like shape is not coupled efficiently to optical fibres or circularized without considerable loss of power.

### Board 3

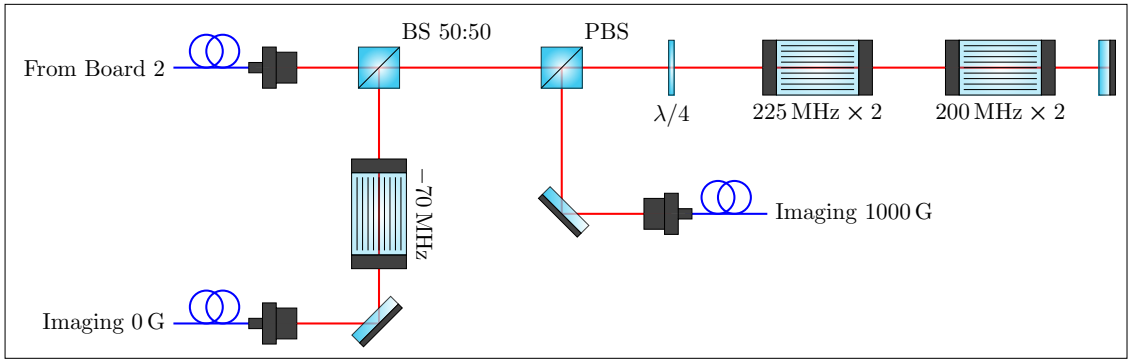


Figure 3.15: Optical circuit of the lithium board 3.

Figure 3.15 shows the schematics for the third optical board of the lithium setup. A beam of light formed by cooling and repumper light sampled after the first amplification stage of board 2 is split using a BS. Both arms are used for imaging of the lithium cloud: the first is frequency shifted so that the cooling light is resonant with the D2 transition of lithium at 0 G, while the second arm is frequency shifted so that it can be used at fields of approximately 1000 G. Multiple output fibres are present for each arm allowing for imaging from different axes in case it is needed, the power coupled to each fibre is approximately 3 mW, sufficient to saturate the lithium transitions during imaging.

[24] Thorlabs, C330TMD

### 3.2.2 Laser locking scheme

In order to keep the laser frequency stable over time, the lasers have to be locked to a reference. For what concerns the lithium laser setup, the D2 laser is frequency stabilized on an optical cavity using the Pound-Drever-Hall (PDH) technique. This cavity — referred to as the "frequency transfer cavity" — is formed by a curved mirror, with Radius of Curvature (RoC) −300 mm, and a flat mirror forming a hemispherical resonator with a linewidth of approximately 0.5 MHz and a finesse of 2000. A detailed description of the cavity mechanical setup is given in [156]. One of the cavity mirrors is glued to a piezoelectric element, this allows to stabilize the cavity itself on the 903.4 nm laser which acts as a reference laser for the whole laboratory. The D1 laser, instead, is frequency locked by offset locking on the D2 laser. In order to achieve the laser frequencies required for the experiment, both D1 and D2 laser are stabilized to have a frequency detuning of −38.3 MHz and −90 MHz from the D1 and D2 transitions, respectively.

#### D2-D1 offset lock

The fine structure splitting between $^2\mathrm{P}_{1/2}$ and $^2\mathrm{P}_{3/2}$ is $\Delta_0 = 10.056\,\mathrm{GHz}$, since the D2 transition is defined as the transition $^2\mathrm{S}_{1/2}\ F = 3/2 \rightarrow {}^2\mathrm{P}_{3/2}\ F = 5/2$, an additional shift of $\Delta_{D2} = -73.30\,\mathrm{MHz}$ has to be considered. Similarly, the D1 transition is $^2\mathrm{S}_{1/2}\ F = 3/2 \rightarrow {}^2\mathrm{P}_{1/2}\ F = 3/2$, again introducing an additional shift of $\Delta_{D1} = -67.35\,\mathrm{MHz}$. Since the D1 and D2 laser have to be locked so that they are frequency shifted by −38.3 MHz and −90 MHz, respectively, the actual frequency difference between the two lasers is

$$\Delta = 10.056\,\mathrm{GHz} + \Delta_{D2} - 90\,\mathrm{MHz} - \Delta_{D1} + 38.3\,\mathrm{MHz} = 9998.38\,\mathrm{MHz}\,.$$

This frequency difference is within the bandwidth of fast photodiode detectors, making it is possible to measure the lasers beat signal.

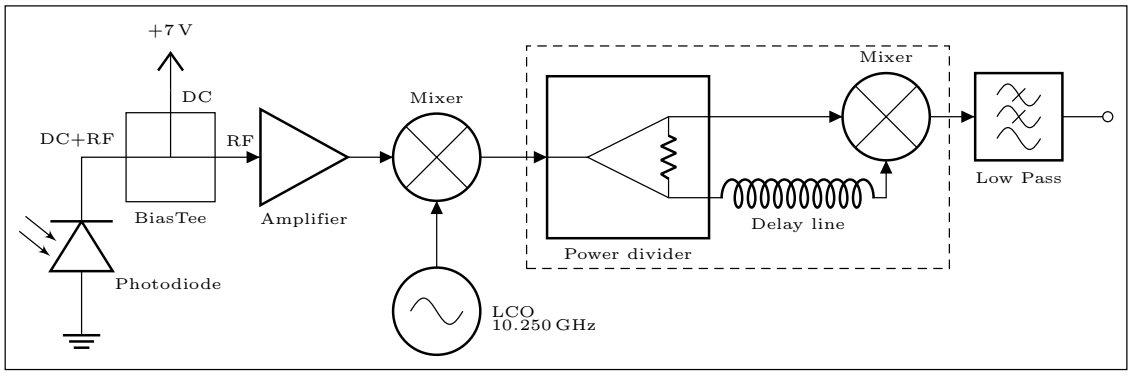


Figure 3.16: Circuit schematic used for D1-D2 lasers offset lock.

As shown in fig. 3.10 the D1 and D2 lasers are merged together using a BS and the resulting signal measured using a fast photodiode[25]. Figure 3.16 shows the electrical circuit schematic used to make a frequency-locked loop for stabilizing the D1-D2 beat signal. A bias-tee[26] is used to polarize, with a constant voltage of 7 V, the photodiode. The RF output of the bias-tee is connected to a low-noise RF amplifier[27]. Since working with signals in the GHz frequency range is complex, the beat signal frequency is reduced to a few hundred MHz by mixing[28] it with another RF signal of similar frequency generated by a 10.250 GHz mechanically-tunable dielectric oscillator[29]. When two RF sinusoidal signals are mixed, *i.e.* their waveforms are multiplied together, the resulting signal can be described as the sum of two terms: one sinusoid oscillating at a frequency given by the sum of the frequencies of the two input signals and one sinusoid oscillating at a frequency given by the difference of the input ones. The sum signal is quickly dissipated in the cables and other electrical components — since it oscillates at approximately 20 GHz — while the difference signal oscillating at roughly 250 MHz remains. An additional frequency step down is performed by mixing[30] the beat signal with an additional reference at 200 MHz, locally generated in the lab, and a 100 MHz low-pass filter[31] is added to remove any remaining high-frequency component. The obtained signal is split[32] and one part is sent directly to a mixer, while the second part goes through a delay line (made by a simple coaxial cable). The phase delay introduced by the cable is $\phi = \omega\tau l$, where $\omega$ is the frequency of the signal, $\tau$ is the characteristic time delay of the cable (for standard RG58 coaxial cables $\tau = 5.13\,\mathrm{ns\,m^{-1}}$) and $l$ is the cable length.

The signal after the mixer is then proportional to $\cos\phi$, and presents oscillations as $\omega$ varies. Since the cosine can be approximated linearly in the region near $\cos\phi \approx 0$, this setup allows to have a linear voltage proportional to small variations of $\omega$, *i.e.* the error signal needed for stabilization [166, 167]. This error signal can then be fed to a Proportional-Integral-Derivative (PID) controller connected to the laser frequency actuators. The *lock point*, *i.e.* the frequency at which the system will try to stabilize, is determined by all $\phi$ that satisfy $\cos\phi = 0$. These lock points

[25] Hamamatsu G4176–03

[26] Mini-Circuits ZX85–12G-S+

[27] Mini-Circuits ZX60–153LN-S+

[28] Mixer: Mini-Circuits ZX05–153LH-S+

[29] SAGE Millimeter, Inc. SOD-10304117-SF-S1

[30] Mixer: Mini-Circuits ZFM-3-S+

[31] Mini-Circuits BLP-100+

[32] Splitter: Mini-Circuits ZFSC-2–4-S+

are determined by the cable length

$$\omega\tau l = \frac{\pi}{2} + n\pi \longrightarrow l = \frac{\pi}{2}\frac{1}{\omega_{\text{lock}}\tau} + n\frac{\pi}{\omega_{\text{lock}}\tau}\,, \qquad n \in \mathbb{Z}$$

where $\omega_{\text{lock}}$ is the frequency that one wishes to lock to. Since coaxial cables are rarely found at an arbitrary length, and building one at the exact length value is challenging, it is convenient to fix the cable length at a commercially-available value and act on the local oscillators used during the frequency step down of the beat signal to ensure that the lock point is located at the proper frequency useful for the experiment. Before the PID, it is recommendable to place a low-pass filter[33], to remove fast variations of the error signal effectively limiting the bandwidth of the PID. An excessively high bandwidth can cause self-oscillation as well as gather high-frequency noise that can compromise the stability of the lock loop.

### 3.2.3 Electro-optic modulator

#### Laser Phase modulation

A frequency modulation must be induced in the D2 laser light before it is possible to stabilize its frequency using the PDH method. To do so EOMs are commonly used. These devices work by exploiting the electro-optic effect observed in non-linear crystals. The application of an electric field to a crystal causes a redistribution of charges within the crystal itself, in turn this causes a change in the electric permittivity of the material. If a laser beam is traversing the crystal, these changes in electric permittivity will affect the phase of the laser electric field. One of the most commonly used crystals for EOMs is $LiNbO_3$ which has become heavily used in the telecommunication market.

If the laser light is linearly polarized and its electric field is parallel to the electric field applied to the EOM crystal, then the light beam acquires a phase (ref. [168], chapter 9)

$$\phi = \frac{2\pi}{\lambda} n_e + \pi\frac{V_m}{V_\pi}\,,$$

where $\lambda$ is the light wavelength, $n_e$ is the extraordinary refractive index of the crystal, $V_m$ is the voltage applied to the crystal faces, and

$$V_\pi = \frac{\lambda}{n_e^3 r_{33}}\frac{d}{l} \tag{3.1}$$

is the so-called *half-wave voltage*, *i.e.* the voltage corresponding to a $\pi$ phase acquired by the electric field. In eq. (3.1), $r_{33}$ is the electro-optic coefficient of

[33] Mini-Circuits BLP-1.9+

the crystal (along the extraordinary axis), $l$ is the length of the crystal (linear dimension along the light propagation axis), and $d$ is the width of the crystal (linear dimension along the axis of the applied electric field). In case of $LiNbO_3$ crystals the parameters $r_{33}$ and $n_3$ take the values (ref. [168], chapter 9)

$$\begin{cases} n_e = 2.200 \\ r_{33} = 30.8 \times 10^{-12}\,\mathrm{m\,V^{-1}} \qquad \text{at } 633\,\mathrm{nm} \end{cases} \tag{3.2}$$

If a sinusoidal modulation $V = V_m \sin(\omega_m t)$ is applied to the crystal, the electric field of the laser beam after it has traversed the EOM can be approximated as [169]

$$\frac{\mathcal{E}}{\mathcal{E}_0} = \cos(\omega t) + \frac{\pi}{2}\frac{V_m}{V_\pi}[\cos((\omega - \omega_m)t) - \cos((\omega + \omega_m)t)]\,,$$

where $\omega$ is the laser fundamental frequency. Therefore, the electric field can be described as a carrier having frequency $\omega$ and two sidebands at frequencies $\omega \pm \omega_m$ having opposite phases. It is the interference between the carrier and the sidebands that allows the generation of an error signal used in PDH stabilization technique. In order to achieve the maximum slope in the PDH error signal, the ratio between the light power in the carrier and the power in the sidebands should be equal to 0.42 [170], leading to a modulation depth $\pi V_m/V_\pi = 1.08$ or an ideal applied voltage of

$$V_m = 1.08\frac{V_\pi}{\pi}\,. \tag{3.3}$$

### EOM design and assembly

A custom design for an EOM was already present at the $Ba^+Li$ experiment [171], but due to engineering and stability issues, a new design was deemed necessary. The new design makes used of a c-cut $LiNbO_3$ crystal with a cross-section area of $d \times d = 2\,\mathrm{mm} \times 2\,\mathrm{mm}$ and a length of $l = 20\,\mathrm{mm}$. With these geometrical values the half-wave voltage results $V_\pi = 204.6\,\mathrm{V}$, and the ideal modulation voltage is $V_m \approx 65\,\mathrm{V}$. This modulation voltage is applied to the crystal by squeezing it between two copper electrodes, thus creating a parallel-plate capacitor. The frequency of modulation should be chosen to be either much larger (smaller) than the stabilization cavity linewidth, this way real (imaginary) part of the error signal is negligible and thus a single lock-in amplifier is needed for the PDH technique [170]. In the $Ba^+Li$ experiment, the transfer cavity used to stabilize the lasers has a linewidth of almost 1 MHz. Thus, the modulation frequency was chosen to be 40 MHz, this value is well above the cavity linewidth and below the bandwidth of silicon commercial photodiodes ($\approx 100\,\mathrm{MHz}$).

Since the low-noise direct digital synthesizer used at the $Ba^+Li$ experiment for generating sinusoidal signal at RF is capable of producing only 2 V peak-to-peak, in order to reach the ideal modulation voltage of 65 V either a low-noise RF amplifier

or a resonant LC configuration is required. The latter option is more attractive since it is a completely passive setup that can also act as a filter further reducing the RF noise. A resonant LC circuit is achieved by placing an inductor in parallel to the crystal capacitor, the voltage drop across the capacitor is then determined by $V_c = V_0 Q$, where $V_0$ is the input voltage and $Q$ is the so called quality factor of the circuit defined as

$$Q = \frac{1}{R}\sqrt{\frac{L}{C}}\,,$$

where $R$ is the series resistance of the circuit, $L$ the inductor inductance and $C$ the crystal capacitance. In order to reach the ideal modulation voltage a minimum $Q$ of 32 is needed. An additional requirement for the design is to be compact (to easily fit on the laser line) and to have clear optical access for the laser to traverse the crystal.

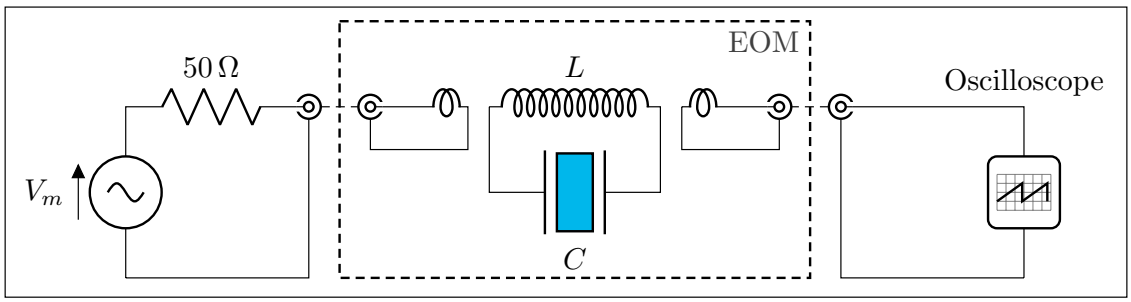


Figure 3.17: Schematic of the EOM electric circuit. The device uses an LC tank to resonantly drive the $LiNbO_3$ crystal with an high peak-to-peak voltage. The RF power is supplied using inductive coupling.

Figure 3.17 shows the electric schematic for the LC circuit and its coupling to the RF generator. Inductive coupling is used to couple RF waves to the LC tank as directly connecting the wave generator would degrade the circuit $Q$ value due to the series resistance (ref. [172], chapter 4); effectively, this scheme uses the inductor of the LC tank as the secondary coil of a step-up resonant transformer. An additional *sensing* coil is installed, and it is used to measure the coupled signal and estimate the resonance frequency. The dielectric constant of lithium niobate is $\epsilon_r = 28.9$ [173] (this value was measured at the audio frequency range, that is a few kHz), this leads to a capacitance of

$$C = \frac{\epsilon_0 \epsilon_r l d}{d} \approx 5.3\,\mathrm{pF}\,.$$

In order to resonate at 40 MHz, the parallel inductance must be $L = 3\,\mu\mathrm{H}$. Coils with this large inductance value are rarely found on the market, therefore the coil was hand-made. In order to design the coil windings, the approximated expression of a cylindrical single-wind inductor can be used to determine its inductance from a

set of geometrical parameters. The expression used is the Wheeler's approximation formula [174]

$$L = \frac{r^2 N^2}{9r + 10D}\,, \tag{3.4}$$

where $r$ is the coil winding radius, $D$ the coil length and $N$ is the number of loops. In Wheeler's formula all linear dimensions must be given in inches. Since multiple geometric parameters intervene in the expression of $L$, the formula is not easily invertible, but a few educated guesses can be made on some dimensions appearing in eq. (3.4): for simplicity the length of the coil $D$ can be taken to be equal to the wire diameter times the number of loops, *i.e.* there is no spacing between consecutive windings; the wire diameter can be chosen to be 1 mm, this is a good values since copper wires with large cross-section present less electric resistance and the coil is sufficiently stiff to maintain the given shape under its own weight. The overall coil length is also limited by the available space, which poses a limit to the number of turns $N$. The final coil configuration was chosen to be

$$\begin{cases} N = 21 \\ r = 7.5\,\text{mm} \\ D \approx 22.4\,\text{mm} \end{cases}$$

The resulting inductance is $L \approx 3.15\,\mu\text{H}$. The coupling coils are made by a single winding using the same 1 mm wire, and placed at a close distance from the coil of the LC tank.

Figure 3.18 shows the 3D CAD of the EOM assembly with the listed components. The crystal (1) and electrodes (2) are pressed together by 3D printed plastic supports (3, 4) held by M2 screws, the electrodes are then soldered to the central Printed Circuit Board (PCB) (8) and act as both electric and mechanical connection for the crystal to the rest of the circuit. The LC tank coil (5) and coupling coils (6) are hand-wound around a 3D plastic support (7) and soldered directly to the central PCB, no direct electrical connection is present between the main LC tank coil and the coupling coils, these coils are kept at a distance of approximately 2 cm from the central coil windings, this way the coupling coefficient between coils is reduced and the circuit $Q$ value improves[34]. The whole circuit is enclosed in a box (11) made of nickel plated aluminium to minimize noise from external sources, the crystal facets are aligned to two small holes on the box sides which allow for optical access.

The completed EOM was characterized with a 2-port Vector Network Analyser (VNA), one port connected to the coupling coil and the second one connected to

[34] If the coupling coefficient between coils was too large, the effects of the finite series resistance of the direct digital synthesizer would degrade the $Q$ value of the resonator.

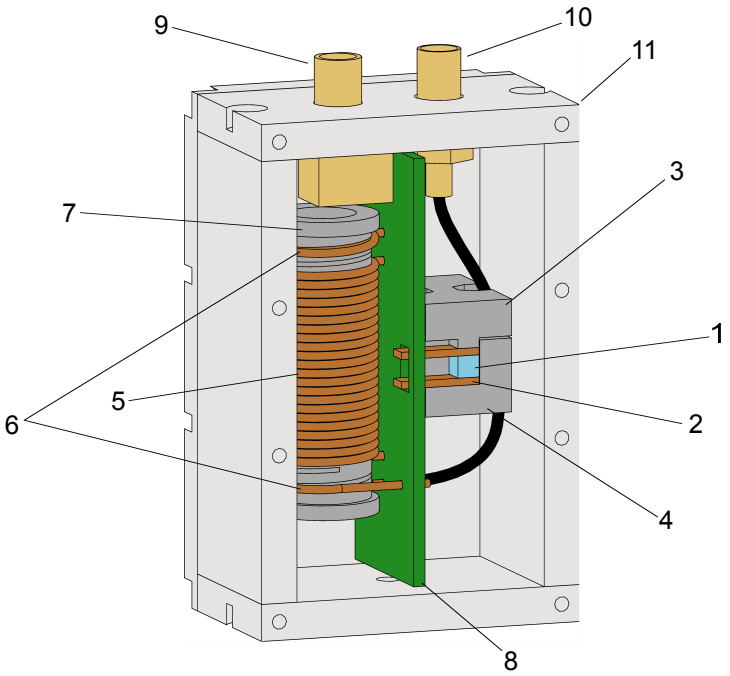


Figure 3.18: CAD representation of the EOM assembly: (1) $LiNbO_3$ crystal. (2) Electrodes. (3) Upper and (4) lower crystal mechanical supports. (5) LC tank main coil, (6) coupling coils, (7) coils mechanical support, (8) PCB, (9) SMA connector, (10) sensing coil cabling and connector, (11) metallic enclosure.

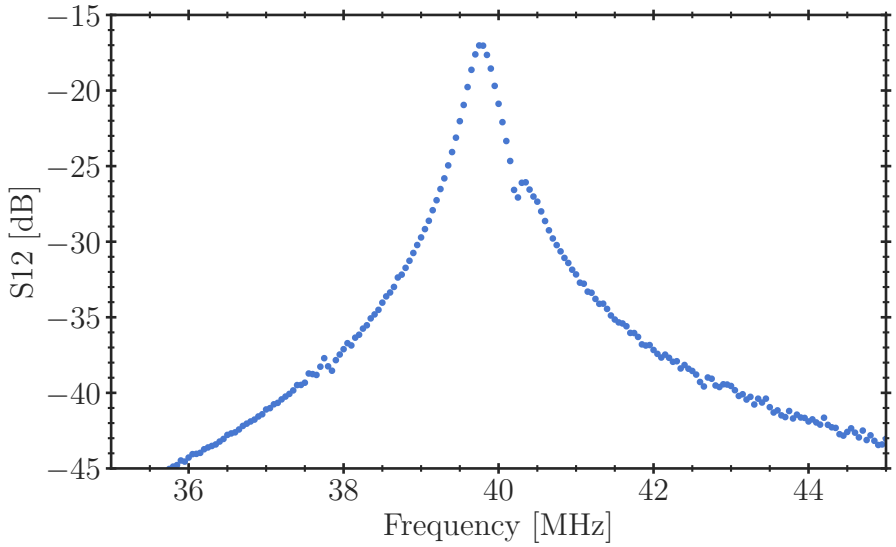


Figure 3.19: EOM resonance frequency measured on the VNA $S_{12}$ parameter trace.

the sensing coil [175]. The VNA is an instrument used to measure the 4 scattering parameters of a two-port network by injecting a sinusoidal signal at different frequencies into the system. These parameters are proportional to the power reflected by each port (parameters $S_{11}$ and $S_{22}$) and to the power transmitted between ports (parameters $S_{12}$ and $S_{21}$). The dependence of the EOM $S_{12}$ parameter versus modulation frequency is shown in fig. 3.19. The curve shows a clear peak centred at 39.9 MHz which correspond to the resonance frequency of the LC tank. The $Q$ value of the resonator can be measured from this curve as the ratio between the centre frequency of the peak and its $-3$ dB bandwidth[35], the resulting value is approximately 106.

### 3.2.4 Experiment-side optics

#### Zeeman slower breadboard

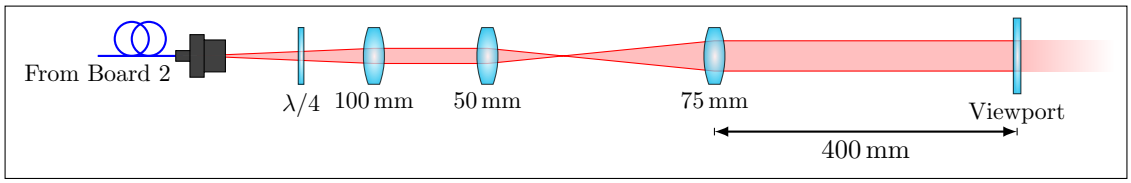


Figure 3.20: Optical circuit of the ZS breadboard placed on experimental table.

To maximize the efficiency of the ZS beam in slowing down the lithium atoms, the ZS beam should have roughly the same shape as the atomic beam. Therefore, it should have the same radius of the oven exit slit ($r_{\text{oven}}$) and the capture range of the MOT ($r_c$) at the corresponding positions along the beam axis. This condition is mathematically expressed as

$$\begin{cases} w(Z_{\text{oven}}) & = w_0\sqrt{1+\left(\frac{Z_{\text{oven}}}{z_0}\right)^2} = r_{\text{oven}} \\ w(Z_{\text{MOT}}) & = w_0\sqrt{1+\left(\frac{Z_{\text{oven}}+Z_1}{z_0}\right)^2} = r_c \end{cases}$$

where $w(z)$ is the beam radius at position $z$, $w_0$ is the beam waist, $Z_{\text{oven}}$ is the distance between the waist position and the lithium oven, $Z_1$ is the distance between the MOT centre and the oven entrance, $z_0 = \pi w_0^2/\lambda$ is the Rayleigh range of the beam. By solving the equation system for the two variables $w_0$ and $Z_{\text{oven}}$ it is possible to determine the waist size of the beam and its position with respect to the oven, thus, completely determining the ZS beam. Given the geometry of the $Ba^+Li$ experiment, the numeric solution yields $w_0 = 37\,\mu$m positioned at a distance

[35] defined as the full width of the curve measured at $-3$ dB from the curve maximum.

$Z_{\text{oven}} = 432\,\text{mm}$ behind the oven exit slit. By propagating the beam throughout the vacuum system and the entrance viewport using the ABCD-matrix formalism, the focusing length and the beam size needed to couple to the optical fibre output can be estimated.

Figure 3.20 shows the optical setup used to shape the laser beam: the fibre output is collimated using a $f = 100\,\text{mm}$ lens and then expanded using a Keplerian telescope made of a $f_1 = 50\,\text{mm}$ and a $f_2 = 75\,\text{mm}$ lenses. The telescope is kept slightly outside the ideal telescope condition $d = f_1 + f_2$, where $d$ is the lenses distance. By placing the lenses at 127 mm rather than 125 mm the resulting beam is convergent and reproduces well the needed shape for the ZS beam having a beam waist of 32 µm at the position $Z_{\text{oven}}$ and a radius of 8.6 cm at the position of the MOT.

### MOT breadboard

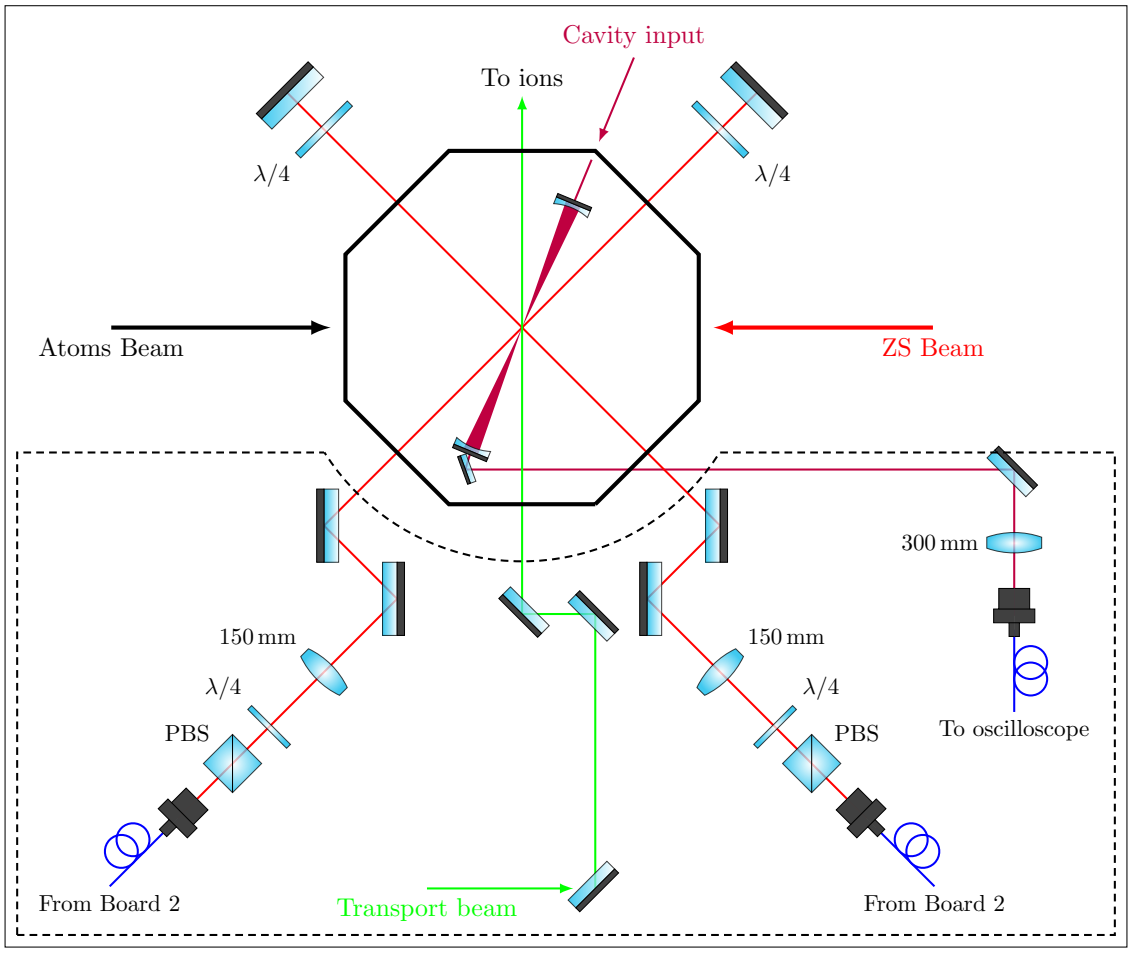


Figure 3.21: Optical circuit of the MOT breadboard on the experimental table.

Figure 3.21 shows the schematic drawing for the MOT breadboard. The MOT is formed by three retro-reflected light beams, obtained by collimating the optical fibre output with a $f = 150\,\text{mm}$ lens, the beam waist is $\sim 10\,\text{mm}$ at the atom location. With an expected power of approximately 15 mW per beam, the MOT capture radius and capture velocity result $r_c \approx 7.5\,\text{cm}$ and $v_c \approx 235\,\text{m}\,\text{s}^{-1}$, respectively. A PBS is placed immediately after the fibre launcher in order to ensure a linear polarization of the light.

The breadboard also hosts the optics for shaping and manipulating the optical transport beam. This beam is formed by laser light at 1064 nm and it is used for transporting the atomic cloud, after cooling to degeneracy, from the MOT chamber to the ion trap and overlap it with the trapped $Ba^+$ ions. The beam is shaped using a three lens telescope with one lens placed on a linear air-bearings translator[36] laying on a smaller breadboard, this setup allows for moving the beam focal point with high precision and stability for more than 10 cm, moving the focal point of the beams coincide with moving the minimum of the dipole trap. A detailed description of the calculations behind the optical transport time and telescope lenses is given in [171]. At the moment of writing, the transport laser and the optical components have been tested, but not yet implemented in the experimental setup.

Additionally, part of the breadboard will be devoted to the analysis of the transmitted light from the optical resonator, *e.g.* by coupling this light into an optical fibre using a collimating lens and two mirrors placed at the edge of the breadboard.

### MOT-z and imaging optics

Lithium imaging will be performed along the vertical axis, with the goal of performing time-of-flight imaging for estimating the atomic cloud velocity distribution and temperature. The imaging beam optics have to merge with the optics for the MOT-z beam, which is also oriented along the vertical axis. Figure 3.22 shows the optical schematic that was designed for the optical elements placed along the z-axis, above and below the MOT chamber. Above the experimental chamber the optical elements are held in a Thorlabs 60 mm-cage system, parts of which had to be custom-made. In this part of the setup, the MOT beam and imaging beam are brought by optical fibres, and collimated using a $f = 150\,\text{mm}$ lens and a $f = 100\,\text{mm}$ lens, respectively. The two beams have orthogonal polarizations and are combined using a PBS. In order to ensure the correct polarization for both beams, a quarter-wave plate is placed between the PBS and the vacuum chamber window.

Below the MOT chamber a $f = 50\,\text{mm}$ objective lens is used to collimate the

[36] Aerotech ABL1000–050-E2-CMS1-PL2-TAS

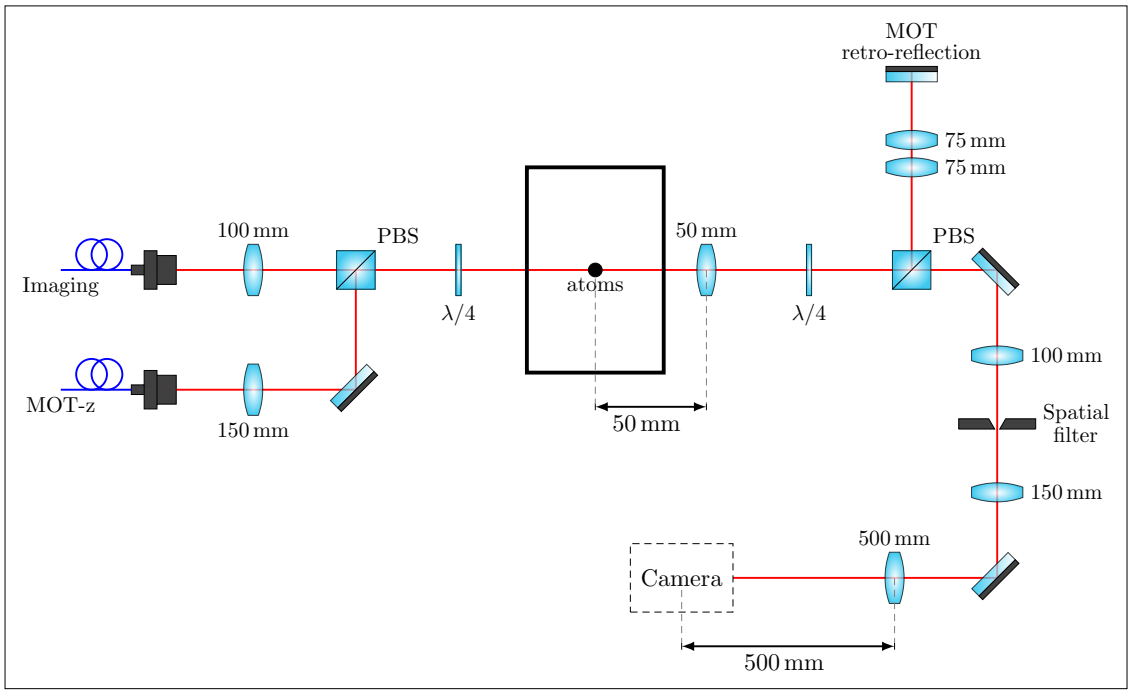


Figure 3.22: Optical circuit for the MOT-z and imaging optics.

fluorescence light emitted by the atomic cloud as well as the MOT-z beam. This lens is supported by a custom-made brass holder which is designed to fit just inside the CF40 re-entrant viewport. Since the MOT-z beam is initially collimated, after the imaging lens it will be strongly convergent. The two beams polarizations are linearized by another quarter-wave plate and the beams are separated with a second PBS, in order to retro-reflect the MOT beam two $f = 75\,\text{mm}$ lenses are used to quickly focus the diverging beam onto the retro-reflection mirror. The collimated fluorescence beam is reshaped by using a 1:1.5 Keplerian telescope, and on the focal point of the telescope a variable iris is positioned for blocking stray light. A $f = 500\,\text{mm}$ lens is then used to focus the light onto a CCD camera[37]. The PBS and imaging lens assembly is mounted on a manual linear translator to allow for adjustments along the vertical axis in order to focus on the atomic cloud position.

## 3.3 Magneto-Optical Trap of lithium

In order to realize the lithium MOT, the D2 laser beam was split into four arms: one dedicated to providing light for the ZS and three arms for generating the MOT. The frequency detuning of each arm was set to the target values reported

[37] Andor iXon Ultra

in table 3.1. Each arm was injected into a separate fibre and brought on the experimental table. The laser power reaching the experimental table is reported in table 3.2.

| **Laser** | **Power** [mW] | |
|---|---|---|
| | Cooling | Repumper |
| MOT $x$-axis | 22.6 | 10.9 |
| MOT $y$-axis | 19.4 | 10.8 |
| MOT $z$-axis | 23.0 | 10.0 |
| ZS | 65.1 | 34.0 |

Table 3.2: List of the laser light powers used in the preparation of the lithium MOT. Measurement error is $\pm 0.1$ for all values.

The first eight coils of the ZS were run at 5.85 A, while the ninth coil (the merging coil) was run at 3.4 A current. These were determined, with a Monte Carlo simulation [176], to be the ideal values that maximize the number of atoms reaching the MOT volume and provide the best merging between the ZS and MOT magnetic fields. The MOT coils were run at approximately 40 A. Given the coils' geometry, at this current value, the field gradient is 25 G cm$^{-2}$. Figure 3.23 shows the picture of the lithium atoms collected by the MOT.

Before any measurements could be made to characterize the MOT, work on the lithium setup had to be suspended due to the loss of UHV in the MOT chamber. While in the initial preparation of the MOT the pressure inside the chamber was below $1 \times 10^{-10}$ mbar[38], it quickly raised up to $1 \times 10^{-7}$ mbar. The pressure kept raising in the following days, until the protection circuit of the NEG-ion pumps was triggered and turned off the pumps. The issue was tracked down to a leak caused by microscopic cracks present in the metal structure of the bottom viewport of the MOT chamber. These cracks may have formed during the machining steps that this particular viewport had to go through to equip it with the resonator mounts.

At the time of writing, this issue is still being dealt with. The flange was shipped to an UHV-specialized company[39] for testing the flange and devising a plan for the repairs. The option of applying VacSeal[40] is being considered. VacSeal is a sealant certified for UHV conditions. It can be applied to the air side of vacuum components to create a thin layer covering cracks that may cause leaks. The sealant requires curing at a temperature above 200 °C for at least one hour. Therefore, for this operation all optics (including the high-finesse optical resonator) will have to be dismounted from the flange.

[38] measured from the residual current of the NEG-ion pumps.

[39] Mori Meccanica srl, Parma, Italy.

[40] Allectra, 330-VACSEAL-S.

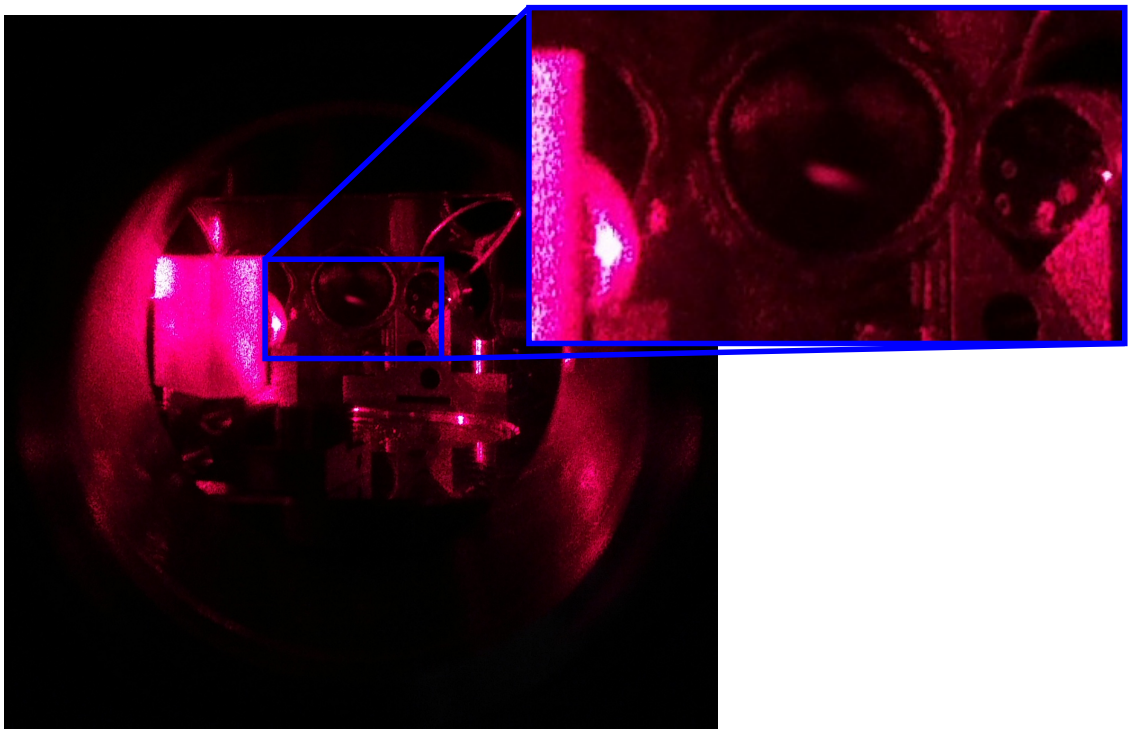

Figure 3.23: Photo of a cloud of lithium atoms trapped in the MOT at the $Ba^{+}Li$ experiment.

# Chapter 4

# High-Finesse optical resonator

This chapter reports on the design and assembly of the lithium high-finesse optical resonator installed in the MOT chamber, which is intended to be used for trapping and cooling a Li cloud. In section 4.1 a quick overview of the fundamental concepts of optical resonators is presented, and a particular emphasis is given on the concepts useful during experimental work. The discussion is based on the material presented in Photonics: optical electronics in modern communications [168]. Section 4.2 provides a description of the design, of the alignment procedure and of the experimental characterization of the lithium optical resonator. Laser linewidth plays an important role when coupling light to a high-finesse resonator: if the laser linewidth is much larger than the resonator linewidth, only a small portion of the laser power will be coupled into the cavity. Therefore, effort has be put in characterizing the 903 nm laser used for the lithium resonator and determining the feedback loop to narrow its linewidth; this work is presented in section 4.3.

## 4.1 General description of an optical cavity

An optical resonator (or cavity) is a device composed by two or more mirrors arranged in a configuration that ensures that light injected into the resonator will perform several reflections before escaping. As a result, an optical resonator shows resonant behaviour at optical frequencies. Cavities formed by two mirrors are usually referred to as *linear cavities*, and the mirrors forming them can be either flat or curved. The name *Fabry-Perot resonators* is commonly used to indicate two-mirror cavities, although, the original design [177] only referred to a flat-mirror interferometer. Linear cavities reflect the injected light beam back onto its path, thus creating an intra-cavity standing wave. An alternative design of an optical resonator is the so-called *ring-cavity*, *i.e.* a cavity formed by more than two mirrors in which the light always circulates in one direction. For these reasons, ring-cavities are also called running-wave cavities. In all optical resonators, the shape and distance of

the mirrors determines the characteristics (waist and resonance frequency) of the intra-cavity standing waves: these are called *proper modes* of the cavity.

This section provides an overview of the main characteristics of optical cavities, in particular the stability, the intra-cavity field and the effects of losses. A more detailed description can be found in ref.s [168, 178, 179].

### 4.1.1 Stability condition of a linear cavity

The stability condition of a linear cavity can be easily obtained using the geometrical optics model. Assuming that a ray of light is bouncing inside a linear cavity, such cavity is stable if the position of the ray does not diverge to infinity after many bounces. Following the matrix formalism for ray propagation, after $n$ bounces the ray position $r_n$ and angle $r'_n$ are

$$\begin{bmatrix} r_n \\ r'_n \end{bmatrix} = \begin{bmatrix} A & B \\ C & D \end{bmatrix}^n \begin{bmatrix} r_0 \\ r'_0 \end{bmatrix},$$

where the ABCD matrix is the round-trip matrix of the resonator, and $r_0, r'_0$ are the ray initial position and initial angle, respectively. If the position $r_n$ is not to diverge, then the following condition must hold true

$$\frac{|A+D|}{2} < 1\,.$$

In case of a cavity formed by two curved mirrors with RoCs $R_1$ and $R_2$ separated by a distance $L$, the round trip matrix is given by

$$\begin{bmatrix} A & B \\ C & D \end{bmatrix} = \begin{bmatrix} 1 & 0 \\ -\frac{1}{R_1} & 1 \end{bmatrix} \begin{bmatrix} 1 & L \\ 0 & 1 \end{bmatrix} \begin{bmatrix} 1 & 0 \\ -\frac{1}{R_2} & 1 \end{bmatrix} \begin{bmatrix} 1 & L \\ 0 & 1 \end{bmatrix}.$$

Then, by performing the matrix multiplication

$$\frac{A+D}{2} = 1 - \frac{2L}{R_1} - \frac{2L}{R_2} + \frac{2L^2}{R_1 R_2}\,,$$

which leads to the stability condition

$$0 \leq g_1 g_2 \leq 1\,, \tag{4.1}$$

where $g_i = (1 - L/R_i)$, $i = 1{,}2$. Cavity configurations that lie on the limit condition $g_1 g_2 = 0$ are referred to as *symmetric confocal*, since they are formed by two identical curved mirrors ($R_1 = R_2 = R$) spaced exactly by their RoC ($L = R$). On the other hand, $g_1 g_2 = 1$ cavities are either concentric cavities ($L = 2R$) or flat mirror cavities ($L/R \to 0$). These two extrema configurations are marginally stable, since any small deviation may render the cavity unstable.

### 4.1.2 Eigenmodes

The proper modes, or *eigenmodes*, of a cavity are determined by the Hermite-Gaussian (TEM) beams that exist with low losses in the resonator. To determine these modes, the self-consistency condition must be satisfied, *i.e.* the beam has to reproduce itself after one round trip. Mathematically, this condition requires the mirror RoC to match the curvature radius $R(z)$ of the constant-phase surface of the beam at the mirror position. This leads to determining the distances of the mirrors from the beam waist position,

$$z_1 = \frac{L(R_2 - L)}{R_2 + R_1 - 2L}\,,$$
$$z_2 = \frac{L(R_1 - L)}{R_2 + R_1 - 2L}\,,$$

and the beam Rayleigh range,

$$z_0 = \left(\frac{\pi w_0^2}{\lambda}\right)^2 = \frac{L(R_1 - L)(R_2 - L)(R_1 + R_2 - L)}{(R_2 + R_1 - 2L)^2}\,,$$

which then determines the beam waist $w_0$. In this frame of reference, the beam waist is positioned at $z = 0$ and the two mirrors are positioned at $z = z_i,\ i = 1{,}2$. It is important to notice how the cavity geometry determines a single value of beam waist, thus defining a *class* of Gaussian beams that can exist in the cavity.

To determine the resonance frequency of the eigenmodes, the field has to accumulate a phase of $2q\pi,\ q \in \mathbb{Z}$ after a round trip, so that it interferes constructively with itself. For the $\mathrm{TEM}_{lm}$ mode, this condition is expressed mathematically as

$$2\pi\frac{\nu}{\nu_{\mathrm{FSR}}} - \zeta(l + m + 1) = 2q\pi\,, \qquad q \in \mathbb{Z}$$

where $\nu$ is the beam frequency, $\nu_{\mathrm{FSR}} = c/(2L)$ is the Free Spectral Range (FSR) of the cavity, and $\zeta$ is the Gouy phase shift given by

$$\zeta = 2\left(\arctan\left(\frac{z_2}{z_0}\right) - \arctan\left(\frac{z_1}{z_0}\right)\right).$$

The cavity resonant frequencies are

$$\nu_{qlm} = \left(q + (l + m + 1)\frac{\zeta}{2\pi}\right)\nu_{\mathrm{FSR}}\,.$$

Modes associated with different $q$ values are referred to as *longitudinal modes*, while modes that differ in the $l$ or $m$ numbers are different *transverse modes*.

A generic spectrum of a Fabry-Perot resonator is shown in fig. 4.1. Different longitudinal modes have resonance frequency differing by one FSR. The resonance frequency of different transverse modes is determined by the sum $l + m$. Cavities where different transverse modes resonate at the same frequency are referred to as *degenerate cavities*, for example all cavities with $\zeta = 0$ are degenerate.

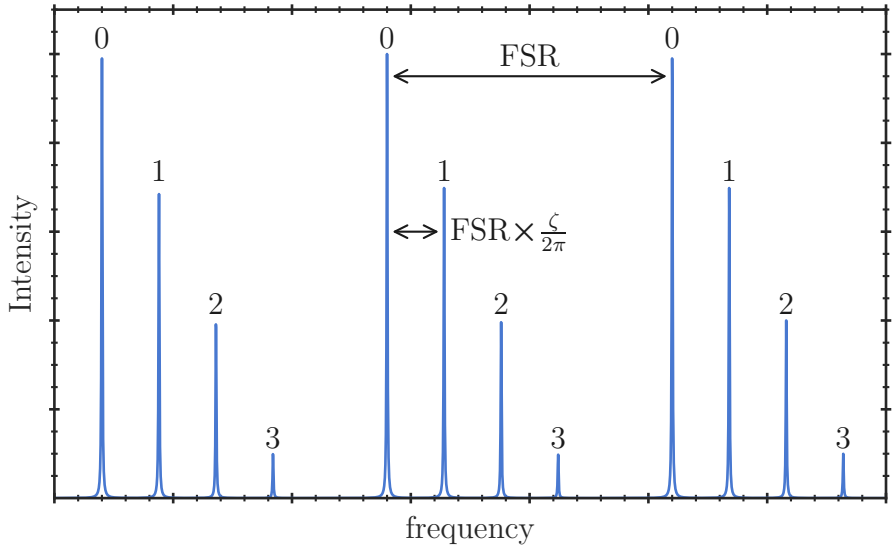


Figure 4.1: Spectrum of a non-degenerate Fabry-Perot resonator. Numbers near peaks are the sum $l+m$ which identifies the resonance of different transverse modes.

### 4.1.3 Cavity losses

Like in all resonating devices, losses in optical resonators will cause a broadening of the resonance line accompanied by the reduction of its amplitude, that is the maximum power that can be accumulated in the resonator is reduced. In optical resonators, the limited dimension of the mirrors will lead to so-called diffraction losses due to the tail of the Hermite-Gaussian beams being cut off at the reflection. Additional "mirror losses" are caused by the mirrors' reflectivity being less than unity, these losses can be distinguished in losses due to absorption from the mirrors material (generally unwanted) and losses due to transmission though the mirrors, which are necessary since light must be coupled and sampled from the cavity. Scattering of photons by the intra-cavity medium can be responsible for further losses.

Finally, tilting of the resonator mirrors from their optimal position can lead to losses depending on the particular mirror configuration of the cavity: for example, in the flat mirror Fabry-Perot a small tilting of the reflective surfaces leads to a divergence of the beam position, which is equivalent to an additional contribution to the overall losses. Conversely, in the spherical mirror Fabry-Perot a tilt of one mirror simply causes a redefinition of the cavity axis, but no further losses [180].

Losses are usually characterized using the photon lifetime

$$\tau_c = L/(c\,\gamma_c)\,, \tag{4.2}$$

where $\gamma_c$ represents the (dimensionless) total loss rate of the cavity. The energy $E$ stored in a passive (with the input beam turned off) optical resonator is determined

by the exponential decay equation

$$E(t) = E(0)e^{-t/\tau_c}\,. \tag{4.3}$$

The finite photon lifetime in the cavity leads to a Lorentzian line shape for the cavity resonance, with a FWHM of

$$\delta\nu = \frac{1}{2\pi\tau_c}\,.$$

Optical resonators are usually characterized in terms of their *finesse*, or quality factor, which is defined as the ratio between the cavity FSR and the cavity linewidth. This quantity is strictly related to the mean number of bounces a photon performs in the resonator before being absorbed by the mirrors or being lost from the cavity.

The cavity finesse and losses can be estimated experimentally by performing a *ring-down measurement* [181]. In this measurement a laser initially coupled to the cavity is suddenly turned off. The light intensity transmitted through the cavity then displays the decay behaviour given by eq. (4.3) which allows for the determination of $\tau_c$ and hence $\delta\nu$. Assuming that the cavity FSR is known, *i.e.* the length of the cavity is known, the finesse can be calculated. If one assumes that $\gamma_c = 1 - R$, where $R$ is the mirror reflectivity, *i.e.* the cavity losses are mostly due to mirror absorption or transmission, the ring-down measurement offers a method to characterize low-loss mirrors [182].

### 4.1.4 Mode matching and misalignment of the input beam

One of the main experimental issues when working with optical cavities is maximizing the coupling of the input beam with a proper mode of the cavity. To do so it is necessary for the input beam to be *mode-matched*. That is, when the beam passes through the partially-reflective input mirror, its waveform should be identical to one of the resonating modes within the cavity volume. The procedure is referred-to as *mode-matching*. Since the output light of a single mode lasers and single mode fibre optics is in the fundamental $\mathrm{TEM}_{00}$ mode, the highest coupling is achieved when mode-matching to the $\mathrm{TEM}_{00}$ mode of the cavity. Practically, this is achieved by using lenses to resize the beam waist and curvature to match the cavity ones. A perfectly matched input implies that all the input power is injected into a single transverse mode. Therefore, by scanning the injected laser frequency, the cavity spectrum is given by a series of peaks spaced by one FSR, these are transmission peaks of different longitudinal modes associated with the same transversal mode.

If an input beam is misaligned, then part of the input power is projected onto multiple transversal modes and will result in spectrum populated with many peaks (similar to the spectrum shown in fig. 4.6). Assuming that the input beam is in

a Hermite-Gaussian mode $\mathrm{TEM}_{lm}$ and that it is slightly misaligned with respect to the corresponding proper mode of the cavity, then the intra-cavity field $\mathcal{E}_{\mathrm{cav}}^{(l,m)}$ generated by this input beam is given by the sum of different proper modes

$$\mathcal{E}_{\mathrm{cav}}^{(l,m)} = \sum_{k=0}^{\infty} c_k \mathrm{TEM}_{(l+k)m} \,, \tag{4.4}$$

where a displacement along a single axis is assumed. The coefficients $c_k$ determine the intra-cavity field and are dependent on the type and magnitude of misalignment. For a Fabry-Perot cavity four possible misalignments can occur:

1. Transverse displacement of the input beam with respect to the optical cavity axis.
2. Angular displacement of the input beam with respect to the optical cavity axis.
3. Waist size mismatch.
4. Waist position mismatch along the cavity axis.

Misalignments connected with displacement of the input axis (1 and 2) will lead to an increase of the coefficient $c_1$ in eq. (4.4), *i.e.* the input power will be mostly coupled into the modes $\mathrm{TEM}_{l\pm1m}$, while waist mismatches (3 and 4) will mostly contribute to the $c_2$ coefficient [183]. As an example, if the input beam is initially perfectly matched to the $\mathrm{TEM}_{00}$ mode, a small displacement will cause the appearance of the peak associated with the $\mathrm{TEM}_{01}$ or $\mathrm{TEM}_{10}$ modes in the spectrum. Similarly, wrong waist size or position will lead to the appearance of the peak associated with the $\mathrm{TEM}_{02}$ or $\mathrm{TEM}_{20}$ modes. These considerations are helpful during the mode matching process to determine which alignment degree of freedom to act on.

## 4.2 The lithium optical resonator

Optical traps are commonly employed to perform evaporative cooling of a quantum gas [140]. Although ODTs can be made using high-power single beam lasers, this solution has a few drawbacks: first, a high-power laser is necessary which can be expensive; second, at high-powers thermal lensing effects can become an issue [184]. The use of in vacuum high-finesse optical resonator for power amplification is an alternative solution which, nevertheless, poses a different set of technical challenges related, for instance, to the design and realization of a stable mechanical support for the cavity.

The lithium high-finesse resonator that was implemented in the $\mathrm{Ba}^{+}\mathrm{Li}$ experiment is intended to be used with a laser having a wavelength of 903 nm. The

| Parameter | value |
|---|---|
| RoC | 100 mm |
| Thickness | 4 mm |
| Diameters: | |
| Mirror 1 | 7.685(1) mm |
| Mirror 2 | 7.687(1) mm |
| Refraction index | 1.45 |
| Reflectivity | 0.999 82 |

(a)

| Parameter | value |
|---|---|
| Mirror distance | 66 mm |
| Waist | 116.2 µm |
| Rayleigh range | 47.0 mm |
| FSR | 2.271 GHz |
| Linewidth | 126.5 kHz |
| Finesse | 17 950 |

(b)

Table 4.1: (a) Physical and optical characteristics of the mirrors used for the lithium high-finesse resonator. Mirrors' diameters were measured using a micrometer. (b) Expected characteristics of the lithium high-finesse optical resonator. Finesse, linewidth and FSR are the calculated using the values of reflectivity provided by the mirrors producer.

characteristics of the concave mirrors available in the laboratory are given in table 4.1a. These mirrors have high reflectivity coating for 903 nm, 671 nm, 451 nm and 493 nm light. The stated reflectivity is the minimum value guaranteed by the producer.

The calculated characteristics of the cavity fundamental mode, finesse, linewidth and FSR are reported in table 4.1b. These values are calculated using the mirror characteristics provided by the producer, thus, they constitute only a rough estimate. The actual characteristic quantities of the optical resonator were measured directly and are reported later in this chapter.

### 4.2.1 Mechanical design

The mechanical support for the cavity mirrors is installed inside the MOT chamber. Due to the limited space available in the chamber, custom-made supports were deemed necessary. One of the main requirements for the mechanical supports is that the two mirrors optical axes must be perfectly aligned. For a spherical Fabry-Perot resonator (like the one described in this thesis), this requirement is not stringent since tilt or displacement will cause a redefinition of the trap axis (as mentioned in section 4.1.4). However, any displacement of the resonator axis can be problematic, because of the limited optical access for the input beam. An additional technical challenge sparks from merging the optical resonator apparatus with the other laser beams of the experiment: the cavity mirrors supports have to be compact enough to avoid blocking the MOT beams and the imaging axis.

The cavity mirrors holders are realized starting from a monolithic piece of titanium characterized by a V-shape basis. A V-shape profile can be build with

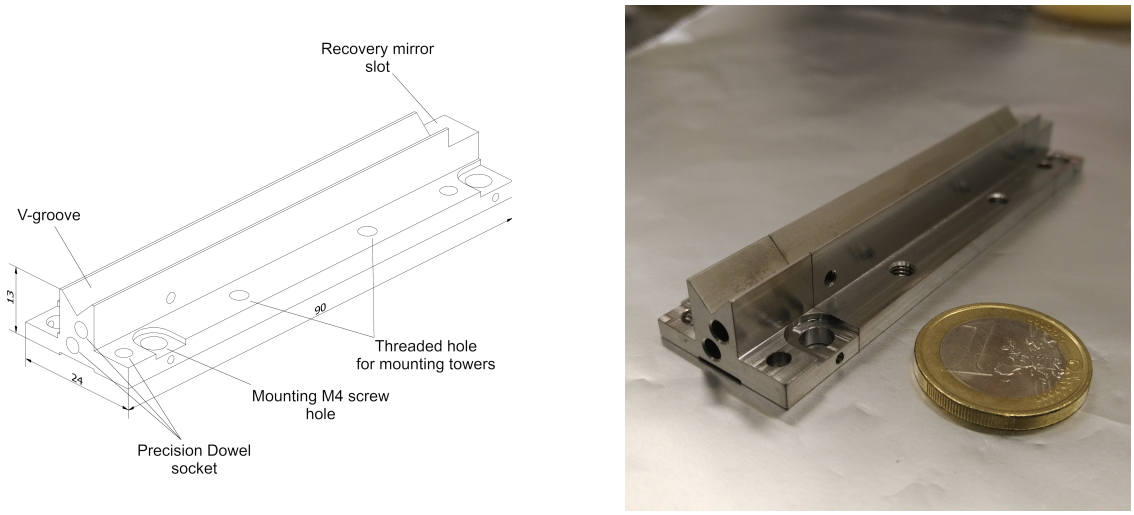


(a) (b)

Figure 4.2: (a) 3D CAD view of the cavity supports. (b) Photograph of the machined titanium pieces.

an extremely high precision, so that two mirrors with exactly the same diameter placed on top of the profile will have their optical axes aligned. The resulting design is shown in fig. 4.2, detailed mechanical drawings are shown in appendix B. The monolithic support was then cut into three parts: two smaller parts on the side where the mirror would be glued to and a larger central piece used only during the mounting process. Thanks to precision holes drilled on the side of the support, the three pieces can be held together to ensure that no misalignment is present between the positions where the two mirrors are placed. Two M4 and precision alignment holes are drilled on both lateral pieces which allow to secure them on the bottom vacuum flange of the MOT chamber. This design ensures that the mirrors' optical axes are properly aligned, while still allowing to remove the central part of the support after the mirrors are glued, thus, leaving clear optical access to the MOT chamber. These supports are also easily removable and re-mountable in case maintenance is to be performed on the MOT chamber.

Due to the specific angle at which the cavity is installed in the MOT chamber, a third flat mirror is needed for recovering the light transmitted through the cavity and tilt it an angle that makes it exit the vacuum chamber from a viewport. For this reason, a flat plane was machined on one side of the support.

To guarantee that the mirrors are in good contact with the V-groove and that they do not move during mounting or alignment, a so-called "mounting tower" was designed to be temporarily placed on the central part of the cavity support during the first cavity alignment. In this mounting tower a micrometer screw is used to gently press from the top the mirrors on the V-shaped groove. Two 250 µm pin

holes with the same diameter of the mirrors were also realized and used to define the optical axis and help with the initial laser alignment phase.

### 4.2.2 Cavity alignment and characterization

In order to couple the light from a fibre launcher to the cavity, an optical circuit has to be designed and realized. For this setup it was decided to operate with a three-lens system: the first two lenses, with focal lengths of −100 mm and 125 mm, form a 1 : 1.25 Keplerian telescope for the collimated light coming from the fibre launcher; the third lens is used to couple the collimated light to the cavity. This final length focal length (400 mm) had to be long enough to ensure that the ideal lens position was far enough from the cavity centre to be outside the vacuum system. Once the cavity geometry is decided and the fundamental $TEM_{00}$ is known, a simple ABCD matrix propagation calculation determines the proper lens positions.

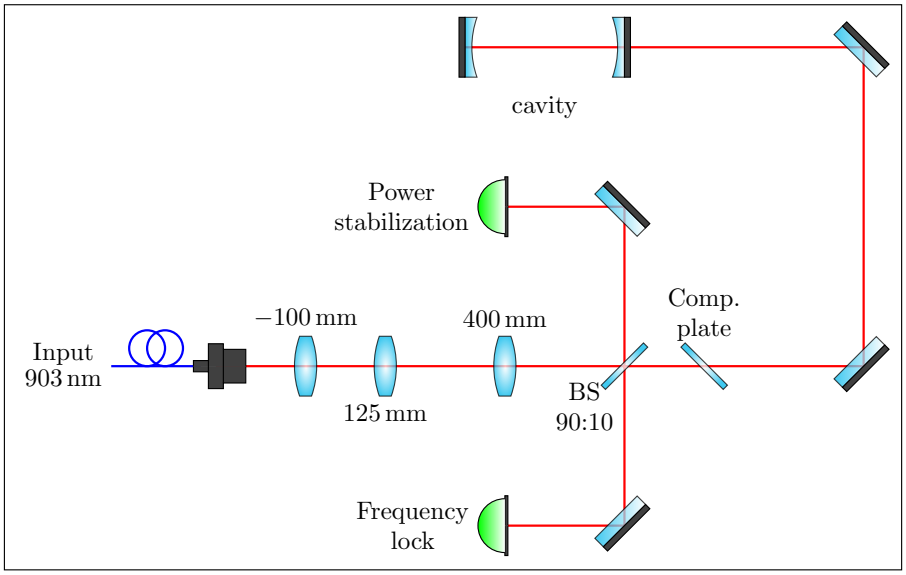


Figure 4.3: Optical circuit schematic for coupling light from a fibre launcher to the lithium optical resonator.

Figure 4.3 shows the final configuration of the optical system used to couple light to the high-finesse optical resonator. After the three coupling lenses a BS 90:10 (transmission:reflection) is used to sample part of the input beam — which is sent to a photodiode for stabilizing the beam power — and to sample part of the light reflected by the cavity, which is used to lock the cavity resonance to the laser frequency. Since the two mirrors used to couple light to the cavity have

a small diameter of 12.7 mm, a compensation plate[1] is used to correct the small displacement introduced by the BS dielectric.

To perform the initial mode-matching, a temporary optical setup was used. In this setup the three coupling lenses and fibre launcher were mounted in their final supports but a 50:50 BS was placed before the cavity to sample the reflected light. An additional 50:50 BS was placed after the cavity to permit measuring the transmitted light both with a Charge-Coupled Device (CCD) camera and a photodiode. The coupling efficiency was determined by measuring the percentage of light not reflected when the laser is at resonance with the cavity. With this setup ready, the cavity alignment was performed following a many-step procedure:

- All vacuum components are cleaned using ultrasound in acetone bath for approximately 10 min.
- The three parts of the cavity supports are joined together with precision dowels, the joined support is mounted on the vacuum flange and tightly screwed in place.
- The coupling optical elements are placed at the calculated ideal distances. To ensure that the laser light axis is roughly collinear with the cavity axis, the two custom-made pin holes, with the same diameter as the mirrors, are placed on the cavity. Beam-walking is performed until the laser goes through both pin holes. The pin holes are then removed.
- The vertical tilting of the cavity mirrors is measured by observing the reflected light from their flat side. It is important that the light retraces its path well, as this means that the mirrors have been machined properly. If the mirrors are found to be considerably non-vertical, they could introduce a strong tilt of the cavity axis.
- Mirrors are placed on the V-groove at the proper distance from the support edge. The two mounting towers are positioned and screwed on the support. Ball-tipped micrometre screws installed on the towers are used to secure the mirrors in place.
- The laser is injected into the cavity through the coupling optics. A slow ($\approx 30$ Hz) voltage ramp is applied to the laser piezoelectric in order to "scan" the cavity spectrum.
- For the initial phase of mode-matching, the intensity distribution of the cavity modes is recorded on the CCD camera. One can expect to observe highly-excited transverse Hermite-Gaussian modes, such as the ones shown in fig. 4.4.

[1] Thorlabs, BCP4210.

The direction of alignment of the intensity peaks in the observed distribution gives a clue to which degree of freedom requires adjustment. Indeed, Figures 4.4a to 4.4c, were observed while the input beam was slightly displaced along the $x$-axis.

- Once the input beam has been roughly aligned to the point where the intensity distribution of highly excited transversal modes in barely visible, the final optimization is done by observing the cavity spectrum recorded by the photodiodes. The optimum configuration is reached when the resonance peak of the fundamental $\mathrm{TEM}_{00}$ mode is maximized.

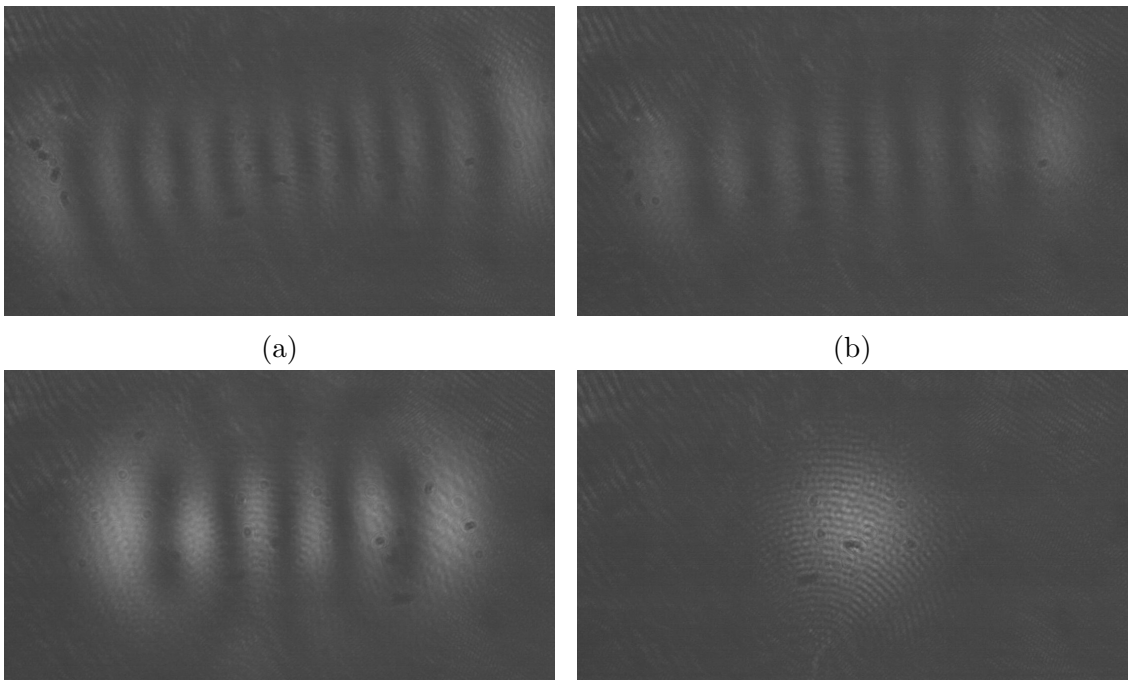

(a) (b)

(c) (d)

Figure 4.4: Excited transversal modes observed during cavity alignment. (a) $\mathrm{TEM}_{0,10}$. (b) $\mathrm{TEM}_{07}$. (c) $\mathrm{TEM}_{05}$. (d) $\mathrm{TEM}_{00}$.

During the initial alignment the cavity was kept in air and injected with a relatively low laser power ($\approx 10\,\mathrm{mW}$), nevertheless the intra-cavity field was powerful enough to cause small particles of dust to be attracted and stick to the mirrors' surface. This caused a progressive deterioration of the coupling efficiency and transmitted power. The issue was solved by cleaning the mirror surface with an organic solvent (acetone) using the usual drop-and-drag method. An interesting effect observed in this case is that although the coupling efficiency of the fundamental mode deteriorated, the $\mathrm{TEM}_{01}$ coupling efficiency remained relatively high, most likely because of the different power distribution of this mode.

After a good coupling efficiency was reached with beam walking, a piezoelectric element was glued[2] first to a custom-made cylindrical titanium block and then glue to the back of one of the two mirrors while the mirror was still locked in position. Then, the cylindrical titanium block was glued to the V-shape. The flange (with the cavity mounted on top) was installed in the MOT vacuum chamber and the optical system was mounted in its final configuration, shown in fig. 4.5. Thorlab's 30 mm cage system is used as a compact holder for all the optical elements, and a number of custom-designed aluminium supports is used to create a periscope with two 0.5-inch mirrors.

Once the cavity and optics are installed in their final configuration and good coupling is still achieved, the mirror without piezoelectric and the piezoelectric support block was glued to the titanium V-groove. After the glue was cured the mounting tower and the central part of the cavity support could be removed, thus completing the resonator assembly.

### Cavity characterization

Throughout the assembly process the cavity was aligned using the 903 nm laser light. Due to technical issues the final characterization was performed with the 671 nm laser used for lithium cooling. The cavity mirrors have high reflectivity at both wavelengths, so comparable results are expected.

Figure 4.6 shows the cavity transmission spectrum using 671 nm laser light. The central highest peak is the $\mathrm{TEM}_{00}$ mode resonance. The peak associated with the $\mathrm{TEM}_{01}$ (or $\mathrm{TEM}_{10}$) is no longer visible, while the $\mathrm{TEM}_{02}$ (or $\mathrm{TEM}_{20}, \mathrm{TEM}_{11}$) mode is still visible, suggesting that the waist position and dimension may need additional adjustments. The final measurement of the coupling efficiency (measured from the reflection spectrum) is

$$\frac{P_{\text{transmitted}}}{P_{\text{in}}} = 82.4\,\% \,.$$

The cavity finesse was determined by performing a ring-down measurement. The 671 nm laser was made to traverse an AOM in double pass configuration before being coupled to the fibre optics leading to the cavity. As the laser was scanned across the cavity resonance, when the transmission peak was near its maximum the AOM was turned off, causing a sudden shutdown of the laser light. The recorded decay of the transmitted power is shown in fig. 4.7. Five different ring-down measurements were performed in quick succession and the results were then averaged together.

[2]Remak, Optical epoxy 353ND/4GM/APAK. After applying the glue and before it solidifies, low-vacuum is used to remove the air bubbles that might have formed.

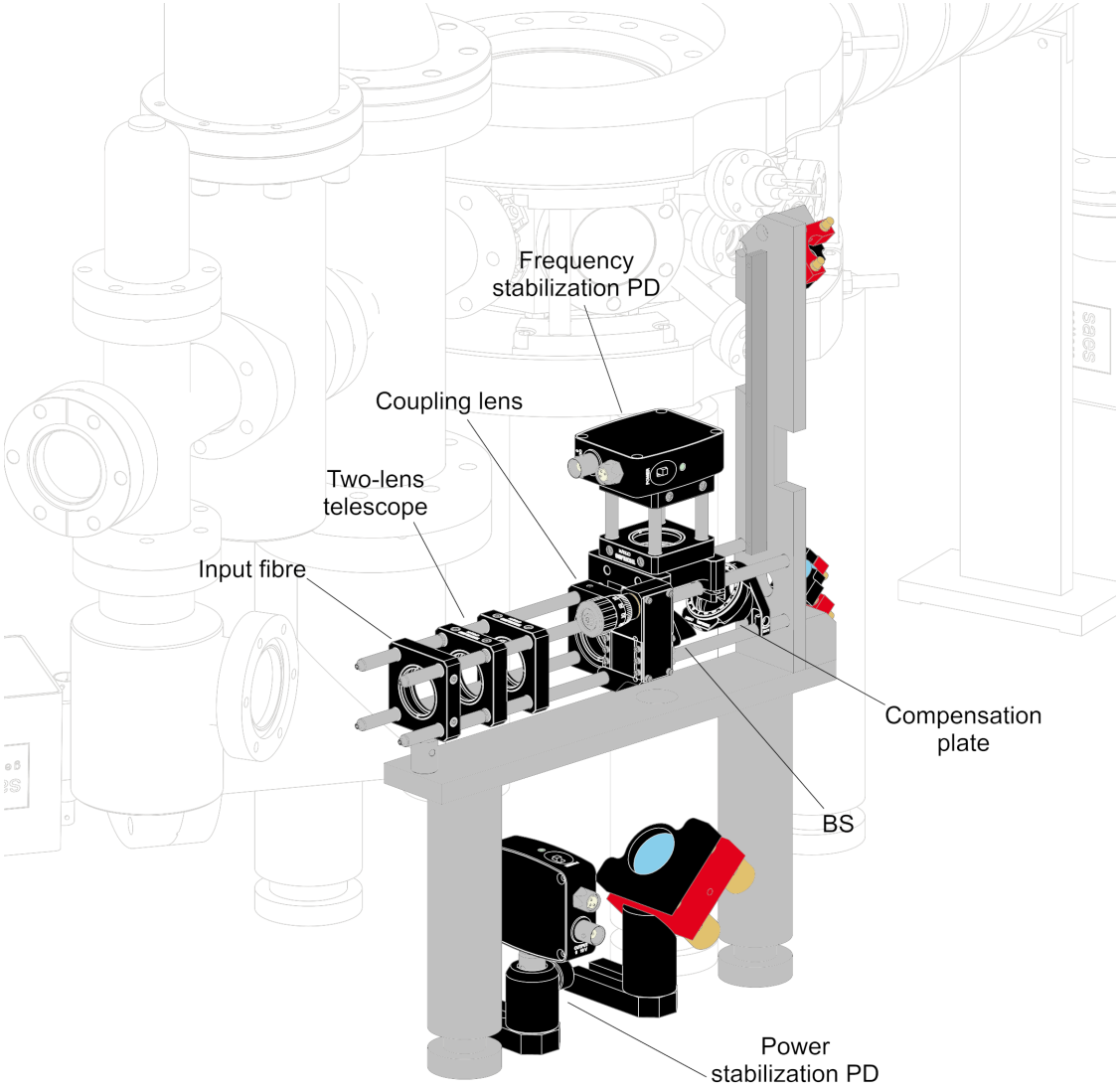


Figure 4.5: 3D CAD view of the optomechanics used for coupling light to the lithium optical resonator. Optics and fibre launcher are not shown.

The best-fit decay time and the derived cavity linewidth are

$$\tau_c = 2.025(6)\,\mu\text{s}\,, \qquad \delta\nu = 78.6(2)\,\text{kHz}\,.$$

From this value the cavity losses, which are mostly caused by mirror losses, and the cavity finesse result

$$\gamma_c = 108.7(3)\ \text{ppm}\,, \qquad \mathcal{F} = 28\,800(80)\,.$$

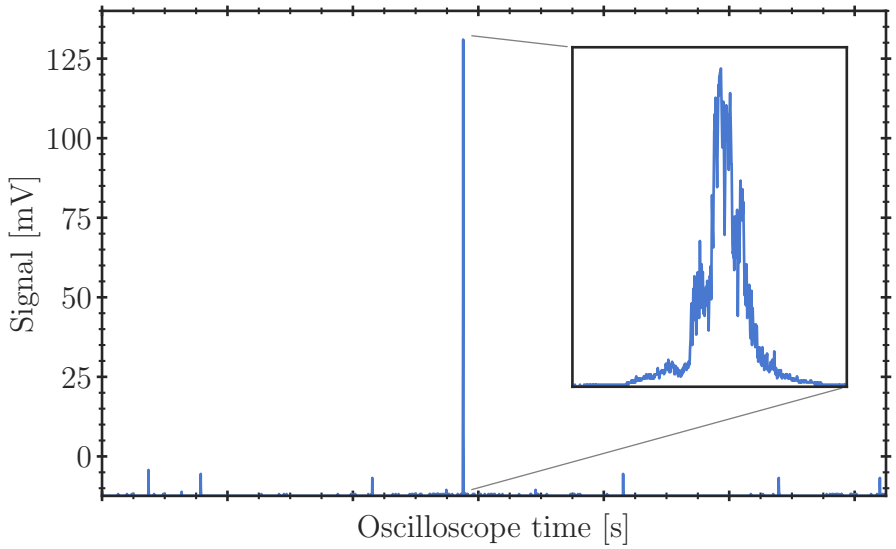


Figure 4.6: Cavity transmission spectrum measured using 671 nm laser light. The spectrum scans a full FSR but has been centred on the $TEM_{00}$ peak, so repeated peaks are not observed. Inset shows a zoom on the central peak.

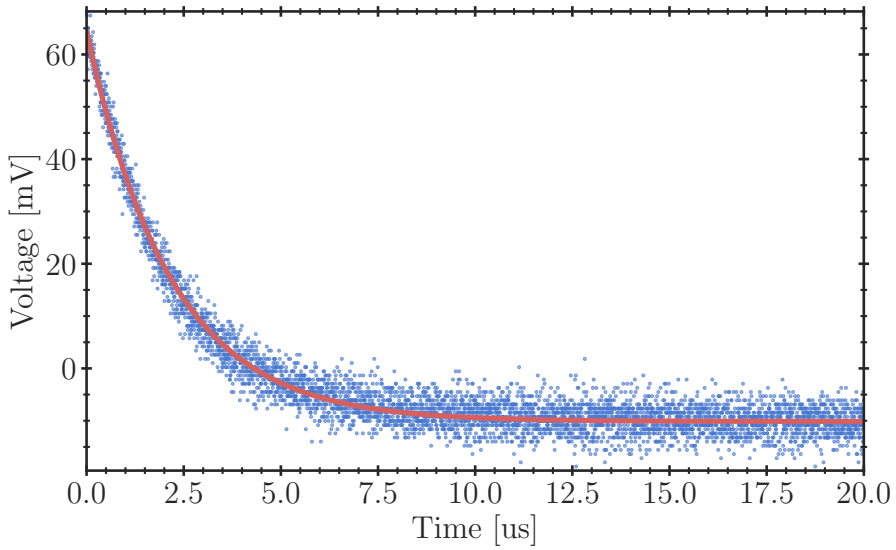


Figure 4.7: Cavity energy decay measured with ring-down method. Red curve is the best-fit for model in eq. (4.3).

## 4.3 903nm laser linewidth

When coupling light to a high-finesse cavity, if the laser linewidth is larger than the cavity linewidth, only a small portion of the laser power will be coupled to the resonator, therefore, a narrow laser is required to reach high coupling efficiencies. Moreover, fluctuations in the laser frequency will lead to fluctuations of the intra-cavity field intensity. If this field is used to trap atoms, the intensity fluctuations may cause parametric heating and atoms loss. Thus, laser frequency stabilization techniques play a pivotal role in atomic physics experiments. Throughout this section a basic familiarity with control theory terminology is assumed, in-depth explanations can be found in [185, 186].

The 903 nm laser used to couple to the lithium high-finesse resonator is a custom-made ECDL where a diffraction grating, mounted on a Piezoelectric Transducer (PZT)-actuated flexure-hinge, is used to select and tune the laser wavelength, a setup known as Littrow configuration [187]. A detailed description of this laser system can be found in [156]. If the intra-cavity field is to be stable, the laser linewidth measured for times longer than the cavity characteristic time $\tau_c$ should be much smaller than the cavity linewidth (a factor of 10 smaller is a good starting point). Fluctuations that occur faster than $\tau_c$ will be suppressed and will contribute little to fluctuations of intensity in the intra-cavity field. Given the characterization reported in section 4.2.2, a laser linewidth of approximately 10 kHz is a good starting point to ensure good coupling.

Laser frequency stabilization techniques work by determining a so-called *error signal*, an electronic signal which is proportional to frequency fluctuations of the laser. This signal is then used in a feedback control loop that acts on the current or on the PZT of the ECDL to keep the frequency stable. Generally, the PZT modulation is capable of correcting only the slow fluctuations associated with changes in the laser central frequency. To achieve proper linewidth narrowing, a fast correction of the laser frequency is needed, this can be realized by applying a modulation on the laser diode current. These techniques require a stable frequency reference, which is usually supplied by a stable Fabry-Perot resonator. Several methods exist to measure the distance between the laser central frequency and the cavity resonance:

- **Side-of-fringe locking**: the side of the cavity transmission peak is used to convert frequency fluctuations in intensity fluctuations. This is the simplest method for frequency stabilization and requires the least optical components. Unfortunately, this method is unable to distinguish between frequency and power fluctuations, since both lead to a change in the transmitted power.

- **Polarization spectroscopy** [188]: a linear polarizer placed inside the reference cavity is used to rotate the laser polarization, such that the polarization state is frequency dependent. Although technically complex, this method

does not require modulating the laser frequency and is independent of power fluctuations.

- **Pound-Drever-Hall technique** [189]: the beat between the leaking intra-cavity field and the power reflected from the cavity is used to determine the error signal. This method is insensitive to power fluctuations, but requires the laser frequency to be modulated to introduce sidebands. Generally, this is the most commonly used method.

At the $Ba^{+}Li$ experiment, the 903 nm laser is stabilized against an ultra-stable cavity which has a finesse of approximately 2000 and a linewidth of approximately 1 MHz, using the PDH technique. To narrow the laser linewidth down to 10 kHz, an appropriate feedback loop has to be designed. Doing so requires the characterization of the free-running laser frequency noise spectrum and, from this characterization, the parameters of an analogue PID controller used in the feedback loop can be determined.

### Pound-Drever-Hall frequency stabilization technique

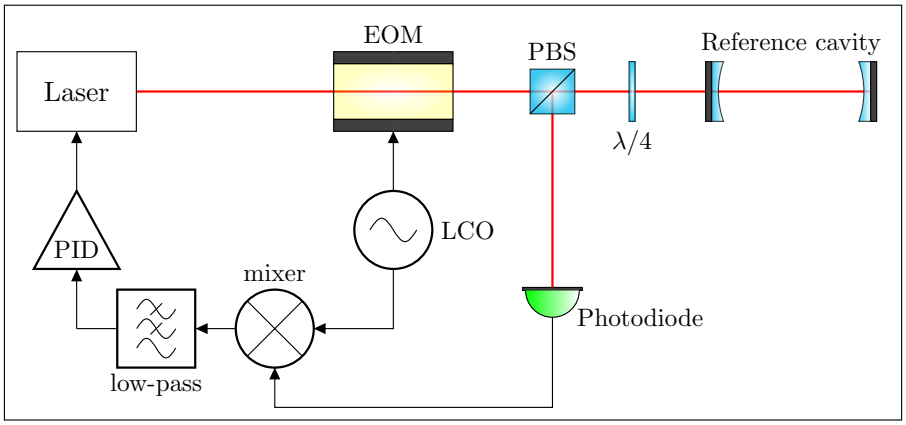


Figure 4.8: Schematic drawing of the setup for PDH stabilization.

Figure 4.8 shows a possible setup for implementing the PDH technique [189]. A laser is modulated by a frequency modulator, *e.g.* an EOM, which introduced sidebands in the laser spectrum. When the laser central frequency is at resonance with the cavity mode the two sidebands are totally reflected, while the carrier will be transmitted and will build up an intra-cavity standing-wave. The reflected sidebands and the leakage field from the cavity are sampled by a PBS and their beat signal is measured by a photodiode. This signal is then demodulated using the lock-in technique to obtain an asymmetric error signal, this signal can then be fed to a PID controller connected to the laser actuators.

As explained in section 3.2.3, after the modulation the laser can be described as the sum of three components

$$\frac{\mathcal{E}}{\mathcal{E}_0} \approx J_0 e^{i\omega t} + J_1\left(e^{i(\omega+\omega_m)t} - e^{i(\omega-\omega)t}\right),$$

here written using phasors notation, with $J_i$ being the i-th Bessel function, and $\omega_m$ is the modulation frequency. The cavity transfer function for the reflected field can be written as

$$R(\omega) = \frac{\mathcal{E}_r}{\mathcal{E}_0} = \frac{-r_1 + (r_1^2 + t_1^2) r_2 e^{i\omega/\nu_{\mathrm{FSR}}}}{1 - r_1 r_2 e^{i\omega/\nu_{\mathrm{FSR}}}},$$

where $\mathcal{E}_r$ is the reflected electric field, $r_1, r_2, t_1, t_2$ are the reflectance and transmittance of the first and second mirror[3] of the Fabry-Perot, respectively, and $\nu_{\mathrm{FSR}}$ is the cavity FSR. Thus, the reflected field from the cavity is

$$\begin{aligned}\mathcal{E}_r &= \sum_k R(\omega_k)\mathcal{E}(\omega_k) \\ &= \mathcal{E}_0\Big[R(\omega)J_0 e^{i\omega t} + J_1\Big(R(\omega+\omega_m)e^{i(\omega+\omega_m)t} - R(\omega-\omega_m)e^{i(\omega-\omega_m)t}\Big)\Big].\end{aligned}$$

The reflected power is

$$\begin{aligned}P_r = \mathcal{E}_r\mathcal{E}_r^* \approx\ & P_c|R(\omega)|^2 + P_s\Big[|R(\omega+\omega_m)|^2 + |R(\omega-\omega_m)|^2\Big] \\ & + 2\sqrt{P_c P_s}[\mathrm{Re}\{X(\omega)\}\cos(\omega_m t) + \mathrm{Im}\{X(\omega)\}\sin(\omega_m t)],\end{aligned} \tag{4.5}$$

where $X(\omega) = R(\omega)R^*(\omega+\omega_m) - R^*(\omega)R(\omega-\omega_m)$ is the ultimate quantity of interest, $P_c = |J_0|^2 P_0$, $P_s = |J_1|^2 P_0$ and $P_0 = \mathcal{E}_0^2$ are the carrier, sideband and input powers, respectively. It is interesting to notice from eq. (4.5) that the imaginary and real parts of the signal $X(\omega)$ are modulated at the same frequency of the laser modulation $\omega_m$ but are 90° out of phase. If the modulation frequency is much larger than the cavity linewidth then the sidebands are totally reflected and $R(\omega \pm \omega_m) \approx -1$, and the error signal $\epsilon$ after the lock-in demodulation is

$$\epsilon \approx -2\sqrt{P_c P_s}\,\mathrm{Im}\{X(\omega)\} = -2\sqrt{P_c P_s}\,\frac{rt^2\sin(\omega/\nu_{\mathrm{FSR}})}{\left(1 - r^2\cos(\omega/\nu_{\mathrm{FSR}})\right)^2 - r^4\sin^2(\omega/\nu_{\mathrm{FSR}})},$$

where $r_1 = r_2 = r$ and $t_1 = t_2 = t$ is assumed. Since the laser central frequency is near resonance $\omega/\nu_{\mathrm{FSR}} \approx 2\pi q + \delta\omega/\nu_{\mathrm{FSR}}$, where $q \in \mathbb{Z}$ and $\delta\omega$ is the (small) frequency fluctuation of the laser. The error signal then is

$$\epsilon \approx -2\sqrt{P_c P_s}\,\frac{rt^2}{(1-r^2)^2}\frac{\delta\omega}{\nu_{\mathrm{FSR}}} \approx -2\sqrt{P_c P_s}\,\frac{r}{1-r^2}\frac{\delta\omega}{\nu_{\mathrm{FSR}}},$$

[3]Here the first (1) mirror is assumed to be the input mirror of the cavity.

introducing the cavity finesse $\mathcal{F} \approx \pi r/(1-r^2)$ and the cavity linewidth $\delta\nu = \nu_{\mathrm{FSR}}/\mathcal{F}$, the error signal finally is

$$\epsilon \approx -2\sqrt{P_c P_s}\,\frac{1}{\pi}\frac{\delta\omega}{\delta\nu} = D\delta\omega\,,$$

where $D = -2\sqrt{P_c P_s}/(\pi\delta\nu)$ is the so called *frequency discriminator*.

The frequency discriminator in part determines the gain of the feedback loop and, ideally, the higher the value of $D$ the easier it is for the feedback loop to suppress small frequency fluctuations [170]. Decreasing the cavity linewidth by, for example, increasing its finesse is a good way to increase $D$. But a reduced cavity linewidth implies that the frequency range where the cavity can act as a discriminator is also reduced, thus, limiting the *lock range*, that is the range of frequencies where the feedback loop can stabilize the laser. Since the discriminator is dependent on both the cavity length (through $\delta\nu$) and the sideband power, the overall performance of the feedback loop will be sensitive to fluctuations in those two parameters.

### Determining the servo loop parameters

Designing the control loop implies determining several parameters such as the loop bandwidth and gain, the photodiode bandwidth, the sideband modulation frequency and the overall cavity geometry. Although some parameters can be measured or determined experimentally, most will have to be decided with an educated guess depending on the specific application.

The PID required bandwidth can be determined experimentally from a measurement of the laser noise Power Spectral Density (PSD) [190]. The PSD is a measurement of the power distribution in each frequency component of a signal, and it is related to the squared absolute value of the Fourier transform of the signal. According to the theory of frequency modulation, the noise PSD spectrum can be divided into two regions depending on whether it is above or below the so-called $\beta$-line defined as $y = 8\ln(2)f/\pi^2$, where $f$ is the frequency of the signal components. The region of the PSD above the $\beta$-line will contribute to the laser linewidth, the larger the noise power in this region the larger the laser linewidth. Conversely, the region of the spectrum below this line will only contribute to the tails of the laser lineshape. Experimentally, the noise PSD is determined by either measuring the error signal[4] $\epsilon$ and performing numeric signal processing or by feeding it directly to a spectrum analyser. Once the noise PSD is known, it is compared with the $\beta$-line, the point where the two curves meet determines the minimum bandwidth required for the feedback loop.

[4]During this procedure the laser has to kept on the cavity resonance either "by-hand" or by acting on the slow actuator with a temporary feedback loop.

The residual PSD above the $\beta$-line after the lock is completed will determine the locked-laser linewidth. To further reduce frequency noise, one can attempt to suppress other noise sources. As mentioned, the PDH technique is sensitive to fluctuations in the cavity length and sideband power. The former can be reduced by using a non-scanning (fixed) temperature-stabilized cavity, while the latter can be controlled by increasing the modulation frequency and using low-noise RF generators. Like in any feedback loop, noise introduced by actuators and sensors (in this case the photodiode) will be indistinguishable from frequency fluctuations, thus low-noise electronics should be used for all the elements of the loop. Generally, larger loop gain will lead, especially in the low-frequency region of the spectrum, to lower residual noise.

Cavity linewidth, modulation frequency and photodiode bandwidth are strictly interlinked. Concerning the cavity linewidth, since commercial lasers can have a sub-MHz free-running linewidth[5] it is convenient to utilize a cavity with a sub-MHz linewidth if one wishes to reduce the laser linewidth even further. The sideband modulation frequency should be much larger than the cavity linewidth, thus RFs are commonly employed. Since the photodiode has to be able to measure a signal that oscillates at the sideband modulation frequency, its bandwidth should be large enough to detect the beat signal.

### 4.3.1 Characterization of the 903 nm laser

In order to measure the laser frequency noise PSD a sensor capable of measuring frequency fluctuations is required, generally this is achieved by using a cavity as a frequency-to-power transducer and a photodiode. Since a cavity has a characteristic response time $\tau_c$, all frequency fluctuations that occur faster than $\tau_c$ are filtered, that is the cavity corresponds to a low-pass filter in frequency space with a cut-off frequency equal to the cavity linewidth. Therefore, it is important to perform the noise PSD measurement on a low-finesse cavity, so that its cutoff frequency is higher than the cutoff frequency of the laser diode, which is commonly of the order of MHz [191].

To characterize the 903 nm laser, a low-finesse cavity was built using, as a temporary support, the central piece of the lithium optical resonator presented in section 4.2. This cavity is formed by a flat and a curved (RoC = 300 mm) concave mirrors placed at a distance of approximately 40 mm. These mirrors have a relatively low reflectivity ($\approx 0.9955$), thus, the cavity linewidth of a few MHz is expected. This cavity was characterized using the 671 nm laser of the lithium optical setup, assuming that the laser is monochromatic[6]. Under the assumption

[5] Toptica, commercial material.

[6] Since the laser has a declared free-running linewidth $\leq 100$ kHz, this approximation is justified.

that the laser is monochromatic, the cavity linewidth can be estimated directly from a measurement of the resonance spectrum, the resulting value for linewidth and finesse are

$$\delta\nu \approx 5\,\mathrm{MHz}\,, \qquad \mathcal{F} \approx 700\ .$$

Although the finesse of a cavity is best determined with a ring-down measurement, at these linewidth values the decay times is of the order of a few tens of nanoseconds, making it quite difficult to record the energy decay of the cavity.

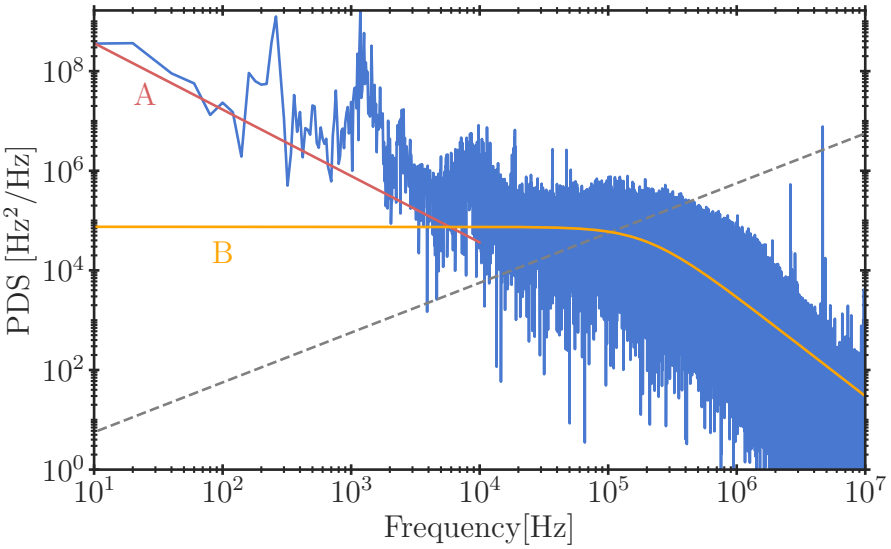


Figure 4.9: 903 nm laser frequency noise PSD computed from a 1 s long measurement of the PDH error signal. $\beta$-line is indicated by the grey line. Traces A and B represent the most common sources of noise in semiconductor lasers: $1/f$ noise (A) and thermal noise (B).

The 903 nm laser was kept at resonance with the low-finesse cavity by stabilizing its frequency using a feedback loop acting on the ECDL piezoelectric. This feedback loop reduces the low-frequency ($< 1\,\mathrm{kHz}$) noise but it is insufficient to narrow the laser linewidth and still allows to measure the PSD at frequencies above the lock bandwidth (1 kHz). Figure 4.9 shows the PSD computed numerically[7] from a long-time (1 s) measurement of the PDH error signal. In this frequency range, the PSD curve can be interpreted as the sum of two major contributions: an $1/f$ flicker noise at ultra low frequencies (trace A) and an additional thermal noise contribution (trace B) [192], which, in this case, presents a cutoff frequency at approximately $2 \times 10^5$ Hz. Since the frequency cutoff points in the noise PSD give a clue at the expected frequency response of the laser diode, a control loop with a bandwidth

[7]Function *periodogram* from the sciPy library.

higher than $2 \times 10^5$ Hz may incur in self-oscillations. The intersection between the PSD curve and the $\beta$-line (dashed grey line) is located at approximately $1 \times 10^5$ Hz, meaning that a fast lock PID with a bandwidth of at least 100 kHz is required to narrow the laser linewidth.

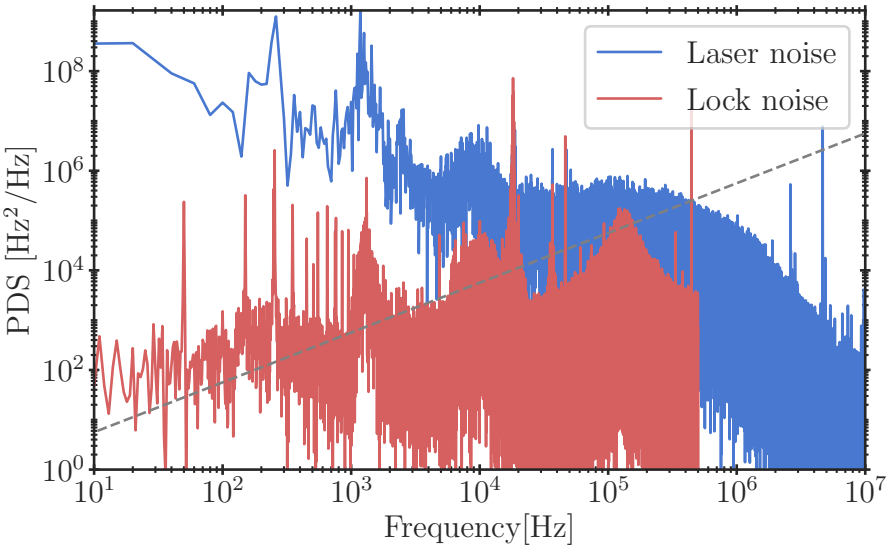


Figure 4.10: Frequency noise PSD computed from a 1 s long measurement of the PDH error signal. $\beta$-line is indicated by the grey line. The red curve is the noise PSD after the lock is performed, while the blue curve is the same as in fig. 4.9.

To test these conclusions, a commercially available PID[8] was temporarily used to lock the 903 nm laser to an ultra-stable cavity. Figure 4.10 shows the noise PSD with the feedback loop active. From this spectrum, the locked laser linewidth can be estimated as [190]

$$\text{FWHM} = \sqrt{8 \log(2) A},$$

where $A$ is the integral of the frequency noise spectrum in the region where such spectrum is above the $\beta$-line. The resulting laser linewidth is 47 kHz. Although the frequency noise is considerably reduced, the majority of the spectrum is still above the $\beta$-line suggesting that more gain or electronics with lower residual noise are needed to narrow the laser linewidth further.

At the moment of writing, a new custom-made PID is being designed with the aim of reaching a locked laser linewidth of 10 kHz. An ideal feedback loop for frequency stabilization should be composed of two PIDs fed by the same error signal: a fast PID working on the full required bandwidth acting on the fast modulation port of the laser, and a slow proportional-integral control (derivative component

[8] Toptica, FALC110

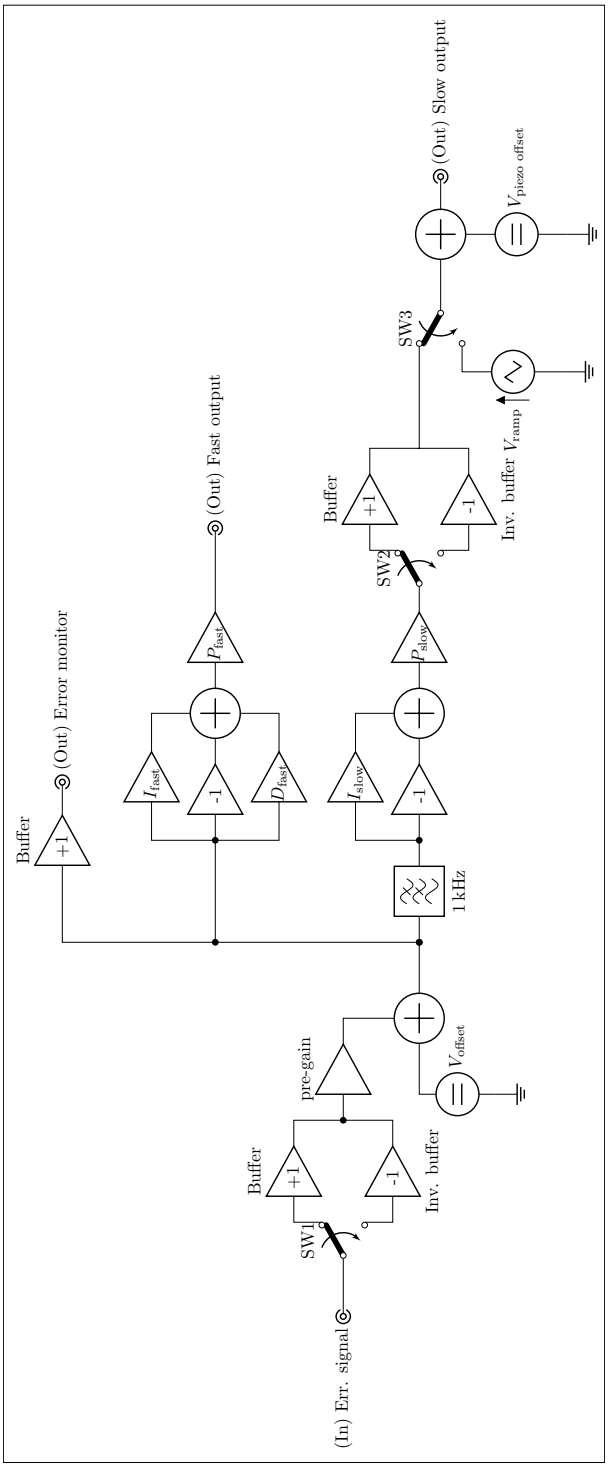


Figure 4.11: PID topology for laser frequency stabilization.

usually is not needed) limited to approximately 1 kHz bandwidth acting on the slow modulation port of the laser. The fast integrator should have a DC roll-off at 1 kHz where the slow PID takes over. Figure 4.11 shows a possible PID topology for the laser frequency stabilization. In fig. 4.11 the two PIDs are shown in non-interacting configuration, that is the overall gain is controlled by the proportional term placed after the derivative and integral terms. It should also be possible to switch the slow PID for a ramp generator with controllable amplitude, so that while the laser piezoelectric is swept across resonance the fast lock can be tested.

# Chapter 5

# Single photon sideband cooling in state-dependent potentials

In this chapter a novel scheme for cooling particles confined in optical potentials is presented. A mathematical model describing the vibrational state of motion of particles trapped in state-dependent non-harmonic optical potentials is developed and used to study different atomic species. An efficient cooling method is proposed to reduce the particle's energy by exciting its motional sidebands.

In section 5.1 an overview of sideband cooling in state-dependent optical potentials is presented. The mathematical model is described in section 5.2. Starting from *ab initio* considerations a master rate equation governing the occupation probabilities of the trap bound levels is obtained. In section 5.3 a numeric solution for sideband cooling of a Two-Level System (TLS) trapped in optical tweezers is presented. In section 5.4 the model is used to study cooling of Li atoms trapped in a cavity-enhanced optical lattice. The cavity parameters are chosen to be the same of the high-finesse optical resonator installed in the MOT chamber presented in chapter 4.

Part of the work presented in this chapter was published in ref. [193].

## 5.1 Sideband cooling in optical potentials

An overview of sideband cooling for particles trapped in harmonic potentials and the assumptions behind that model were presented in section 2.1.5. These assumptions are seldom verified when describing particles trapped in optical potentials. First, optical potentials are rarely deep enough to be well approximated as harmonic. Therefore, the actual shape of the trap has to be taken into account. Second, the potential depth generated by a light field is proportional to the atomic polarizability $\alpha(\omega)$, where $\omega$ is the light field frequency. Generally, different electronic configurations of the atom have a different polarizability response, in practice

the potential experienced by the atom in its internal ground state can be different from the potential experienced when it is in its internal excited state. In this case one refers to the optical trap as being *state-dependent*.

To avoid the issue of working in state-dependent potentials, it is possible to make use of traps operating at the so-called "magic" wavelengths. These are wavelength values for which the polarizabilities of the ground ($\alpha_g(\omega)$) and excited ($\alpha_e(\omega)$) states involved in the cooling transition are equal. Unfortunately, for many atomic species the exact values of the magic wavelengths are either not precisely determined or experimentally difficult to achieve. A second option is performing sideband cooling using two-photon Raman transitions. With this method the levels used for cooling can be two sublevels (*e.g.* hyperfine or Zeeman) of the electronic ground state manifold [194] that experience the same trapping potential. Even so, being able to perform single photon sideband cooling remains an attractive proposition as the method is in principle faster (higher scattering rate) and technically simpler (only one laser light is needed).

A semiclassical model for sideband cooling of a TLS in a state-dependent harmonic potential was developed by ref. [195]. The authors conclude that cooling occurs mainly via the difference in the potential energy accumulated during the motion by a particle in the internal ground or excited state, *i.e.* a "Sisyphus-like" effect that is independent of the momentum transfer between the particle and the photons. Cooling is shown to occur only under the condition of $\alpha_g \leq \alpha_e$, while heating is predicted in the opposite case $\alpha_g > \alpha_e$.

However, a recent experimental study [196] observed that, in the case of $\alpha_g > \alpha_e$, cooling is still possible using a laser blue detuned with respect to the free atom transition frequency. The blue detuned laser acts as a "Sisyphus cap", *i.e.* a particle is resonant with the cooling transition only when it has potential energy $E_{\text{cap}}$. As a result, a particle with energy $E \leq E_{\text{cap}}$ is cooled until is not resonant with the cooling laser, and a particle with $E > E_{\text{cap}}$ is heated up and eventually lost from the trap. Effectively, the "Sisyphus-like" effect observed is acting as a repeller, *i.e.* when the particle energy is close to a certain critical value it is pushed to either higher or lower energies.

This interpretation suggests a new method for cooling particles to low vibrational states: if the position of the "Sisyphus cap" could be precisely controlled (by controlling the detuning of the cooling laser), it would be possible to gently "push" the particles' energy toward the ground state of motion while minimizing the particle loss. To this end, a mathematical model describing the vibrational state of trapped particles must be developed taking into account the optical potential shape, the difference in polarizability between ground and excited states as well as the time dependence of the cooling laser detuning.

## 5.2 1D mathematical model

### 5.2.1 System Hamiltonian

In order to develop the mathematical description of sideband cooling for state-dependent traps a TLS having linewidth $\gamma$, mass $m$, ground state $|g\rangle$, and excited state $|e\rangle$ is considered. The TLS is trapped in a constant non-harmonic potential $V$ with a state-dependent depth $V_{\mathrm{T},j}$, where $j = g, e$ indicates the ground and the excited internal state of the particle, respectively. The only constraint posed on the potential $V$ is that it's a continuos and differentiable function of space, *i.e.* it is a physically realizable potential.

The TLS is coupled to the cooling laser, which has an electric field

$$\boldsymbol{\mathcal{E}}_{\mathrm{c}} = \boldsymbol{\epsilon}\, \mathcal{E}_0^{(\mathrm{c})} \cos(\mathbf{k}_{\mathrm{c}} \cdot \mathbf{r} - \omega_{\mathrm{c}} t)\,,$$

where $\boldsymbol{\epsilon}$ is the light polarization, $\mathcal{E}_0^{(\mathrm{c})}$ the field amplitude, $\mathbf{k}_{\mathrm{c}}$ the laser wavevector, $\mathbf{r}$ is the spatial coordinate, and $\omega_{\mathrm{c}}$ the laser pulsation. The problem of a particle interacting with an external electromagnetic field can be treated — in the dipole approximation — with two complementary approaches: the so-called *minimal coupling* approach (ref. [60], chapter 11), which consists in substituting the particle momentum $\mathbf{p}$ with $\mathbf{p} - (e/c)\mathbf{A}$, $\mathbf{A}$ being the magnetic vector potential. The second approach is called the *direct coupling* approach, it consists in introducing a perturbation Hamiltonian $H' = -\mathbf{d}\cdot\boldsymbol{\mathcal{E}}$, where $\mathbf{d}$ is the particle's dipole momentum and $\boldsymbol{\mathcal{E}}$ is the electric field. If the electromagnetic field is treated as an external, non-dynamic quantity then the two approaches have been demonstrated to be mathematically equivalent [197]. In direct coupling formalism, the system Hamiltonian is written as

$$H = H_0 + V - \mathbf{d}\cdot\boldsymbol{\mathcal{E}}_{\mathrm{c}} = H_0 + V + H'\,, \tag{5.1}$$

where $H_0$ represents the Hamiltonian of the unperturbed TLS. To describe the reduction of kinetic energy of the bound particle, it is convenient to transition to the occupation number representation of eq. (5.1) by introducing the number states $|g, n_g\rangle$ and $|e, m_e\rangle$, where $g$ ($e$) indicates the ground (excited) internal state of the TLS. These states indicate the number of vibrational quanta possessed by the TLS in the internal ground or excited state. Notably, $|n_g\rangle$ and $|m_e\rangle$ are associated with different wavefunctions, since we consider state-dependent potentials.

The complete Fock space is the tensor product of the two subspaces $\{|g, n_g\rangle\} \otimes \{|e, m_e\rangle\}$. For each subspace two different creation and annihilation operators must be introduced: $\hat{b}^\dagger_{n_g}$ ($\hat{b}^\dagger_{m_e}$) and $\hat{b}_{n_g}$ ($\hat{b}_{m_e}$) are the creation and annihilation operators for a vibrational quantum in the spectrum $\{|g, n_g\rangle\}$ ($\{|e, m_e\rangle\}$). All operators follow a bosonic algebra. With these definitions the second-quantization form of

one-particle $\hat{O}(1)$ and two-particle $\hat{O}(2)$ operators is given by (ref. [198], chapter 1)

$$\hat{O}^{(\mathrm{SQ})}(1) = \sum_{i,j} \langle i|\hat{O}(1)|j\rangle \ \hat{b}_i^\dagger \, \hat{b}_j \, ,$$
$$\hat{O}^{(\mathrm{SQ})}(2) = \sum_{i,j} \sum_{i',j'} \langle i,j|\hat{O}(2)|i',j'\rangle \ \hat{b}_i^\dagger \, \hat{b}_j^\dagger \hat{b}_{i'} \, \hat{b}_{j'} \, ,$$

where the indices $i, i', j, j'$ run over all possible states $\{|g, n_g\rangle\}$ and $\{|e, m_e\rangle\}$. The products $\hat{b}_i^\dagger \, \hat{b}_j$ can be more conveniently written as the projectors $\hat{P}_{j\to i} = |i\rangle \langle j|$.

In second-quantization form, the first term appearing in eq. (5.1) is

$$\begin{aligned} H_0 &= \sum_{n_g,n_g'} \left\langle g, n_g \middle| H_0 \middle| g, n_g' \right\rangle \ |g, n_g\rangle \left\langle g, n_g' \right| + \sum_{m_e,m_e'} \langle e, m_e|H_0|e, m_e'\rangle \ |e, m_e\rangle \langle e, m_e'| \\ &= \sum_{n_g,n_g'} E_g \delta_{n_g,n_g'} \ |g, n_g\rangle \left\langle g, n_g' \right| + \sum_{m_e,m_e'} E_e \delta_{m_e,m_e'} \ |e, m_e\rangle \langle e, m_e'| \\ &= E_g \, |g, n_g\rangle \langle g, n_g| + E_e \, |e, m_e\rangle \langle e, m_e| \ , \end{aligned} \tag{5.2}$$

where $E_g$ and $E_e$ represent the energies of the TLS internal states. Diagonal terms are not considered since it is assumed that $H_0$ is diagonal in the $|g\rangle \, , |e\rangle$ basis. The second term of eq. (5.1) is

$$\begin{aligned} V &= \sum_{n_g,n_g'} \left\langle g, n_g \middle| V \middle| g, n_g' \right\rangle \ |g, n_g\rangle \left\langle g, n_g' \right| + \sum_{m_e,m_e'} \langle e, m_e|V|e, m_e'\rangle \ |e, m_e\rangle \langle e, m_e'| \\ &= \sum_{n_g,n_g'} E_{n_g} \delta_{n_g,n_g'} \ |g, n_g\rangle \left\langle g, n_g' \right| + \sum_{m_e,m_e'} E_{m_e'} \delta_{m_e,m_e'} \ |e, m_e\rangle \langle e, m_e'| \\ &= E_{n_g} \, |g, n_g\rangle \langle g, n_g| + E_{m_e} \, |e, m_e\rangle \langle e, m_e| \ , \end{aligned} \tag{5.3}$$

where $E_{n_g}$ and $E_{m_e}$ represent the energies of the bound levels of the potential experienced by the TLS in its internal ground and excited states of the TLS. Again, $V$ is assumed to be diagonal in the $|n_g\rangle \, , |m_e\rangle$ basis, thus off-diagonal terms are not considered. The sums of terms in eqs. (5.2) and (5.3) can be conveniently written as

$$H_0 + V = E_{g,n_g} \, |g, n_g\rangle \langle g, n_g| + E_{e,m_e} \, |e, m_e\rangle \langle e, m_e|$$

where $E_{g,n_g} = E_g + E_{n_g}$ and $E_{e,m_e} = E_e + E_{m_e}$. Lastly, the coupling term of eq. (5.1) is

$$H' = \sum_{n_g,m_e} \langle e, m_e|H'|g, n_g\rangle \ |e, m_e\rangle \langle g, n_g| + \sum_{n_g,m_e} \langle g, n_g|H'|e, m_e\rangle \ |g, n_g\rangle \langle e, m_e| \ ,$$

where only the non-diagonal terms have been kept since $\langle i|\mathbf{d}|i\rangle = 0$, $i = g, e$. The matrix elements are given by

$$\begin{aligned}\langle e, m_e|-\mathbf{d}\cdot\boldsymbol{\mathcal{E}}_{\mathrm{c}}|g, m_g\rangle &= \frac{e_0}{2}\left\langle e, m_e\middle|\mathbf{r}\cdot\boldsymbol{\epsilon}\,\mathcal{E}_0^{(\mathrm{c})}\left(e^{i(\mathbf{k}_{\mathrm{c}}\cdot\mathbf{r}-\omega_{\mathrm{c}}t)}+e^{-i(\mathbf{k}_{\mathrm{c}}\cdot\mathbf{r}-\omega_{\mathrm{c}}t)}\right)\middle|g, m_g\right\rangle \\ &= \frac{\hbar\Omega}{2}\Big[\,\langle m_e|e^{i\mathbf{k}_{\mathrm{c}}\cdot\mathbf{r}}|n_g\rangle\, e^{-i\omega_{\mathrm{c}}t}+\,\langle m_e|e^{-i\mathbf{k}_{\mathrm{c}}\cdot\mathbf{r}}|n_g\rangle\, e^{i\omega_{\mathrm{c}}t}\Big]\,,\end{aligned} \tag{5.4}$$

where $\mathbf{d} = -e_0\mathbf{r}$, $\Omega = e_0\mathcal{E}_0/\hbar\,\langle e|\mathbf{r}\cdot\boldsymbol{\epsilon}|g\rangle$ is the Rabi frequency, and $e_0$ is the signless elementary electric charge. The exponential terms $e^{\pm i\mathbf{k}_{\mathrm{c}}\cdot\mathbf{r}}$ has been approximated as 1 in the integration over $|g\rangle$ and $|e\rangle$, this can be justified by considering that most atomic wavefunctions are confined to just a few nm, while visible and near UV light — commonly used to manipulate atoms — has a wavelength of a few hundreds nm, thus $\mathbf{k}_{\mathrm{c}}\cdot\mathbf{r} \ll 1$. The same approximation cannot be applied in the terms $\langle m_e|e^{-i\mathbf{k}_{\mathrm{c}}\cdot\mathbf{r}}|n_g\rangle$ since these are bound states wavefunction the dimension of which is determined by the potential geometry, which is comparable with the light wavelength. In order to eliminate the time dependency from the interaction Hamiltonian $H'$, the RWA is used to remove the terms oscillating as $e^{i\omega_{\mathrm{c}}t}$ in eq. (5.4), leading to

$$\begin{aligned}H' &= \frac{\hbar\Omega}{2}\left(\sum_{n_g,m_e} M_{n_g,m_e}\,e^{-i\omega_{\mathrm{c}}t}\,|e, m_e\rangle\,\langle g, n_g| + \sum_{n_g,m_e} M^*_{n_g,m_e}\,e^{+i\omega_{\mathrm{c}}t}\,|g, n_g\rangle\,\langle e, m_e|\right) \\ &= \frac{\hbar\Omega}{2}\sum_{n_g,m_e}\left(M_{n_g,m_e}\,e^{-i\omega_{\mathrm{c}}t}\,|e, m_e\rangle\,\langle g, n_g| + M^*_{n_g,m_e}\,e^{+i\omega_{\mathrm{c}}t}\,|g, n_g\rangle\,\langle e, m_e|\right),\end{aligned}$$

with $M_{n_g,m_e} = \langle m_e|e^{i\mathbf{k}_{\mathrm{c}}\cdot\mathbf{r}}|n_g\rangle$. Then, a transformation to a frame of reference rotating at the same frequency $\omega_{\mathrm{c}}$ as the laser is performed (further mathematical details on the RWA and the rotating frame transformation are given in appendix C). The final form of the interaction Hamiltonian is

$$\begin{aligned}H' =& \frac{\hbar\Omega}{2}\sum_{n_g,m_e}\left(M_{n_g,m_e}\,|e, m_e\rangle\,\langle g, n_g| + M^*_{n_g,m_e}\,|g, n_g\rangle\,\langle e, m_e|\right) \\ &+ \frac{\hbar\omega_{\mathrm{c}}}{2}\left(\sum_{n_g}|g, n_g\rangle\,\langle g, n_g| - \sum_{m_e}|e, m_e\rangle\,\langle e, m_e|\right),\end{aligned}$$

The fully quantized Hamiltonian is then written as

$$\begin{aligned}H =& \sum_{n_g}\left(E_{g,n_g}+\frac{\hbar\omega_c}{2}\right)|g, n_g\rangle\langle g, n_g| + \\ &+ \sum_{m_e}\left(E_{e,m_e}-\frac{\hbar\omega_c}{2}\right)|e, m_e\rangle\langle e, m_e| + \\ &+ \frac{\hbar\Omega}{2}\sum_{n_g,m_e}\left[M_{m_e,n_g}|g, n_g\rangle\langle e, m_e| + M^*_{m_e,n_g}|e, m_e\rangle\langle g, n_g|\right].\end{aligned} \tag{5.5}$$

An implicit approximation has been introduced when performing the transformation to a rotating frame of reference: the transformation has been performed by assuming the system is a TLS, effectively by modifying only the wavefunction related to the $|g\rangle$ and $|e\rangle$ states. In fact — due to the presence of the bound levels — it is a multi-level system and the rotating frame transformation should take into account the complete wavefunctions $\{|g, n_g\rangle\}$ and $\{|e, m_e\rangle\}$. In principle, it is possible to perform the rotating frame transformation using a more complex rotation matrix [199]. However, the transformation can still be performed approximating the system as a TLS as long as the energy difference $E_{g,n_g+1} - E_{g,n_g}$ remains small compared to $E_e - E_g$, in other words if the trap frequencies are small compared to the resonant laser frequency.

### 5.2.2 Spontaneous emission and master rate equation

In order to take into account the spontaneous emission, which itself may cause changes in the TLS motional state [200], the open system dynamics have to be taken into account. The most general quantum dynamics[1] for open quantum systems are generated by the Gorini-Kossakowski-Sudarshan-Lindblad equation [201, 202, 203] (often referred to as Lindblad equation)

$$\dot{\rho} = -i[H, \rho] + \sum_j L_j \, \rho \, L_j^\dagger - \frac{1}{2}\Big\{ L_j^\dagger \, L_j, \rho \Big\} , \tag{5.6}$$

where $\rho$ is the system density matrix, $L_j$ are the decay operators describing the non-coherent collapse of the system wavefunction, and $j = (n_g, m_e)$ runs over all bound states indices. The expression of $L_j$ is [204]

$$L_{m_e,n_g} = \sqrt{\gamma_{m_e,n_g}} \, |g, n_g\rangle\langle e, m_e| \ , \tag{5.7}$$

with rates $\gamma_{m_e,n_g}$ given by [205]

$$\gamma_{m_e,n_g} = \frac{\gamma}{2} \int_{-1}^{+1} \mathrm{d}u \, N(u) \Big| \langle n_g | e^{iku\hat{z}} | m_e \rangle \Big|^2 . \tag{5.8}$$

The integration over $u$ averages over all possible direction of the emitted photon wavevector $k$ weighted by the dipole emission angular distribution $N(u) = 3(1 + u^2)/8$. For $u = \pm 1$ the photon is emitted along the trap axis, in this case the

[1] This assumes that the interaction between the atom and the electromagnetic vacuum can be modelled as a Markovian interaction between a system and a bath. The term "Markovian" entails that the system dynamics and the bath dynamics are separable (no correlations between the two), and that any system perturbation on the bath leaves the bath in thermal equilibrium. Generally, the atom-vacuum interaction fulfils all these assumptions.

momentum transfer is maximal, on the other hand $u = 0$ indicates a photon emitted orthogonal to the trap axis and no change in the motional state can occurs.

Different methods allow for a direct solution of the Lindblad equation, *e.g.* wavefunction Monte Carlo (described in section 5.3.2). However, if the coupling between ground and excited states is weak, *i.e.* the natural decay dynamics is much faster than any other dynamics in the system [206], it is possible to perform an adiabatic elimination of the excited states and obtain a master rate equation describing the occupation of different ground state bound levels. A sufficient condition for this approximation is $\Omega/\gamma \ll 1$, *i.e.* the cooling laser must have a relatively low intensity.

The adiabatic elimination is performed following the procedure presented by Reiter and Sørensen [207]. The Hamiltonian in eq. (5.5) can be written as the sum of 4 terms

$$H = H_g + H_e + V_+ + V_- \,,$$

where

$$\begin{aligned}
H_g &= \sum_{n_g} \left( E_{g,n_g} + \frac{\hbar\omega_c}{2} \right) |g, n_g\rangle\langle g, n_g| \,, \\
H_e &= \sum_{n_g} \left( E_{e,m_e} - \frac{\hbar\omega_c}{2} \right) |e, m_e\rangle\langle e, m_e| \,, \\
V_- &= \frac{\hbar\Omega}{2} \sum_{n_g, m_e} M^*_{m_e,n_g} \, |g, n_g\rangle\langle e, m_e| \,, \\
V_+ &= \frac{\hbar\Omega}{2} \sum_{n_g, m_e} M_{m_e,n_g} \, |e, m_e\rangle\langle g, n_g| \,.
\end{aligned}$$

Th term $H_g$ ($H_e$) describes the dynamic evolution of the ground (excited) states. The perturbative excitation (de-excitation) term $V_+$ ($V_-$) includes all terms proportional to projectors of the form $|e, m_e\rangle \langle g, n_g|$ ($|g, n_g\rangle \langle e, m_e|$). The adiabatic elimination is performed by introducing the *effective* Hamiltonian ($H_{\text{eff}}$) and decay operators ($L^{\text{eff}}_{m_e,n_g}$), that describe the dynamics of the vibrational states associated to the electronic ground state

$$\begin{aligned}
H_{\text{eff}} &= -\frac{1}{2} V_- \left[ H_{\text{NH}}^{-1} + \left( H_{\text{NH}}^{\dagger} \right)^{-1} \right] V_+ + H_g \,, \\
L^{\text{eff}}_{m_e,n_g} &= L_{m_e,n_g} H_{\text{NH}}^{-1} V_+ \,,
\end{aligned}$$

where

$$\begin{aligned}
H_{\text{NH}}^{-1} &= (H_{\text{NH}} - E_g - \omega_{\text{c}})^{-1}, \\
H_{\text{NH}} &= H_e - \frac{i}{2} \sum_j L_j^{\dagger} L_j \,.
\end{aligned}$$

It follows that

$$H_{\mathrm{NH}} = \sum_{m_e} \left( E_{e,m_e} - \frac{\hbar\omega_c}{2} - \frac{i}{2}\sum_{n_g} \gamma_{m_e,n_g} \right) |e,m_e\rangle\langle e,m_e| \,,$$
$$H_{\mathrm{NH}}^{-1} = \sum_{n_e} \frac{1}{\Delta_{m_e,n_g} - i\frac{\gamma}{2}} |e,m_e\rangle\langle e,m_e| \;,$$

where $\Delta_{m_e,n_g} = (E_{e,m_e} - E_{g,n_g})/\hbar - \omega_c$. The effective Hamiltonian and decay operators result in

$$H_{\mathrm{eff}} = -\left(\frac{\hbar\Omega}{2}\right)^2 \sum_{n_g,n_g'} \left[ \sum_{m_e} \Delta_{m_e,n_g'} \frac{M_{m_e,n_g} M_{n_g',m_e}}{\Delta_{m_e,n_g'}^2 + \frac{\gamma^2}{4}} \right] \left|g,n_g\right\rangle\!\left\langle g,n_g'\right| + \sum_{n_g} E_{g,n_g} |g,n_g\rangle\langle g,n_g| \;,$$
$$L_{\mathrm{eff}}^{(n_g,m_e)} = \sqrt{\gamma_{n_g,m_e}} \frac{\hbar\Omega}{2} \sum_{n_g'} \frac{M_{n_g',m_e}}{\Delta_{m_e,n_g'} - i\frac{\gamma}{2}} \left|g,n_g\right\rangle\!\left\langle g,n_g'\right| \;. \tag{5.9}$$

To describe the dynamics of the ground state, the Lindblad equation (eq. (5.6)) is re-written in terms of the effective operators (eq. (5.9))

$$\dot{\rho} = -i[H_{\mathrm{eff}},\rho] + \sum_{n_g,m_e} L_{\mathrm{eff}}^{(n_g,m_e)} \rho \left(L_{\mathrm{eff}}^{(n_g,m_e)}\right)^\dagger - \frac{1}{2}\left\{ \left(L_{\mathrm{eff}}^{(n_g,m_e)}\right)^\dagger L_{\mathrm{eff}}^{(n_g,m_e)},\, \rho \right\}.$$

Finally, if one considers the diagonal elements $\Pi_{n_g} = \langle g,n_g|\rho|g,n_g\rangle$, the expectation value of the commutator $[H_{\mathrm{eff}},\rho]$ is zero, and the other terms yield

$$\begin{aligned} \dot{\Pi}_{n_g} = &- \sum_{m_e,n_g'} \left|\gamma_{m_e,n_g'}\right| \left|M_{n_g,m_e}\right|^2 \Gamma\!\left(\Delta_{m_e,n_g}\right) \Pi_{n_g} \\ &+ \sum_{n_g'} \left( \sum_{m_e} \left|\gamma_{m_e,n_g}\right| \left|M_{n_g',m_e}\right|^2 \Gamma\!\left(\Delta_{m_e,n_g'}\right) \right) \Pi_{n_g'} \,, \end{aligned} \tag{5.10}$$

where $\Gamma(\Delta) = (\Omega/2)^2/(\Delta^2 + \gamma^2/4)$ is the scattering rate function.

The first, negative term on the right-hand side of eq. (5.10) represents the loss of population from the state $|g,n_g\rangle$ due to transitions to the excited states $|e,m_e\rangle$ followed by spontaneous decay to $\left|g,n_g'\right\rangle$, while the second term represents the increase of the $|g,n_g\rangle$ population due to an absorption-spontaneous emission cycle starting from the $\left|g,n_g'\right\rangle$ level.

To generalize the model to a multilevel system, in particular to the hyperfine structure of an atom, one can perform the following substitutions in eq. (5.10): $n_g \to (F_g, m_{F_g}, n_g)$, $m_e \to (F_e, m_{F_e}, m_e)$ and $n_g' \to (F_g', m_{F_g}', n_g')$, where $F_g$ ($F_e$) and $m_{F_g}$ ($m_{F_e}$) denote different hyperfine states of the ground (excited) state manifold of the atom. In general $\gamma$ and $\Omega$ will also depend on the particular $(F_g, m_{F_g})$, $(F_e, m_{F_e})$ combination considered via the associated transition line strengths [109].

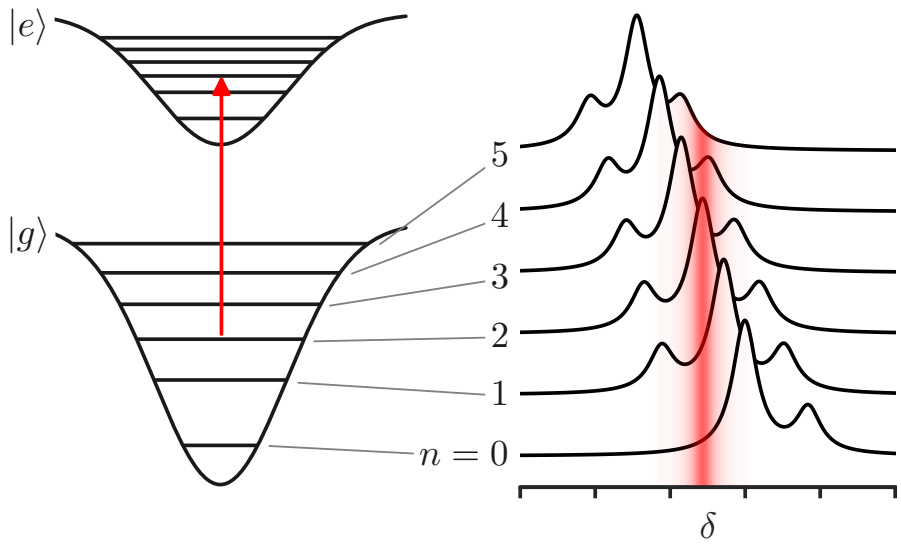


Figure 5.1: (Left) Sketch of the trap potential for ground ($|g\rangle$) and excited ($|e\rangle$) states. The red arrow indicates the position of a laser resonant with the $|g, 2\rangle \rightarrow |e, 2\rangle$ transition. (Right) Sketch of the spectrum of a particle confined in a state-dependent optical potential (with $|V_{\mathrm{T},g}| > |V_{\mathrm{T},e}|$). The red halo indicates the frequency region of high scattering rate from a laser resonant with the $|g, 2\rangle \rightarrow |e, 2\rangle$ transition.

The matrix elements $M_{n_g,m_e}$ determine how different bound states are coupled by the cooling laser beam. The exponential term can be expanded to the first order Taylor series

$$\langle n_g|e^{ik\hat{z}}|m_e\rangle \approx I_{m_e,n_g} + ik\,\langle n_g|\hat{z}|m_e\rangle + \mathcal{O}\Big((kz)^2\Big)\,.$$

For the purpose of this explanation the potential is assumed harmonic, and the overlap integrals $I_{m_e,n_g} = \langle n_g|m_e\rangle$ are approximated by a Kronecker delta $\delta_{n_g,m_e}$. Under this assumption

$$\langle n_g|e^{ik\hat{z}}|m_e\rangle \approx \delta_{m_e,n_g} + i\,\eta\left[(m_e+1)\,\delta_{m_e+1,n_g} + m_e\,\delta_{m_e-1,n_g}\right],$$

where $\eta$ is the Lamb-Dicke parameter (as defined in section 2.1.5), which is assumed to be much smaller than 1. Therefore, under the harmonic approximation, the particle spectrum presents a *carrier* transition of relative intensity 1 which does not change the motional quantum number and two additional *sideband* transitions which are associated to a change of a single vibrational quantum. These sideband transitions are referred to as the *red sideband* and *blue sideband* and are associated with the loss and gain of a vibrational quantum, respectively. The sideband transitions have a relative intensity $\eta^2$. Beyond the harmonic approximation, the matrix elements $\langle n_g|e^{ik\hat{z}}|m_e\rangle$ can be calculated numerically. Also in this case, the

spectrum presents three transitions: the carrier and the two sidebands. Sideband transitions of higher order ($|m_e - n_g| > 1$), contribute to the elements $\langle n_g|e^{ik\hat{z}}|m_e\rangle$ with terms of order $\mathcal{O}(\eta^2)$ or higher. Therefore, they can be neglected as long as $\eta \ll 1$.

The position of the carrier and sideband transitions are given by the Lorentzian function $\Gamma\left(\Delta_{m_e,n_g}\right)$, which is peaked at $\Delta_{m_e,n_g} = 0$, thus the positions of the sideband and the carrier transitions depend on the particular choice of $m_e$ and $n_g$. The particle absorption spectrum is sketched in fig. 5.1. The configuration of this spectrum shows the Sisyphus-cap effect introduced by ref. [196]: a laser beam resonant with the $|g, n_g\rangle$ carrier transition will cause excitation of the blue sidebands of levels with number $n' > n$, thus causing heating. Contrarily, the same laser will be resonant with the red sidebands of levels with $n' < n$ and, resulting in a reduction of the vibrational level.

The work developed in this chapter aims at studying the possibility of realizing a novel scheme for cooling particles confined in state-dependent optical potentials with $\alpha_g < \alpha_e$. In this scheme a laser is first made resonant with the free space TLS transition ($\Delta = 0$) and then slowly detuned toward the blue side ($\Delta > 0$). This way, the laser becomes resonant with the red sideband of all bounds levels, from the least to the most bound one. Effectively, the laser cools the bound levels sequentially, avoiding scattering on the blue sideband of levels which are still populated. In the following sections, the efficiency of this cooling scheme is investigated in the specific cases of Li and Yb trapped in optical tweezers and optical lattices.

## 5.3 Sideband cooling of TLS in optical tweezers

Optical tweezers have become common tools for manipulating single atoms, single molecules, or ions [208, 133, 209] with the aim of isolating individual particles. In this section, the cooling scheme proposed at the end of the previous paragraph is applied to two-level particles trapped in optical tweezers. Dipolar traps, such as optical tweezers, constitute a simple case to study since they are formed by a single laser beam. The trap depth and trap frequencies can be independently controlled, since laser power and trap waist are independent parameters. The different case of a cavity-enhanced lattice will be considered in the next section.

A numeric simulation of eq. (5.10) was performed by considering two separate TLSs trapped in an optical tweezer generated by a highly focused single beam laser. In order to perform two simulations under different but still experimentally feasible conditions, the simulation was performed for two TLSs with considerably different mass and spectroscopic properties. Specifically, the two TLSs have the transition frequencies and the masses of Li and Yb. With respect to Yb, the two-level approximation is particularly well suited for the bosonic isotopes for which there is no hyperfine splitting.

| **Parameter** | **Li** | **Yb** |
|---|---|---|
| Transition line | $^2S_{1/2} \rightarrow {}^2P_{1/2}$ | $^1S_0 \rightarrow {}^3P_1$ |
| $\lambda$ | 1064 nm | 532 nm |
| $w_0$ | 700 nm | 700 nm |
| $P$ | 47.5 mW | 25.8 mW |
| $s_0$ | 0.1 | 0.1 |
| $\Omega$ | $8.15 \times 10^6$ rad/sec | $2.56 \times 10^5$ rad/sec |
| $\tau$ | 3.3 ms | 110 ms |
| $\gamma$ | $2\pi$ 5.8 MHz [165] | $2\pi$ 182 kHz [210] |
| $m$ | 6 u | 171 u |
| $\alpha_g$ | 270 a.u. | 280 a.u. [211] |
| $\alpha_e$ | 191 a.u. | 224 a.u. [211] |

Table 5.1: Parameters used for simulating sideband cooling of a TLS trapped in an optical tweezer. Parameters $\lambda$, $w_0$ and $P$ are the wavelength, waist and power of the optical tweezer's laser beam, respectively. $s_0$ is the intensity of the cooling laser in units of $I_{\text{sat}}$ and $\tau$ is the duration of the cooling laser frequency sweep. The last four parameters are the linewidth, mass and polarizabilities of the TLS. u is the atomic mass unit.

Table 5.1 shows the parameters used in the simulation and the properties of the transitions that were considered. The trap wavelength $\lambda$, waist $w_0$, and power $P$ were set to values similar to the ones used in experiments reported in literature [212, 213]. The cooling laser relative intensity $s_0 = I/I_{\text{sat}}$, where $I_{\text{sat}}$ is the saturation intensity of the atomic transition, is chosen to be 0.1. Due to the direct relation between $s_0$ and the ratio $\Omega/\gamma$ this ensures that the condition $\Omega/\gamma \ll 1$ is satisfied. The terms $\alpha_g$ and $\alpha_e$ are the atomic polarizabilities for the ground and the excited states, respectively, and were computed following the method presented in [214]. To convert from atomic units to SI units, $\alpha_g$ and $\alpha_e$ have to be multiplied by $2\pi\hbar \times 2.488\,32 \times 10^{-8}\,\text{A}^2\text{s}^4/\text{kg}$.

Although not strictly necessary, it is convenient to define some approximated quantities which are commonly used in the experimental field when referring to sideband cooling. The equivalent harmonic trapping frequency is defined as

$$\omega_{\text{T},i} = \frac{1}{w_0}\sqrt{2\frac{|V_{\text{T},i}|}{m}}\,, \quad i = g, e$$

where

$$V_{\text{T},i} = \alpha_i \frac{I(x,y,z)}{2\epsilon_0 c}\,, \quad i = g, e$$

is the trap's potential depth when the TLS is in its ground ($g$) or excited ($e$) state, $I(x, y, z)$ is the intensity distribution of the trap's laser beam — typically, $I(x, y, z)$ has a Gaussian shape if the laser is emitting in its fundamental mode — $\epsilon_0$ is the vacuum permittivity. It is possible to define a Lamb-Dicke parameter for the ground state manifold as

$$\eta_g = \frac{2\pi}{\lambda_c}\sqrt{\frac{\hbar}{2m\omega_{T,g}}}\,. \tag{5.11}$$

The simulation outcomes are discussed in terms of the approximated parameters $\omega_{T,g}$ and $\eta_g$. The values of power $P$ reported in table 5.1 are chosen such that the ground state Lamb-Dicke parameter $\eta_g$ is equal to 0.2. Since the laser frequency is swept between two values — these will be defined later in the text — the parameter $\tau$ indicates the time it takes the cooling laser to perform the sweep. The values of the parameter $\tau$ were chosen to be 3.3 ms (Li) and 110 ms (Yb). In the visualization of the simulation results, the time is expressed in units of $\eta_g^2\gamma t$, as this represents the sideband effective scattering rate [200].

| **Parameter** | **Li** | **Yb** |
|---|---|---|
| $V_{T,g}$ | 3.7 mK | 2.1 mK |
| $V_{T,e}$ | 2.6 mK | 1.7 mK |
| $\omega_{T,g}$ | 732 kHz | 101 kHz |
| $\omega_{T,e}$ | 617 kHz | 90 kHz |
| $\eta_g$ | 0.2 | 0.2 |
| $\Delta\alpha$ | −17 % | −11 % |

Table 5.2: Physical parameters of the trap used in the sideband cooling simulation.

Table 5.2 shows the physical parameters of the trap computed using the parameters reported in table 5.1. The differential polarizability $\Delta\alpha = (\alpha_e - \alpha_g)/(\alpha_e + \alpha_g)$ indicates of the relative difference in atomic polarizability between the ground and the excited states. A negative value of $\Delta\alpha$ implies $V_{T,g} > V_{T,e}$. For both atomic species the equivalent harmonic trapping frequency $\omega_{T,g}$ is smaller than the transition linewidth $\gamma$. The condition $\omega_{T,g} > \gamma$ is required to be able to resolve the sideband transitions from the carrier transition, thus achieving ground state cooling. However, it will be shown in next sections that it is still possible to achieve a reduction of the trapped particles' energy of motion even if $\omega_{T,g} \lesssim \gamma$.

### 5.3.1 Numerical simulation of sideband cooling

Equation (5.10) is a matrix first-order differential equation of the form

$$\dot{\mathbf{\Pi}} = \mathbf{C} \cdot \mathbf{\Pi}\,,$$

where $\mathbf{C}$ is the coefficient matrix and $\mathbf{\Pi}$ is a column vector, the elements of which are the populations $\Pi_{n_g}$. If $\mathbf{C}$ is time-independent, the general solution is a linear combination of eigenvectors of $\mathbf{C}$. Since the coefficients appearing in eq. (5.10) are not time-independent, a dense partition of time is introduced and $\mathbf{C}$ is approximated as constant over each (small) time interval. Therefore, the solution is given by diagonalizing $\mathbf{C}$ over each time interval. A simulation code was developed using the Python language, with the aim of determining the matrix elements of $\mathbf{C}$ while the laser frequency is swept linearly in time.

### Initialization and preliminary calculations

Before the $\mathbf{C}$ matrix can be determined, several preliminary calculations have to be performed in order to determine the bound levels energies and wavefunctions starting from the parameters listed in table 5.1. First, a single beam optical trap (optical tweezer) is considered. The trap's laser intensity is given by the formula (ref. [168], chapter 2)

$$I(x,y,z) = I_0 \left| \frac{w_0}{w(z)} H_0\left(\sqrt{2}\frac{x}{w(z)}\right) e^{-(x/w(z))^2} H_0\left(\sqrt{2}\frac{y}{w(z)}\right) e^{-(y/w(z))^2} \right|^2 ,$$

where $I_0 = 2P/(\pi w_0^2)$ is the peak intensity, $w_0$ is the beam waist, $w(z)$ is the $1/e^2$ radius at position $z$ so that $w(z=0) = w_0$, $H_0(x)$ is the zero-th order Hermite polynomial, the trapping laser propagates along the $z$-axis, and the phase term has been omitted. The trap depth is computed as [215]

$$V_{\mathrm{T},i}(x,y,z) = -\frac{1}{2\epsilon_0 c} \mathrm{Re}\{\alpha_i\} I(x,y,z), \quad i = g, e$$

Since the potential $V_{\mathrm{T},i}(x,y,z)$ is Gaussian, a numeric method is needed to compute the trap bound levels and wavefunctions. A well-known approximation method for bound states is the *WKB* approximation (ref. [60], chapter 8): the energy of the n-th bound level $E = E_n$ has a value such that

$$n + \frac{1}{2} = \frac{\sqrt{2m}}{\pi\hbar} \int_{R_-}^{R_+} \sqrt{E - V(r)}\, \mathrm{d}r \ , \tag{5.12}$$

where $V(r)$ is the potential energy, $R_\pm$ are the classical inversion points where the particle's total energy equals the potential energy. In code, the WKB integral is computed as a summation over dense partition of space $r$, the energy of each bound levels is found by solving eq. (5.12) as a root finding problem. The n-th bound state wavefunctions are approximated by the n-th harmonic oscillator wavefunction that best approximates the curvature of the potential at energy $E_n$. Due to numerical limitations, the simulation works on a truncated basis of 60 bound levels for each of the ground state and excited state manifold, for a total of 120 states simulated.

### Matrix elements derivation and simulation main loop

The off-diagonal elements of the matrix **C** are given by

$$C_{n_g,h_g} = \sum_{m_e} \left|\gamma_{m_e,n_g}\right| \left|M_{h_g,m_e}\right|^2 \Gamma\left(\Delta_{m_e,h_g}\right),$$

as indicated in eq. (5.10). Each of the three multipliers appearing in the expression of $C_{n_g,h_g}$ is computed and stored in a temporary matrix. The decay rate $\gamma_{m_e,n_g}$ is computed as $\gamma/2(|\langle n_g|m_e\rangle|^2 + 7/16\,|ik\,\langle n_g|\hat{z}|m_e\rangle|^2)$, additional terms are neglected, the value $7/16$ is a numeric approximation of the integral over $u$ presented in eq. (5.8). These values are stored in a matrix called *decay_couplings*. The matrix elements $M_{h_g,m_e}$ are computed using the expression $\langle n_g|m_e\rangle + ik\,\langle n_g|\hat{z}|m_e\rangle$ and are stored in a matrix called *couplings*. The scattering rate $\Gamma\left(\Delta_{m_e,h_g}\right)$ is computed from the expression of the Lorentzian function $\Gamma(\Delta) = (\Omega/2)^2/(\Delta^2 + \gamma^2/4)$ and the values are stored in the *scatrates* matrix. These three temporary matrices are organized such that the element at the $n$-th row and $m$-th column corresponds to the appropriate rate between the $n$-th ground state bound level and the $m$-th excited state bound level. All overlap integrals, such as $\langle n_g|m_e\rangle$, are computed numerically.

Once these three matrices are defined, the matrix **C** is computed with the following code:

```
#
# Computes the matrix C for sideband cooling simulation.
#

# N: number of bound states in ground state manifold

def compute_matrix(laser_frequency):
    # scattering rates for a given laser frequency
    scatrates = compute_scatrates(laser_frequency)
    # create an (NxN) empty matrix
    C = [[0.0]*N for _ in range(N)]

    for ng in range(N):
        for mg in range(N):
            # diagonal terms are computed separately
            if ng == mg:
                continue
            # matrix element
            rate = np.sum(
                decay_couplings[ng] * \
                couplings[mg] * \
                scatrates[mg]
```

```
23              )
                C[ng][mg] += rate
25
    # convert to np.array
27  C = np.array(C, dtype=np.float64)
    # diagonal terms are the sum of other rates
29  # on the same row, with negative sign
    C -= np.diag(np.sum(C, axis=0))
31  # clean small values (limits numeric noise)
    C[np.abs(C) <= 1e-10] = 0.0
33
    return C
```

Since the off-diagonal elements in the $n$-th row represent the rate of transition from the $n$-th level all other bound levels with vibrational number different from $n$ and since the sum of all the rates has to be zero (conservation of probability), the diagonal elements of the matrix $\mathbf{C}$ are computed as the sum of the rates on the same row multiplied by $-1$.

The main loop of the simulation is concerned with changing the laser frequency value over time and re-calculating the matrix $\mathbf{C}$, diagonalizing it at every time interval $\delta t$ and returning a list of occupation probabilities $\Pi_n$. The code of the main loop is:

```
#
2 # Computes the list of occupation probabilities
  # over a partition of time.
4 #

6 # dt: time step between each solution.
  # f0: start frequency for the laser sweep.
8 # f1: stop frequency for the laser sweep.
  # tau: time taken to sweep from f0 to f1.
10 # p0: starting occupation probability.

12 # list of occupation probabilities
  pns = [p0]
14
  while t < tmax:
16    # increase time
      t += dt
18    # compute laser frequency
      f = f0 + (f1-f0)/tau * t
20    # compute C matrix
      C = compute_matrix(laser_frequency = f)
22    # diagonalize
```

```
    eigvals, eigvects = np.linalg.eig(C)
24  c = np.linalg.inv(eigvects) @ pns[-1]
    pn = eigvects @ (c * np.exp(eigvals * dt))
26  # store result
    pns.append(pn)
```

The output of the simulation is the list *pns*, which contains the occupation probabilities for all levels at different times. These can be used to compute other quantities of interests such as the average occupation number $\langle n(t)\rangle$ or the average particle's energy. The variables $f_0$ and $f_1$ determine the initial and final frequency of the cooling laser, $f_0$ corresponds to the free-space (unperturbed) TLS transitions frequency, while the final frequency $f_1$ is carefully adjusted to minimize the resulting average occupation number $\langle n(t)\rangle$. The optimization is done as follows: a first simulation is performed by setting $f_1$ equal to the frequency of the $n_g = 1 \rightarrow m_e = 0$ red sideband; when the cooling laser reaches this value, since the sidebands are not well resolved from carrier transitions, heating occurs and the value of $\langle n(t)\rangle$ suddenly increases. The frequency value for which $\langle n(t)\rangle$ is at a minimum is then extracted, and a second, independent simulation is performed where $f_1$ is set to the value that gave the best result for $\langle n(t)\rangle$ in the previous simulation.

### 5.3.2 Wavefunction Monte Carlo simulation

In order to compute the dynamics described by eq. (5.1) independently of the approximations performed to obtain eq. (5.10), a Wavefunction Monte Carlo (WFMC) simulation of Hamiltonian 5.1 was developed. Such simulation is not afflicted by the adiabatic elimination of excited states and follows a different mathematical approach in solving the Lindblad equation.

The WFMC method is a stochastic method used to simulate the dynamics of open quantum systems. Different, yet similar, algorithms use a wavefunction-based approach to achieve such result and have been developed concurrently and independently by different people [216, 217, 218, 219]. The method developed by Dalibard *et al.* [216] is sometimes referred to as the *quantum jumps approach*. In this approach the system wavefunction is made to evolve according to the Schrödinger equation with a non-Hermitian Hamiltonian[2]

$$H_{\mathrm{NH}} = H - \frac{i\hbar}{2}\sum_j L_j^\dagger L_j \,.$$

The non-Hermitian component of the Hamiltonian causes a variation of the norm

[2]It is interesting to note that this non-Hermitian Hamiltonian is the same as the one used in section 5.2 to perform the adiabatic elimination of excited states.

of the wavefunction, such that after a small time $\delta t$ the quantity

$$\delta p = \delta t \sum_j \langle \psi(t) | L_j^\dagger L_j | \psi(t) \rangle$$

indicates the probability that a quantum jump occurred in the time range $t \to t+\delta t$ time. As a result, $\langle \psi(t+\delta t) | \psi(t+\delta t) \rangle = 1 - \delta p$ is the probability of remaining in the state $|\psi\rangle$. When a quantum jump does occur, the wavefunction $|\psi(t)\rangle$ is projected using a Lindblad operator $L_j$ and then normalized to 1

$$\psi(t+\delta t) = \frac{L_j \, |\psi(t)\rangle}{\sqrt{\langle \psi(t) | L_j^\dagger L_j | \psi(t) \rangle}}$$

The collapse operator $L_j$ that performs the measurement is chosen randomly, by weighting each $L_j$ with their associated rate $\gamma_j$.

The algorithm for the WFMC is thus:

1. Start from a pure state $|\psi(0)\rangle$.
2. Generate a random number $r$ between 0 and 1.
3. Integrate Schrödinger equation with Hamiltonian $H_{\text{NH}}$ until $\langle \psi(t) | \psi(t) \rangle = r$, at this point a quantum jump occurs.
4. Randomly choose a collapse operator $L_j$ weighted by its decay rate. Collapse and normalize the wavefunction.
5. Loop from point 2 until a stop time is reached.

This method defines a so-called *quantum trajectory*, *i.e.* a particular time evolution of the system wavefunction $|\psi\rangle$. This wavefunction can be used to compute quantities of interest, such as expectation values of different operators, which then must be averaged over multiples trajectories. If the initial state is not a pure state but a mixture with probabilities $p_n$

$$\rho = \sum_n p_n \, |\psi_n(t)\rangle\langle\psi_n(t)| \ ,$$

each trajectory should be initialized with a different $|\psi_n(0)\rangle$ randomly selected according to the distribution of $p_n$.

The sideband cooling WFMC simulation is implemented using the Python language in the QuTiP framework [220]. This framework implements the algorithm presented above and integrates the wavefunction using the Runge–Kutta–Fehlberg method (RKF45) that solves differential equations with fourth order accuracy and estimates the error with a fifth order accuracy (ref. [221], chapter 17). The simulation parameters are defined as in the beginning of section 5.3. Results are averaged over 250 trajectories.

### 5.3.3 Results

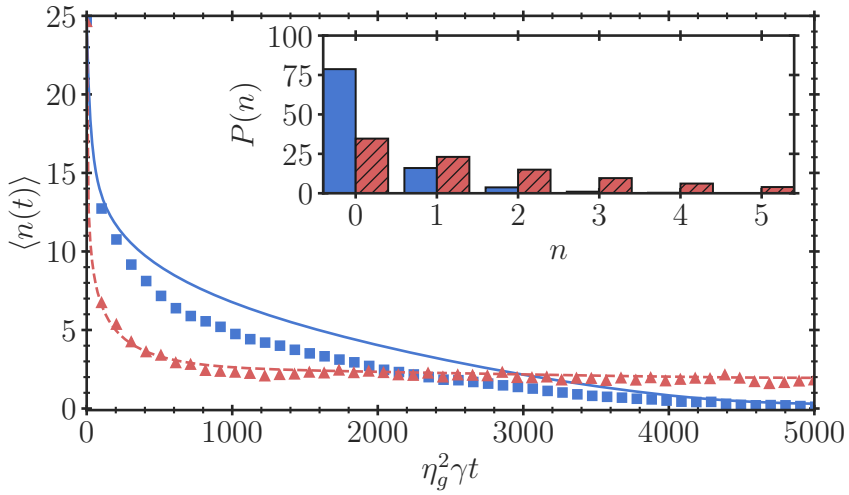


Figure 5.2: Average occupation number as a function of time during sideband cooling of Yb (blue solid line) and Li (red dashed line). The data are obtained by numerical integration of eq. (5.10). The blue squares and the red triangles indicate the results from a quantum Monte Carlo simulation for Yb and Li, respectively. The time axis has been scaled by the sideband scattering rate $\eta_g^2\gamma$. Inset shows the occupation probability of the lowest bound levels after cooling of Yb (blue bars) and Li (red hatched bars) for the analytic result only.

Figure 5.2 shows the results of a single numeric solution of eq. (5.10) as the laser frequency is swept in time. The average occupation number is reduced over time for both Li and Yb atoms, until the particles reach a steady mean energy level. The ground state occupation after the laser sweep is 78.7 % for Yb and 34.6 % for Li, corresponding to an energy reduction of 98.2 % and 92.0 % for the two species, respectively.

In spite of the fact that the product between the red sideband linewidth $\eta_g^2\gamma$ and the laser sweep time are kept equal in the simulation, the dynamic behaviour of the occupation number of Yb and Li is qualitatively different. In particular, Li atoms reach the minimum attainable energy after approx. 1/3 of the sweep time. This discrepancy can be attributed to the different values of the ratio $\omega_T/\gamma$, which are 0.57 and 0.126 for Yb and Li, respectively. The occupation probability distribution after the cooling process is a thermal distribution (shown inset fig. 5.2), and the associated temperatures are 4.3 µK and 114 µK for Yb and Li, respectively. The WFMC simulation results are shown by the square and triangle markers and qualitatively agree with the numerical solution, according to the WFMC simulation

the ground state occupation probabilities after cooling are 88.0 % for Yb and 38.0 % for Li.

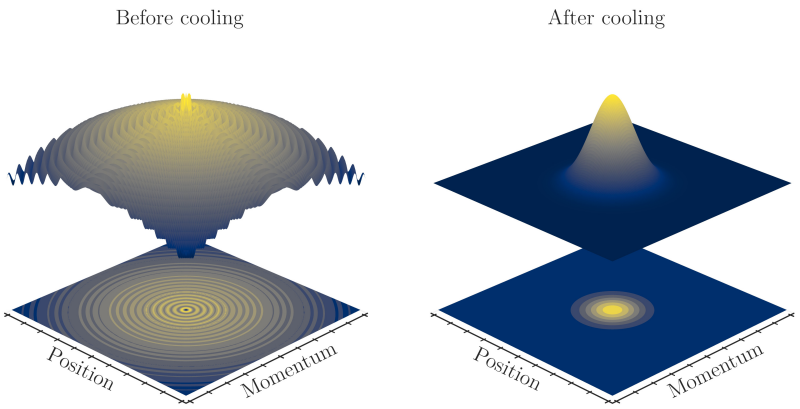


Figure 5.3: Wigner quasiprobability distribution before and after cooling of Yb. Vertical axes have been scaled for better visualisation.

To better visualize the effects of the cooling in phase space, fig. 5.3 shows the Wigner quasiprobability distribution before and after cooling in the case of Yb atoms. The Wigner quasiprobability distribution is a statistical distribution used to describe quantum states in phase space [222], it cannot be strictly interpreted as a probability distribution since it can assume negative values when it describes a state with no classical equivalent. Initially, the atom is broadly spread in phase space (fig. 5.3, left plot) indicating a relatively hot particle. At the end of the laser sweep, the distribution in the phase space is compressed near the origin (fig. 5.3, right plot), showing a reduction of particle momentum and occupied positions, thus demonstrating the cooling of the particle's motion. This final distribution has a Gaussian shape and it is similar to the occupation probability of a Fock state with $n = 0$. Both distributions are centred on the origin as expected for a particle in a symmetric potential.

Since the minimum achievable value for $\langle n(t) \rangle$ is strongly dependent on the choice of the experimental parameters, it is instructive to simulate sideband cooling with varying values for the trap depth, the difference in polarizability and the cooling laser frequency sweep time. Figure 5.4 shows the mean occupation number after cooling for different values of the Lamb-Dicke parameter $\eta_g$, which is changed by varying the trap depth. As a result, also the ratio $\omega_T/\gamma$ is varied (top $x$-axis). As $\eta_g$ is increased the minimum achievable value for the average occupation number is considerably increased. This is an expected result, since the motional sidebands are less resolved when the condition for the Lamb-Dicke regime is relaxed and the ratio $\omega_T/\gamma$ is increased. The increase of the minimum $\langle n(t) \rangle$ is more pronounced in the case of Li. This can be attributed to the fact that the $\omega_T/\gamma$ ratio is far smaller

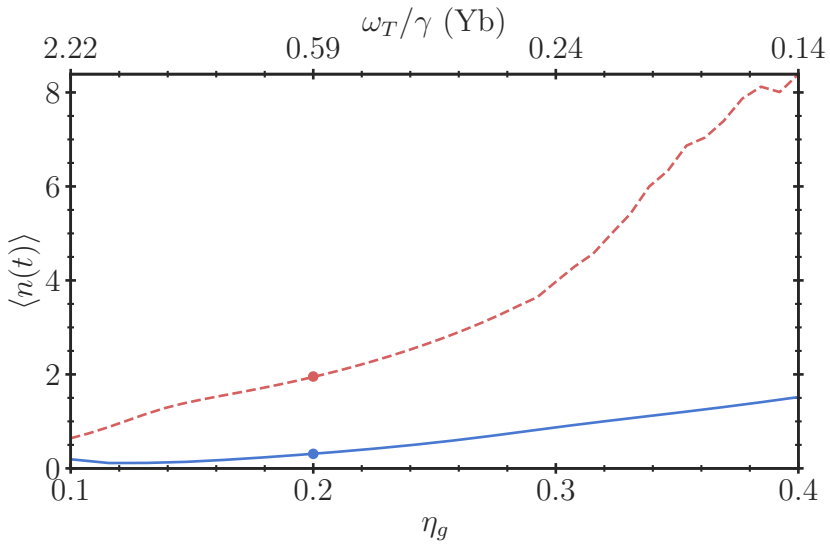


Figure 5.4: Average occupation number after the frequency sweep of the cooling laser as a function of the ground state Lamb-Dicke parameter for Yb (blue solid line) and Li (red dashed line). The x-axis above the plot reports the values of the ratio $\omega_T/\gamma$ for Yb, the corresponding values for Li can be obtained by rescaling the axis by the ratio of the atomic linewidths. Solid dots indicate the parameters used in the simulations of fig. 5.2. Different values of $\eta_g$ are obtained by changing the trapping laser power.

for Li with respect to Yb due to the different atomic linewidths.

The difference in polarizability determines the difference between the trap depths experienced by an atom in the ground or in the excited internal state. Therefore, this quantity determines the spread of the sidebands' transition frequencies. As the energy difference between the carrier and the sidebands increases, the coupling strength between levels with different motional state decreases, resulting in a lower efficiency of the cooling process. By artificially changing the atomic polarizability of the excited state, the dependence of the minimum achievable occupation number on the difference in polarizability $\Delta\alpha = (\alpha_e - \alpha_g)/(\alpha_e + \alpha_g)$ can be studied. The results of this simulation are shown in fig. 5.5.

As predicted, the further away the system is from the magical trapping condition, the worst is the minimum achievable $\langle n\rangle$. Cooling of Yb is more efficient than Li except for the region where $\Delta\alpha < -0.3$, in which the two curves cross each other and present a similar slope. The fact that at small values of $|\Delta\alpha|$ the Yb $\langle n\rangle$ is smaller than the one of Li is due to the smaller atomic linewidth. For increasing values of $|\Delta\alpha|$ the results for Yb quickly increase since the reduction of the excited state potential depth reduces the resolution between sideband and carrier transitions.

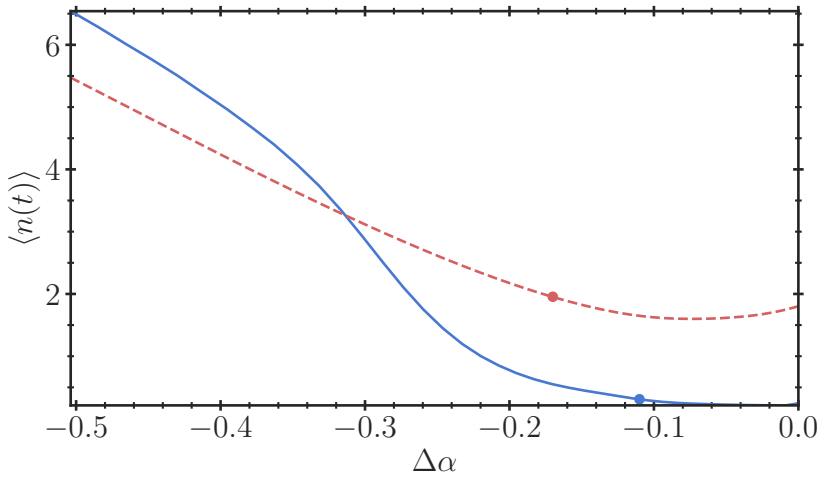


Figure 5.5: Average occupation number after cooling as a function of the difference in polarizability $\Delta\alpha$ for Yb (blue solid line) and Li (red dashed line). $\Delta\alpha = 0$ implies a magic trapping condition, while negative values are associated with a trap for which a particle in its internal ground state is more bound than a particle in the excited state. Solid dots indicate the parameters used in the simulations of fig. 5.2. Different values of $\Delta\alpha$ are obtained by changing the atomic polarizability for the excited state only.

Finally, fig. 5.6 shows the cooling efficiency as a function of the frequency sweep duration when the start and stop frequencies are kept constant. A threshold-like effect is observed if the laser sweep time is gradually reduced. This is due to the fact that, if the laser spends insufficient time at resonance with a given sideband transition, there will be a reduced population transfer between bound levels, which limits the reduction of vibrational quanta.

## 5.4 Sideband cooling of Lithium in optical lattice

As detailed in chapter 4, a high-finesse optical resonator is installed in the MOT chamber of the Li setup. For an input power of 300 mW the resonator is capable of generating a dipole trap with depths $13\,500 E_{\mathrm{rec}}$ (26.3 mK) and $11\,250 E_{\mathrm{rec}}$ (22.0 mK), where $E_{\mathrm{rec}}$ is the recoil energy, for the $^2\mathrm{S}_{\frac{1}{2}}$ and $^2\mathrm{P}_{\frac{1}{2}}$ levels of $^6$Li, respectively. The trap depth is sufficient to allow for the resolution of sideband transition from carriers, but with a trapping laser wavelength of 903 nm the trap potential is state-dependent.

The dipole trap generated between the resonator mirrors is intended to be used for evaporative cooling after the MOT sequence until the Li cloud is brought to

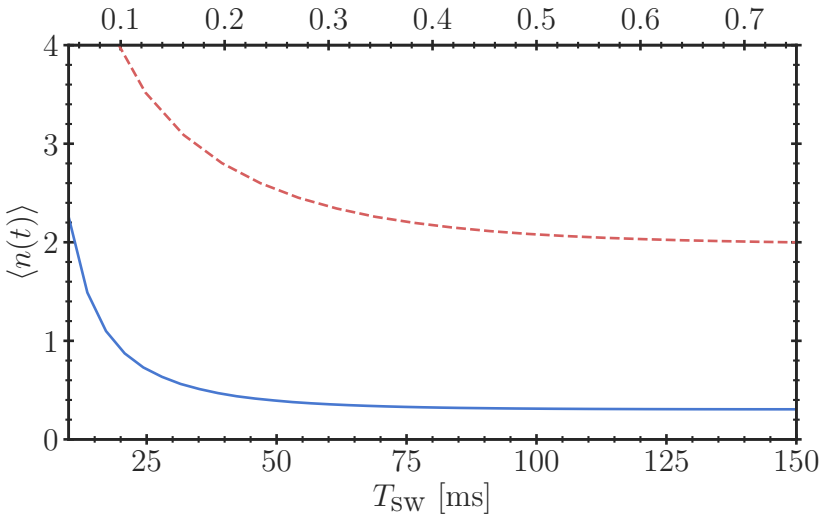


Figure 5.6: Average occupation number after cooling as a function of the sweep duration $T_{\mathrm{sw}}$ for Yb (blue solid line) and Li (red dashed line). The lower (upper) axis indicates the sweep duration for Yb (Li).

degeneracy. Single photon sideband cooling can be used to speed up and facilitate this process: instead of starting evaporative cooling with a gas at the temperature of a cMOT ($\approx 40\,\mu\mathrm{K}$), a sideband cooling sequence can be performed before evaporation in order to further reduce the cloud temperature. With this method degeneracy would be reached with a reduced loss of particles and faster, facilitating a higher repetition rate in the experimental run.

The model developed in this work is suitable to describe sideband cooling for particles trapped in optical lattices. Lithium in particular requires to take into account the full Hyperfine Structure (HFS) since the separation between two HFS levels is comparable with the frequency spread of sideband and carriers of different bound states. Therefore, eq. (5.10) is modified to support a multi-level system such as the hyperfine structure of Li as indicated in section 5.2.

The trapping laser polarization is assumed orthogonal to the lattice axis and with a fixed direction ($\pi$-polarized light). Under these assumptions, the lattice potential can be written as

$$V_{\mathrm{T},i}(z) = V_{0,i} \cos^2(k_{\mathrm{T}} z)\,, \quad i = g, e \tag{5.13}$$

where $k_{\mathrm{T}} = 2\pi/\lambda_{\mathrm{T}}$ is the wavevector of the optical lattice at wavelength $\lambda_{\mathrm{T}}$ and $V_{0,i}$ is the trap depth experienced by an atom in the ground ($i = g$) or the excited ($i = e$) state. The energy levels and the corresponding wavefunctions of a particle moving in a potential as in eq. (5.13) are the solutions of a Mathieu equation [223]. These are computed using Wolfram Mathematica separately before starting the simulation in Python.

The initial bound levels populations are calculated by assuming that Li atoms are suddenly transferred from a free particle state to a bound level state. The atoms are initially assumed to be well described by a Gaussian wavepacket

$$\psi_\sigma(x) = \frac{1}{\sqrt{\sigma\sqrt{2\pi}}}\, e^{-\frac{x^2}{4\sigma^2}}\, e^{i\frac{p_0}{\hbar}x}\,,$$

where $\sigma$ is the spatial extension of the wavepacket at $t = 0$, $p_0 = \sqrt{mk_BT_0}$ is the momentum associated with the group velocity of the wavepacket and $k_B$ is the Boltzmann constant. The population of the n-th bound level is $\Pi_n = c_n^2$, where:

$$c_n = \frac{1}{\sqrt{\sigma\sqrt{2\pi}}}\,\frac{1}{\sqrt{2^n n!\sqrt{\pi}}}\left(\frac{m\omega_T}{\hbar}\right)^{1/4}\int_{-\infty}^{\infty} e^{-\left(\frac{m\omega_T}{2\hbar}+\frac{1}{4\sigma^2}\right)x^2 + i\frac{p_0}{\hbar}x}\, H_n\!\left(\sqrt{\frac{m\omega_T}{\hbar}}\,x\right).$$

By substituting the Hermite polynomials $H_n(x)$ with the Gould-Hopper polynomials[3] $H_n(x, y)$ using the relation $H_n(2x, -1) = H_n(x)$, the integral can be rewritten in a solvable form [224]. The initial temperature and dimension of the atomic cloud are chosen to be $T_0 = 40\,\mu\text{K}$ and $\sigma = 500\,\mu\text{m}$ since these values are commonly observed in experiments involving lithium [126]. With these conditions the initial average occupation number is calculated to be 16.2.

The hyperfine levels are initialized with equal population, *i.e.* the atomic cloud is not in a polarized state. Throughout the simulation the magnetic field is assumed constant and at a low value (near 0 G), this choice also makes it possible to neglect the atom-atom collision interactions which tend to play a role near high-field Feshbach resonances.

Results of the numeric solution of eq. (5.10) are shown in fig. 5.7. The final occupation number (averaged over different hyperfine levels) is 0.7, with a corresponding ground state occupation probability of 47.7 %.

Due to the hyperfine configuration of Li the system can be efficiently cooled by using three laser frequencies (the addressed transitions are shown in the inset of fig. 5.7) swept together. The light detunings with respect to the fine structure $D_1$ transition of Lithium are set to: $\Delta_0$ from $-67.35\,\text{MHz}$ to $-12.65\,\text{MHz}$, $\Delta_1$ from $-93.45\,\text{MHz}$ to $-38.75\,\text{MHz}$ and $\Delta_2$ from $160.8\,\text{MHz}$ to $215.5\,\text{MHz}$.

The bound levels' energies (and thus the sideband transitions) are also dependent on the radial position of the atom in the optical trapping potential. Generally, in an atomic cloud confined in an optical lattice the atoms do not lay exactly on the trap axis where the potential depth is maximal. In order to estimate the effects of the radial distribution of a particle within a single lattice site, the simulation is run multiple times with the atom displaced at a distance $x$ from the trap axis.

[3] These are the solutions to the heat Fourier equation and are different from the usual definition of bivariate Hermite polynomials.

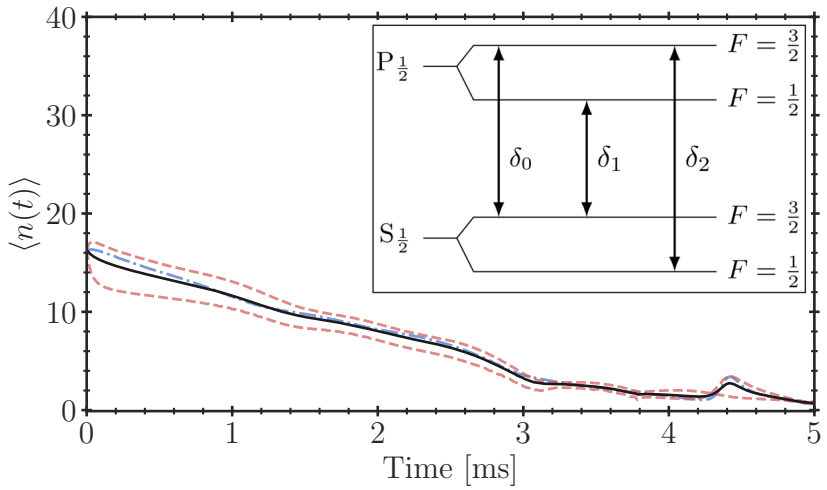


Figure 5.7: Average occupation number of Li atoms in the $F = 3/2$ (red dashed lined) and $F = 1/2$ (blue dotted line) states as a function of time. The black solid line shows the average of the hyperfine levels. Inset: internal levels of the electronic ground state of $^6$Li. The arrows indicate the transitions that were addressed in the simulation.

Since a standing wave trap is considerably shallower along the transversal axis, $x$ can be approximated as a classical variable. Figure 5.8 shows the results of these simulations, the cooling laser sweep parameters are left as previously indicated.

Due to the different bound state configuration, the laser sweep can only cool efficiently the atoms located near the trap axis while atoms located at a distance greater than $\geq 10\,\%$ of the trap waist will experience heating. Assuming that the radial density of the atomic cloud follows a Boltzmann distribution, for an initial temperature of $T = 40\,\mu\mathrm{K}$ the width of the radial density distribution is approximately $10\,\mu\mathrm{m}$, i.e. $8.6\,\%$ of the optical lattice waist.

Given these sweep detunings, at higher magnetic fields we observe that cooling is no longer efficient for some hyperfine states, in particular when the magnetic field is increased over $20\,\mathrm{G}$ several hyperfine states become weakly resonant with the cooling laser and, therefore, are not cooled effectively.

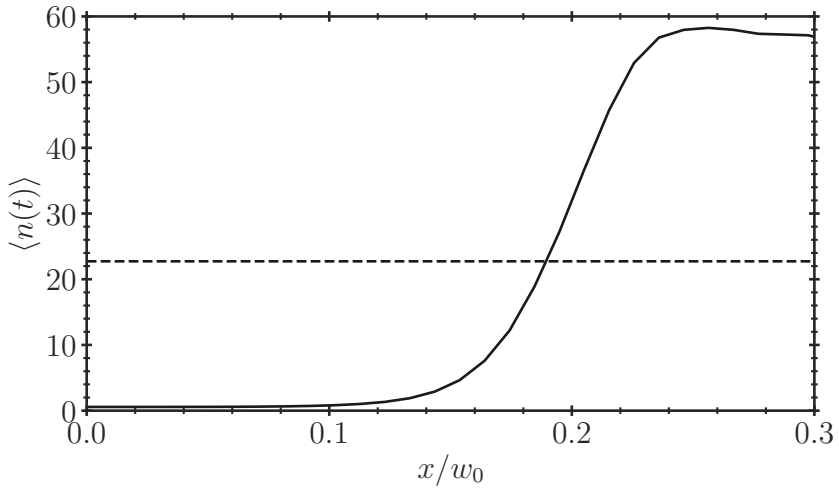


Figure 5.8: Final average occupation number as a function of the atoms' position along the trap radial axis $x$. Dashed line indicates the initial average occupation number. The x-axis is in units of the trap laser waist $w_0$.

# Chapter 6

# Conclusions

This thesis presents the realization of an experimental apparatus for the production of ultracold $^6$Li gases, and of a novel scheme for fast laser cooling of optically trapped particles. This new scheme is based on a linear frequency sweep of a cooling laser, which cools particles starting from the highest bound energy level and proceeding sequentially to the lower energy levels. At the $Ba^+$Li experiment at LENS, this scheme is intended to be used for providing an efficient cooling stage for the fast preparation of ultracold $^6$Li gases. By using sideband cooling, atoms can be cooled close to their ground state of motion, leading to a reduction of the particle loss and of the time necessary for evaporative cooling in the preparation of a quantum gas. Ultimately, this method would allow for faster preparation of cold clouds of atoms, leading to higher repetition rates for experiments working with neutral particles.

A major portion of this work has been the development of a mathematical model describing the vibrational state of particles trapped in a non-harmonic state-dependent optical potential. The model is developed from first principles: first, the Hamiltonian of particle trapped in an arbitrary optical potential and interacting with laser light is determined in direct coupling formalisms. The Hamiltonian is then written in second quantization, by introducing the composite bases of the internal atomic states and the vibrational states of the optical potential. The Lindblad equation describing the time evolution of the system is then simplified using adiabatic state elimination. The resulting master rate equation describes the occupation probability of each bound level in the optical trap, and it is easily applicable to multi-level particles trapped in an optical potential of arbitrary shape, as long as the eigenvalues and eigenfunctions of such potential are known.

This thesis examines the specific case of an optical potential where the ground state of the particle is more tightly bound than its excited state ($\alpha_g > \alpha_e$). In this condition, semiclassical models of sideband cooling in harmonic state-dependent potentials suggest that cooling is not possible with a fixed laser frequency. Using both direct integration and Monte Carlo technique, numeric simulations were

performed considering different atoms, specifically $^{6}$Li and $^{174}$Yb, trapped with an optical tweezer. This allowed to explore the model parameter space with atoms having considerably different mass and transition linewidth. Results show that, in experimentally feasible conditions, it is possible to reduce the particles' average vibrational quantum number by more than 90 % using a laser frequency sweep.

To apply this novel cooling scheme in the $Ba^{+}Li$ experiment, a two-mirror optical resonator will be used to create a deep optical lattice. The resonator's optomechanics was designed to be as simple as possible, while still ensuring mirror alignment and stability. High-reflectivity mirrors were used to form the cavity, this way a sufficiently deep optical lattice can be generated by coupling a low power semiconductor laser diode, without need of additional optical amplification. The completed resonator was installed inside the MOT vacuum chamber, and was characterized using optical methods: the cavity finesse and linewidth are 28 800(80) and 78.6(2) kHz, respectively. Specific simulations where performed to assess the efficacy of single-photon sideband cooling of $^{6}$Li in a cavity-enhanced optical lattice. Results suggest that the entirety of the lithium cloud can be cooled and that a ground state occupation probability of 47.7 % is achievable after a 10 ms-long frequency sweep. The experimental setup for the realization of cold clouds of $^{6}$Li atoms was assembled and tested. The behaviour of the Li oven was characterized, and the transversal velocity of the atomic beam was estimated using spectroscopic techniques. Finally, the first cloud of $^{6}$Li atoms trapped in a MOT was observed.

In the near future, additional experimental work should be carrier out: due to the narrow cavity linewidth of the high-finesse resonator, frequency fluctuations of the laser coupled to the cavity must be precisely stabilized. Using a commercially-available PID controller, it was possible to stabilize the laser using PDH technique and achieve a linewidth of 47 kHz. A new low-noise PID controller is currently being developed with the aim of achieving a locked laser linewidth of 10 kHz or less, almost an order of magnitude smaller than the cavity linewidth.

The results presented in this thesis show that this novel cooling scheme can be employed to reduce the time required to produce a cold cloud of neutral particles. This scheme provides an alternative method for cooling atomic species for which the so-called magic wavelength — which ensures equal trapping depth for the ground and excited states — is either not known or difficult to achieve experimentally. Further exploration of the parameter space of the model presented might yield interesting results. For example, if the sidebands and carrier of the $n$-th bound level are distant enough from the sidebands and carrier of the $(n+1)$-th level, particles in different vibrational states could be addressed independently. This could be useful to engineer specific vibrational states or to evaporate particles in selected energy levels. By using quantum optimal control algorithms (such as CRAB [225]) is would be possible to optimize the shape of the frequency sweep used for sideband cooling, possibly further reducing the residual average occupation number.

# Appendix A

# Drawings of MOT coils supports

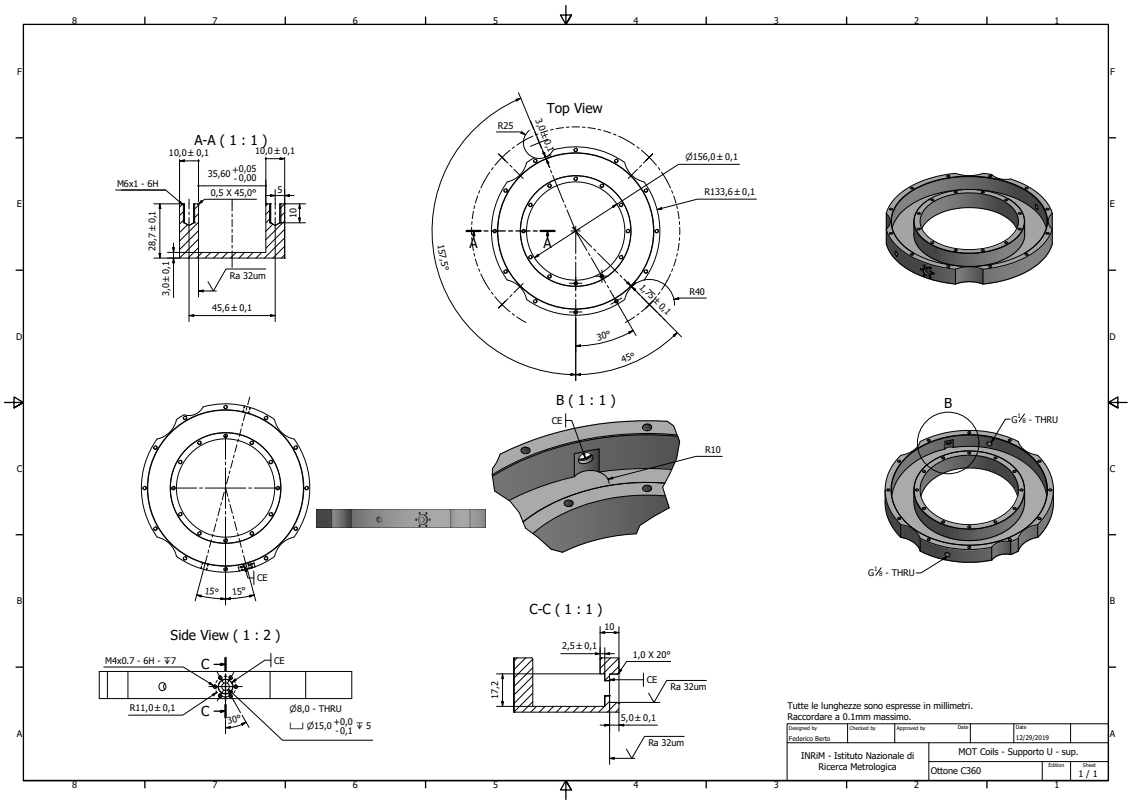

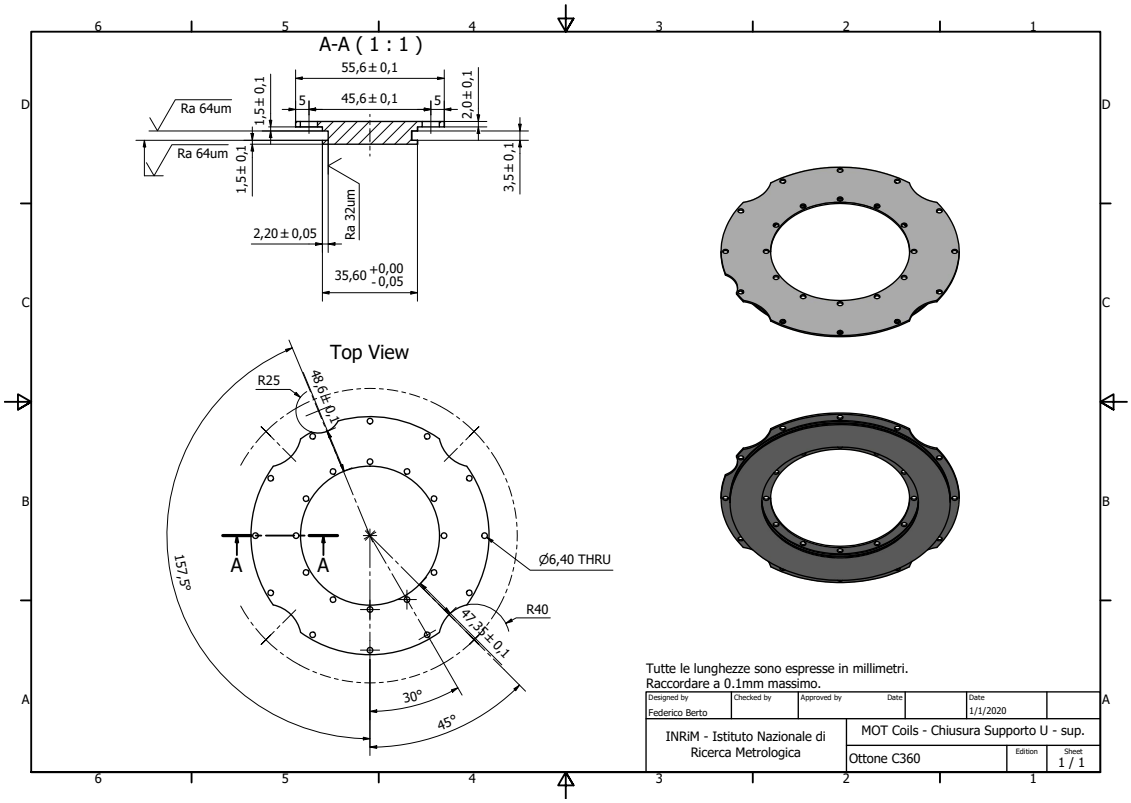
A-A ( 1 : 1 )
55,6 ± 0,1
45,6 ± 0,1
Ra 64um
Ra 64um
1,5 ± 0,1
2,0 ± 0,1
3,5 ± 0,1
2,20 ± 0,05
Ra 32um
35,60 +0,00 -0,05
Top View
R25
48,6 ± 0,1
157,5°
Ø6,40 THRU
R40
47,35 ± 0,1
30°
45°
Tutte le lunghezze sono espresse in millimetri.
Raccordare a 0.1mm massimo.
Designed by
Federico Berto
Checked by
Approved by
Date
Date
1/1/2020
INRiM - Istituto Nazionale di Ricerca Metrologica
MOT Coils - Chiusura Supporto U - sup.
Ottone C360
Edition
Sheet
1 / 1

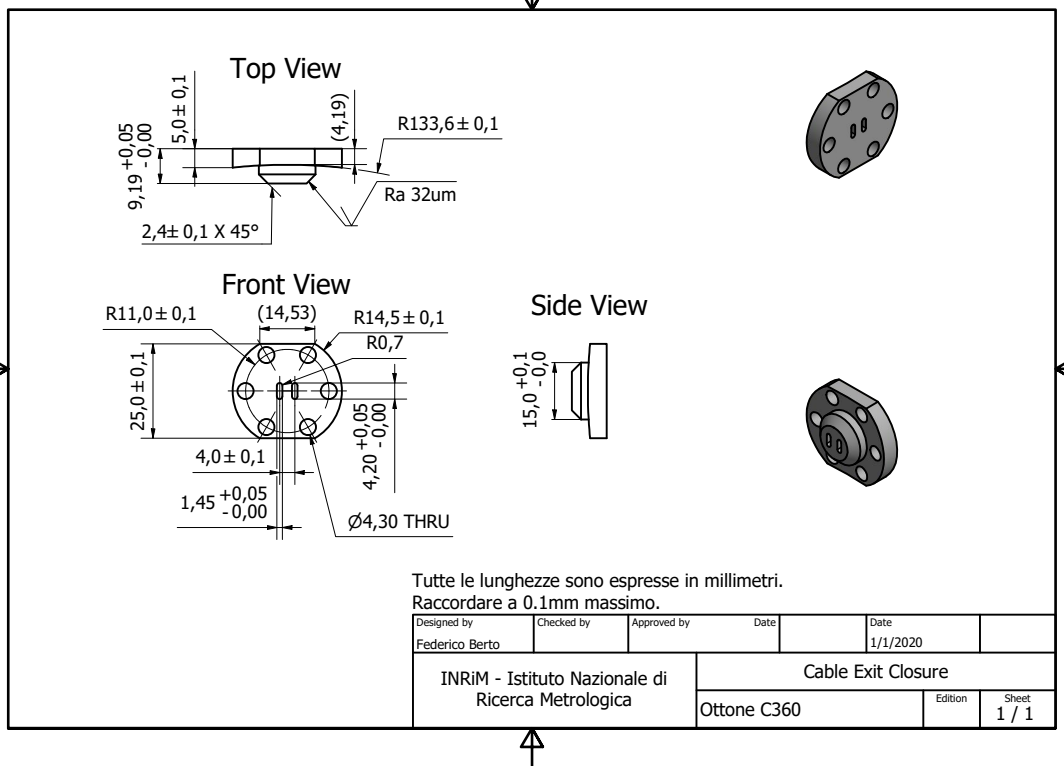
Top View
5,0 ± 0,1
(4,19)
R133,6 ± 0,1
9,19 +0,05 -0,00
Ra 32um
2,4± 0,1 X 45°
Front View
R11,0 ± 0,1
(14,53)
R14,5 ± 0,1
R0,7
25,0 ± 0,1
4,20 +0,05 -0,00
4,0 ± 0,1
1,45 +0,05 -0,00
Ø4,30 THRU
Side View
15,0 +0,1 -0,0
Tutte le lunghezze sono espresse in millimetri.
Raccordare a 0.1mm massimo.
Designed by
Federico Berto
Checked by
Approved by
Date
Date
1/1/2020
INRiM - Istituto Nazionale di Ricerca Metrologica
Cable Exit Closure
Ottone C360
Edition
Sheet
1 / 1

# Appendix B

# Drawings of Li optical resonator supports

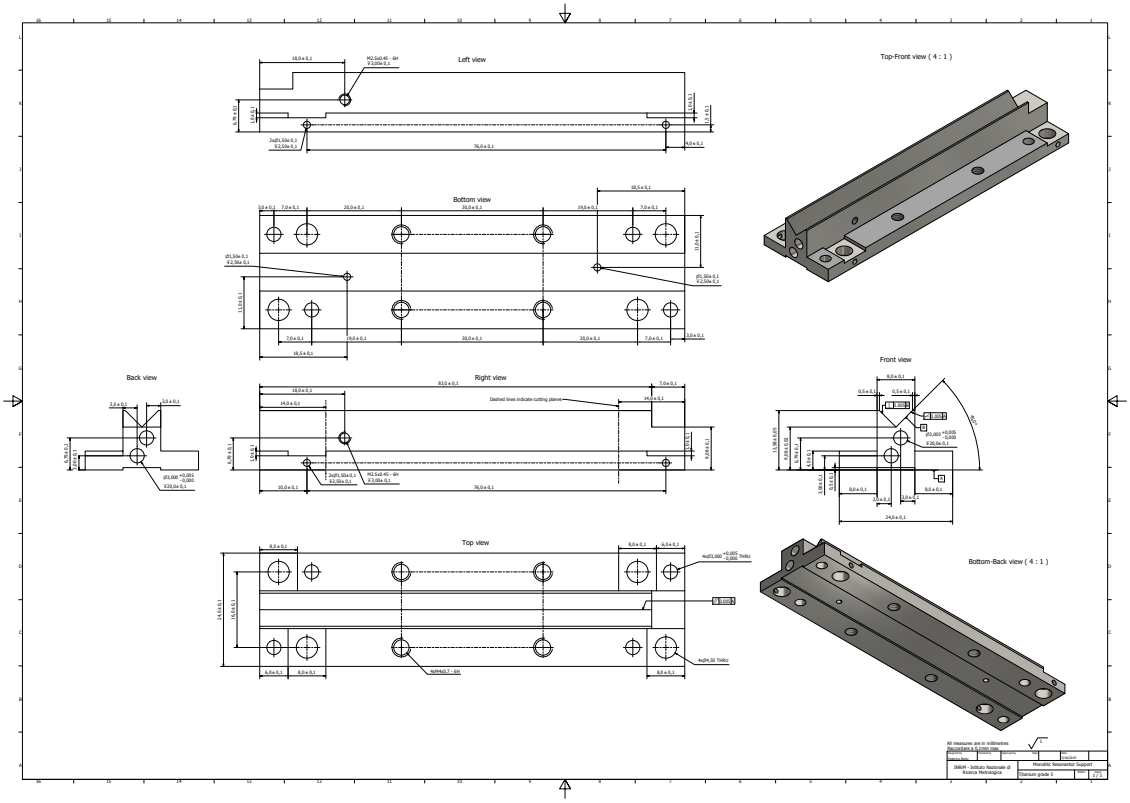

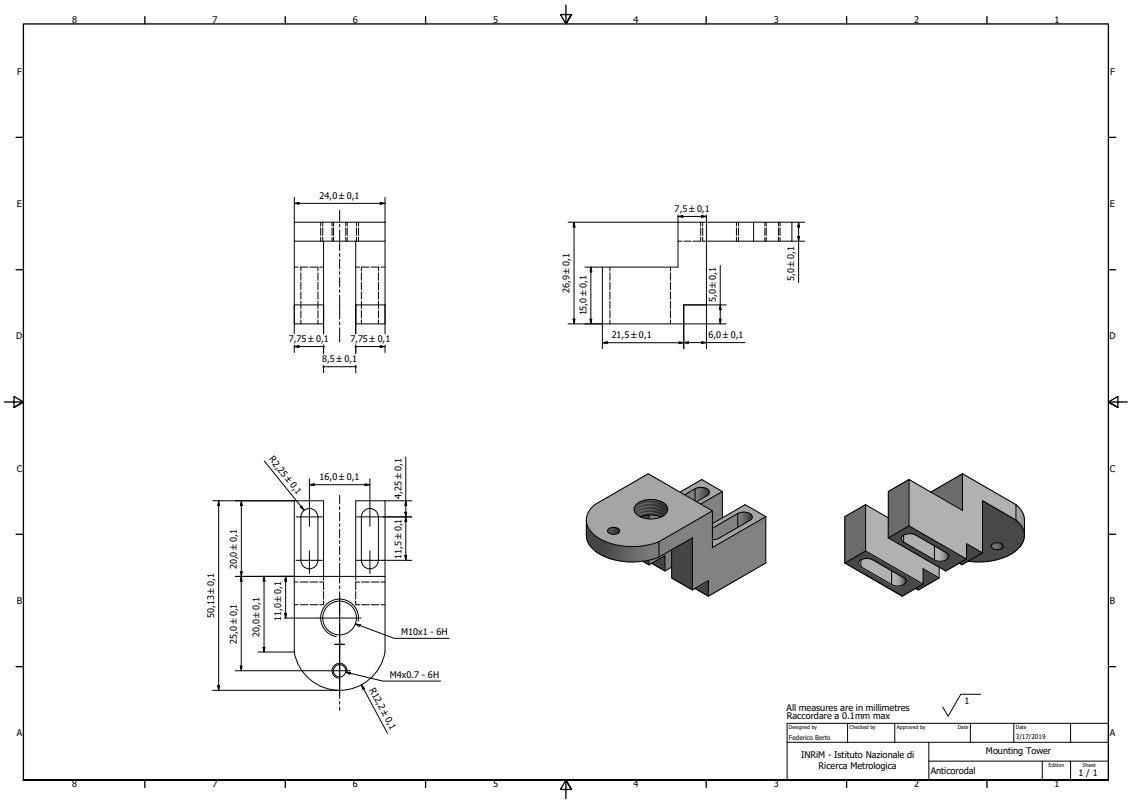
24,0± 0,1
7,75± 0,1
7,75± 0,1
8,5± 0,1
7,5± 0,1
26,9± 0,1
15,0± 0,1
5,0± 0,1
5,0± 0,1
21,5± 0,1
6,0± 0,1
R2,25±0,1
16,0± 0,1
4,25± 0,1
11,5± 0,1
20,0± 0,1
50,13± 0,1
11,0± 0,1
20,0± 0,1
25,0± 0,1
M10x1 - 6H
M4x0.7 - 6H
R12,2± 0,1
All measures are in millimetres
Raccordare a 0.1mm max
Designed by
Federico Berto
Checked by
Approved by
Date
3/17/2019
INRiM - Istituto Nazionale di Ricerca Metrologica
Mounting Tower
Anticorodal
Edition
Sheet
1 / 1

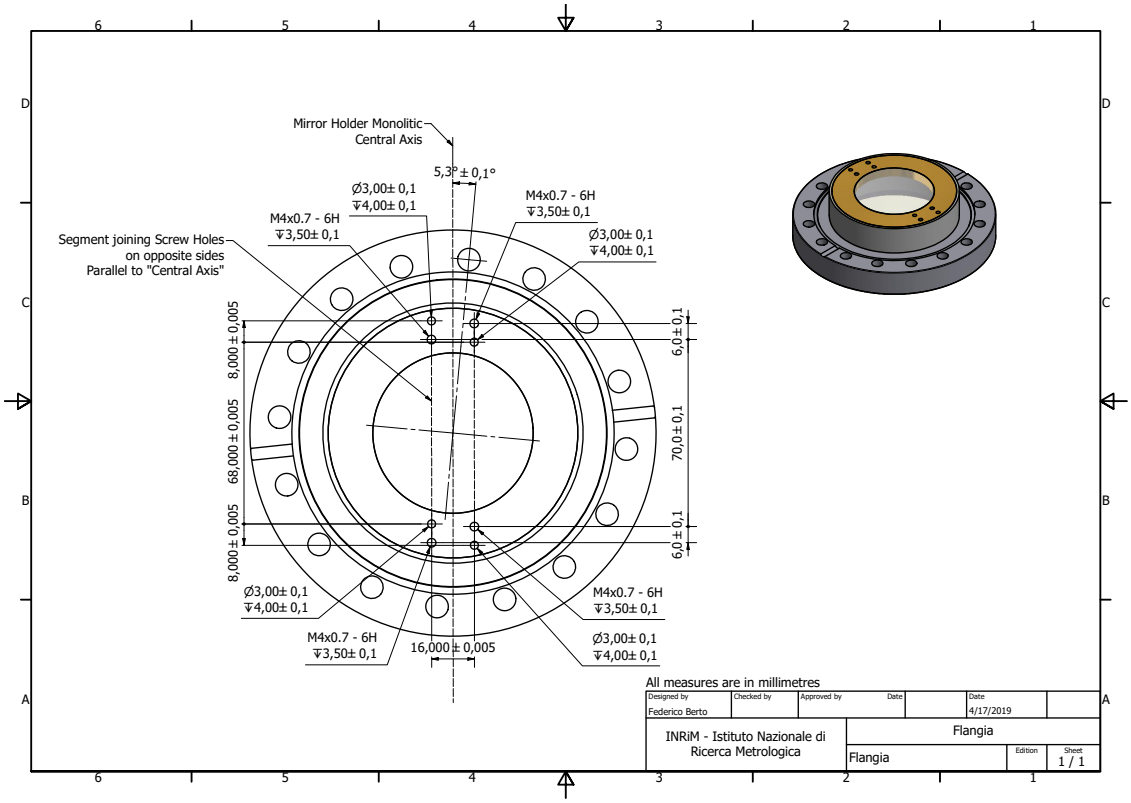
Mirror Holder Monolitic
Central Axis
5,3° ± 0,1°
Ø3,00± 0,1
Ŧ4,00± 0,1
M4x0.7 - 6H
Ŧ3,50± 0,1
Segment joining Screw Holes
on opposite sides
Parallel to "Central Axis"
8,000 ± 0,005
68,000 ± 0,005
8,000 ± 0,005
6,0± 0,1
70,0± 0,1
6,0 ± 0,1
16,000 ± 0,005
All measures are in millimetres
Designed by
Federico Berto
Checked by
Approved by
Date
4/17/2019
INRiM - Istituto Nazionale di Ricerca Metrologica
Flangia
Edition
Sheet
1 / 1

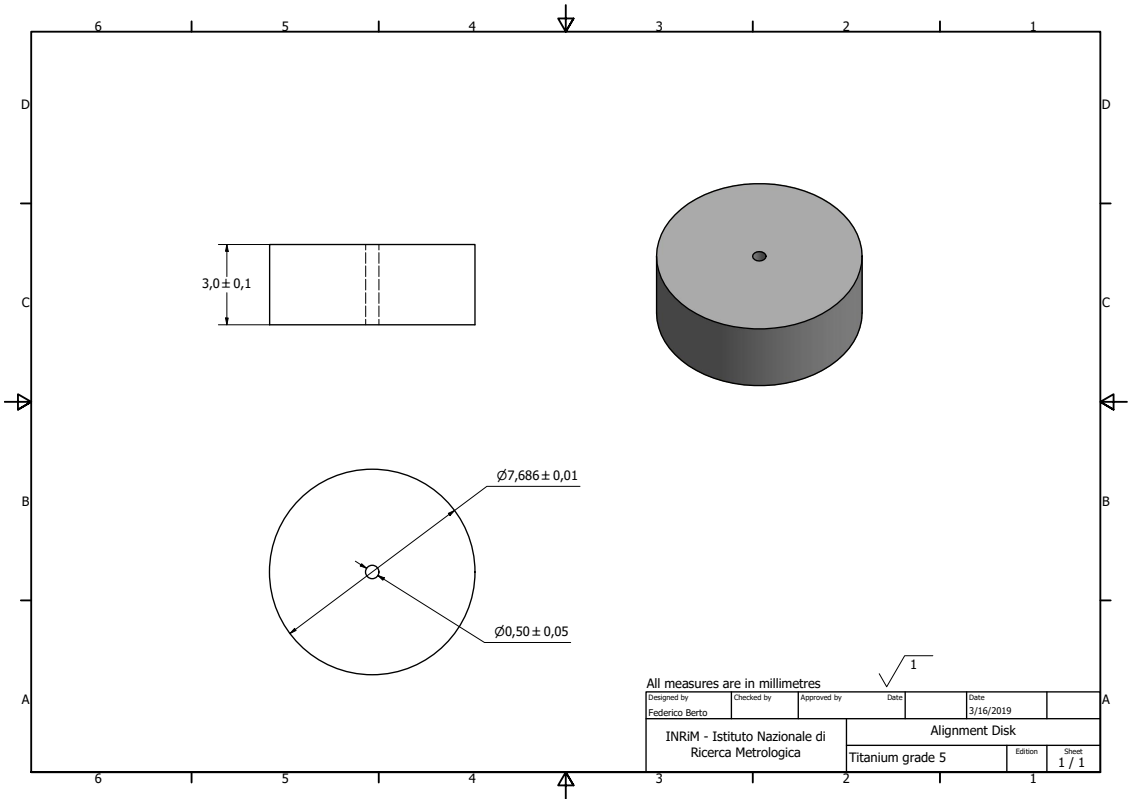
3,0 ± 0,1
Ø7,686 ± 0,01
Ø0,50 ± 0,05
All measures are in millimetres
Designed by
Federico Berto
Checked by
Approved by
Date
3/16/2019
INRiM - Istituto Nazionale di Ricerca Metrologica
Alignment Disk
Titanium grade 5
Edition
Sheet
1 / 1

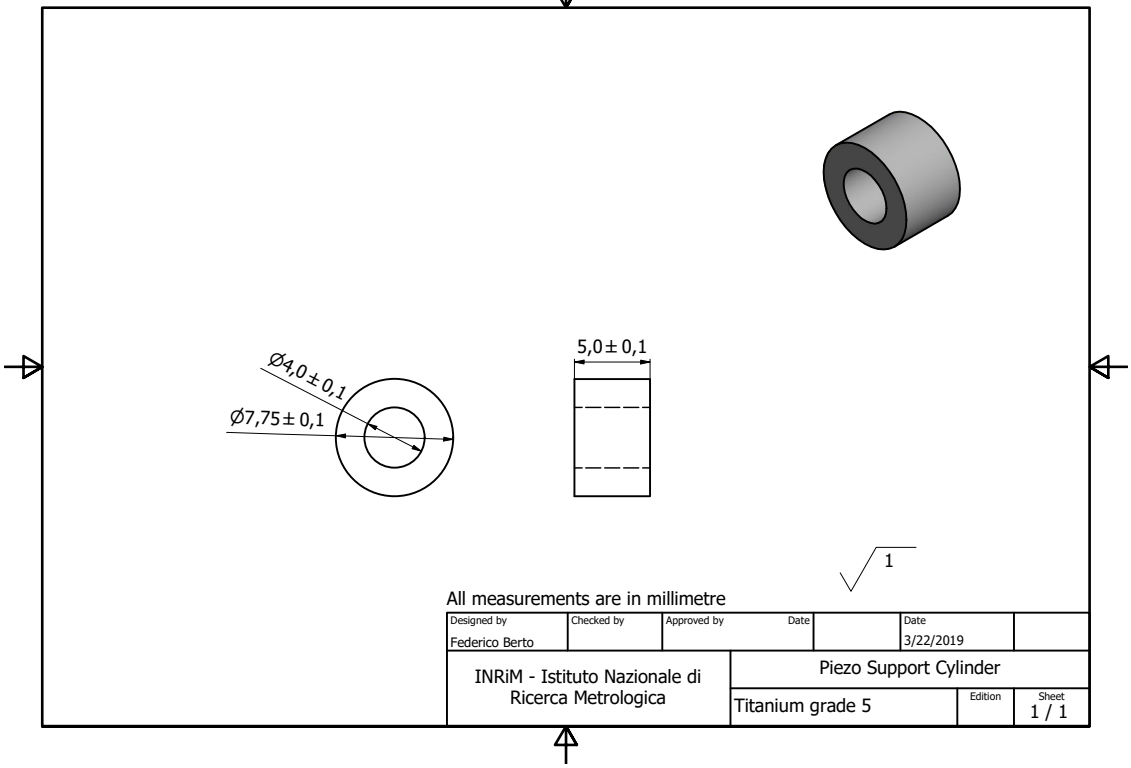
Ø4,0 ± 0,1
Ø7,75 ± 0,1
5,0 ± 0,1
All measurements are in millimetre
Designed by
Federico Berto
Checked by
Approved by
Date
3/22/2019
INRiM - Istituto Nazionale di Ricerca Metrologica
Piezo Support Cylinder
Titanium grade 5
Edition
Sheet
1 / 1

# Appendix C

# RWA and rotating-frame transformation

In this appendix additional mathematical details concerning to the RWA and the transformation to a rotating frame of reference are presented.

## C.1 Rotating wave approximation (RWA)

In the semiclassical treatment of matter-light interactions, the Hamiltonian of an atom interacting with photons having an electric field $\boldsymbol{\mathcal{E}}_{\mathrm{c}} = \boldsymbol{\epsilon}\, \mathcal{E}_0^{(\mathrm{c})} \cos(\mathbf{k}_{\mathrm{c}} \cdot \mathbf{r} - \omega_{\mathrm{c}} t)$ can be written as

$$H = H_0 - \mathbf{d} \cdot \boldsymbol{\mathcal{E}}_{\mathrm{c}}\,,$$

where $H_0$ is the unperturbed atom Hamiltonian and $\mathbf{d}$ the atom's dipole moment. The atom is approximated as a TLS with states

$$|g\rangle = \begin{pmatrix} 1 \\ 0 \end{pmatrix} \qquad |e\rangle = \begin{pmatrix} 0 \\ 1 \end{pmatrix},$$

and its Hamiltonian takes the form

$$H_0 = \frac{\hbar}{2} \begin{pmatrix} -\omega_0 & 0 \\ 0 & \omega_0 \end{pmatrix},$$

where $\omega_0$ is the Bohr frequency of the TLS. The system wavefunction $|\psi\rangle = c_g\,|g\rangle + c_e\,|e\rangle$ has to respect the Schrödinger equation

$$i\hbar \frac{\partial\,|\psi\rangle}{\partial t} = (H_0 - \mathbf{d} \cdot \boldsymbol{\mathcal{E}}_{\mathrm{c}})\,|\psi\rangle = (H_0 - H')\,|\psi\rangle\ .$$

Under the assumption that the matter-light interaction term can be considered as a small perturbation of the system, the expansion coefficients $c_g$ and $c_e$ can be found

using first order time perturbation theory (ref. [60], chapter 8)

$$\begin{cases} c_g(t) &= (i\hbar)^{-1} \int c_e(t) \, \langle g|H'|e\rangle \, e^{-i\omega_0 t'} \, \mathrm{d}t' \ , \\ c_e(t) &= (i\hbar)^{-1} \int c_g(t) \, \langle e|H'|g\rangle \, e^{+i\omega_0 t'} \, \mathrm{d}t' \ , \end{cases}$$

and

$$\langle e|H'|g\rangle = \frac{e_0}{2} \left\langle e \middle| (\mathbf{r} \cdot \boldsymbol{\epsilon} \, \mathcal{E}_0^{\mathrm{c}}) \left( e^{i(\mathbf{k}_{\mathrm{c}} \cdot \mathbf{r} - \omega_{\mathrm{c}} t)} + e^{-i(\mathbf{k}_{\mathrm{c}} \cdot \mathbf{r} - \omega_{\mathrm{c}} t)} \right) \middle| g \right\rangle \ ,$$

where $\mathbf{d} = -e_0 \mathbf{r}$ has been used and $e_0$ is the elementary electric charge. The exponential term $e^{i\mathbf{k}_{\mathrm{c}} \cdot \mathbf{r}}$ can be approximated as 1, this can be justified by considering that most atomic wavefunctions are confined to just a few nm, while visible and near UV light — commonly used to manipulate atoms — has a wavelength of a few hundreds nm, thus $\mathbf{k}_{\mathrm{c}} \cdot \mathbf{r} \ll 1$. This approximation is distinct from the RWA, and (strictly speaking) non-necessary other than for mathematical simplicity. It follows that

$$\langle e|H'|g\rangle = \frac{\hbar\Omega}{2} \left( e^{-i\omega_{\mathrm{c}} t} + e^{i\omega_{\mathrm{c}} t} \right) ,$$

and $\Omega = e_0 \mathcal{E}_0 \, \langle e|\mathbf{r} \cdot \boldsymbol{\epsilon}|g\rangle \, / \hbar$ is the Rabi frequency. By inserting this final expression into the formulae for $c_g(t)$ and $c_e(t)$, two types of terms are obtained: one term oscillates in time at frequency $\omega_{\mathrm{c}} - \omega_0$ — this difference is commonly referred to as the *detuning* and indicated as $\Delta$ — and a second one oscillating at $\omega_{\mathrm{c}} + \omega_0$. If the light field is nearly resonant with the TLS transition then the terms oscillating at $\omega_{\mathrm{c}} + \omega_0$ average out in the time integral and can be neglected. This step is the RWA approximation.

The approximated interaction Hamiltonian that leads to the same approximated expressions of $c_g(t)$ and $c_e(t)$ is

$$H' = \frac{\hbar\Omega}{2} \begin{pmatrix} 0 & e^{-i\omega_{\mathrm{c}} t} \\ e^{i\omega_{\mathrm{c}} t} & 0 \end{pmatrix} .$$

## C.2 Rotating frame transformation

The rotating frame transformation is a geometric transformation to a frame of reference that rotates at the frequency of the laser. The aim of this transformation is to remove the time dependency terms from the interaction Hamiltonian $H'$. Following from the previous section the complete Hamiltonian of a TLS interacting with a laser $\boldsymbol{\mathcal{E}}_{\mathrm{c}}$ is written in matrix form as

$$H = \frac{\hbar}{2} \begin{pmatrix} -\omega_0 & \Omega e^{-i\omega_{\mathrm{c}} t} \\ \Omega e^{i\omega_{\mathrm{c}} t} & \omega_0 \end{pmatrix} .$$

To perform the rotating frame transformation, a rotation matrix is introduced

$$U = \begin{pmatrix} e^{if(t)} & 0 \\ 0 & e^{-if(t)} \end{pmatrix} ,$$

where $f(t)$ is an arbitrary c-valued function. The system wavefunction is rotated as $\psi_{\mathrm{RF}} = U\psi$, while the rotated Hamiltonian is obtained as follows (ref. [226], lecture 3)

$$\begin{aligned} i\hbar\frac{\partial\psi_{\mathrm{RF}}}{\partial t} &= i\hbar\frac{\partial U\psi}{\partial t} \\ &= i\hbar\begin{pmatrix} ie^{if(t)}\dot{f}(t) & 0 \\ 0 & -ie^{-if(t)}\dot{f}(t) \end{pmatrix}\psi + i\hbar U\frac{\partial\psi}{\partial t} \\ &= i\hbar\begin{pmatrix} i\dot{f}(t) & 0 \\ 0 & -i\dot{f}(t) \end{pmatrix}U\psi + UH\psi \\ &= \hbar\begin{pmatrix} -\dot{f}(t) & 0 \\ 0 & +\dot{f}(t) \end{pmatrix}\psi_{\mathrm{RF}} + UHU^{\dagger}\psi_{\mathrm{RF}}\,, \end{aligned}$$

that is

$$\begin{aligned} H_{\mathrm{RF}} &= UHU^{\dagger} + \hbar\begin{pmatrix} -\dot{f}(t) & 0 \\ 0 & +\dot{f}(t) \end{pmatrix} \\ &= \hbar\begin{pmatrix} -\frac{\omega_0}{2} - \dot{f}(t) & \Omega e^{i\omega_c t}e^{2if(t)} \\ \Omega e^{-i\omega_c t}e^{-2if(t)} & \frac{\omega_0}{2} + \dot{f}(t) \end{pmatrix}. \end{aligned}$$

If one chooses $f(t) = -\omega_c/2t$ the time dependency of anti-diagonal terms is removed and the Hamiltonian results in

$$H_{\mathrm{RF}} = \frac{\hbar}{2}\begin{pmatrix} -\omega_0 + \omega_c & \Omega \\ \Omega & \omega_0 - \omega_c \end{pmatrix} = \frac{\hbar}{2}\begin{pmatrix} \Delta & \Omega \\ \Omega & -\Delta \end{pmatrix}.$$

# Appendix D

# Equivalence of existing sideband cooling models

In this appendix the equivalence between the model presented in chapter 5 and the sideband cooling model presented in chapter 2 is demonstrated under the assumptions of a harmonic state-independent trapping potential.

Under these assumptions the bound states for the TLS internal ground and excited states are equal $|n_g\rangle = |n_e\rangle$ and the overlap integrals $\langle n_g|m_e\rangle$ can be computed as Kronecker deltas $\delta_{n_g,m_e}$, thus the matrix elements $\langle m_e|e^{-i\mathbf{k_c}\cdot\mathbf{r}}|n_g\rangle$ result

$$\langle m_e|e^{-i\mathbf{k_c}\cdot\mathbf{r}}|n_g\rangle = \delta_{m_e,n_g} + i\,\eta\left[(m_e+1)\,\delta_{m_e+1,n_g} + m_e\,\delta_{m_e-1,n_g}\right],$$

By direct substitution, the decay rates $\gamma_{m_e,n_g}$ (eq. (5.8)) and the matrix elements $M_{n_g,m_e}$ become

$$\begin{aligned}\gamma_{m_e,n_g} &= \frac{\gamma}{2}\delta_{n_g,m_e} + \frac{\gamma}{2}\eta^2\alpha\left[(m_e+1)\,\delta_{n_g,m_e+1} + m_e\,\delta_{n_g,m_e-1}\right],\\ M_{n_g,m_e} &= \delta_{m_e,n_g} + \eta^2\left[(n_g+1)\,\delta_{m_e,n_g+1} + n_g\,\delta_{m_e,n_g-1}\right],\end{aligned}$$

where $\alpha = \int_{-1}^{+1} u^2 N(u)\,\mathrm{d}u = 2/5$. From now on, the subscript $g, e$ in $n_g$ and $m_e$ will be dropped, as it is not needed any more. Substitution in eq. (5.10) gives

$$\begin{aligned}\dot{\Pi}_n = &-\sum_k \Big\{\frac{\gamma}{2}\Gamma(\Delta_{kn})|M_{nk}|^2\\ &\qquad + \frac{\gamma}{2}\eta^2\alpha\left[k|M_{n,k-1}|^2\Gamma(\Delta_{k-1,n}) + (k+1)|M_{n,k+1}|^2\Gamma(\Delta_{k+1,n})\right]\Big\}\Pi_n\\ &+\sum_k \Big\{\frac{\gamma}{2}\Gamma(\Delta_{nk})|M_{kn}|^2\\ &\qquad + \frac{\gamma}{2}\eta^2\alpha\left[n|M_{k,n-1}|^2\Gamma(\Delta_{n-1,k}) + (n+1)|M_{k,n+1}|^2\Gamma(\Delta_{n+1,k})\right]\Big\}\Pi_k\,.\end{aligned}$$

After inserting the expression for $M_{n,k}$ and some manipulation, one arrives at

$$\begin{aligned}\dot{\Pi}_n = -\Big\{ &\cancel{\frac{\gamma}{2}\Gamma(\Delta_{kn})} + \frac{\gamma}{2}\eta^2[(n+1)\Gamma(\Delta_{n+1,n}) + n\Gamma(\Delta_{n-1,n})] \\ &+ \frac{\gamma}{2}\eta^2\alpha[(n+1)\Gamma(\Delta_{nn}) + n\Gamma(\Delta_{nn})]\Big\}\Pi_n \\ + &\cancel{\frac{\gamma}{2}\Gamma(\Delta_{kn})}\Pi_n + \frac{\gamma}{2}\eta^2[n\Gamma(\Delta_{n,n-1})\Pi_{n-1} + (n+1)\Gamma(\Delta_{n,n+1})\Pi_{n+1}] \\ &+ \frac{\gamma}{2}\eta^2\alpha[n\Gamma(\Delta_{n-1,n-1})\Pi_{n-1} + (n+1)\Gamma(\Delta_{n+1,n+1})\Pi_{n+1}]\,,\end{aligned}$$

where terms in orders of $\eta^4$ have been neglected. With the relations $\Gamma(\Delta_{n\pm1,n}) = \Gamma(\Delta\pm\nu)$ and $\Gamma(\Delta_{n,n\pm1}) = \Gamma(\Delta\mp\omega_{\mathrm{tr}})$, where $\omega_{\mathrm{tr}}$ is the harmonic potential frequency, the rate equation results

$$\begin{aligned}\dot{\Pi}_n &= -\frac{\gamma}{2}\eta^2\{(n+1)[\Gamma(\Delta+\omega_{\mathrm{tr}}) + \alpha\Gamma(\Delta)] + n[\Gamma(\Delta-\omega_{\mathrm{tr}}) + \alpha\Gamma(\Delta)]\}\Pi_n \\ &\quad + \frac{\gamma}{2}\eta^2\Big\{\Pi_{n+1}(n+1)[\Gamma(\Delta-\omega_{\mathrm{tr}}) + \alpha\Gamma(\Delta)] \\ &\qquad + \Pi_{n-1}n[\Gamma(\Delta+\omega_{\mathrm{tr}}) + \alpha\Gamma(\Delta)]\Big\} \\ &= -\eta^2\{[(n+1)\,A_+ + n\,A_-]\Pi_n + (n+1)\,A_-\,\Pi_{n+1} + n\,A_+\,\Pi_{n-1}\}\,,\end{aligned}$$

where

$$\begin{aligned}A_+ &= \gamma[\Gamma(\Delta+\omega_{\mathrm{tr}}) + \alpha\Gamma(\Delta)]\,, \\ A_- &= \gamma[\Gamma(\Delta-\omega_{\mathrm{tr}}) + \alpha\Gamma(\Delta)]\,.\end{aligned}$$

These relations are identical to eq. (2.15) and eq. (2.14) presented in section 2.1.5.

# Appendix E

# Ion detection algorithm

Fast and accurate determination of ions' temperature plays a crucial role in trapped ions experiments. In particular, if the ions' temperature can be determined in real time, then inline automated feedback protocols can be implemented for the reduction and compensation of excess micromotion in RF traps. For this purpose, an established technique is ion thermometry using high-resolution imaging [227, 228], which allows for the determination of the ions' temperature and heating rates from a measurement of their delocalization in position space.

A fast data analysis algorithm is a necessary component of any automated control protocol. For the specific case of high-resolution imaging of ions, 2D images must be processed with the aim of extrapolating the ions number, positions, and size of their delocalization. With this aim in mind, an ion-detection algorithm was developed at the $Ba^+Li$ experiment capable of counting and determining the size of ions without any *a priori* knowledge.

## E.1 Implementation

The RMS spread of the ion in position space is directly proportional to the square root of its temperature or, equivalently, the average excitation number of the trap. Therefore, the ion's fluorescence is expected to form a Gaussian-like intensity peak when recorded by a CCD camera[1]. An exemplary image of 6 ions trapped in the Paul trap at the $Ba^+Li$ experiment is shown in fig. E.1a, the data is a 2D array of 8-bit integers representing the intensity at each pixel. To determine the ions spread in position space, the analysis algorithm is required to detect any Gaussian-like peaks and perform a fit of a 2D Gaussian on each peak. To do so, the following multi-step algorithm has been devised:

[1] Andor, iXon Ultra 888

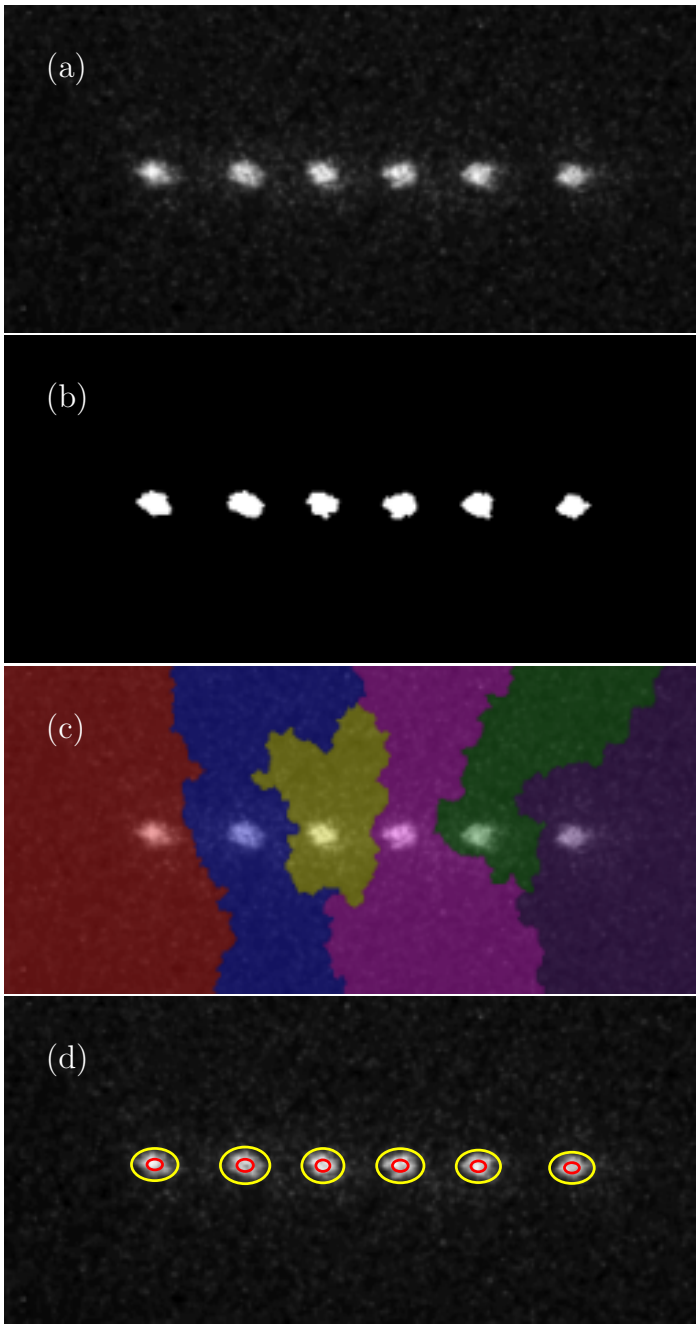


Figure E.1: Visual representation of various steps of the ion-detection algorithm. Image data is stored as a 2D $164 \times 342$ 8-bit array. (a) Raw image. (b) Image after thresholding and morphological opening. (c) Image after the application of the watershed algorithm. The image has been divided into different regions indicated by different colours. (d) Fitting results: the red and yellow circles indicate one time and three times the RMS spread of the ion distribution, respectively.

1. **Thresholding:** Otsu's threshold is used to filter out low-intensity noise. Otsu's method is particularly suited for automated image thresholding as it was devised to separate the pixels of an image into two classes: foreground (high-intensity) and background (low-intensity).

2. **Opening:** the so-called *salt-and-pepper noise* is an image noise characterized by the random activation or inactivity of single pixels, giving the impression that white or black powder was sprinkled over the image (hence the name). The *opening* is a morphological operation that is capable of removing small objects from the foreground. The results of applying Otsu's threshold followed by morphological opening on fig. E.1a are shown in fig. E.1b. Small dark-regions that may be present in the remaining white regions do not constitute a problem for the remainder of the algorithm.

3. **Labelling:** each group of connected white pixels is labelled with a number starting from 0 (background).

4. **Watershed:** the watershed algorithm treats the image as if the intensity of the pixels represents the height of a surface in 3D. This algorithm is then capable of determining the border lines that run across the ridges of this surface. By using the labelled regions from the previous step as seed points for the watershed algorithm, it will divide the image into multiple regions each containing a single ion's signal. The results of applying the watershed on fig. E.1a are shown in fig. E.1c.

5. **Fitting:** each region determined by the watershed is guaranteed to contain the signal from a single ion. Therefore, it is possible to fit a single Gaussian-peak per region to determine the position and spread of the ion. The model used in the fit is a 2D Gaussian function summed to a fist-order polynomial baseline. The results of the fitting are shown in fig. E.1d. This fitting step is always performed on the original image, the information obtained from the previous steps is only used to determine the initial point of the fitting procedure and which region of the image this procedure is performed on. This way any small changes in the ion signal which were introduced during noise cleaning (step 1 and 2), will not affect the determination of the ion's RMS spread.

The watershed algorithm constitutes both the strong and weak point of this ion-detection algorithm. On the one hand, it allows for the automatic fracturing of the image into regions that are guaranteed to contain only one ion's signal. This enables the possibility performing the fitting step on multiple ions in parallel; theoretically, the ion detection should not slow down if the number of ions seen by the camera increases. Preliminary test show that a repetition rate of 10 frames per second is achievable. On the other hand, as it can be clearly seen from fig. E.1c,

after the watershed the image is cut into regions of considerable different size and shape. This can be a problem for fitting step, since it is impossible to determine if a region is encompassing a sufficiently large amount of background pixels, which are required for a proper determination of the signal's baseline.

# Bibliography


[1] L. Fallani and A. Kastberg. "Cold atoms: A field enabled by light". In: *EPL (Europhysics Letters)* 110.5 (June 2015), p. 53001. DOI: 10.1209/0295-5075/110/53001.

[2] Cheng Chin et al. "Feshbach resonances in ultracold gases". In: *Reviews of Modern Physics* 82.2 (Apr. 2010), pp. 1225–1286. DOI: 10.1103/revmodphys.82.1225.

[3] M. Saffman, T. G. Walker, and K. Mølmer. "Quantum information with Rydberg atoms". In: *Reviews of Modern Physics* 82.3 (Aug. 2010), pp. 2313–2363. DOI: 10.1103/revmodphys.82.2313.

[4] Maciej Lewenstein et al. "Ultracold atomic gases in optical lattices: mimicking condensed matter physics and beyond". In: *Advances in Physics* 56.2 (Mar. 2007), pp. 243–379. DOI: 10.1080/00018730701223200.

[5] Omjyoti Dutta et al. "Non-standard Hubbard models in optical lattices: a review". In: *Reports on Progress in Physics* 78.6 (May 2015), p. 066001. DOI: 10.1088/0034-4885/78/6/066001.

[6] F. Nogrette et al. "Single-Atom Trapping in Holographic 2D Arrays of Microtraps with Arbitrary Geometries". In: *Physical Review X* 4.2 (May 2014), p. 021034. DOI: 10.1103/physrevx.4.021034.

[7] I. Bloch. "Quantum Gases". In: *Science* 319.5867 (Feb. 2008), pp. 1202–1203. DOI: 10.1126/science.1152501.

[8] R Miller et al. "Trapped atoms in cavity QED: coupling quantized light and matter". In: *Journal of Physics B: Atomic, Molecular and Optical Physics* 38.9 (Apr. 2005), S551–S565. DOI: 10.1088/0953-4075/38/9/007.

[9] Immanuel Bloch, Jean Dalibard, and Wilhelm Zwerger. "Many-body physics with ultracold gases". In: *Reviews of Modern Physics* 80.3 (July 2008), pp. 885–964. DOI: 10.1103/revmodphys.80.885.

[10] Stefano Giorgini, Lev P. Pitaevskii, and Sandro Stringari. "Theory of ultracold atomic Fermi gases". In: *Reviews of Modern Physics* 80.4 (Oct. 2008), pp. 1215–1274. DOI: 10.1103/revmodphys.80.1215.

[11] Immanuel Bloch, Jean Dalibard, and Sylvain Nascimbène. "Quantum simulations with ultracold quantum gases". In: *Nature Physics* 8.4 (Apr. 2012), pp. 267–276. DOI: 10.1038/nphys2259.

[12] Hannes Bernien et al. "Probing many-body dynamics on a 51-atom quantum simulator". In: *Nature* 551.7682 (Nov. 2017), pp. 579–584. DOI: 10.1038/nature24622.

[13] D. Jaksch and P. Zoller. "The cold atom Hubbard toolbox". In: *Annals of Physics* 315.1 (Jan. 2005), pp. 52–79. DOI: 10.1016/j.aop.2004.09.010.

[14] C. Monroe. "Quantum information processing with atoms and photons". In: *Nature* 416.6877 (Mar. 2002), pp. 238–246. DOI: 10.1038/416238a.

[15] Th. Udem, R. Holzwarth, and T. W. Hänsch. "Optical frequency metrology". In: *Nature* 416.6877 (Mar. 2002), pp. 233–237. DOI: 10.1038/416233a.

[16] Susannah M. Dickerson et al. "Multiaxis Inertial Sensing with Long-Time Point Source Atom Interferometry". In: *Physical Review Letters* 111.8 (Aug. 2013), p. 083001. DOI: 10.1103/physrevlett.111.083001.

[17] Brenton C. Young et al. "Lasers for an optical frequency standard using trapped $Hg^+$ ions". In: AIP, 1999. DOI: 10.1063/1.57474.

[18] Ch. Roos et al. "Quantum State Engineering on an Optical Transition and Decoherence in a Paul Trap, Ion". In: *Physical Review Letters* 83.23 (Dec. 1999), pp. 4713–4716. DOI: 10.1103/physrevlett.83.4713.

[19] Pengfei Wang et al. "Single ion qubit with estimated coherence time exceeding one hour". In: *Nature Communications* 12.1 (Jan. 2021). DOI: 10.1038/s41467-020-20330-w.

[20] N. Huntemann et al. "Single-Ion Atomic Clock with $3 \times 10^{-18}$ Systematic Uncertainty". In: *Physical Review Letters* 116.6 (Feb. 2016), p. 063001. DOI: 10.1103/physrevlett.116.063001.

[21] F DiFilippo et al. "Accurate atomic mass measurements from Penning trap mass comparisons of individual ions". In: *Physica Scripta* T59 (Jan. 1995), pp. 144–154. DOI: 10.1088/0031-8949/1995/t59/018.

[22] Michael Drewsen. "Ion Coulomb crystals". In: *Physica B: Condensed Matter* 460 (Mar. 2015), pp. 105–113. DOI: 10.1016/j.physb.2014.11.050.

[23] R. Blümel et al. "Chaos and order of laser-cooled ions in a Paul trap". In: *Physical Review A* 40.2 (July 1989), pp. 808–823. DOI: 10.1103/physreva.40.808.

[24] H. M. VAN HORN. "Dense Astrophysical Plasmas". In: *Science* 252.5004 (Apr. 1991), pp. 384–389. DOI: 10.1126/science.252.5004.384.

[25] Peter Horak, Aurélien Dantan, and Michael Drewsen. "Optically induced structural phase transitions in ion Coulomb crystals". In: *Physical Review A* 86.4 (Oct. 2012), p. 043435. DOI: 10.1103/physreva.86.043435.

[26] Klaus Mølmer and Anders Sørensen. "Multiparticle Entanglement of Hot Trapped Ions". In: *Physical Review Letters* 82.9 (Mar. 1999), pp. 1835–1838. DOI: 10.1103/physrevlett.82.1835.

[27] I. Pogorelov et al. "Compact Ion-Trap Quantum Computing Demonstrator". In: *PRX Quantum* 2.2 (June 2021), p. 020343. DOI: 10.1103/prxquantum.2.020343.

[28] Michał Tomza et al. "Cold hybrid ion-atom systems". In: *Rev. Mod. Phys. 91, 035001 (2019)* (Aug. 2017). DOI: 10.1103/RevModPhys.91.035001. arXiv: 1708.07832 [physics.atom-ph].

[29] Zbigniew Idziaszek et al. "Multichannel quantum-defect theory for ultracold atom-ion collisions". In: *New Journal of Physics* 13.8 (Aug. 2011), p. 083005. DOI: 10.1088/1367-2630/13/8/083005.

[30] Pascal Weckesser et al. "Observation of Feshbach resonances between a single ion and ultracold atoms". In: (May 2021). arXiv: 2105.09382 [physics.atom-ph].

[31] Felix H. J. Hall et al. "Light-Assisted Ion-Neutral Reactive Processes in the Cold Regime: Radiative Molecule Formation versus Charge Exchange". In: *Physical Review Letters* 107.24 (Dec. 2011), p. 243202. DOI: 10.1103/physrevlett.107.243202.

[32] Arne Härter et al. "Single Ion as a Three-Body Reaction Center in an Ultracold Atomic Gas". In: *Physical Review Letters* 109.12 (Sept. 2012), p. 123201. DOI: 10.1103/physrevlett.109.123201.

[33] Tomas Sikorsky et al. "Spin-controlled atom-ion chemistry". In: *Nature Communications* 9.1 (Mar. 2018). DOI: 10.1038/s41467-018-03373-y.

[34] Lothar Ratschbacher et al. "Controlling chemical reactions of a single particle". In: *Nature Physics* 8.9 (July 2012), pp. 649–652. DOI: 10.1038/nphys2373.

[35] Theodore P. Snow and Veronica M. Bierbaum. "Ion Chemistry in the Interstellar Medium". In: *Annual Review of Analytical Chemistry* 1.1 (July 2008), pp. 229–259. DOI: 10.1146/annurev.anchem.1.031207.112907.

[36] U. Bissbort et al. "Emulating Solid-State Physics with a Hybrid System of Ultracold Ions and Atoms". In: *Physical Review Letters* 111.8 (Aug. 2013), p. 080501. DOI: 10.1103/physrevlett.111.080501.

[37] Michael Knap et al. "Time-Dependent Impurity in Ultracold Fermions: Orthogonality Catastrophe and Beyond". In: *Physical Review X* 2.4 (Dec. 2012), p. 041020. DOI: 10.1103/physrevx.2.041020.

[38] D. J. Larson et al. "Sympathetic cooling of trapped ions: A laser-cooled two-species nonneutral ion plasma". In: *Physical Review Letters* 57.1 (July 1986), pp. 70–73. DOI: 10.1103/physrevlett.57.70.

[39] A. Kellerbauer et al. "Buffer gas cooling of ion beams". In: *Nuclear Instruments and Methods in Physics Research Section A: Accelerators, Spectrometers, Detectors and Associated Equipment* 469.2 (Aug. 2001), pp. 276–285. DOI: 10.1016/s0168-9002(01)00286-8.

[40] Corinna Kollath, Michael Köhl, and Thierry Giamarchi. "Scanning tunneling microscopy for ultracold atoms". In: *Physical Review A* 76.6 (Dec. 2007), p. 063602. DOI: 10.1103/physreva.76.063602.

[41] Andrew T. Grier et al. "Observation of Cold Collisions between Trapped Ions and Trapped Atoms". In: *Physical Review Letters* 102.22 (June 2009), p. 223201. DOI: 10.1103/physrevlett.102.223201.

[42] Oleg P. Makarov et al. "Radiative charge-transfer lifetime of the excited state of $(NaCa^+)$". In: *Physical Review A* 67.4 (Apr. 2003), p. 042705. DOI: 10.1103/physreva.67.042705.

[43] Ziv Meir et al. "Experimental apparatus for overlapping a ground-state cooled ion with ultracold atoms". In: *Journal of Modern Optics* 65.5-6 (Nov. 2017), pp. 501–519. DOI: 10.1080/09500340.2017.1397217.

[44] Shinsuke Haze et al. "Observation of elastic collisions between lithium atoms and calcium ions". In: *Physical Review A* 87.5 (May 2013), p. 052715. DOI: 10.1103/physreva.87.052715.

[45] Winthrop W. Smith, Oleg P. Makarov, and Jian Lin. "Cold ion-neutral collisions in a hybrid trap". In: *Journal of Modern Optics* 52.16 (Nov. 2005), pp. 2253–2260. DOI: 10.1080/09500340500275850.

[46] Christoph Zipkes et al. "A trapped single ion inside a Bose-Einstein condensate". In: *Nature* 464.7287 (Mar. 2010), pp. 388–391. DOI: 10.1038/nature08865.

[47] L. Ratschbacher et al. "Decoherence of a Single-Ion Qubit Immersed in a Spin-Polarized Atomic Bath". In: *Physical Review Letters* 110.16 (Apr. 2013), p. 160402. DOI: 10.1103/physrevlett.110.160402.

[48] Stefan Schmid, Arne Härter, and Johannes Hecker Denschlag. "Dynamics of a Cold Trapped Ion in a Bose-Einstein Condensate". In: *Physical Review Letters* 105.13 (Sept. 2010), p. 133202. DOI: 10.1103/physrevlett.105.133202.

[49] A. Härter and J. Hecker Denschlag. "Cold atom-ion experiments in hybrid traps". In: *Contemporary Physics* 55.1 (Jan. 2014), pp. 33–45. DOI: 10.1080/00107514.2013.854618.

[50] Carlo Sias and Michael Köhl. "Hybrid quantum systems of ions and atoms". In: (Jan. 2014). arXiv: 1401.3188 [cond-mat.quant-gas].

[51] Ch. Schneider et al. "Optical trapping of an ion". In: *Nature Photonics* 4.11 (Oct. 2010), pp. 772–775. DOI: 10.1038/nphoton.2010.236.

[52] Thomas Huber et al. "A far-off-resonance optical trap for a Ba+ ion". In: *Nat Commun* 5 (2014), p. 5587. ISSN: 2041-1723. DOI: 10.1038/ncomms6587.

[53] Elia Perego, Lucia Duca, and Carlo Sias. "Electro-Optical Ion Trap for Experiments with Atom-Ion Quantum Hybrid Systems". In: *Applied Sciences* 10.7 (Mar. 2020), p. 2222. DOI: 10.3390/app10072222.

[54] T. Schmid et al. "Rydberg Molecules for Ion-Atom Scattering in the Ultracold Regime". In: *Physical Review Letters* 120.15 (Apr. 2018), p. 153401. DOI: 10.1103/physrevlett.120.153401.

[55] Philipp Wessels et al. "Absolute strong-field ionization probabilities of ultracold rubidium atoms". In: *Communications Physics* 1.1 (July 2018). DOI: 10.1038/s42005-018-0032-5.

[56] Christoph Zipkes. "A Trapped Single Ion Inside a Bose-Einstein Condensate". PhD thesis. Robinson College, Cambridge, 2011.

[57] Marko Cetina, Andrew T. Grier, and Vladan Vuletić. "Micromotion-Induced Limit to Atom-Ion Sympathetic Cooling in Paul Traps". In: 109.25 (Dec. 2012), p. 253201. DOI: 10.1103/physrevlett.109.253201.

[58] Christoph Zipkes et al. "Kinetics of a single trapped ion in an ultracold buffer gas". In: 13.5 (May 2011), p. 053020. DOI: 10.1088/1367-2630/13/5/053020.

[59] P Langevin. "Une formule fondamentale de théorie cinétique". In: *Ann. Chim. et Physique* 5 (1905), pp. 269–300.

[60] Leonard Schiff. *Quantum mechanics*. 3rd edition. New York: McGraw-Hill, 1968. ISBN: 978-0070856431.

[61] E. Tiesinga et al. "A spectroscopic determination of scattering lengths for sodium atom collisions". In: *Journal of Research of the National Institute of Standards and Technology* 101.4 (July 1996), p. 505. DOI: 10.6028/jres.101.051.

[62] R. Côté and A. Dalgarno. "Ultracold atom-ion collisions". In: *Physical Review A* 62.1 (June 2000), p. 012709. DOI: 10.1103/physreva.62.012709.

[63] J Hasted. "Inelastic collisions between ions and atoms". In: *Proc. R. Soc. Lond. A*. Vol. 212. 1952, pp. 235–248. DOI: 10.1098/rspa.1952.0078.

[64] H. Schmaljohann et al. "Dynamics and thermodynamics in spinor quantum gases". In: *Applied Physics B* 79.8 (Dec. 2004), pp. 1001–1007. DOI: 10.1007/s00340-004-1664-6.

[65] David Reens et al. “Controlling spin flips of molecules in an electromagnetic trap”. In: *Physical Review A* 96.6 (Dec. 2017), p. 063420. DOI: 10.1103/physreva.96.063420.

[66] Giacomo Cappellini. “Two-orbital quantum phyics in Yb Fermi gases expliting the $^1S_0 \rightarrow {}^3P_0$ clock transition”. PhD thesis. University of Florence, 2015.

[67] Moritz Höfer. “A two-orbital quantum gas with tunable interactions”. PhD thesis. University of Munich, 2017.

[68] Marco Anderlini et al. “Controlled exchange interaction between pairs of neutral atoms in an optical lattice”. In: *Nature* 448.7152 (July 2007), pp. 452–456. DOI: 10.1038/nature06011.

[69] Wade G. Rellergert et al. “Measurement of a Large Chemical Reaction Rate between Ultracold Closed-Shell $^{40}Ca$ Atoms and Open-Shell $^{174}Yb^+$ Ions Held in a Hybrid Atom-Ion Trap”. In: *Physical Review Letters* 107.24 (Dec. 2011), p. 243201. DOI: 10.1103/physrevlett.107.243201.

[70] Felix H.J. Hall et al. “Ion-neutral chemistry at ultralow energies: dynamics of reactive collisions between laser-cooled $Ca^+$ ions and Rb atoms in an ion-atom hybrid trap”. In: *Molecular Physics* 111.14-15 (Apr. 2013), pp. 2020–2032. DOI: 10.1080/00268976.2013.780107.

[71] Felix H. J. Hall and Stefan Willitsch. “Millikelvin Reactive Collisions between Sympathetically Cooled Molecular Ions and Laser-Cooled Atoms in an Ion-Atom Hybrid Trap”. In: *Physical Review Letters* 109.23 (Dec. 2012), p. 233202. DOI: 10.1103/physrevlett.109.233202.

[72] Christoph Zipkes et al. “Cold Heteronuclear Atom-Ion Collisions”. In: *Physical Review Letters* 105.13 (Sept. 2010), p. 133201. DOI: 10.1103/physrevlett.105.133201.

[73] Artjom Krükow et al. “Reactive two-body and three-body collisions of $Ba^+$ in an ultracold Rb gas”. In: *Physical Review A* 94.3 (Sept. 2016), p. 030701. DOI: 10.1103/physreva.94.030701.

[74] Artjom Krükow. “Three-Body Reaction Dynamics in cold Atom-Ion Experiments”. PhD thesis. Universität Ulm, 2016.

[75] Jesús Pérez-Ríos. “Vibrational quenching and reactive processes of weakly bound molecular ions colliding with atoms at cold temperatures”. In: *Physical Review A* 99.2 (Feb. 2019), p. 022707. DOI: 10.1103/physreva.99.022707.

[76] M. Knoop, M. Vedel, and F. Vedel. “Lifetime, collisional-quenching, and j-mixing measurements of the metastable 3Dlevels of $Ca^+$”. In: *Physical Review A* 52.5 (Nov. 1995), pp. 3763–3769. DOI: 10.1103/physreva.52.3763.

[77] J. Deiglmayr et al. "Reactive collisions of trapped anions with ultracold atoms". In: *Physical Review A* 86.4 (Oct. 2012), p. 043438. DOI: 10.1103/physreva.86.043438.

[78] Stefan Willitsch et al. "Cold Reactive Collisions between Laser-Cooled Ions and Velocity-Selected Neutral Molecules". In: *Physical Review Letters* 100.4 (Jan. 2008), p. 043203. DOI: 10.1103/physrevlett.100.043203.

[79] B. Roth et al. "Ion-neutral chemical reactions between ultracold localized ions and neutral molecules with single-particle resolution". In: *Physical Review A* 73.4 (Apr. 2006), p. 042712. DOI: 10.1103/physreva.73.042712.

[80] Peter F. Staanum et al. "Probing Isotope Effects in Chemical Reactions Using Single Ions". In: *Physical Review Letters* 100.24 (June 2008), p. 243003. DOI: 10.1103/physrevlett.100.243003.

[81] Dieter Gerlich and Stevan Horning. "Experimental investigation of radiative association processes as related to interstellar chemistry". In: *Chemical Reviews* 92.7 (Nov. 1992), pp. 1509–1539. DOI: 10.1021/cr00015a003.

[82] Hauke Doerk, Zbigniew Idziaszek, and Tommaso Calarco. "Atom-ion quantum gate". In: *Physical Review A* 81.1 (Jan. 2010), p. 012708. DOI: 10.1103/physreva.81.012708.

[83] Lê Huy Nguyên et al. "Micromotion in trapped atom-ion systems". In: *Physical Review A* 85.5 (May 2012), p. 052718. DOI: 10.1103/physreva.85.052718.

[84] T. Secker et al. "Controlled long-range interactions between Rydberg atoms and ions". In: *Physical Review A* 94.1 (July 2016), p. 013420. DOI: 10.1103/physreva.94.013420.

[85] Anders Sørensen and Klaus Mølmer. "Quantum Computation with Ions in Thermal Motion". In: *Physical Review Letters* 82.9 (Mar. 1999), pp. 1971–1974. DOI: 10.1103/physrevlett.82.1971.

[86] Richard P. Feynman. "Simulating physics with computers". In: *International Journal of Theoretical Physics* 21.6-7 (June 1982), pp. 467–488. DOI: 10.1007/bf02650179.

[87] R. Blatt and C. F. Roos. "Quantum simulations with trapped ions". In: *Nature Physics* 8.4 (Apr. 2012), pp. 277–284. DOI: 10.1038/nphys2252.

[88] A. Negretti et al. "Generalized Kronig-Penney model for ultracold atomic quantum systems". In: *Physical Review B* 90.15 (Oct. 2014), p. 155426. DOI: 10.1103/physrevb.90.155426.

[89] Christoph Maschler and Helmut Ritsch. "Cold Atom Dynamics in a Quantum Optical Lattice Potential". In: *Physical Review Letters* 95.26 (Dec. 2005), p. 260401. DOI: 10.1103/physrevlett.95.260401.

[90] R. Gerritsma et al. "Bosonic Josephson Junction Controlled by a Single Trapped Ion". In: *Physical Review Letters* 109.8 (Aug. 2012), p. 080402. DOI: 10.1103/physrevlett.109.080402.

[91] Daniel Keefer and Regina de Vivie-Riedle. "Pathways to New Applications for Quantum Control". In: *Accounts of Chemical Research* 51.9 (Aug. 2018), pp. 2279–2286. DOI: 10.1021/acs.accounts.8b00244.

[92] Jennifer L. Herek et al. "Quantum control of energy flow in light harvesting". In: *Nature* 417.6888 (May 2002), pp. 533–535. DOI: 10.1038/417533a.

[93] A. Assion. "Control of Chemical Reactions by Feedback-Optimized Phase-Shaped Femtosecond Laser Pulses". In: *Science* 282.5390 (Oct. 1998), pp. 919–922. DOI: 10.1126/science.282.5390.919.

[94] L. Zhu et al. "Coherent Laser Control of the Product Distribution Obtained in the Photoexcitation of HI". In: *Science* 270.5233 (Oct. 1995), pp. 77–80. DOI: 10.1126/science.270.5233.77.

[95] Felix H.J. Hall et al. "Light-assisted cold chemical reactions of barium ions with rubidium atoms". In: *Molecular Physics* 111.12-13 (June 2013), pp. 1683–1690. DOI: 10.1080/00268976.2013.770930.

[96] Xin Tong et al. "State-selected ion-molecule reactions with Coulomb-crystallized molecular ions in traps". In: *Chemical Physics Letters* 547 (Sept. 2012), pp. 1–8. DOI: 10.1016/j.cplett.2012.06.042.

[97] Brianna R. Heazlewood and Timothy P. Softley. "Low-Temperature Kinetics and Dynamics with Coulomb Crystals". In: *Annual Review of Physical Chemistry* 66.1 (Apr. 2015), pp. 475–495. DOI: 10.1146/annurev-physchem-040214-121527.

[98] N. Poli et al. "Optical atomic clocks". In: *La rivista del Nuovo Cimento - Vol. 036 - Issue 12 - Pag. 555-624 - Year 2013* 36 (Jan. 2014), pp. 555–624. ISSN: 0393697X, 0393697X. DOI: 10.1393/ncr/i2013-10095-x. arXiv: 1401.2378 [physics.atom-ph].

[99] Andrew D. Ludlow et al. "Optical atomic clocks". In: *Reviews of Modern Physics* 87.2 (June 2015), pp. 637–701. DOI: 10.1103/revmodphys.87.637.

[100] Gretchen K Campbell et al. "The absolute frequency of the $^{87}$Sr optical clock transition". In: *Metrologia* 45.5 (Sept. 2008), pp. 539–548. DOI: 10.1088/0026-1394/45/5/008.

[101] C. Champenois et al. "Ion ring in a linear multipole trap for optical frequency metrology". In: *Physical Review A* 81.4 (Apr. 2010), p. 043410. DOI: 10.1103/physreva.81.043410.

[102] Tobias Bothwell et al. "JILA SrI optical lattice clock with uncertainty of $2.0\times10^{-18}$". In: *Metrologia* 56.6 (Oct. 2019), p. 065004. DOI: 10.1088/1681-7575/ab4089.

[103] W. F. McGrew et al. "Atomic clock performance enabling geodesy below the centimetre level". In: *Nature* 564.7734 (Nov. 2018), pp. 87–90. DOI: 10.1038/s41586-018-0738-2.

[104] Amar C. Vutha, Tom Kirchner, and Pierre Dubé. "Collisional frequency shift of a trapped-ion optical clock". In: *Physical Review A* 96.2 (Aug. 2017), p. 022704. DOI: 10.1103/physreva.96.022704.

[105] A. M. Hankin et al. "Systematic uncertainty due to background-gas collisions in trapped-ion optical clocks". In: *Physical Review A* 100.3 (Sept. 2019), p. 033419. DOI: 10.1103/physreva.100.033419.

[106] T. Rosenband et al. "Observation of the $^1S_0 \rightarrow {}^2P_0$ Clock Transition $^{27}Al^+$". In: *Physical Review Letters* 98.22 (May 2007), p. 220801. DOI: 10.1103/physrevlett.98.220801.

[107] Eric R. Hudson. "Sympathetic cooling of molecular ions with ultracold atoms". In: *EPJ Techniques and Instrumentation* 3.1 (Dec. 2016). DOI: 10.1140/epjti/s40485-016-0035-0.

[108] Peter Van Der Straten H. J. Metcalf. *Laser Cooling and Trapping*. SPRINGER NATURE, Sept. 1999. 323 pp. ISBN: 0387987479.

[109] D.A. Steck. *Quantum and Atom Optics*. URL: http://steck.us/teaching.

[110] Keith D. Bonin Vitaly V Kresin. *Electric-Dipole Polarizabilities of Atoms, Molecules, and Clusters*. WSPC, Nov. 1997. 270 pp. ISBN: 9810224931.

[111] John V. Prodan and William D. Phillips. "Chirping the light—fantastic? Recent NBS atom cooling experiments". In: 8.3-4 (Jan. 1984), pp. 231–235. DOI: 10.1016/0079-6727(84)90019-3.

[112] John V. Prodan, William D. Phillips, and Harold Metcalf. "Laser Production of a Very Slow Monoenergetic Atomic Beam". In: 49.16 (Oct. 1982), pp. 1149–1153. DOI: 10.1103/physrevlett.49.1149.

[113] T.W. Hänsch and A.L. Schawlow. "Cooling of gases by laser radiation". In: 13.1 (Jan. 1975), pp. 68–69. DOI: 10.1016/0030-4018(75)90159-5.

[114] K. Kowalski et al. "Magneto-optical Trap: Fundamentals and Realization". In: (2010). DOI: 10.12921/CMST.2010.SI.02.115-129.

[115] Christopher J. Foot. *Atomic Physics*. OXFORD UNIV PR, Jan. 2005. 346 pp. ISBN: 0198506961.

[116] Wolfgang Petrich et al. "Behavior of atoms in a compressed magneto-optical trap". In: 11.8 (Aug. 1994), p. 1332. DOI: 10.1364/josab.11.001332.

[117] M. Drewsen et al. “Investigation of sub-Doppler cooling effects in a cesium magneto-optical trap”. In: 59.3 (Sept. 1994), pp. 283–298. DOI: 10.1007/bf01081396.

[118] Giacomo Valtolina. “Development of an experimental apparatus for the production and study of ultracold atomic gases of fermionic lithium”. MA thesis. Università degli studi di Milano, 2012.

[119] Paul D. Lett et al. “Observation of Atoms Laser Cooled below the Doppler Limit”. In: 61.2 (July 1988), pp. 169–172. DOI: 10.1103/physrevlett.61.169.

[120] J. Dalibard and C. Cohen-Tannoudji. “Laser cooling below the Doppler limit by polarization gradients: simple theoretical models”. In: 6.11 (Nov. 1989), p. 2023. DOI: 10.1364/josab.6.002023.

[121] Claude N. Cohen-Tannoudji and William D. Phillips. “New Mechanisms for Laser Cooling”. In: 43.10 (Oct. 1990), pp. 33–40. DOI: 10.1063/1.881239.

[122] A. Aspect et al. “Laser Cooling below the One-Photon Recoil Energy by Velocity-Selective Coherent Population Trapping”. In: *Physical Review Letters* 61.7 (Aug. 1988), pp. 826–829. DOI: 10.1103/physrevlett.61.826.

[123] M. S. Shahriar et al. “Continuous polarization-gradient precooling-assisted velocity-selective coherent population trapping”. In: 48.6 (Dec. 1993), R4035–R4038. DOI: 10.1103/physreva.48.r4035.

[124] M Weidemüller et al. “A Novel Scheme for Efficient Cooling below the Photon Recoil Limit”. In: 27.2 (July 1994), pp. 109–114. DOI: 10.1209/0295-5075/27/2/006.

[125] M A Ol-shanii and V G Minogin. “Three-dimensional velocity-selective coherent population trapping of (3+1)-level atoms”. In: 3.6 (Dec. 1991), pp. 317–322. DOI: 10.1088/0954-8998/3/6/001.

[126] A. Burchianti et al. “Efficient all-optical production of largeLi6quantum gases usingD1gray-molasses cooling”. In: *Physical Review A* 90.4 (Oct. 2014), p. 043408. DOI: 10.1103/physreva.90.043408.

[127] Paul Hamilton et al. “Sisyphus cooling of lithium”. In: 89.2 (Feb. 2014), p. 023409. DOI: 10.1103/physreva.89.023409.

[128] Gregers Poulsen. “Sideband Cooling of Atomic and Molecular Ions”. PhD thesis. University of Aarhus, 2011.

[129] Stig Stenholm. “The semiclassical theory of laser cooling”. In: 58.3 (July 1986), pp. 699–739. DOI: 10.1103/revmodphys.58.699.

[130] Immanuel Bloch. “Ultracold quantum gases in optical lattices”. In: *Nature Physics* 1.1 (Oct. 2005), pp. 23–30. DOI: 10.1038/nphys138.

[131] Cecilia Muldoon et al. “Control and manipulation of cold atoms in optical tweezers”. In: *New Journal of Physics* 14.7 (July 2012), p. 073051. DOI: 10.1088/1367-2630/14/7/073051.

[132] C. Ospelkaus et al. “Ultracold Heteronuclear Molecules in a 3D Optical Lattice”. In: *Physical Review Letters* 97.12 (Sept. 2006), p. 120402. DOI: 10.1103/physrevlett.97.120402.

[133] Loïc Anderegg et al. “An optical tweezer array of ultracold molecules”. In: *Science* 365.6458 (Sept. 2019), pp. 1156–1158. DOI: 10.1126/science.aax1265.

[134] David G. Grier and Yael Roichman. “Holographic optical trapping”. In: 45.5 (Feb. 2006), p. 880. DOI: 10.1364/ao.45.000880.

[135] A. Mosk et al. “Resonator-enhanced optical dipole trap for fermionic lithium atoms”. In: *Optics Letters* 26.23 (Dec. 2001), p. 1837. DOI: 10.1364/ol.26.001837.

[136] Nicolas Schlosser et al. “Sub-poissonian loading of single atoms in a microscopic dipole trap”. In: *Nature* 411.6841 (June 2001), pp. 1024–1027. DOI: 10.1038/35082512.

[137] Mark Kasevich and Steven Chu. “Laser cooling below a photon recoil with three-level atoms”. In: 69.12 (Sept. 1992), pp. 1741–1744. DOI: 10.1103/physrevlett.69.1741.

[138] Simon Stellmer et al. “Laser Cooling to Quantum Degeneracy”. In: 110.26 (June 2013), p. 263003. DOI: 10.1103/physrevlett.110.263003.

[139] Jiazhong Hu et al. “Creation of a Bose-condensed gas of87Rb by laser cooling”. In: *Science* 358.6366 (Nov. 2017), pp. 1078–1080. DOI: 10.1126/science.aan5614.

[140] Wolfgang Ketterle and N.J. Van Druten. “Evaporative Cooling of Trapped Atoms”. In: *Advances In Atomic, Molecular, and Optical Physics*. Elsevier, 1996, pp. 181–236. DOI: 10.1016/s1049-250x(08)60101-9.

[141] K. B. Davis, M. -O. Mewes, and W. Ketterle. “An analytical model for evaporative cooling of atoms”. In: 60.2-3 (1995), pp. 155–159. DOI: 10.1007/bf01135857.

[142] Klaus Blaum. “High-accuracy mass spectrometry with stored ions”. In: *Physics Reports* 425.1 (Mar. 2006), pp. 1–78. DOI: 10.1016/j.physrep.2005.10.011.

[143] Wolfgang Paul. “Electromagnetic traps for charged and neutral particles”. In: *Reviews of Modern Physics* 62.3 (July 1990), pp. 531–540. DOI: 10.1103/revmodphys.62.531.

[144] D. Leibfried et al. "Quantum dynamics of single trapped ions". In: *Reviews of Modern Physics* 75.1 (Mar. 2003), pp. 281–324. DOI: 10.1103/revmodphys.75.281.

[145] D. J. Berkeland et al. "Minimization of ion micromotion in a Paul trap". In: *Journal of Applied Physics* 83.10 (May 1998), pp. 5025–5033. DOI: 10.1063/1.367318.

[146] Timm F. Gloger et al. "Ion-trajectory analysis for micromotion minimization and the measurement of small forces". In: *Physical Review A* 92.4 (Oct. 2015), p. 043421. DOI: 10.1103/physreva.92.043421.

[147] Y. Ibaraki, U. Tanaka, and S. Urabe. "Detection of parametric resonance of trapped ions for micromotion compensation". In: *Applied Physics B* 105.2 (Mar. 2011), pp. 219–223. DOI: 10.1007/s00340-011-4463-x.

[148] A. Härter et al. "Minimization of ion micromotion using ultracold atomic probes". In: *Applied Physics Letters* 102.22 (June 2013), p. 221115. DOI: 10.1063/1.4809578.

[149] Christian Schneider et al. "Influence of static electric fields on an optical ion trap". In: *Physical Review A* 85.1 (Jan. 2012), p. 013422. DOI: 10.1103/physreva.85.013422.

[150] Martin Enderlein et al. "Single Ions Trapped in a One-Dimensional Optical Lattice". In: *Physical Review Letters* 109.23 (Dec. 2012), p. 233004. DOI: 10.1103/physrevlett.109.233004.

[151] Leon Karpa et al. "Suppression of Ion Transport due to Long-Lived Subwavelength Localization by an Optical Lattice". In: *Physical Review Letters* 111.16 (Oct. 2013), p. 163002. DOI: 10.1103/physrevlett.111.163002.

[152] Alexander Lambrecht et al. "Long lifetimes and effective isolation of ions in optical and electrostatic traps". In: *Nature Photonics* 11.11 (Oct. 2017), pp. 704–707. DOI: 10.1038/s41566-017-0030-2.

[153] Ziv Meir et al. "Dynamics of a Ground-State Cooled Ion Colliding with Ultracold Atoms". In: 117.24 (Dec. 2016), p. 243401. DOI: 10.1103/physrevlett.117.243401.

[154] Alexander Kramida and Yuri Ralchenko. *NIST Atomic Spectra Database, NIST Standard Reference Database 78*. en. 1999. DOI: 10.18434/T4W30F.

[155] Jasmeet Kaur et al. "Magic wavelengths in the alkaline-earth-metal ions". In: *Physical Review A* 92.3 (Sept. 2015), p. 031402. DOI: 10.1103/physreva.92.031402.

[156] Elia Perego. "A novel setup for trapping and cooling Barium ions for atom-ion experiments". PhD thesis. Politechnic of Turin, 2019.

[157] E. R. I. Abraham et al. "Singlets-wave scattering lengths ofLi6andLi7". In: *Physical Review A* 53.6 (June 1996), R3713–R3715. DOI: 10.1103/physreva.53.r3713.

[158] Randall G. Hulet, Jason H. V. Nguyen, and Ruwan Senaratne. "Methods for preparing quantum gases of lithium". In: *Review of Scientific Instruments* 91.1 (Jan. 2020), p. 011101. DOI: 10.1063/1.5131023.

[159] L. N. Rozanov. *Vacuum technique*. London New York: Taylor & Francis, 2002. ISBN: 041527351X.

[160] Robert Krebs. *The History and Use of Our Earth's Chemical Elements*. Greenwood, July 2006. 448 pp. ISBN: 0313334382.

[161] R C Weast; M J Astle; W H Beyer. *CRC Handbook of Chemistry and Physics*. Taylor & Francis Ltd, June 1984. 1604 pp. ISBN: 0367712601.

[162] P T Greenland, M A Lauder, and D J H Wort. "Atomic beam velocity distributions". In: *Journal of Physics D: Applied Physics* 18.7 (July 1985), pp. 1223–1232. DOI: 10.1088/0022-3727/18/7/009.

[163] Elettra Neri. "Mass imbalanced Fermi mixtures with 2- and 3-body resonantinteractions". PhD thesis. Università di Firenze, 2018.

[164] URL: http://quantumgases.lens.unifi.it/.

[165] M. E. Gehm. "Preparation of an Optically-Trapped Degenerate Fermi Gas of 6Li: Finding theRoute to Degeneracy". PhD thesis. Duke University, 2003.

[166] U. Schünemann et al. "Simple scheme for tunable frequency offset locking of two lasers". In: *Review of Scientific Instruments* 70.1 (Jan. 1999), pp. 242–243. DOI: 10.1063/1.1149573.

[167] Yusuke Hisai et al. "Evaluation of laser frequency offset locking using an electrical delay line". In: *Applied Optics* 57.20 (July 2018), p. 5628. DOI: 10.1364/ao.57.005628.

[168] Amnon Yariv. *Photonics : optical electronics in modern communications*. New York Oxford: Oxford University Press, 2007. ISBN: 9780195179460.

[169] C Mok et al. "Design and construction of an efficient electro-optic modulator for laser spectroscopy". In: *Canadian Journal of Physics* 84.9 (Sept. 2006), pp. 775–786. DOI: 10.1139/p06-074.

[170] Eric D. Black. "An introduction to Pound-Drever-Hall laser frequency stabilization". In: *American Journal of Physics* 69.1 (Jan. 2001), pp. 79–87. DOI: 10.1119/1.1286663.

[171] Amelia Detti. "A new experimental apparatus for atom-ion quantum mixtures". PhD thesis. University of Florence, 2019.

[172] Christopher Bowick. *RF Circuit Design*. Elsevier Science & Technology, Nov. 2007. 256 pp. ISBN: 0750685182.

[173] A Mansingh and A Dhar. "The AC conductivity and dielectric constant of lithium niobate single crystals". In: *Journal of Physics D: Applied Physics* 18.10 (Oct. 1985), pp. 2059–2071. DOI: 10.1088/0022-3727/18/10/016.

[174] H.A. Wheeler. "Simple Inductance Formulas for Radio Coils". In: *Proceedings of the IRE* 16.10 (Oct. 1928), pp. 1398–1400. DOI: 10.1109/jrproc.1928.221309.

[175] Seon-Jae Jeon and Dong-Wook Seo. "Coupling Coefficient Measurement Method with Simple Procedures Using a Two-Port Network Analyzer for a Multi-Coil WPT System". In: *Energies* 12.20 (Oct. 2019), p. 3950. DOI: 10.3390/en12203950.

[176] Lucia Duca. *private communication*. 2021.

[177] A Fabry C; Perot. "Theorie et applications d'une nouvelle methode de spectroscopie interferentielle". In: *Ann. Chim. Phys.* 16.7785 (1899), p. 7.

[178] Orazio Svelto. *Principles of Lasers*. Springer-Verlag GmbH, Aug. 2010. ISBN: 1441913017.

[179] Joseph Verdeyen. *Laser electronics*. Englewood Cliffs, N.J: Prentice Hall, 1995. ISBN: 9780137066667.

[180] Michael Hercher. "The Spherical Mirror Fabry-Perot Interferometer". In: *Applied Optics* 7.5 (May 1968), p. 951. DOI: 10.1364/ao.7.000951.

[181] G. Rempe et al. "Measurement of ultralow losses in an optical interferometer". In: *Optics Letters* 17.5 (Mar. 1992), p. 363. DOI: 10.1364/ol.17.000363.

[182] Christina J. Hood, H. J. Kimble, and Jun Ye. "Characterization of high-finesse mirrors: Loss, phase shifts, and mode structure in an optical cavity". In: *Physical Review A* 64.3 (Aug. 2001), p. 033804. DOI: 10.1103/physreva.64.033804.

[183] Dana Z. Anderson. "Alignment of resonant optical cavities". In: *Applied Optics* 23.17 (Sept. 1984), p. 2944. DOI: 10.1364/ao.23.002944.

[184] W. Koechner. "Thermal Lensing in a Nd:YAG Laser Rod". In: *Applied Optics* 9.11 (Nov. 1970), p. 2548. DOI: 10.1364/ao.9.002548.

[185] Karl Johan Åström and Richard M. Murray. *Feedback Systems. An Introduction for Scientists and Engineers*. Princeton: Princeton University Press, 2010. ISBN: 9780691135762. DOI: 10.2307/j.ctvcm4gdk.

[186] John Bechhoefer. "Feedback for physicists: A tutorial essay on control". In: *Reviews of Modern Physics* 77.3 (Aug. 2005), pp. 783–836. DOI: 10.1103/revmodphys.77.783.

[187] L. Ricci et al. "A compact grating-stabilized diode laser system for atomic physics". In: *Optics Communications* 117.5-6 (June 1995), pp. 541–549. DOI: 10.1016/0030-4018(95)00146-y.

[188] T.W. Hansch and B. Couillaud. "Laser frequency stabilization by polarization spectroscopy of a reflecting reference cavity". In: *Optics Communications* 35.3 (Dec. 1980), pp. 441–444. DOI: 10.1016/0030-4018(80)90069-3.

[189] R. W. P. Drever et al. "Laser phase and frequency stabilization using an optical resonator". In: *Applied Physics B Photophysics and Laser Chemistry* 31.2 (June 1983), pp. 97–105. DOI: 10.1007/bf00702605.

[190] Gianni Di Domenico, Stéphane Schilt, and Pierre Thomann. "Simple approach to the relation between laser frequency noise and laser line shape". In: *Applied Optics* 49.25 (Aug. 2010), p. 4801. DOI: 10.1364/ao.49.004801.

[191] Richard W. Fox, Chris W. Oates, and Leo W. Hollberg. "Stabilizing diode lasers to high-finesse cavities". In: *Cavity-Enhanced Spectroscopies*. Elsevier, 2003, pp. 1–46. DOI: 10.1016/s1079-4042(03)80017-6.

[192] Simone Borri et al. "Frequency-Noise Dynamics of Mid-Infrared Quantum Cascade Lasers". In: *IEEE Journal of Quantum Electronics* 47.7 (July 2011), pp. 984–988. DOI: 10.1109/jqe.2011.2147760.

[193] F. Berto et al. "Prospects for single-photon sideband cooling of optically trapped neutral atoms". In: *Physical Review Research* 3.4 (Nov. 2021), p. 043106. DOI: 10.1103/physrevresearch.3.043106.

[194] Michael Gröbner et al. "Degenerate Raman sideband cooling of K39". In: *Physical Review A* 95.3 (Mar. 2017), p. 033412. DOI: 10.1103/physreva.95.033412.

[195] R. Taïeb et al. "Cooling and localization of atoms in laser-induced potential wells". In: *Physical Review A* 49.6 (June 1994), pp. 4876–4887. DOI: 10.1103/physreva.49.4876.

[196] Alexandre Cooper et al. "Alkaline-Earth Atoms in Optical Tweezers". In: *Physical Review X* 8.4 (Dec. 2018), p. 041055. DOI: 10.1103/physrevx.8.041055.

[197] K. Rzążewski and R. W. Boyd. "Equivalence of interaction hamiltonians in the electric dipole approximation". In: *Journal of Modern Optics* 51.8 (May 2004), pp. 1137–1147. DOI: 10.1080/09500340408230412.

[198] Alexander L. Fetter and J. D. Walecka. *Quantum Theory of Many-Particle Systems*. Dover Publications Inc., May 2003. ISBN: 0486428273. DOI: 10.1002/9783527667550.ch8.

[199] K. B. Whaley and J. C. Light. "Rotating-frame transformations: A new approximation for multiphoton absorption and dissociation in laser fields". In: *Physical Review A* 29.3 (Mar. 1984), pp. 1188–1207. DOI: 10.1103/physreva.29.1188.

[200] J. Javanainen and S. Stenholm. "Laser cooling of trapped particles III: The Lamb-Dicke limit". In: *Applied Physics* 24.2 (Feb. 1981), pp. 151–162. DOI: 10.1007/bf00902273.

[201] G. Lindblad. "On the generators of quantum dynamical semigroups". In: *Communications in Mathematical Physics* 48.2 (June 1976), pp. 119–130. DOI: 10.1007/bf01608499.

[202] Andrzej Kossakowski Vittorio Gorini and E. C. G. Sudarshan. "Completely positive dynamical semigroups of N-level systems". In: *Journal of Mathematical Physics* 17.5 (1976), p. 821. DOI: 10.1063/1.522979.

[203] Heinz-Peter Breuer and Francesco Petruccione. *The Theory of Open Quantum Systems*. Oxford University Press, Feb. 2002. ISBN: 0198520638.

[204] Daniel Manzano. "A short introduction to the Lindblad master equation". In: *AIP Advances* 10.2 (Feb. 2020), p. 025106. DOI: 10.1063/1.5115323.

[205] A P Kazantsev, G I Surdutovich, and V P Yakovlev. *Mechanical Action of Light on Atoms*. WORLD SCIENTIFIC, Aug. 1990. DOI: 10.1142/0585.

[206] E Brion, L H Pedersen, and K Mølmer. "Adiabatic elimination in a lambda system". In: *Journal of Physics A: Mathematical and Theoretical* 40.5 (Jan. 2007), pp. 1033–1043. DOI: 10.1088/1751-8113/40/5/011.

[207] Florentin Reiter and Anders S. Sørensen. "Effective operator formalism for open quantum systems". In: *Physical Review A* 85.3 (Mar. 2012), p. 032111. DOI: 10.1103/physreva.85.032111.

[208] M. A. Norcia, A. W. Young, and A. M. Kaufman. "Microscopic Control and Detection of Ultracold Strontium in Optical-Tweezer Arrays". In: *Physical Review X* 8.4 (Dec. 2018), p. 041054. DOI: 10.1103/physrevx.8.041054.

[209] Jessie T. Zhang et al. "Forming a Single Molecule by Magnetoassociation in an Optical Tweezer". In: *Physical Review Letters* 124.25 (June 2020), p. 253401. DOI: 10.1103/physrevlett.124.253401.

[210] K.B. Blagoev and V.A. Komarovskii. "Lifetimes of Levels of Neutral and Singly Ionized Lanthanide Atoms". In: *Atomic Data and Nuclear Data Tables* 56.1 (Jan. 1994), pp. 1–40. DOI: 10.1006/adnd.1994.1001.

[211] F. Scazza. *private communication*. 2021.

[212] Y. Yu et al. "Motional-ground-state cooling outside the Lamb-Dicke regime". In: *Physical Review A* 97.6 (June 2018), p. 063423. DOI: 10.1103/physreva.97.063423.

[213] S. Saskin et al. "Narrow-Line Cooling and Imaging of Ytterbium Atoms in an Optical Tweezer Array". In: *Physical Review Letters* 122.14 (Apr. 2019), p. 143002. DOI: 10.1103/physrevlett.122.143002.

[214] M. S. Safronova, U. I. Safronova, and Charles W. Clark. "Magic wavelengths for optical cooling and trapping of lithium". In: *Physical Review A* 86.4 (Oct. 2012), p. 042505. DOI: 10.1103/physreva.86.042505.

[215] Rudolf Grimm, Matthias Weidemüller, and Yurii B. Ovchinnikov. "Optical Dipole Traps for Neutral Atoms". In: *Advances In Atomic, Molecular, and Optical Physics*. Elsevier, 2000, pp. 95–170. DOI: 10.1016/s1049-250x(08)60186-x.

[216] Jean Dalibard, Yvan Castin, and Klaus Mølmer. "Wave-function approach to dissipative processes in quantum optics". In: *Physical Review Letters* 68.5 (Feb. 1992), pp. 580–583. DOI: 10.1103/physrevlett.68.580.

[217] R. Dum, P. Zoller, and H. Ritsch. "Monte Carlo simulation of the atomic master equation for spontaneous emission". In: *Physical Review A* 45.7 (Apr. 1992), pp. 4879–4887. DOI: 10.1103/physreva.45.4879.

[218] Howard Carmichael. *An open systems approach to quantum optics : lectures presented at the Université Libre de Bruxelles October 28 to November 4, 1991*. Berlin, Heidelberg: Springer Berlin Heidelberg, 1993. ISBN: 9783540476207.

[219] G. C: Hegerfeldt and T.S. Wilser. "Ensemble or Individual System, Collapse or no Collapse: A Description of a Single Radiating Atom". In: *Classical and Quantum Systems*. Ed. by World Scientific. Proceedings of the Second International Wigner Symposium. World Scientific. 1992, pp. 104–105.

[220] J.R. Johansson, P.D. Nation, and Franco Nori. "QuTiP 2: A Python framework for the dynamics of open quantum systems". In: *Computer Physics Communications* 184.4 (Apr. 2013), pp. 1234–1240. DOI: 10.1016/j.cpc.2012.11.019.

[221] William H. Press et al. *Numerical recipes: the art of scientific computing*. Cambridge Cambridgeshire New York: Cambridge University Press, Sept. 2007. 1248 pp. ISBN: 978-0521880688.

[222] E. Wigner. "On the Quantum Correction For Thermodynamic Equilibrium". In: *Physical Review* 40.5 (June 1932), pp. 749–759. DOI: 10.1103/physrev.40.749.

[223] J. N. L. Connor et al. "Eigenvalues of the Schrödinger equation for a periodic potential with nonperiodic boundary conditions: A uniform semiclassical analysis". In: *The Journal of Chemical Physics* 80.10 (May 1984), pp. 5095–5106. DOI: 10.1063/1.446581.

[224] D. Babusci, G. Dattoli, and M. Quattromini. "On integrals involving Hermite polynomials". In: (Mar. 2011). arXiv: 1103.1210 [math-ph].

[225] Tommaso Caneva, Tommaso Calarco, and Simone Montangero. "Chopped random-basis quantum optimization". In: *Physical Review A* 84.2 (Aug. 2011), p. 022326. DOI: 10.1103/physreva.84.022326.

[226] Jonathan Keeling. *Light-Matter Interactions and Quantum Optics*. URL: https://www.st-andrews.ac.uk/~jmjk/keeling/teaching/quantum-optics.pdf.

[227] Bharath Srivathsan et al. "Measuring the temperature and heating rate of a single ion by imaging". In: *New Journal of Physics* 21.11 (Nov. 2019), p. 113014. DOI: 10.1088/1367-2630/ab4f43.

[228] S. Knünz et al. "Sub-millikelvin spatial thermometry of a single Doppler-cooled ion in a Paul trap". In: *Physical Review A* 85.2 (Feb. 2012), p. 023427. DOI: 10.1103/physreva.85.023427.

This Ph.D. thesis has been typeset by means of the TEX-system facilities. The typesetting engine was pdfLATEX. The document class was `toptesi`, by Claudio Beccari, with option `tipotesi=scudo`. This class is available in every up-to-date and complete TEX-system installation.